UNIVERSITY OF SOUTHAMPTON

FACULTY OF ENGINEERING, SCIENCE & MATHEMATICS

School of Chemistry

Engineering Substrates for SERS: Fundamentals and Applications

by

Sumeet Mahajan

Thesis for the degree of Doctor of Philosophy

September 2008

UNIVERSITY OF SOUTHAMPTON

ABSTRACT

FACULTY OF ENGINEERING, SCIENCE & MATHEMATICS
SCHOOL OF CHEMISTRY

Doctor of Philosophy

ENGINEERING SUBSTRATES FOR SERS: FUNDAMENTALS & APPLICATIONS

by Sumeet Mahajan

This work describes studies on sphere segment void (SSV) substrates for surface-enhanced Raman and resonant Raman scattering (SER(R)S) and their application in detecting and differentiating mutations in DNA sequences. SSV substrates are fabricated using the colloidal crystal templating strategy which has been optimized, improved and extended during this thesis work. Successful fabrication of substrates with a range of metals such as rhodium, nickel, platinum, palladium and gold was carried out although the bulk of the work presented in this thesis deals with gold SSV substrates. SSV substrates have unique optical and plasmonic properties, which can be manipulated controllably using the sphere size used for templating and film height during electrodeposition; allowing their tuning for SERS suiting a particular excitation laser. This tailoring of substrates for visible to infrared range of laser wavelengths is demonstrated establishing the plasmon engineering approach for optimum SERS with different media, metal and laser wavelengths. Not only the SERS peak intensities but also the spectral continuum (background) observed on SSV substrates has been found to be correlated to the strength of plasmons on the surface and nature of molecules adsorbed on the surface. The substrates have also been found to be suitable for SERRS with enhancements ~10^3 stronger than for SERS. All these studies permitted the development of a biosensing application based on SER(R)S.

Using gold SSV substrates a SER(R)S application for detecting DNA sequences has been developed wherein the stability and reusability of substrates as well as the extreme sensitivity of detection is demonstrated. The detection methodology has been extended further by developing a method for distinguishing mutations in DNA sequences by carrying out denaturation (melting) of surface-bound duplexes. The melting can be induced thermally or electrochemically and monitored by SER(R)S. With this method, termed SERS-melting, it has been possible to discriminate mutations using sequences in the CFTR gene with model synthetic oligonucleotides as well as with unpurified PCR amplicons. Flexibility in the choice of the label, which can be either non-resonant, partially resonant or resonant with the laser employed and electroactive at the same time is demonstrated. The electrochemically induced SERS-melting method has been found to be dependent on pH and ionic strength of the buffer solution.

TABLE OF CONTENTS

Declaration of Authorship

I, Sumeet Mahajan,

declare that the thesis entitled

Engineering Substrates for SERS: Fundamentals and Applications

and the work presented in the thesis are both my own, and have been generated by me as the result of my own original research. I confirm that:

- this work was done wholly or mainly while in candidature for a research degree at this University;
- where any part of this thesis has previously been submitted for a degree or any other qualification at this University or any other institution, this has been clearly stated;
- where I have consulted the published work of others, this is always clearly attributed;
- where I have quoted from the work of others, the source is always given. With the exception of such quotations, this thesis is entirely my own work;
- I have acknowledged all main sources of help;
- where the thesis is based on work done by myself jointly with others, I have made clear exactly what was done by others and what I have contributed myself;
- parts of this work have been published as:

Papers

1. Sumeet Mahajan, James Richardson, Tom Brown and Philip Bartlett, "SERS-Melting: A new Method for Discriminating Mutations in DNA Sequences" *J. Am. Chem. Soc.*, 10.1021/ja805517q, **2008**.
2. Sumeet Mahajan, Jeremy Baumberg, Andrea Russell and Philip Bartlett, "Reproducible SERRS from Structured Gold Surfaces", *Phys. Chem. Chem. Phys.*, 9 (45), **2007**, 6016-6020.
3. Mamdouh Abdelsalam, Sumeet Mahajan, Philip Bartlett, Jeremy Baumberg, Andrea Russell, "SERS at Structured Palladium and Platinum Surfaces", *J. Am. Chem. Soc.*, 129 (23) **2007,** 7399-7406.
4. Robin Cole, Jeremy Baumberg, F. J Garcia de Abajo, Sumeet Mahajan, Mamdouh Abdelsalam, Philip Bartlett, "Understanding Plasmons in Nanoscale Voids", *Nano Letters*, 7 (7), **2007**, 2094-2100.
5. Sumeet Mahajan, Mamdouh Abdelsalam, Yoshi Suguwara, Jeremy Baumberg, Suzanne Cintra, Andrea Russell, Philip Bartlett, "Tuning Plasmons on Nanostructured Substrates for NIR-SERS", *Phys. Chem. Chem. Phys.*, 9(1), **2007,** 104-109.
6. Tim Kelf, Yoshi Sugawara, Jeremy Baumberg, Mamdouh Abdelsalam, Suzanne Cintra, Sumeet Mahajan, Andrea Russell and Philip Bartlett, "Localized and Delocalized Plasmons in Metallic Nanovoids", *Phys. Rev. B*, 74, **2006**, 245415-26.
7. Robin Cole, Jeremy Baumberg, Sumeet Mahajan, Mamdouh Abdelsalam, Philip Bartlett, "Easily Coupled Whispering Gallery Plasmons in Dielectric Nanospheres Embedded in Gold Films", *Phys. Rev. Lett. 97*, **2006,** 137401-4.

Patents

1. Detection of Mutations in DNA Sequences; Inventors: Sumeet Mahajan, James Richardson, Tom Brown and Phil Bartlett, British Patent Application No. 0803593.3.
2. Colour Change Material and Method of Manufacture thereof. Inventors: Jeremy Baumberg, Sumeet Mahajan, Robin Cole and Phil Bartlett, British Patent Application number 0709846.0; PCT Int. Pat. Applied.

Signed: .....[redacted].....

Date: 11/11/2008

Acknowledgements

It is with great pleasure that I acknowledge everyone who has helped me during the last three years. I would like to especially thank Phil for being an excellent supervisor to me; my PhD experience turned out to be exactly what I had dreamt for, so in that sense he is my ideal supervisor. I also thank Mamdouh for teaching me the initial skills and for his invaluable help and support throughout. I am grateful for the support and motivation provided by Andrea and Jeremy during the last three years. I acknowledge Tom for his collaboration for the DNA work and am also grateful for his support. I thank Pat for the discussions on spectroscopy and help.

Thanks are due to everyone in the Bartlett group. In particular, I would like to thank Mohamed for his guidance with some electrochemistry experiments, discussions and constant encouragement to finish my thesis; Liz for her initial help with contact angle measurements and useful discussions throughout; Fabrice for his help with Raman; Maciej, David, Magda, Thomas and others for the enlightening coffee breaks and the camaraderie at work place making the Bartlett group a great group to work in.

I also thank Robin and Bruno for the experiments in Physics, insightful discussions on plasmons and exchange of ideas; James for the DNA synthesis work and Alistair Clark for the vapour deposition on slides and general trouble-shooting support.

I would also like to thank people of the school; Clare, Sally, Jan, Nanou and Bevy for helping in my PhD going smoothly. I acknowledge the scholarship from ORSAS for my PhD.

Last but not the least I acknowledge the help from my family, especially my wife for her enormous patience and support during the course of this thesis without which none of this would have been possible.

1 Introduction

1.1 Nano-/micro scale structuring in nature and photonic crystals

The blue iridescent colour of the wings of a morpho butterfly (Figure 1.1), the strength of an abalone shell and the self-cleaning nature of a lotus leaf is due to their respective structure appropriately patterned on the micro or nano-scale. Another example of nature's abundant architectural masterpieces is the Opal; a class of popular, naturally occurring, precious stones. The word opal has its roots in the Sanskrit word, 'upala', meaning "precious stone", which evolved to Greek 'opallios' and the Roman word 'opalus' meaning "to see a change of colour" [4]. Natural opals consist of tiny spheres of hydrated silica (SiO_2*nH_2O) arranged in parallel planes, serving as diffraction gratings, making them highly iridescent [4]. These opalescent gemstones, consisting of a three-dimensional lattice of sub-micron dielectric spheres, are natural photonic crystals, since they modulate propagating photons just like semi-conductor crystals modulate the flow of electrons. Further, similar to inhibition of electrons of certain energies within semi-conductors, due to their band gap, a photonic crystal can prohibit propagation of electromagnetic (EM) waves at certain energies and in certain directions.

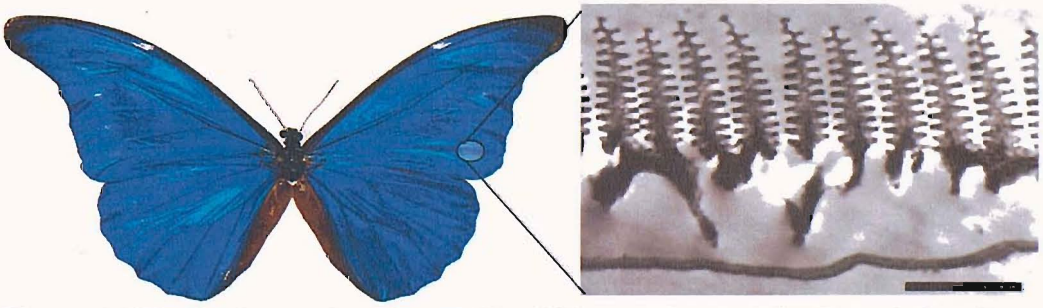

Figure 1.1 Morpho rhetenor butterfly. (a) Blue iridiscent wings and (b) Transmission electron microscope (TEM) image of the wing-scale cross-sections; Scale bar: 1.6 μm. Adapted from [2]

The inhibition of propagating EM waves for a range of wavelengths inside the structure is called the photonic band gap. If the inhibition is in all dimensions the material is said to possess a complete band gap. However, the periodic arrangement of silica dielectric spheres as in an opal in the face-centred cubic (FCC) geometry does not create a complete photonic band gap though it does inhibit propagation of certain wavelengths in certain directions [6-8]. Thus, the opal structure displays stop-bands or has a pseudo-band gap rather than a complete one. Nevertheless, the opaline structure does have interesting optical properties as even partial gaps over a wide range of angles would entail intense reflectivity

over those angles. In a host of applications a partial photonic band gap is sufficient and a complete band gap is not necessary. However, the real challenge has been the fabrication of photonic crystals as almost all of the initial work has been carried out with lithographic techniques, again borrowing the prevalent techniques from the semi-conductor industry, which are not only complex but also expensive.

1.2 Colloidal assembly

A possible way to overcome the fabrication challenges is the use of self-assembly methods. Artificial opals can be fabricated by self-assembling colloidal spheres of different materials and diameters on a variety of substrates. Silica [9], polymethylmethacrylate (PMMA) and polystyrene latex spheres [10] have been used for the formation of colloidal crystal films. Silica and polystyrene spheres are available commercially from many suppliers with extremely low polydispersity (less than 1%), alternatively they can be easily synthesized [11, 12]. Latex spheres have the advantage that they can be removed rather easily by dissolution in organic solvents such as toluene, tetrahydrofuran or dimethylformamide or by calcination compared to silica spheres which have to be etched out using hydrofluoric acid (HF) solutions. The fabrication process itself depends on the kind of material used for the spheres.

Silica spheres are heavier (density ~ 2.2 g/cm^3) than latex (density ~ 1.05 g/cm^3) ones and hence, more suitable for formation of 3-D crystals using gravitational sedimentation. Formation of colloidal crystals under the influence of gravity alone is extremely slow and can take from days to months [13]. Other disadvantages include lack of control over the morphology of the top layer, the settling rate and the number of layers itself [12]. The settling can be accelerated using techniques such as centrifugation and filtration. The sedimentation rate has to be controlled among other parameters to obtain a 3-D ordered lattice. The settling rate can also be controlled by carrying out the assembly under the influence of an electric field. This method is referred to as the electrophoretic deposition method [14] wherein the colloidal suspension is held between two parallel electrodes and a voltage is used to move the particles to the bottom electrode. One of the most popular techniques used for obtaining 3-D assembly of colloidal spheres on planar surfaces is the vertical deposition method. In this technique a hydrophilic substrate is vertically immersed into the colloidal sphere solution and the liquid is allowed to evaporate [9]. This yields a controlled number of multilayers depending on the concentration of the suspension and the sphere size. In this case capillary forces

are responsible for the ordering of spheres. This mechanism of crystal assembly is essentially similar to Nagayama's method for 2-D assembly on planar surfaces [15]. Colloids have been ordered into 3-D structures by using flow cell techniques as well, where aqueous suspensions of colloids are squeezed through a patterned substrate (assembly in confined spaces) [16]. One end of the flow cell is patterned such that it retains the particles and allows the solvent to go through. Nitrogen gas is blown over the colloidal particles while being simultaneously sonicated resulting in ordering of the spheres on the substrate. A summary of methods for obtaining multilayer colloidal crystals is shown pictorially in Figure 1.2.

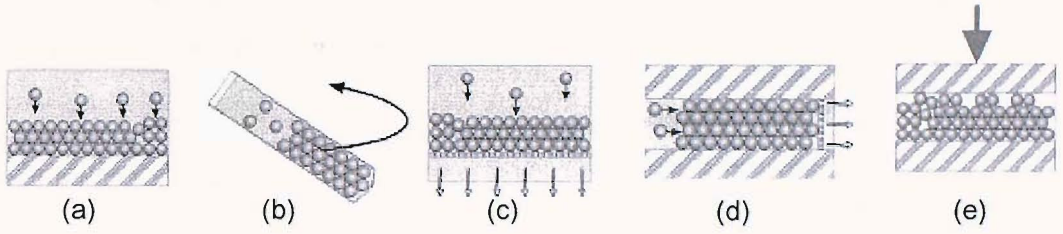

Figure 1.2 Three-dimensional colloidal crystal assembly methods. (a) Sedimentation, (b) centrifugation, (c) filtration, (d) flow cell, squeezing through slits and (e) pressing [3].

The 3-D colloidal crystals fabricated by the above methods form ordered either face-centred cubic (FCC) or a hexagonal close packed (HCP) colloidal crystals. The FCC packing has a minute preference over HCP due slightly higher entropy of $0.001k_BT$ per sphere than the HCP arrangement [17]. That the ordering is driven by entropy is long known [18] and adequately explains this phase separation behaviour of spheres and rods [19] from colloidal suspensions. The physical explanation is that the loss in positional entropy of the phase separated particles is more than compensated by the gain in translational entropy of the particles remaining in the colloidal suspension.

The work presented in this thesis uses a monolayer of ordered spheres on a planar surface. Hence, only a summary of the main 3-D assembly techniques has been presented. Many of the 2-D methods described in section 1.2.1 are related to them.

1.2.1 2-D assembly methods

2-D assembly of spheres on planar surfaces has been carried out by various methods. The earliest report on fabrication of ordered monolayers of colloidal spheres is by Fischer and Zingsheim in 1981 [20]. Employing a suspension of 312 nm spheres they drop coated the substrate and allowed the liquid to evaporate. Small regions on the glass substrate showed a monolayer of hexagonal close

packed spheres. Around the same time Deckman and Dunsmuir demonstrated that spin coating could be used to obtain ordered monolayers of polystyrene colloidal particles [21]. They reported imperfections in crystal ordering included point defects, dislocations and grain boundaries. Typical single crystal domains comprised of 50-1000 spheres. This method has been extensively used by researchers to create masks for depositing substances through them in what has been termed as nano-sphere lithography [22]. A simple modification of the drop coating method was demonstrated by Micheletto *et al.* in which the evaporation rate of the liquid is controlled by the temperature and humidity in a closed box [1]. For nucleation of spheres the glass substrate was tilted such that the ordering started from the top edge (Figure 1.3).

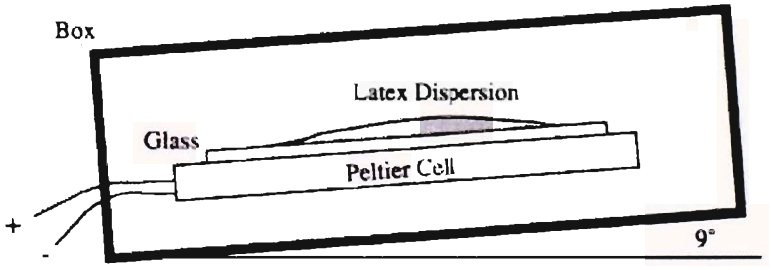

Figure 1.3 Drop coating method of Micheletto *et al.* [1] for obtaining monolayer assembly of latex spheres under controlled humidity and temperature conditions

The mechanism of formation of 2-D crystals from latex particles on planar surfaces by evaporation, also called the 'convective assembly method', from suspensions has been elucidated by Nagayama and coworkers [23-27]. Their work has led to an understanding of assembly methods which involve evaporation of colloidal suspension on planar surfaces and the ordering process. There are two steps to the process, (a) nucleation at the evaporating end and (b) convective particle transport from the interior of the suspension to the growing edge of ordered spheres. The ordering itself takes place due to the 'capillary' attractive forces developed between the particles due to surface tension at the sphere-air interface (schematic shown in Figure 1.4) when their micro-menisci drop below the sphere diameter [26]. The shape of the meniscus at the evaporating boundary controls the number of layers with a higher slope leading to a larger number of layers. The so called 'vertical deposition' also relies on the same mechanism [9]. A variant of the 'vertical

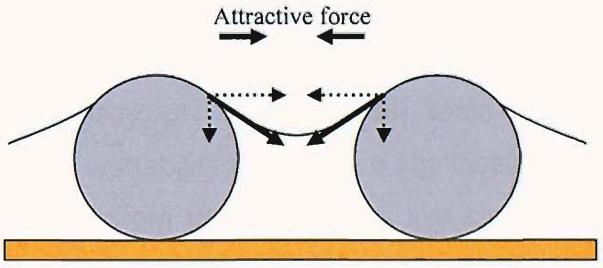

Figure 1.4 Attractive capillary forces between spheres develop as the liquid level drops below their diameter. The horizontal components of the surface tension forces push the spheres towards each other.

deposition' method has been proposed by Nagayama *et al.*; it involves withdrawing the substrate from the sphere solution to yield a monolayer by a continuous convective assembly process [15]. Other methods for assembly of monolayers include field-induced assembly and that using the Langmuir-Blodgett (LB) approach [14, 28]. Modifications to various methods outlined above have been going on in a bid to improve, hasten and control the assembly of colloidal particles. For example Kim *et al.* use a water soluble polymer to modify the viscoelastic properties of the colloidal sphere solution in a convective assembly process to improve the quality of the 2-D crystals [29], though the results seem to suggest only a modest success. A rapid method using convective assembly has also been reported wherein the colloidal sphere suspension is confined between two glass substrates (separated by approximately 100 microns) one of which is withdrawn very slowly at a fixed rate to yield ordered assembly [30]. Another recent improvement in quality of the colloidal crystals has been suggested by carrying out the self-assembly under negative pressure, wherein the dependence on polydispersity, impurity and surface roughness of spheres is reduced [31]. The authors report an average domain size of 30 x 250 μm^2 over a region of 0.65 x 0.45 cm^2.

Currently, the most successful methods are those which rely on the convective assembly technique. However, making a robust and defect free template is still a challenge as the possibility of introducing imperfections in the crystal occurs at each step of the fabrication process. Geometrical factors such as inhomogeneity of size even of a few percent [32], and surface roughness, which prevents assembly at exact array sites, affect the formation. Physical considerations such as humidity & temperature [32, 33], viscosity, pH, additives [34], ionic strength, concentration of spheres [31] and surface wettability also have a significant role in the formation of the colloidal crystal apart from general factors like cleanliness. Hence, although methods of assembly have been studied by various researchers there is plenty of scope for improvement. The domain sizes of colloidal crystals need to be improved to greater than the current benchmark of about 100 microns squared [31, 35].

Apart from the use of colloidal crystals for photonic applications they can be used as templates or moulds. Colloidal sphere templating has become an important means of fabricating ordered films on the micro- and nano-scale [20-22, 36]. By the choice of diameter of the spheres employed the structures can be scaled as

required. This bottom-up method is simpler and much more economical compared to lithography and other micro-fabrication techniques. However, the utilization of the colloidal crystals themselves, or their inverse casts, for various applications requires their formation to be of high quality, or defect-free, in the first place.

1.3 Colloidal crystal templated materials

As mentioned earlier, the colloidal crystal assembled on a flat surface is often used as a template for making its cast or inverse structure. The opal structure does not possess a full photonic band gap [7]. However, for the 'inverse opal', it was predicted that a band gap might exist under suitable conditions due its higher dielectric contrast than the periodic arrangement of dielectric spheres themselves [7, 37, 38]. The minimum index contrast required for opening of a complete band gap for the 'inverse' colloidal crystal templated structure is 2.8 [7], which is achievable for only a few materials such as silicon and some transition metal oxides such as TiO_2. Moreover, the band gap is very sensitive to defects and closes at disorder magnitudes of less than two percent even in the presence of high index contrast [39]. Nevertheless, even a partial gap over a range of angles is sufficient for many applications [6] and hence, 'inverse opal' materials are very attractive for photonic studies.

Initially, the motivation to obtain a variety of colloidal crystal templated structures was the search for a full photonic band gap material. Thereafter, fabricating novel materials became an end in itself and soon, it was realized that even though many of them were not successful as full photonic band gap materials they had numerous other applications not only in photonics but as catalyst materials, filters and so on. As a consequence, a large number of materials are reported in literature where the interstitial space between the spheres has been infiltrated with inorganic, metallic, semi-conductor or polymer precursors and then consolidated to give the final material [13, 40]. Several methods have been studied for infiltration of the void space between the spheres. For metals alone, electroless deposition assisted by nanoparticles [10], infiltration by colloidal metals, *in-situ* reduction of metal salts [41] and direct infiltration of metal using vapour deposition [22] among others [40], have been employed. With these methods blockage of certain areas occurs as the solution or vapour enters from the exposed side of the template. The walls, especially if prepared using (nano)particles possess intrinsic surface roughness. Thus they may be suitable for certain catalytic studies but are rather irreproducible for a lot of photonic applications. The severest drawback is the

sturdiness of the structure. Even after post processing procedures such as sintering, besides undergoing a significant amount of shrinkage, the structures remain fragile and lack the durability required for large scale use. The spheres are removed by etching, if silica spheres are used and by dissolution or calcination, if polymer spheres are used. The use of electrodeposition, where possible, as a technique for fabricating 'inverse opal' (colloidal crystal templated) structures mitigates these problems and has numerous other benefits mentioned briefly in the following section (1.3.1).

1.3.1 Colloidal crystal templated electrodeposited materials

The first report on the use of electrodeposition for preparing colloidal templated films was by Braun and Wiltzius [42]. The primary motivation behind using electrochemical deposition was that by the previous detailed methods it had been difficult to fully mineralize the interstitial space and create durable structures. Using colloidal 0.466 μm polystyrene and 1 μm silica spheres as templates the authors fabricated CdS and CdSe photonic crystals. The spheres were removed after the electrodeposition by dissolving in toluene and 4.8 % HF solution, respectively. Soon after it was demonstrated that macroporous films of gold [43, 44], silver [45], platinum, palladium, cobalt [46] and conducting polymers [47] could be fabricated using this methodology. Among all methods of making metallic films using the templating technique, electrodeposition has the greatest advantages. Apart from alleviating the 'shrinkage' problem, electrodeposition provides precise control of the morphology and structure, results in a dense and smooth film, the growth of the metal films starts from the bottom and the whole of the interstitial volume gets filled, and there is no need for any post-processing. The only requirement is that the substrate used should be conducting in nature. Since the first report of electrochemically deposited nanostructured films for photonic crystals [42] our group has led the development of electrochemically deposited metal films using colloidal sphere templates [46, 48]. These films are called sphere segment void (SSV) substrates in this thesis.

1.4 Properties of sphere segment void substrates

Colloidal spheres are available commercially in the size range from 20 nm to several microns. Thus, surfaces can be created on length scales spanning over two orders of magnitude. Interesting properties appear in nanostructured substrates when their length scales match the critical dimensions of the fundamental interaction responsible for the phenomenon. By varying the sphere size and film thickness, structural features in sphere segment void substrates get modulated over various length scales from a few nanometres to the sphere diameter used for templating. A schematic showing the morphological changes and concurrent colour changes in an optical image with different film heights on sphere segment void substrates is shown in Figure 1.5. Matching the structural features to (a) the magnetic domain size (~50 nm) gives rise to interesting magnetic properties [49, 50], (b) the superconducting coherence length (~200 nm) gives rise to superconducting properties [51] and (c) the photon wavelength (~500 nm) gives rise to unique optical properties [52] in these materials. The structuring in SSV substrates also affects the wetting properties of the surface and by varying the height of the templated film the surface wettability can be tuned from being hydrophilic to extremely hydrophobic [53]. In this thesis however, only the photonics, the consequent plasmonic properties of SSV substrates and their applications are described. The morphology of the substrates with variation in film height is discussed in context of plasmons generated in section 1.4.2 later in the chapter.

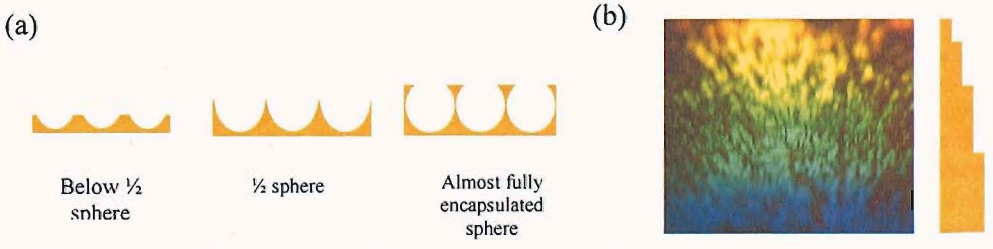

Figure 1.5 (a) Different geometries obtained by templating with the same spheres but with different film heights. (b) An image of a highly iridescent 900 nm sphere templated gold film with different film heights.

1.4.1 Plasmons and surface plasmon polaritons

The coherent or collective oscillation of charges in a metal is called a plasmon. The term surface plasmon refers to the fluctuation of charges at the metal dielectric interface. A surface plasmon oscillation coupled to an electromagnetic wave is called a surface plasmon polariton (SPP). SPPs cannot be generated on a flat surface by optical fields due to a momentum mismatch (even though the

energy may be the same) with photons (see Figure 1.6). There are three ways in which this momentum mismatch can be overcome; (a) using a prism for coupling, (b) scattering from a defect on a surface and (c) scattering from a periodically corrugated metal surface such as a diffraction grating [5]. A periodic corrugation scatters a photon, incident at an angle θ, and provides it with extra momentum, nG, where $G = 2\pi/a$ and 'a' is the period of the grating. If k_{sp} and k_0 (= ω/c) are the momentum wave-vectors for the SPP and the incoming photon, respectively, then by conservation of momentum;

$$k_{sp} = k_0 \sin\theta \pm nG \qquad 1.1$$

It follows from Equation 1.1 that not only can the SPP mode provide the extra momentum to help couple a photon into the surface; it could also decay and radiate a photon by losing momentum to the surface.

Metallic SSV structures patterned on the appropriate sub-micron length scale possessing periodic voids (cavities) of dielectric allow 'direct' coupling of radiation

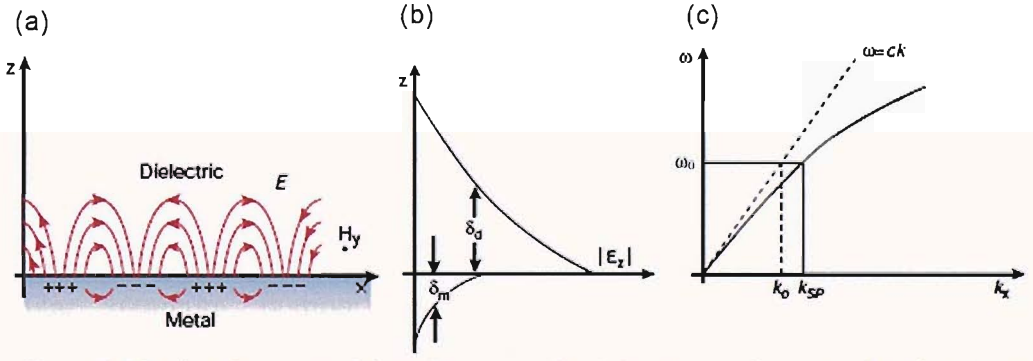

Figure 1.6 Surface plasmons polaritons have a combined electromagnetic wave and surface charge character as shown in (a). This combined character also leads to the field component perpendicular to the surface being enhanced near the surface and decaying exponentially with distance away from it (b). δ_a and δ_m represent the characterstic decay length above the surface and in the metal, respectively. (c) The dispersion curve for a surface plasmon (SP) mode shows the momentum mismatch problem that must be overcome in order to couple light and SP modes together, with the SP mode always lying beyond the dashed line, that is, it has greater momentum ($\hbar k_{SP}$) than a free space photon ($\hbar k_0$) of the same frequency (ω_0). Adapted from [2, 5].

with the surface. Moreover, it is a much more controlled and simpler experiment to do compared to other methods of coupling light into SPP modes [5, 54, 55]. Hence, there has been a lot of interest in SPPs on nanostructured surfaces in recent years further aided by the discovery of a 2-D SPP band gap [56]. It has been shown by Barnes and coworkers that if the periodicity of the structure is half the effective wavelength of the SPP an energy gap is formed. A corollary to this effect is the high enhancement of electric fields at the edges of the band gap,

which can simplistically be understood again as channelling of energy from the prohibited states into the allowed energy range. Further, there is a confinement of the electric field in the direction perpendicular to the surface owing to the longitudinal wave nature of the plasmons as shown in Figure 1.6b. Thus, in general, under suitable conditions the existence of SPP modes on nanostructured surfaces causes large increases in optically generated local electric fields on the surface [5, 57] and hence, such substrates find application in surface-enhanced Raman scattering (SERS)[58].

1.4.2 Plasmon modes on sphere segment void substrates

By controlling the amount of charge passed during electrodeposition a number of different and complex morphologies can be generated for the templated films. The structure can vary from an array of shallow dishes, to disconnected voids, to almost encapsulated air spheres. Hence, the interaction and coupling with optical fields generates different plasmon modes. In this thesis the structure of SSV substrates is described in terms of normalized thickness; normalized to the sphere diameter (*D*) used for templating the sphere segment void substrates. This stems from the fact that at the same normalized thickness all substrates would morphologically appear the same. With this terminology, a 0.5 *D* thickness means that the film is electrochemically grown to half of the sphere diameter used for templating. The SPP modes have been modelled for an encapsulated void in an infinite expanse of metal using the Mie theory wherein their wave functions can be described using spherical harmonics similar to atomic orbitals, labelled by *L* (angular quantum number) and *m* (azimuthal quantum number) [59]. Improvements in modelling, trying to match theory with experiment has led to new insights over the years. Solutions to modes for the sphere segment voids follow from that of a fully spherical cavity and hence, the same convention is adopted for mode labelling as ${}^{m}L = {}^{0,1,2\cdots}P, D, F\ldots$Intuitively, it is apparent that the L=0 mode or the S mode is forbidden due to symmetry considerations in a truncated cavity. The main types of SPP modes generated on SSV substrates are described below based on the current level of understanding [55, 60, 61].

1.4.2.1 Bragg plasmons

For thicknesses of samples less than 0.3 *D*, the surface takes the form of a hexagonal array of shallow dishes as in a diffraction grating. SPP modes are formed when surface plasmons couple to incident light. The modes generated on the top surface between the shallow dishes scatter multiple times at the rims of the

voids (Figure 1.7b) and hence can be modelled using Bragg diffraction. Since, the surface is anisotropic their energies strongly depend on the angle of incident radiation and the direction of propagation. These are delocalized modes and can

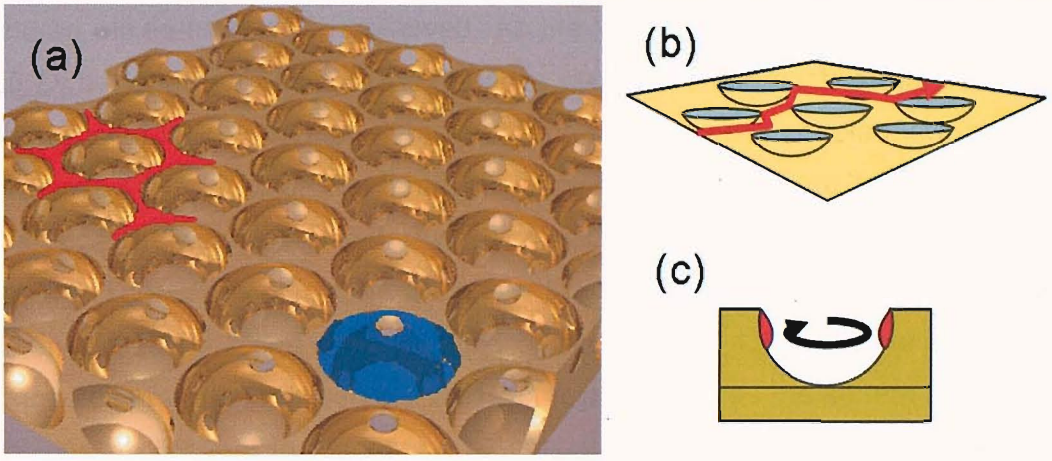

Figure 1.7 Schematic of surface and localized plasmons on nano-void substrate. (a) Bragg (red) and Mie (blue) plasmons with the surface grown to 0.75 D. (b) Bragg plasmons are delocalized on the flat surface connecting the voids while (c) Mie plasmons are localized in the voids.

travel several microns on silver and gold before decaying. On thin samples, only pure Bragg modes are seen. The Bragg modes disappear as the top surface breaks into islands at ~0.35 *D* and reappear again above 0.75 *D*. Above 0.75 *D* there are two kinds of surfaces, flat connected, which support Bragg plasmons, shown in red, and voids, which support Mie plasmons, shown in blue, in Figure 1.7a.

1.4.2.2 Mie plasmons

As the thicknesses increase above 0.3 *D* high energy localized plasmon modes are observed trapped inside the voids. When a surface plasmon polariton wave is reflected between barriers such as in a spherical cavity it will interfere with itself and form a localized mode (Figure 1.7c). The energies continuously red shift as the thickness of the film (depth of voids) increases. In other words as the voids get more and more truncated the energy of Mie plasmons increases. These void plasmons are modelled using the Mie scattering theory, hence, are called Mie plasmons. Since, the voids are symmetric and largely isotropic; the Mie plasmons are independent of the angle of incident light and their electric fields are not influenced by those from the neighbouring voids.

1.4.2.3 Mixed plasmon modes and plasmon hybridization

Between shallow dishes and fully encapsulated voids, the surface breaks up into disconnected islands interspersed with voids. This occurs due to the existence of a physical barrier to electroplating between adjoining spheres either because they

are in contact or 'necks' appear to form between the close-packed spheres. The Bragg modes vanish just below half-sphere film height and reappear when the islands join again above three-quarter film height. In between these two extreme structures mixed modes are observed. As the voids become deeper (film height >0.35 *D*) the energy of Mie plasmon modes drops and approaches that of Bragg plasmons producing mixing of states [60]. The Bragg modes couple (flow into the voids) with the Mie plasmons and mixed plasmon modes are formed due to interference between the two. These mixed modes have strong localized symmetry. The Bragg plasmons depend on the periodicity (pitch) of the sample and hence, can be tuned by a variation of sphere size. On the other hand Mie plasmons can be tuned by varying the film height as well as the sphere size. Both could thus be brought in resonance by varying the sphere size and film height resulting in strong localized fields.

Further, SSV substrates display many modes in experiments which cannot be explained by the Mie equations or by the simplistic view of mixing between the Bragg and the Mie modes. A dipolar rim mode associated with charge build up at the rim of the voids is postulated [61]. It exists when the rim is complete for the voids hence, both below 0.3 *D* and above 0.75 *D*. This mode has an m=1 symmetry (lies in the x-y plane) therefore couples or hybridizes with other modes with the same symmetry [61]. This plasmon hybridization takes place between the rim mode and the void modes above 0.75 *D* when the void modes become strong. For example coupling between the ^1P mode and the rim mode results in a lower energy mode denoted as ^1P+ and a higher energy mode denoted as ^1P-. As consequence of this hybridization there is an affect on the electric field distribution of the plasmon modes. Since, the increase in electric fields are responsible for the surface enhancement observed on SSV substrates this also has a profound affect on the surface-enhanced Raman spectral intensities and these implications would be discussed in detail in Chapter 4.

1.5 Raman spectroscopy

Raman spectroscopy is a very selective 'finger-printing' technique for identifying molecules. The advantage of the Raman technique over other contemporary methods such as infrared or fluorescence spectroscopy is that it can detect several molecular species simultaneously, requires no sample preparation and can be performed under any environment. It relies on the scattering of photons by a molecule. Most of the incident light is elastically 'Rayleigh' scattered. However,

some of it undergoes inelastic scattering and results in Stokes and anti-Stokes radiation corresponding to whether the molecule absorbs or releases energy. The Stokes and anti-Stokes lines are a characteristic 'finger-print' for a particular molecule, as they are determined by the spacing of the vibrational levels of the ground state. Classical treatment of the Raman process is shown in a schematic band energy diagram in Figure 1.8. The selection rule for the process is that the molecule should undergo a change in polarizability on account of the vibration. The molecule is excited from the ground to a 'virtual' state and a photon is emitted

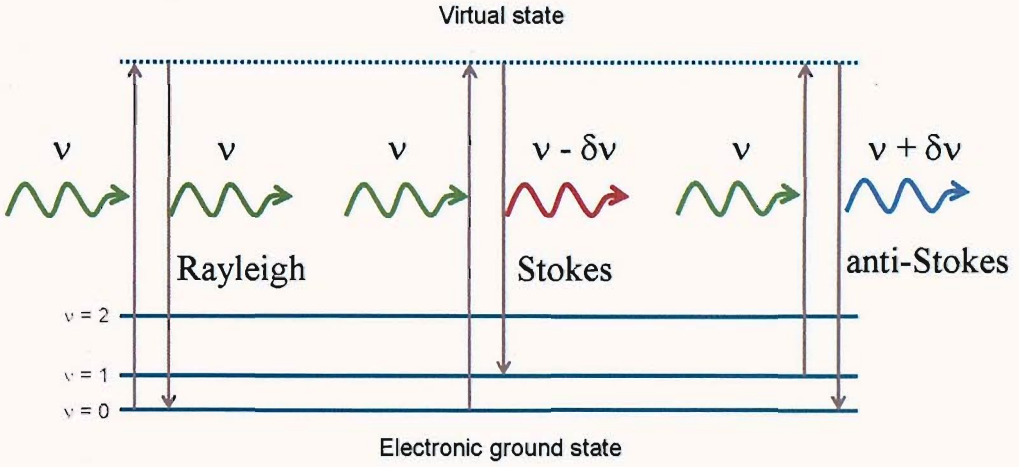

Figure 1.8 Schematic band energy representation showing the different transitions in Rayleigh and Raman (Stokes and anti-Stokes) scattering.

with a lower frequency (Stokes) than the incident beam when it relaxes to a vibrational state higher than the original. If the excitation takes place from a higher vibrational level in the ground state and the molecule relaxes back to a lower vibrational energy level, the scattered photon carries more energy than the incident photon (anti-Stokes).

This whole process can also be understood as a change in polarization of the molecule when interacting with the oscillating electric field of the incident electromagnetic wave. Upon illumination the electron cloud around the molecule will tend to vibrate with the frequency of the incident light though distorted by the intrinsic molecular oscillation; this is the polarized state or the 'virtual' state, as it is not a fixed state. Since the molecular vibration occurs at a much smaller frequency than the incident optical field (which would hence, average out to zero), the most probable way for the molecule to relax is to re-radiate the absorbed photon albeit in a random direction. However, in a very few cases the vibrating electronic field of the molecule is able to alter the oscillation induced by the incident optical field. In these cases a photon would be emitted with a modified frequency; with the

molecular vibration frequency either added or subtracted from the incident photon. It is intuitive from the aforementioned description that Raman scattering would be very weak.

The only drawback with the Raman technique as such is the low probability of its occurrence, that is, it has a very small cross-section of the order of 10^{-30} cm^2/molecule [62] and hence, the signals are extremely weak and/or require a large amount of sample. The signal can be increased by a few orders of magnitude if the molecule can be excited to its next electronic state. This is called resonance Raman scattering. However, it is limited to only certain molecules and by the laser wavelengths available for excitation.

1.5.1 Surface enhanced Raman scattering

An alternative is to carry out the surface-enhanced Raman experiment. First observed by Fleishmann *et al.* in 1974 [63] while examining the Raman spectra of pyridine on an electrochemically roughened silver surface. The roughening was carried out by several reduction oxidation cycles on a silver electrode and the extraordinary large signals were implicitly attributed to the increase in the surface area due to electrochemical roughening. Later Jeanmaire and Van Duyne [64] observed that the large signals could be observed even with one reduction oxidation roughening cycle and hence, the 'giant' Raman signal could not be due to an increase in surface area alone. This was worked out independently at the same time by Albrecht and Creighton [65] that the unusually large Raman intensities could not solely be due to the increase in surface area. Both groups concluded that there had to be a surface enhancement effect to explain the unusually large signal. Thus, the phenomena got its name as surface-enhanced Raman scattering or SERS.

The intensities in Raman scattering depend on the strength of the induced dipole moment, *P*. Further, $P = \alpha E$ where α is the polarizability and *E* is the electric field strength. For a particular molecule the polarizability is fixed, though adsorption on a surface may cause it to be different from that of a free molecule. Hence, signals can be enhanced if one can increase the strength of the electric field experienced by the molecule. Thus, surface-enhanced Raman scattering (SERS) overcomes the primary disadvantage of conventional Raman and is an extremely sensitive analytical tool for detecting surface species.

Most of the signal enhancement routinely observed, of the order of 10^6 in SERS compared to conventional Raman is attributed to the large increase in local electric

field as explained by the electromagnetic theory [66]. A nano-patterned 'plasmonic' substrate does precisely that, it generates enhanced electric fields at the surface. This increases the strength of the induced dipole moment leading to large Raman signals on the surface or SERS. However, reports of single-molecule detection with enhancements of the order of 10^{14} [67, 68] whereas the electromagnetic theory predicted only ~10^{11}-10^{12} enhancement for those structures, suggested that some other mechanism was also in play. This is commonly called the chemical enhancement effect and is still not fully understood [69-71]. The current theory suggests the formation of an adatom or metal-molecule complex to which charge transfer takes place leading to an increase in the cross-section and hence an enhancement in the Raman signal. This mechanism is similar to resonance enhancement mediated by metal orbitals. This model relies on the observation that the SERS signals strongly depend on the nature of the molecule and on the electrode potentials suggesting chemical interaction of the molecule with the surface [66].

Apart from this 'extra' enhancement there is the issue of the enhancement of the background observed in a SERS spectrum, as well. This problem has been discussed very succinctly by Moskovits in his review [71]. The background commonly attributed to fluorescence or more generally, luminescence, is always observed on the structured film, it is much higher than flat substrates but gets hugely enhanced when the molecule under study gets adsorbed on the surface. Another fundamental issue regarding signal intensity in SERS is its dependence on the surface concentration of the species. This has been partially addressed by Lipowski's group using electrochemical potential to control the surface excess of a host of molecules [72, 73]. However, conclusive evidence is yet to be obtained owing to the irreproducibility and the ill-defined geometry of the substrates usually employed for SERS.

Traditional SERS substrates have been plagued by irreproducibility as they have been prepared by techniques lacking atomistic control. This is understandable for electrochemically roughened [58] or vapour deposited metal surfaces [74] due to the intrinsic nature of the processes involved in the fabrication. Colloidal crystal templated 'inverse opal' structured gold films have been demonstrated to be useful for SERS by Tessier *et al.* [75, 76], where the substrates are fabricated by infiltration of the interstitial volume by nanoparticles and hence, not expected to give reproducible signals. The SSV substrates prepared by electrodeposition and

discussed in this thesis have also been shown to work well for SERS [77]. The SERS signals from such electrodeposited structured films show standard deviations less than 10 % compared to more than 1000 % for electrochemically roughened surfaces [78, 79].

Further, a typical SERS experiment is carried out using a visible laser. This can cause photochemical reactions, interference due to fluorescence (for example in coloured samples), and degeneration, especially of large biological molecules, which are not only delicate but also tend to auto-fluoresce [80]. A way to circumvent this is by using lower energy excitation sources in the near infrared (NIR). The first demonstration of SERS with a NIR source using the Fourier-transform Raman (FT-Raman) technique was by Hendra and coworkers [81]. They used a 1064 nm wavelength laser but soon after the usefulness of NIR-SERS was demonstrated with 785 and 830 nm lasers sources [82]. Large enhancement factors similar or higher than with visible lasers have been reported for NIR-SERS [83] and even single-molecule detection has been shown to be possible [67].

Furthermore, as mentioned previously the Raman signals can also be increased by several orders of magnitude by carrying out the resonant Raman experiment. Similarly, the intensities in SERS can be increased by at least a few orders of magnitude by carrying out the surface-enhanced resonance Raman scattering (SERRS) experiment. It was first demonstrated by Van Duyne in 1977 [64]. The enhancement observed in SERRS is postulated to be due to increased polarization and therefore an increase in the cross-section of the molecule due to excitation into a higher electronic state.

Nevertheless, similar to SERS with visible and NIR lasers almost all of the work with SERRS has been carried out on roughened surfaces and aggregated colloidal particles, which predictably are irreproducible and also lack the tunability for different laser excitations. Therefore, analytical applications of SER(R)S (SERS or SERRS), in general, have remained elusive for the want of reproducible, stable and portable substrates.

1.6 DNA detection and mutation discrimination

The development of simple, reliable, high-throughput methods to detect DNA sequences and genetic variations in them is crucial for the development of DNA-based diagnostics and forensics, more so after the unravelling of the human genome and increasing implication of mutations in hereditary diseases. The application of SERS to analysis of DNA was pioneered by Vo-Dinh and colleagues

[84] using rough silver surfaces formed by thermal evaporation of thin silver films onto 100 nm alumina particles dropped coated on glass. In these original experiments DNA was hybridized on nitrocellulose membranes and then the labelled double stranded DNA was spotted onto the SERS substrate for analysis. In subsequent studies they showed that SERS detection could be used on DNA arrays with multi-spectral imaging [85] and when the DNA probes were attached to the SERS active rough silver surface [86-88]. Flocculated silver colloids have also been used very successfully by Graham, Smith and their colleagues for SER(R)S detection of DNA, including the use of different labels for multiplex genotyping [89], quantitative SERRS using two wavelengths and different dyes [90, 91], and the development of SERRS beacons [92]. In their recent work they have shown that the same methods can be used on a commercially available structured gold surface [93]. However, none of these methods have been used for identifying or distinguishing mutations in DNA sequences.

A variety of methods for identifying mutations [94] have been described in the literature using either solution based or surface methods. Solution based methods include the identification of single strand conformational polymorphism [95, 96], use of denaturing gradient gel electrophoresis [95, 97], or quantitative polymerase chain reaction based approaches. The latter have the advantages that they do not require a chromatographic separation step and that they can be used to detect several sequences simultaneously. The most widely used methods are based on fluorescent detection schemes such as those used in Molecular Beacons® [98], Taqman® [99], Scorpions® [100] or Hybridization Probes®[101].

The use of surface based approaches offers the attraction of an array approach to the detection of mutations, the opportunity to control the conditions locally at the surface, and the ability to produce simple, portable biosensor devices. A variety of sensing approaches have been investigated including the measurement of mass changes using a quartz crystal microbalance [102, 103], nanomechanical detection using microcantilevers [104], local refractive index changes using surface plasmon resonance [105, 106]], electrochemical changes [107-109] using either impedance measurements [110-113] or redox labels [114-119], and fluorescence [120-122] though only few have used differential denaturation for distinguishing mutations [100].

In a typical solid-phase analytical system using differential denaturation, a single-strand DNA (ssDNA) probe is immobilized on the substrate and then hydridized to

'target' sequences from solution. The resulting DNA duplexes are then denatured, typically either by ramping the temperature or by washing with solutions of decreasing ionic strength (stringency washing). Mutations are detected by monitoring the denaturation process; since mutations possess base pair mismatches which destabilize the duplex relative to the perfectly complementary target and therefore these duplexes denature more readily compared to the perfect match, hence, called differential denaturation.

Though optical wave guides [123], optical scan arrays [124] and temperature gradient assay platforms [125] have been employed for detecting mutations, fluorescence is currently the preferred technique using the differential denaturation strategy [126]. However, surface-enhanced Raman or resonant Raman scattering (SER(R)S) has been shown to possess significant advantages compared to fluorescence [86, 127, 128]; these include the ability to multiplex because of the narrow line width (~10 nm) and molecular specificity of SER(R) spectra [93, 128], flexibility in the choice of labels [129, 130], insensitivity to quenching by oxygen or other species [127], and excellent sensitivity [131]. In addition SER(R)S has the benefit of using a single excitation wavelength without imposing any inflexibility on the choice of donor, which is the case in FRET (Forster or Fluorescence Resonance Energy Transfer). When compared with surface-plasmon resonance (SPR) [106] or electrochemical detection methods [109], SER(R)S is molecule-specific and much more sensitive. Finally SER(R)S is a highly surface-sensitive technique so that there is no significant interference from species that are not at or close to (typically < 100 nm) the surface.

As mentioned above although advances have been made in the application of SERS for DNA diagnostics none of the methods have been used in dsDNA melting studies to discriminate between mutations. In this thesis, work is described that shows the application of SERS combined with either thermal or electrochemical cycling to discriminate mutations. Although there are a few reports of mutation detection by monitoring temperature [106, 132] induced denaturation using SPR, to date fluorescence monitoring remains the dominant technique with several systems commercially available [133, 134]. The use of an applied electric field to affect hybridization and to determine mutations by the application of a constant potential (-300 mV) followed by measuring the change in fluorescence with time has been described by Sosnowski *et al.*[135]. In their work the probes were immobilized in a 1 micron thick gel-permeation layer coating the electrode

and denaturation was brought about by a complex mechanism involving a mixture of effects rather than as the result of simple electrostatic repulsion at the metal surface [136, 137]. The use of electrochemical scanning dehybridization using fluorescence monitoring for SNP recognition has been recently demonstrated on silicon substrates with surface-bound hairpin (molecular beacons) probes [138, 139]. However, in these experiments the authors were unable to generate sufficient difference to distinguish single point mutation targets from the perfect match when using linear DNA probes. There are also a few reports on monitoring electrochemical denaturation with other techniques such as SPR [140], impedance [141] and chemiluminescence [142] in which a constant potential was applied [135] for denaturation unlike the potential scanning technique used in the method described in this thesis.

1.7 Research aims and thesis overview

In this thesis work the monolayer method of assembly of spheres for fabricating sphere segment void substrates was studied in more detail for improving it and making it more reproducible. Systematic studies were carried out towards this effect. The range of sphere diameters for which large area monolayer templates could be fabricated needed to be extended. Optimization was carried out for fabrication of polystyrene sphere templates for a diameter range from 200 to 1600 nm and the results are summarized in Chapter 2 along with experimental details of other methods and techniques used in this thesis.

Further, one of the aims during the thesis work was to study the effect of surface treatment on the quality of the colloidal sphere templates and hence, sphere segment void substrates. A quantitative parameter was also developed to compare the quality of the substrates using image analysis. During this bid to improve the quality some other interesting structural formulations were discovered using the same idea of colloidal crystal templating. These included the novel idea of patterning wires as a consequence of the need to remove the dependence on the glass base on which the structured substrates have been historically and predominantly studied. The work related to improvement and further development of SSV substrates is presented in Chapter 3.

Furthermore, though the optical and plasmonic properties of SSV substrates had been found to be structure dependent [52, 54, 59] systematic studies were warranted linking these with SERS for which the substrates had been found suitable [77, 79]. During this course of this thesis this work was carried forward.

The optical properties of gold, nickel, palladium and platinum SSV substrates and their modulation by refractive index of the medium in which the substrates are placed were studied. Further, the mechanism of SERS on substrates with plasmonic properties is well known. A schematic showing the plasmon aided SERS mechanism is presented in Figure 1.9. Plasmons generated on the surface not only couple the incoming laser radiation but also help couple out the scattered radiation from the molecule. It predicts that for best enhancements for SERS one should not only have plasmons supported on the substrate which help couple the incoming laser but also have plasmons which couple to the outgoing scattered photons. The inter-dependence of plasmon modes and SERS implies that it would be imperative to design substrates for use with a particular excitation laser and target molecule for optimum SERS. Hence, the tunability of SSV substrates needed to be demonstrated wherein they are tailored for use with a particular

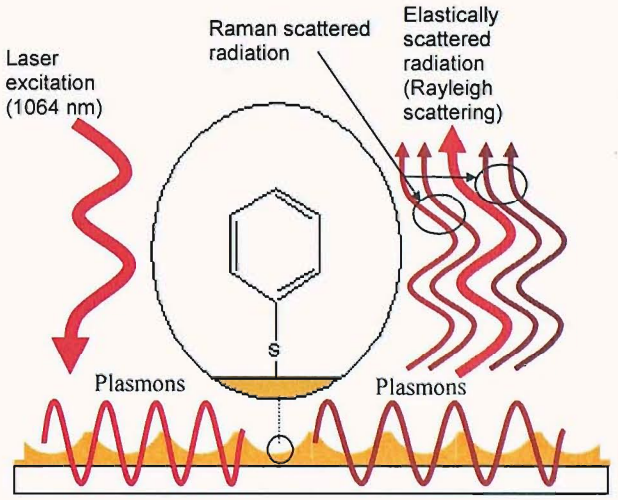

Figure 1.9 Principle of plasmon aided SERS. Plasmons help in coupling the incoming as well as outgoing radiation.

excitation wavelength spanning from visible to near infrared region. Another aim of the studies was establish the link between plasmon resonances and SERS enhancements on SSV substrates. If reasonably successful, this would allow the formulation of a plasmon engineering approach across different laser wavelengths, different metals (gold, palladium, platinum) and different mediums (air & water) using SSV substrates. Results from these studies are presented in Chapter 4.

Having established the reproducibility, scalability and tunability of SSV substrates for SERS it was befitting that the sensitivity also be demonstrated to pave the way for developing applications. Also, one of the ways to increase the sensitivity of SERS is to use resonant SERS or SERRS, wherein the laser energy overlaps with an electronic excitation of the molecule under investigation. SERRS

and its reproducibility were studied on gold SSV substrates. The enhancement obtained on these substrates for SERRS was compared with SERS. All these results are discussed in Chapter 5.

The necessary groundwork having been laid (both by previous and studies during this thesis work) an analytical application was developed for SSV substrates based on SER(R)S wherein detecting DNA sequences was envisaged. This was taken a step forward by showing the ability to differentiate mutations on DNA sequences utilizing SER(R)S. Owing to the thermal and electrochemical stability of SSV substrates differential denaturation (melting) of double stranded DNA (dsDNA) approaches based on either of these could be used in conjunction with SER(R)S, rendering easy and fast discrimination of mutations. Thus, a novel method called SERS-melting for discriminating mutations was established. The reusability of the substrates, the extreme sensitivity of detection as well as the flexibility of the method was studied. The results for DNA detection and mutation discrimination are shown and discussed in Chapter 6.

In Chapter 7, conclusions along with some results and issues identified where further work could be carried out are presented.

1.8 References

[1] R. Micheletto, H. Fukuda, and M. Ohtsu, Langmuir 11:3333 (1995).
[2] P. Vukusic and J. R. Sambles, Nature 424:852 (2003).
[3] O. D. Velev and A. M. Lenhoff, Curr. Opin. Colloid In. 5:56 (2000).
[4] A. Goldberg-Gist, in Chem. Eng. News, Vol. 81, 2003, p. 59.
[5] W. L. Barnes, A. Dereux, and T. W. Ebbesen, Nature 424:824 (2003).
[6] V. L. Colvin, MRS Bulletin August:637 (2001).
[7] K. Busch and S. John, Phys. Rev. E 58:3896 (1998).
[8] K. M. Ho, C. T. Chan, and C. M. Soukalis, Phys. Rev. Lett. 65:3152 (1990).
[9] P. Jiang, J. F. Bertone, K. S. Hwang, and V. L. Colvin, Chem. Mater. 11:2132 (1999).
[10] O. D. Velev, A. M. Tessier, A. M. Lenhoff, and E. W. Kaler, Nature 401:548 (1999).
[11] M. Bardosova and R. H. Tredgold, J. Mater. Chem. 12:2835 (2002).
[12] Y. N. Xia, B. Gates, Y. D. Yin, and Y. Lu, Adv. Mater. 12:693 (2000).
[13] A. Stein, Micropor. Mesopor. Mater. 44-45:227 (2001).
[14] M. Trau, A. Saville, and A. Aksay, Science 272:706 (1996).
[15] A. S. Dimitrov and K. Nagayama, Langmuir 12:1303 (1996).
[16] S. H. Park and Y. Xia, Chem. Mater. 10:1745 (1998).
[17] S.-C. Mau and D. A. Huse, Phys. Rev. E 59:4396 (1999).
[18] P. A. Forsyth, J. S. Macrcelja, D. J. Mitchell, and B. W. Ninham, Adv. Colloid Interfac. 9:37 (1978).
[19] M. Adams, Z. Dogic, S. L. Keller, and S. Fraden, Nature 393:349 (1998).
[20] U. C. Fischer and H. P. Zingsheim, J. Vac. Sci. Technol. 9:881 (1981).
[21] H. W. Deckman and J. H. Dunsmuir, Appl. Phys. Lett. 41:377 (1982).

[22] J. C. Hulteen and R. P. Vanduyne, J. Vac. Sci. Technol. A 13:1553 (1995).
[23] N. D. Denkov, O. D. Velev, P. A. Kralchevsky, I. B. Ivanov, H. Yoshimura, and K. Nagayama, Langmuir 8:3183 (1992).
[24] K. Nagayama, Colloid Surface A 109:363 (1996).
[25] C. D. Dushkin, H. Yoshimura, and K. Nagayama, Chem. Phys. Lett. 204:455 (1993).
[26] P. A. Kralchevsky and K. Nagayama, Langmuir 10:23 (1994).
[27] N. D. Denkov, O. Velev, P. A. Kralchevsky, I. B. Ivanov, H. Yoshimura, and K. Nagayama, Nature 361:26 (1993).
[28] S.-R. Yeh, M. Seul, and B. I. Shraiman, Nature 386:57 (1997).
[29] M. H. Kim, H. K. Choi, and O. O. Park, Appl. Phys. Lett. 88:143127 (2006).
[30] M. H. Kim, S. H. Im, O. O. Park, and S. H. Im, Adv. Funct. Mater. 15:1329 (2005).
[31] J. Zhang, H. Liu, Z. Wang, and N. Ming, J. Appl. Phys. 103:013517 (2008).
[32] S. Wong, V. Kitaev, and G. A. Ozin, J. Amer. Chem. Soc. 125:15589 (2003).
[33] Y.-H. Ye, F. LeBlanc, A. Hache, and V.-V. Truong, Appl. Phys. Lett. 78:52 (2001).
[34] X. Chen, Z. Sun, Z. Chen, W. Shang, K. Zhang, and B. Yang, Colloid Surface A 315:89 (2008).
[35] Z.-Z. Gu, S. Meng, S. Hayami, A. Fujishima, and O. Sato, J. Appl. Phys. 90:2042 (2001).
[36] F. Burmeister, W. Badowsky, T. Braun, S. Wieprich, J. Boneberg, and P. Leiderer, Appl. Surf. Sci. 144-145:461 (1999).
[37] S. John and K. Busch, J. Lightwave Technol. 17:1931 (1999).
[38] H. S. Sozuer, J. W. Haus, and R. Inguva, Phys. Rev. B 45:13962 (1992).
[39] Z.-Y. Li and Z.-Q. Zhang, Phys. Rev. B 62:1516 (2000).
[40] O. D. Velev and E. W. Kaler, Adv. Mater. 12:531 (2000).
[41] H. Yan, C. F. Blanford, B. T. Holland, M. Parent, W. H. Smyrl, and A. Stein, Adv. Mater. 11:1003 (1999).
[42] P. V. Braun and P. Wiltzius, Nature 402:603 (1999).
[43] J. E. G. J. Wijnhoven, S. J. M. Zevenhuizen, M. A. Hendriks, D. Vanmaekelbergh, J. J. Kelly, and W. L. Vos, Adv. Mater. 12:888 (2000).
[44] P. N. Bartlett, J. J. Baumberg, P. R. Birkin, M. A. Ghanem, and M. C. Netti, Chem. Mater. 14:2199 (2002).
[45] M. E. Abdelsalam, P. N. Bartlett, J. J. Baumberg, and S. Coyle, Adv. Mater. 16:90 (2004).
[46] P. N. Bartlett, P. R. Birkin, and M. A. Ghanem, Chem. Commun.:1671 (2000).
[47] P. N. Bartlett, P. R. Birkin, M. A. Ghanem, and C.-S. Toh, J. Mater. Chem. 11:849 (2001).
[48] M. A. Ghanem, P. N. Bartlett, and P. R. Birkin, Proceedings - Electrochemical Society 2000-25:180 (2001).
[49] A. A. Zhukov, A. V. Goncharov, P. A. J. de Groot, P. N. Bartlett, and M. A. Ghanem, J. Appl. Phys. 93:7322 (2003).
[50] A. A. Zhukov, A. V. Goncharov, P. A. J. de Groot, P. N. Bartlett, M. A. Ghanem, H. Kupfer, R. J. Pugh, and G. J. Tomka, IEE Proc.-A 150:257 (2003).
[51] A. A. Zhukov, E. T. Filby, M. A. Ghanem, P. N. Bartlett, and P. A. J. de Groot, Physica C 404:455 (2004).
[52] P. N. Bartlett, J. J. Baumberg, S. Coyle, and M. E. Abdelsalam, Faraday Discuss. 125:117 (2004).
[53] M. E. Abdelsalam, P. N. Bartlett, T. Kelf, and J. Baumberg, Langmuir 21:1753 (2005).
[54] T. A. Kelf, Y. Sugawara, J. J. Baumberg, M. Abdelsalam, and P. N. Bartlett, Phys. Rev. Lett. 95 (2005).
[55] T. A. Kelf, in School of Physics and Astronomy, University of Southampton, Southampton, 2005, p. 163.
[56] S. C. Kitson, W. L. Barnes, and J. R. Sambles, Phys. Rev. Lett. 77:2670 (1996).

[57] T. W. Ebbesen, H. J. Lezec, H. F. Ghaemi, T. Thio, and P. A. Wolff, Nature 391:667 (1998).
[58] Z. Q. Tian, J. Raman Spectrosc. 36:466 (2005).
[59] S. Coyle, M. C. Netti, J. J. Baumberg, M. A. Ghanem, P. R. Birkin, P. N. Bartlett, and D. M. Whittaker, Phys. Rev. Lett. 8717 (2001).
[60] T. A. Kelf, Y. Sugawara, R. M. Cole, J. J. Baumberg, M. E. Abdelsalam, S. Cintra, S. Mahajan, A. E. Russell, and P. N. Bartlett, Phys. Rev. B 74:Art. No. 245415 (2006).
[61] R. M. Cole, J. J. Baumberg, F. J. G. d. Abajo, S. Mahajan, M. Abdelsalam, and P. N. Bartlett, Nano Lett. 7:2094 (2007).
[62] R. L. McCreery, Raman Spectroscopy for Chemical Analysis, Wiley-Interscience, 2000.
[63] M. Fleischmann, P. J. Hendra, and A. J. McQuillan, Chem. Phys. Lett. 26:163 (1974).
[64] D. L. Jeanmaire and R. P. Van Duyne, J. Electroanal. Chem. 84:1 (1977).
[65] M. G. Albrecht and J. A. Creighton, J. Amer. Chem. Soc. 99:5215 (1977).
[66] K. Kneipp, H. Kneipp, I. Itzkan, R. R. Dasari, and M. S. Feld, J. Phys.-Condens. Mat. 14:R597 (2002).
[67] K. Kneipp, H. Kneipp, G. Deinum, I. Itzkan, R. R. Dasari, and M. S. Feld, Appl. Spectrosc. 52:175 (1998).
[68] K. Kneipp, H. Kneipp, R. Manoharan, I. Itzkan, R. R. Dasari, and M. S. Feld, J. Raman Spectrosc. 29:743 (1998).
[69] K. Kneipp, A. S. Haka, H. Kneipp, K. Badizadegan, N. Yoshizawa, C. Boone, K. E. Shafer-Peltier, J. T. Motz, R. R. Dasari, and M. S. Feld, Appl. Spectrosc. 56:150 (2002).
[70] K. Kneipp, H. Kneipp, I. Itzkan, R. R. Dasari, and M. S. Feld, Chem. Phys. 247:155 (1999).
[71] M. Moskovits, J. Raman Spectrosc. 36:485 (2005).
[72] L. Stolberg, J. Lipkowski, and D. E. Irish, J. Electroanal. Chem. 300:563 (1991).
[73] A. G. Brolo, D. E. Irish, G. Szymanski, and J. Lipkowski, Langmuir 14:517 (1998).
[74] J. C. Hulteen, D. A. Treichel, M. T. Smith, M. L. Duval, T. R. Jensen, and R. P. Van Duyne, J. Phys. Chem. B 103:3854 (1999).
[75] P. M. Tessier, O. D. Velev, A. T. Kalambur, A. M. Lenhoff, J. F. Rabolt, and E. W. Kaler, Adv. Mater. 13:396 (2001).
[76] P. M. Tessier, O. D. Velev, A. T. Kalambur, J. F. Rabolt, A. M. Lenhoff, and E. W. Kaler, J. Amer. Chem. Soc. 122:9554 (2000).
[77] S. Cintra, M. Abdelsalem, P. N. Bartlett, J. J. Baumberg, T. Kelf, Y. Sugawara, and A. E. Russell, Faraday Discuss. 132:191 (2005).
[78] Z. Q. Tian, B. Ren, and D. Y. Wu, J. Phys. Chem. B 106:9463 (2002).
[79] M. E. Abdelsalam, P. N. Bartlett, J. J. Baumberg, S. Cintra, T. Kelf, and A. E. Russell, Electrochem. Commun. 7:740 (2005).
[80] P. Hendra, C. H. Jones, and G. M. Warnes, Fourier Transform Raman Spectroscopy - Instrumentation and Chemical Applications, Ellis Horwood Limited, 1991.
[81] A. Crookell, M. Fleischmann, M. Hanniet, and P. J. Hendra, Chem. Phys. Lett. 149:123 (1988).
[82] S. M. Angel and M. L. Myrick, Anal. Chem. 61:1648 (1989).
[83] K. Kneipp, R. R. Dasari, and Y. Wang, Appl. Spectrosc. 48:951 (1994).
[84] T. Vo-Dinh, K. Houck, and D. L. Stokes, Anal. Chem. 66:3379 (1994).
[85] T. Vo-Dinh, D. L. Stokes, G. D. Griffin, M. Volkan, U. J. Kim, and M. I. Simon, J. Raman Spectrosc. 30:785 (1999).
[86] M. Culha, D. Stokes, L. R. Allain, and T. Vo-Dinh, Anal. Chem. 75:6196 (2003).
[87] N. R. Isola, D. L. Stokes, and T. Vo-Dinh, Anal. Chem. 70:1352 (1998).
[88] T. Vo-Dinh, L. R. Allain, and D. L. Stokes, J. Raman Spectrosc. 33:511 (2002).

[89] D. Graham, B. J. Mallinder, D. Whitcombe, N. D. Watson, and W. E. Smith, Anal. Chem. 74:1069 (2002).
[90] K. Faulds, W. E. Smith, and D. Graham, Analyst 130:1125 (2005).
[91] K. Faulds, F. McKenzie, W. E. Smith, and D. Graham, Angew. Chem. Int. Ed. 46:1829 (2007).
[92] K. Faulds, L. Fruk, D. C. Robson, D. G. Thompson, A. Enright, W. E. Smith, and D. Graham, Faraday Discuss. 132:261 (2006).
[93] R. J. Stokes, A. Macaskill, J. A. Dougan, P. G. Hargreaves, H. M. Stanford, W. E. Smith, K. Faulds, and D. Graham, Chem. Commun.:2811 (2007).
[94] P. Nollau and C. Wagener, Clin. Chem. 43:1114 (1997).
[95] M. Bernat, E. Titos, and J. Clària, Genet. Mol. Res. 1:72 (2002).
[96] M. Orita, H. Iwahana, H. Kanazawa, K. Hayashi, and T. Sekiya, Proc. Natl. Acad. Sci. USA 86:2766 (1989).
[97] R. Myers, S. Fischer, L. Lerman, and T. Maniatis, Nucl. Acids Res. 13:3131 (1985).
[98] S. Tyagi and F. R. Kramer, Nat. Biotechnol. 14:303 (1996).
[99] P. M. Holland, R. D. Abramson, R. Watson, and D. H. Gelfand, Proc. Natl. Acad. Sci. USA 88:7276 (1991).
[100] D. Whitcombe, J. Theaker, S. P. Guy, T. Brown, and S. Little, Nat. Biotechnol. 17:804 (1999).
[101] C. T. Wittwer, M. G. Herrmann, A. A. Moss, and R. P. Rasmussen, Biotechniques 22:130 (1997).
[102] F. Caruso, E. Rodda, D. N. Furlong, K. Niikura, and Y. Okahata, Anal. Chem. 69:2043 (1997).
[103] Y. Okahata, M. Kawase, K. Niikura, F. Ohtake, H. Furusawa, and Y. Ebara, Anal. Chem. 70:1228 (1998).
[104] R. McKendry, J. Y. Zhang, Y. Arntz, T. Strung, M. Hegner, H. P. Lang, M. K. Baller, U. Certa, E. Meyer, H. J. Guntherodt, and C. Gerber, Proc. Natl. Acad. Sci. USA 99:9783 (2002).
[105] K. Nakatani, S. Sando, and I. Saito, Nat. Biotechnol. 19:51 (2001).
[106] A. J. Thiel, A. G. Frutos, C. E. Jordan, R. M. Corn, and L. M. Smith, Anal. Chem. 69:4948 (1997).
[107] J. J. Gooding, Electroanalysis 14:1149 (2002).
[108] K. Kerman, M. Kobayashi, and E. Tamiya, Meas. Sci. Technol. 15:R1 (2004).
[109] T. G. Drummond, M. G. Hill, and J. K. Barton, Nat. Biotechnol. 21:1192 (2003).
[110] X. Li, J. S. Lee, and H.-B. Kraatz, Anal. Chem. 78:6096 (2006).
[111] T. Lee and Y. Shim, Anal. Chem. 73:5629 (2001).
[112] C. Z. Li, Y. T. Long, J. S. Lee, and H. B. Kraatz, Chem. Commun.:574 (2004).
[113] Y.-T. Long, C.-Z. Li, T. C. Sutherland, H.-B. Kraatz, and J. S. Lee, Anal. Chem. 76:4059 (2004).
[114] K. Hashimoto, K. Ito, and Y. Ishlmori, Anal. Chem. 66:3830 (1994).
[115] T. Ihara, M. Nakayama, M. Murata, K. Nakano, and M. Maeda, Chem. Commun.:1609 (1997).
[116] K. M. Millan and S. R. Mikkelsen, Anal. Chem. 65:2317 (1993).
[117] E. Paleček, M. Masařík, R. Kizek, D. Kuhlmeier, J. Hassmann, and J. Schülein, Anal. Chem. 76:5930 (2004).
[118] J. Wang, D. Xu, A. Kawde, and R. Polsky, Anal. Chem. 73:5576 (2001).
[119] C. J. Yu, Y. Wan, H. Yowanto, J. Li, C. Tao, M. D. James, C. L. Tan, G. F. Blackburn, and T. J. Meade, J. Amer. Chem. Soc. 123:11155 (2001).
[120] H. Du, C. M. Strohsahl, J. Camera, B. L. Miller, and T. D. Krauss, J. Amer. Chem. Soc. 127:7932 (2005).
[121] A. Ramachandran, J. Flinchbauch, P. Ayoubi, G. A. Olah, and J. R. Malayer, Biosens. Bioelectron. 19:727 (2003).

[122] H. Wang, J. Li, H. Liu, Q. Liu, Q. Mei, Y. Wang, J. Zhu, N. He, and Z. Lu, Nucl. Acids Res. 30:e61 (2002).
[123] D. I. Stimpson, J. V. Hoijer, W. T. Hsieh, C. Jou, J. Gordon, T. Theriault, R. Gamble, and J. D. Baldeschwieler, Proc. Natl. Acad. Sci. USA 92:6379 (1995).
[124] E. B. Khomyakova, E. V. Dreval, M. Tran-Dang, M. C. Potier, and F. P. Soussaline, Cell. Mol. Biol. 50:217 (2004).
[125] H. Mao, M. A. Holden, M. You, and P. S. Cremer, Anal. Chem. 74:5071 (2002).
[126] R. T. Ranasinghe and T. Brown, Chem. Commun.:5487 (2005).
[127] G. Braun, S. J. Lee, M. Dante, T. Q. Nguyen, M. Moskovits, and N. Reich, J. Amer. Chem. Soc. 129:6378 (2007).
[128] Y. C. Cao, R. Jin, and C. A. Mirkin, Science:1536 (2002).
[129] K. Faulds, W. E. Smith, and D. Graham, Anal. Chem. 76:412 (2004).
[130] D. Graham, W. E. Smith, A. M. T. Linacre, C. H. Munro, N. D. Watson, and P. C. White, Anal. Chem. 69:4703 (1997).
[131] K. Faulds, R. P. Barbagallo, J. T. Keer, W. E. Smith, and D. Graham, Analyst 129:567 (2004).
[132] K. A. Peterlinz, R. M. Georgiadis, T. M. Herne, and M. J. Tarlov, J. Amer. Chem. Soc. 119:3401 (1997).
[133] M. G. Herrmann, J. D. Durtschi, C. T. Wittwer, and K. V. Voelkerding, Clin. Chem. 53:1544 (2007).
[134] L. S. Meuzelaar, K. Hopkins, E. Liebana, and A. J. Brookes, J. Mol. Diagn. 9:30 (2007).
[135] R. G. Sosnowski, E. Tu, W. F. Butler, J. P. O'Connell, and M. J. Heller, Proc. Natl. Acad. Sci. USA 94:1119 (1997).
[136] S. K. Kassegne, H. Reese, D. Hodko, J. M. Yang, K. Sarkar, D. Smolko, P. Swanson, D. E. Raymond, M. J. Heller, and M. J. Madou, Sensor Actuat B-Chem. 94:81 (2003).
[137] C. F. Edman, D. E. Raymond, D. J. Wu, E. Tu, R. G. Sosnowski, W. F. Butler, M. Nerenberg, and M. J. Heller, Nucl. Acids Res. 25:4907 (1997).
[138] F. Wei, C. L. Chen, L. Zhai, N. Zhang, and X. S. Zhao, J. Amer. Chem. Soc. 127:5306 (2005).
[139] F. Wei, P. Qu, L. Zhai, C. L. Chen, H. F. Wang, and X. S. Zhao, Langmuir 22:6280 (2006).
[140] R. J. Heaton, A. W. Peterson, and R. M. Georgiadis, Proc. Natl. Acad. Sci. USA 98:3701 (2001).
[141] F. Wei, B. Sun, W. Liao, J. Ouyang, and X. S. Zhao, Biosens. Bioelectron. 18:1149 (2003).
[142] A. M. Spehar-Deleze, L. Schmidt, R. Neier, S. Kulmala, N. de Rooij, and M. Koudelka-Hep, Biosens. Bioelectron. 22:722 (2006).

2 Materials and Methods

The experimental procedures described in this chapter are the general methods employed throughout the work. Details about specific experiments are provided in the results chapters corresponding to the particular study.

2.1 Materials

All aqueous solutions were prepared using de-ionized water (resistivity:18 MΩ.cm) from a Purite Select water purifying system. Argon (Pureshield Argon, 99.998 %) and Nitrogen (oxygen free) were supplied by BOC gases, while air was used from the compressed air supply provided in the laboratory through the School of Chemistry utilities. The chemicals employed during the course of this thesis work are listed in Table 2.1

Table 2.1 List of chemicals

Chemical	CAS number	Description/Purity/ Grade	Supplier
Acetonitrile	75-05-8	E Chromasolv HPLC	Riedel-de-Haen
Ag (wire, Φ 500μm)	7440-22-4	99.9 %	GoodFellow
Ammonium tetrachloropalladate	13820-40-1	99.99 %	Aldrich
Benzenethiol	108-98-5	99+%	Aldrich
Brightener E3	-	-	Metalor
Cysteamine	156-57-0	98%	Sigma
Dimethylformamide	68-12-2	HPLC	Fisher
Ethanol	64-17-5	HPLC	Rathburn
Gold (Wire, Φ 300μm)	7440-57-5	99.9 %	Agar
Gold plating solution (ECF 60)	-	Sulfite based, Cyanide free	Technic (Metalor)
Hexachloroplatinic acid	18497-13-7	99.9 %	Aldrich
Hexammineruthenium (III)	123334-23-6	98 %	Aldrich
Hydrochloric acid	7647-01-0	37-38 % Aristar	BDH
Isopropanol	67-63-0	HPLC	Rathburn
3-Mercaptopropan-1-ol	19721-22-3	95 %	Aldrich

3-Mercaptopropionic acid	107-96-0	99+ %	Aldrich
Mercury	7439-97-6	99.9998 %, Electronic	Alfa Aesar
Mercury (I) chloride	10112-91-1	99.5 %, ACS reagent	Alfa Aesar
Nickel (II) sulfate hexahydrate	10101-97-0	99.99 %	Aldrich
Platinum (mesh)	7440-06-4	99.9 %	Goodfellow
Polystyrene colloidal spheres	-	1 % wt. solutions	Duke Scientific
Potassium chloride	7447-40-7	99.9 %	Fluka
Potassium hydroxide	1310-58-3	AnalaR	BDH
Propanethiol	107-03-9	99 %	Aldrich
Rhodium(III) chloride	20765-98-4	99.9 %	Alfa Aesar
Sodium chloride	7647-14-5	99.9 %, AnalaR	BDH
Sodium hydroxide	1310-58-3	98 %, AnalaR	BDH
Sodiumdihydrogenorthophospate (Sodium phosphate monobasic)	7558-80-7	98 %, anhydrous	Sigma
Sulphuric acid	7664-93-9	99.999 %	Sigma
Tetrabutylammoniumtetrafluoro-borate	429-42-5	99 %	Aldrich
Trizma base (Tris-(hydroxyethyl)aminoethane)	77-86-1	99.9 %	Sigma

2.2 Electrodes

Home made saturated calomel electrodes (SCE) and Silver/Silver chloride (Ag/AgCl) electrode were prepared according to standard procedures [2]. They were stored in saturated KCl solutions when not in use.

2.3 Preparation of structured substrates

2.3.1 Assembly of colloidal spheres

Standard microscope 1 mm thick glass slides were obtained from Menzel-Gläser. A thin layer of chromium, about 10 nm followed by approximately 200 nm of gold was deposited on them on one side by thermal vapour deposition. Each glass slide was cut carefully, to avoid any scratches on the gold, through the glass side into 19 mm x 12 mm pieces. These gold coated slide pieces were then cleaned by sonication in isopropyl alcohol (IPA) for 90 min. The cleaned gold surfaces were

then dipped in 10 mM cysteamine solution prepared in ethanol for at least 48 h. In general, they were left soaking in the cysteamine solution for longer times but not exceeding 1-2 months.

For making the template by assembling colloidal spheres the gold slide pieces, after the cysteamine treatment, were washed thoroughly with de-ionized water. A thin layer cell was constructed with a 22 mm square, ~200 micron thick #2 cover slip (Agar Scientific), using Parafilm (Pechiney Plastic Inc.) as the spacer (~100 microns) A schematic of the thin layer cell construction is given with typical dimensions. A gap was left at the top of the thin layer cell to allow for filling in the colloidal sphere solution with the help of a 20 µl micro-pipette. The spheres, obtained as 1 wt % aqueous solutions from Duke Scientific Corp., were NIST traceable particle size standards with a polydispersity of 1-2 %.

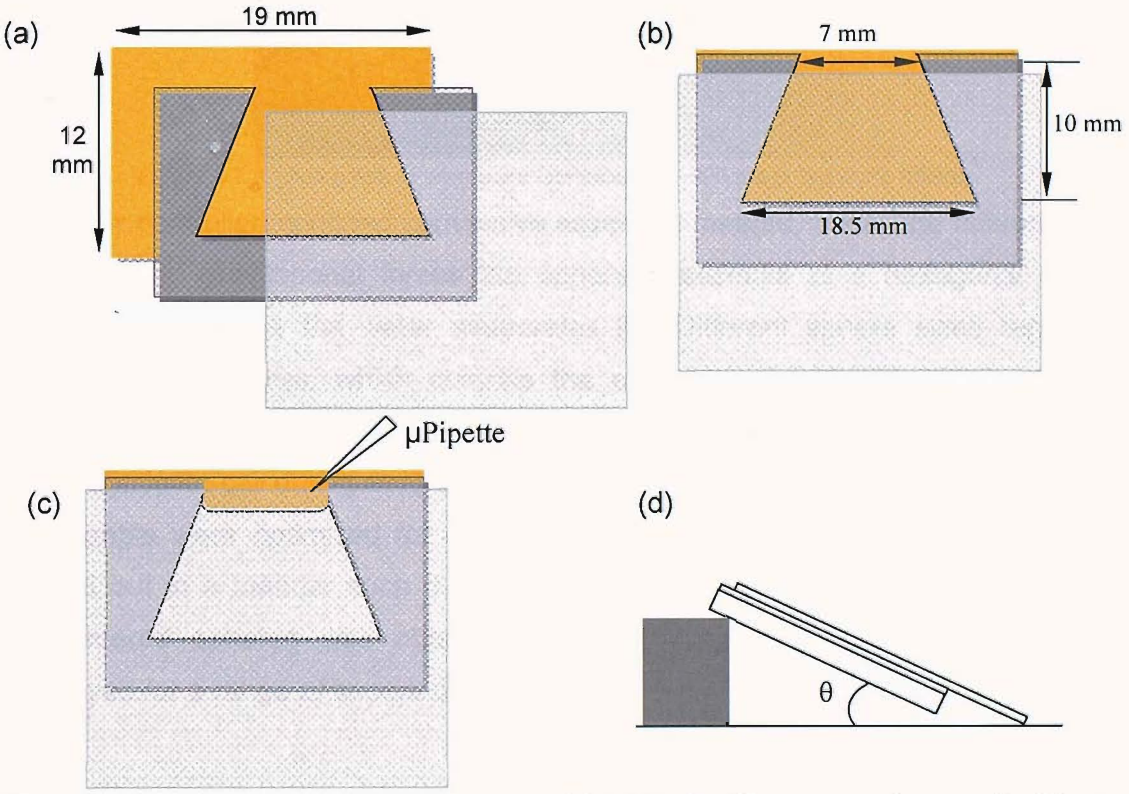

Figure 2.1 Thin layer cell. (a) The components: Gold slide, Parafilm spacer and cover slip. (b) An assembled thin layer cell after adhesion of the spacer with the gold slide and parafilm. (c) A thin layer cell filled using a micro-pipette with colloidal sphere suspension and showing the shape of the meniscus along the width of the cell. (d) Side view of a thin layer cell containing the colloidal solution placed in a constant temperature incubator.

The assembly method used is a modification of the vertical deposition technique propounded by Colvin and co-workers [3]. It relies on the principles of convective assembly as studied by Nagayama and co-workers [4-6]. Our method of colloidal sphere deposition can be termed as controlled confined convective assembly technique. The self-assembly of colloidal spheres is carried out under controlled

temperature conditions, in a cooled incubator, in a thin layer cell in an aqueous medium. The trapezoidal shape of the thin layer cell helps attain a flat meniscus shape in the middle leading to the assembly of spheres progressing radially outwards from the middle. This shape has also been utilized Tessier *et al.* for fabricating macroporous colloidal crystal films in their modified drying drop method [7]. Large area templates could be obtained with our method. An examples of colloidal crystal template is shown in Figure 2.2.

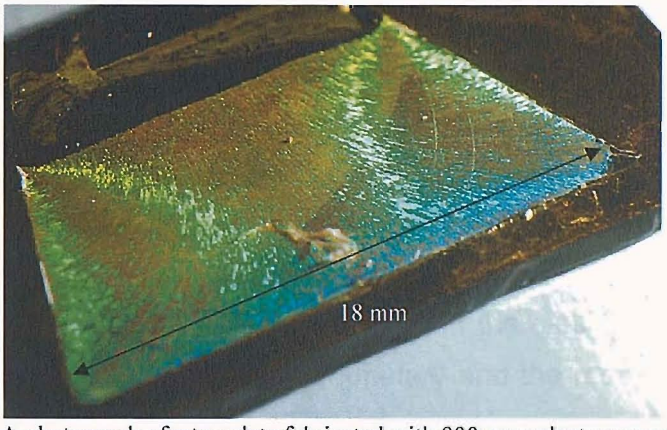

Figure 2.2 A photograph of a template fabricated with 900 nm polystyrene spheres.

For our controlled confined convective assembly method, under the influence of capillary and gravitational forces the spheres assemble in a hexagonal close packed structure as the water evaporates [8]. Different sphere sizes required different temperatures, which controls the evaporation and convective particle transport rate. The settling rate of the spheres was manipulated by the slant angle of the thin layer cell during evaporation. Both these parameters of temperature and slant angle were optimized for each particular sphere size. The assembly was carried out in a manner such that a monolayer template of hexagonally packed well-ordered spheres was obtained. The following table lists the conditions employed for a range of sphere diameters.

Table 2.2 Temperature and slant angle employed for template fabrication for different sphere diameters

Sphere Diameter (nm) / **Parameter**	200	350	400	500	600	700	800	900	1000	1100	1600
Temperature (°C)	7.5	12	12	15	15	15	20	25.5	27.5	32.5	45
Slant Angle (Deg)	90	90	75	25	15	15	7	7	0	0	0

2.3.2 Electrodeposition

Electrodeposition of gold was carried out through this monolayer of polystyrene latex spheres assembled on the surface, which served as a template. The electrodeposition was carried out from a commercial electroplating solution. The electroplating bath (ECF 60 purchased from Technic Inc.) was cyanide-free and based on a gold sulfite complex. Brightener E3 was utilized as an additive for our gold electrodeposition also obtained from Technic Inc. The effect of brightener was observed using SEM and cyclic voltammetry. Figure 2.3 shows the SEM images of gold substrates templated with 600 nm spheres and fabricated by electrodeposition with and without brightener in the plating bath. Figure 2.4 shows the cyclic voltammograms recorded in the electroplating solution containing different amounts of the additive. The nucleation characteristics are clearly altered by the addition of the brightener solution as evident by the change in the onset potential and the change in the slope of the curve in the electron transfer region. The exact composition of the additive is proprietary and the mechanism of action of additives is at best speculative. Nevertheless, it can be seen that not only the electrochemical potential of the onset of nucleation but also the kinetics of electron transfer is altered. Nevertheless, the best results were obtained with the proportion of 50 µl of brightener added to 10 ml of the plating bath (called the full bright plating solution) to give a smooth bright finish of the deposit. For preparation of all gold structured substrates in this thesis the brightener solution was used at this concentration.

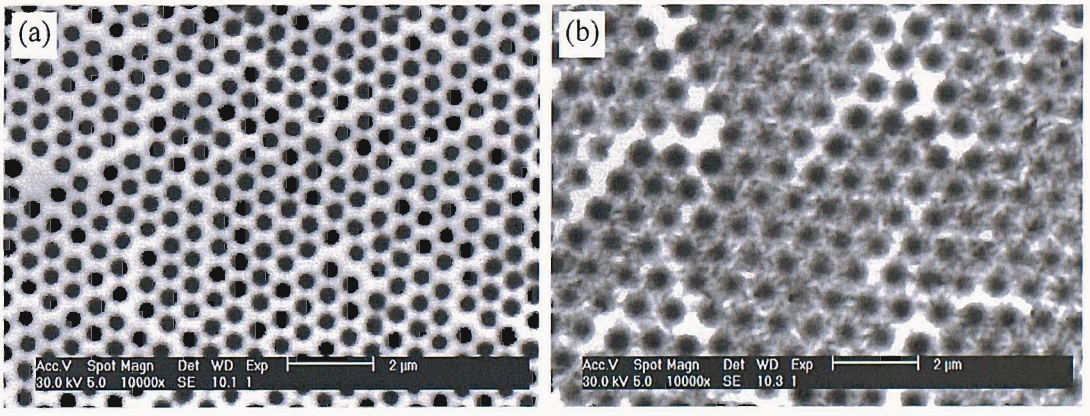

Figure 2.3 ESEM images of structured substrates prepared (a) with (50 µl/10 ml solution) and (b) without the brightener for similar amount of charge passed during electrodeposition. The scale bar is 2

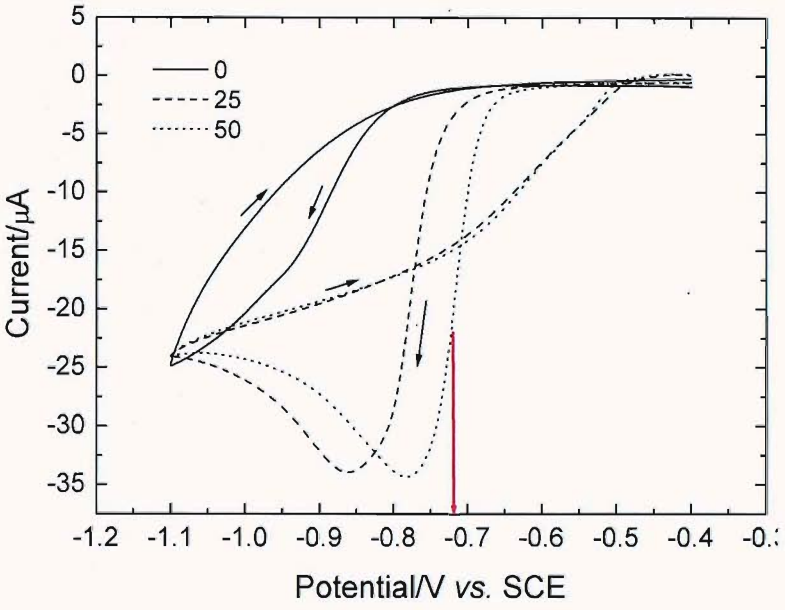

Figure 2.4 Effect of brightener studied with cyclic voltammetry. Three concentrations of the gold electroplating bath are shown containing 0, 25 and 50 μl of additive in 10 ml of electroplating solution. The scans are recorded on a 1 mm gold disc electrode polished to 0.03 μm finish at a scan rate of 20 mV/s at room temperature.

The electrodeposition was carried out in a glass cell at room temperature under potentiostatic conditions in a typical three-electrode configuration in a quiescent solution. The potential was controlled by an Autolab PGSTAT30 potentiostat. The area other than that of the template was masked by applying an insulating paint (common clear nail varnish). The charge required for deposition was calculated based on the exposed area, sphere diameter used and the film height. A home made saturated calomel electrode (SCE) and a platinum mesh were used as the

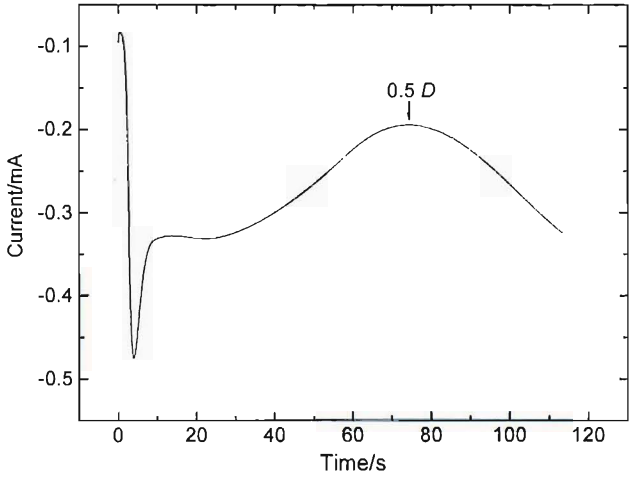

Figure 2.5 A typical chronoamperogram obtained for electroplating gold 480 nm through a 600 nm sphere template at -0.72 V (vs. SCE).

counter electrode, while the template served as the working electrode. Typically, the template was immersed in the plating solution for 5 min before applying the potentiostatic pulse. A potential of -0.72 V vs. SCE (based on nucleation characteristics obtained with cyclic voltammetry; shown by a red arrow in Figure 2.4) was applied till the requisite amount of charge was passed during the deposition process. The potential was chosen to correspond to the mixed control regime in the cyclic voltammogram; the deposits will tend to get rough near or above the diffusion controlled potential (-0.78 V) and the deposition will be extremely slow in or below the electron transfer controlled region (-0.68 V). A typical current transient for electrodeposition of gold through a 600 nm sphere template is shown in Figure 2.5. The shape of the transient shows the development of the void geometry and follows the changes in the area exposed to the plating solution. The area where the electrodeposition can occur is the least at half of the sphere diameter and hence, the cathodic current undergoes a minimum.

After the electrodeposition the polymer spheres were removed by dissolving in dimethylformamide by sonication at least for 2 h. This resulted in the metallic 'inverse opal' film with an array of interconnected voids of depth depending on the charge passed during the electrodeposition. A schematic of the whole fabrication process is presented in Figure 2.6.

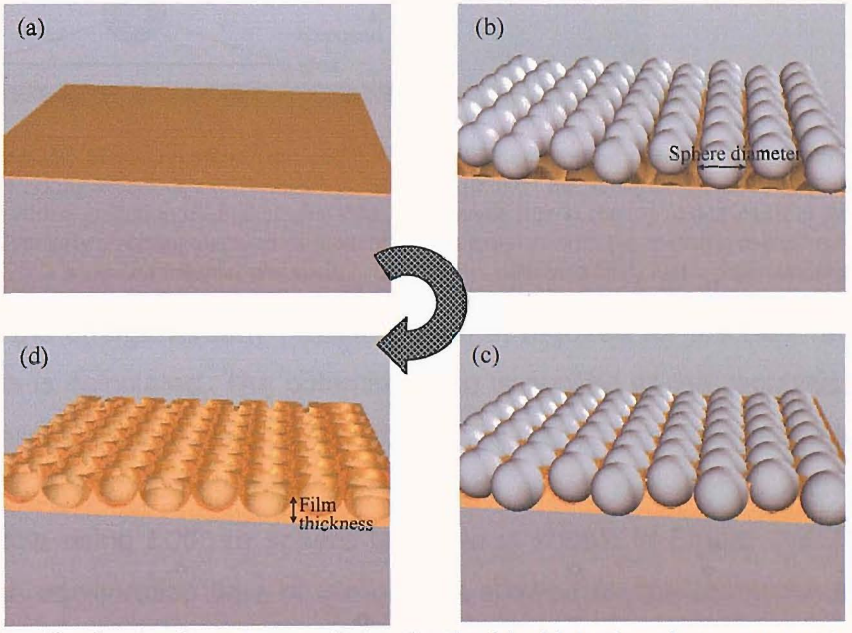

Figure 2.6 Schematic showing the sequence of steps involved in fabrication of nanostructured substrates. Starting from (a) treated gold coated substrate, on which (b) polystyrene spheres are assembled to yield a monolayer template, thereafter (c) controlled electrodeposition is carried out through the template and finally (d) spheres are removed by dissolution to give the structured film. The thickness of the film can be controlled by the charge passed during the electrodeposition.

For preparing a sample with the thickness increasing along the length of the sample such that it would possess a gradation of film heights steadily increasing from thin to thick, the colloidal sphere template is withdrawn from the plating solution in steps. Figure 2.7 shows a schematic of the setup used for preparing a graded substrate. Typically, the substrate was withdrawn in steps of 0.5 mm or 1 mm. Step sizes smaller than 0.25 mm did not have proper gradation since the meniscus of the plating solution did not appear to move. A rectangular area of the colloidal template was left exposed by masking the rest using an insulating varnish (clear nail paint). The meniscus of the plating solution was carefully aligned with the top edge of the exposed area and the electroplating potential was applied till the requisite charge for the thinnest film height was passed. Thereafter, the template was withdrawn upwards by the step size desired. The differential charge

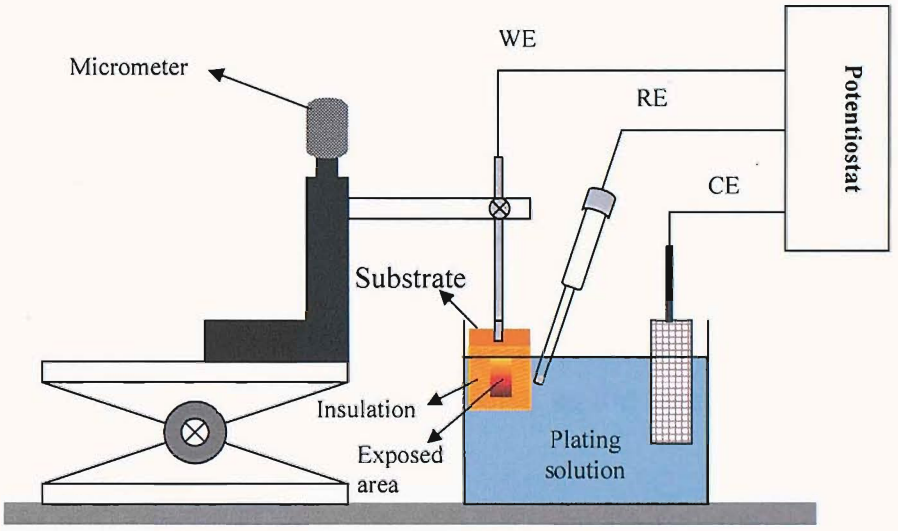

Figure 2.7 Schematic of electrodeposition setup for fabricating graded substrates. The micrometer attached to the working electrode (WE) holder is used to withdraw the substrate upwards sequentially to obtain a sample with a gradation of thicknesses, with the thinnest film at the top and thickest at the bottom of the sample. Typically a rectangular area of the template is exposed with the masking carried out with an insulating varnish. A saturated calomel electrode is used as the reference (RE) and a platinum mesh as the counter (CE).

(subtracting the charge already passed from that required for the new height) for the new area is calculated. The potential pulse is applied till the requisite amount of charge passes. This process is repeated for all steps till the end of the template is reached. A set of current transients for each of the steps while fabricating a graded sample using 500 nm sphere template is shown in Figure 2.9. Between each step an equilibration time of 3 min. was allowed for the meniscus to settle. The first transient in Figure 2.9, that is, for 0.1 *D* has prolonged nucleation characteristics and the cathodic peak occurs at around 4 s; this is probably due to the displacement of residual cysteamine or other molecules present on the surface

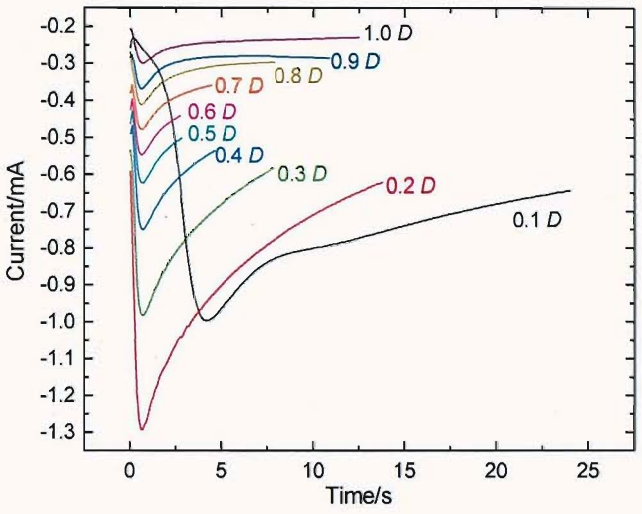

Figure 2.9 Current transients for each step recorded while fabricating a graded gold sample using a 500 nm sphere template. The film heights (in terms of sphere diameter, *D*) based on the calculated charge for each of the steps are indicated beside each transient. The area for each step was 1 mm x 3.3 mm.

as a result of the sphere assembly process for preparing the template. For all the other transients the cathodic peak occurs at the same potential, probably signifying the same deposition characteristics at each step, that is, of gold ions from solution on to the electrodeposited gold surface. Since, the template is withdrawn after each transient the exposed area of the template changes along with the area on which the actual deposition occurs (the interstitial area between the spheres). This is reflected in the transients as the time reduces till 0.5 *D* and then again increases.

A graded gold structured substrate, with the template spheres still embedded in, fabricated with the above stated methodology is shown in Figure 2.8. The

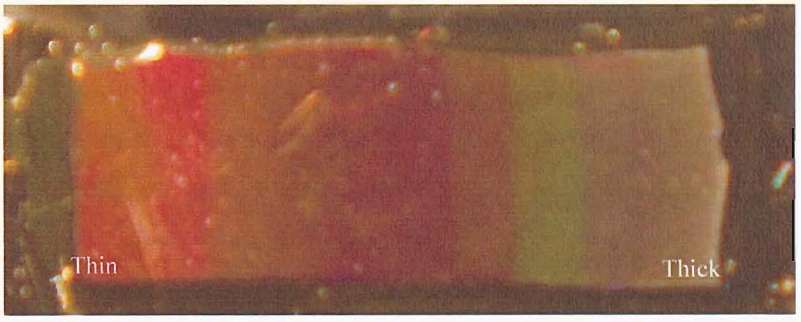

Figure 2.8 A photograph of gold graded substrate with the sphere template still embedded in the structure. The template consists of 600 nm diameter (*D*) spheres. The gradation is from 0.1 to 1 *D* from left to right in 10 steps of 1 mm each.

substrate has been fabricated with 10 steps of 1 mm each. The 1 mm bands can be easily distinguished on the substrate owing to the different colour exhibited by the structure at different thicknesses. SEM images for a similar graded gold

sample templated with 700 nm spheres at different film heights are shown in Figure 2.10. The SEM images presented in Figure 2.10a & b clearly show the monolayer assembly of the template and that the electroplating takes place conformally around the spheres filling the entire interstitial volume.

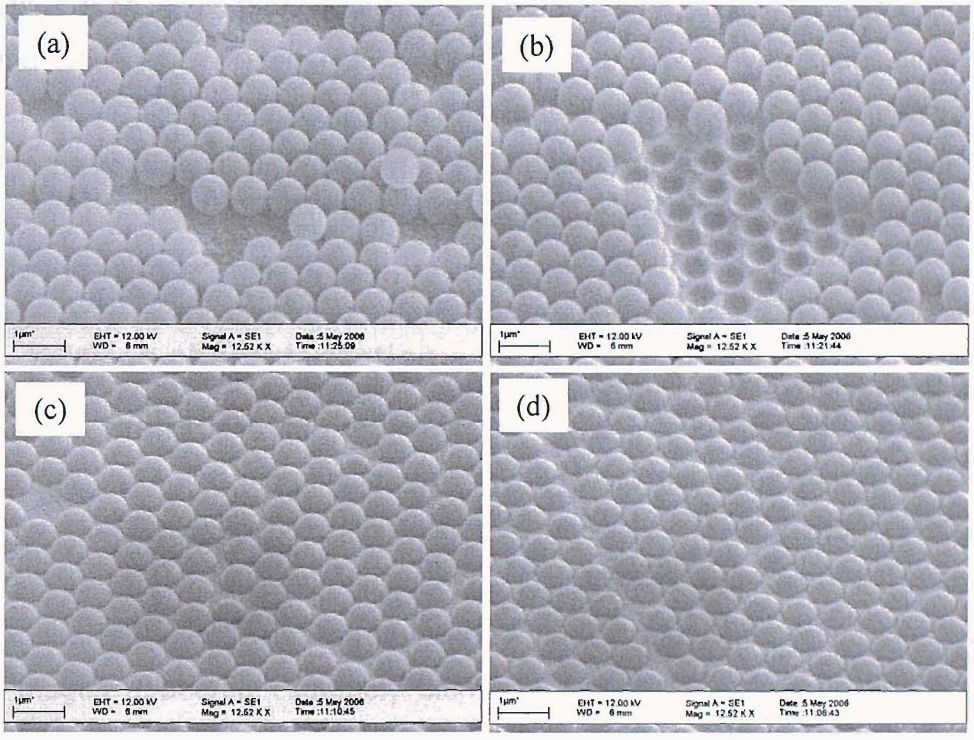

Figure 2.10 SEM images of a (a) 700 nm diameter (*D*) sphere template utilized for making a graded gold sample. Steps with (b) 140 nm (0.1 *D*) (c) 350 nm (0.5 *D*) and (d) 525 nm (0.75 *D*) film thickness grown through the template are shown.

Nickel substrates were fabricated by electrodepositing through polystyrene sphere templates using the plating conditions published earlier by Bartlett *et al.* [9]. Briefly, a 50 mM $NiSO_4$ solution was used and electroplating was carried out potentiostatically at -0.95 V *vs.* SCE. Similarly for fabricating palladium and platinum sphere segment void substrates the recipes published by Bartlett *et al.* [10] were used. Palladium and platinum films were deposited from 50 mM solutions of ammonium tetrachloropalladate and hexachloroplatinic acid, under potentiostatic conditions at 0.25 V and 0.05 V *vs.* SCE respectively. Rhodium electrodeposition was carried out using a 50 mM $RhCl_3$ solution with 0.1 M NaCl at a constant potential of -0.17 V *vs.* SCE. The plating efficiencies for all the different depositions were individually determined by comparing the actual height with those theoretically expected by the amount of charge passed. For gold, nickel, palladium, platinum and rhodium they were calculated to be 85 %, 90 %, 100 %, 100 % and 95 %, respectively.

2.4 Electrochemical characterization

All electrochemical measurements were carried out with an EcoChemie Autolab PGSTAT30 potentiostat/galvanostat. Cyclic voltammetry, chronocoulometry and chronoamperometry were used during the course of the work presented in this thesis. Chronocoulometry was used to measure the surface coverage of single strand DNA (ssDNA) on gold surfaces. The procedure for measuring surface coverage is given in section 2.8 of this chapter. For *in situ* SERS measurements under electrochemical control an EcoChemie μAutolabIII potentiostat/galvanostat was employed. The conditions for individual measurements will be mentioned where the corresponding results are discussed.

2.5 Surface characterization

2.5.1 Scanning electron microscopy

The structure and morphology of the structured films were investigated using Philips XL30 environmental scanning electron microscope (ESEM). For imaging gold films, an accelerating voltage of 30 kV was employed. In practice the resolution of the images with this electron microscope was limited to 30 nm and the images appeared extremely blurred above 20,000 magnification (1 micron scale bar). High resolution images were taken with a Jeol 6500F Field Emission Gun Scanning Electron Microscope (FEGSEM) with the electron beam energized at 15 kV. It was possible to reach nanometre resolution easily with this electron microscope. Some images were also taken with the LEO 1455VP SEM in the Nanofabrication facility in the School of Physics.

2.5.2 Atomic force microscopy

Surface roughness of flat films was evaluated by Atomic Force Microscopy (AFM) using a Topometrix AFM Explorer™ in the contact mode. 5μm x 5μm scan areas were imaged after optimizing the PID values for each sample at a scan rate of 10 μm/s. Root mean square (RMS) roughness values were recorded for the whole area of the image after fitting a second order plane for levelling the images using the Topometrix SPMLab NT Version 5 analysis software.

2.5.3 Contact angle measurements

Contact angle measurements on surfaces was carried out on a Drop Shape Analysis System (DSA 100 from KRÜSS Gmbh) equipped with a CCD camera for imaging. Deionized water under static conditions with a drop volume of 1 μl was employed in the experiments. Drop Shape Analyzer software provided with the

system was used for fitting the drop shapes to find the contact angle of water on the surface.

2.6 Reflectance measurements

2.6.1 Normal incidence

For reflectance spectra recorded in the normal incidence mode a BX51TRF Olympus microscope illuminated with an incoherent white light source coupled to an Ocean Optics visible (400-900 nm) or a near infrared NIR512 (850-1800 nm) spectrometer was employed. A 20x normal (NPlan) or 20x IR (IRPlan) objective with a numerical aperture of 0.46 and 0.40 respectively, was used to record the spectra. All spectra were normalized with respect to that recorded on flat gold deposited on glass slides by vapour deposition. Gold was chosen for normalization as its absorbance is fairly constant over the wavelength range studied; it is chemically stable and serves to give a direct comparison between the reflectance characteristics of structured versus flat (unstructured) film. A CCD camera (Olympus DP2) mounted on the microscope enabled the simultaneous recording of optical images of the area whose spectrum was being monitored.

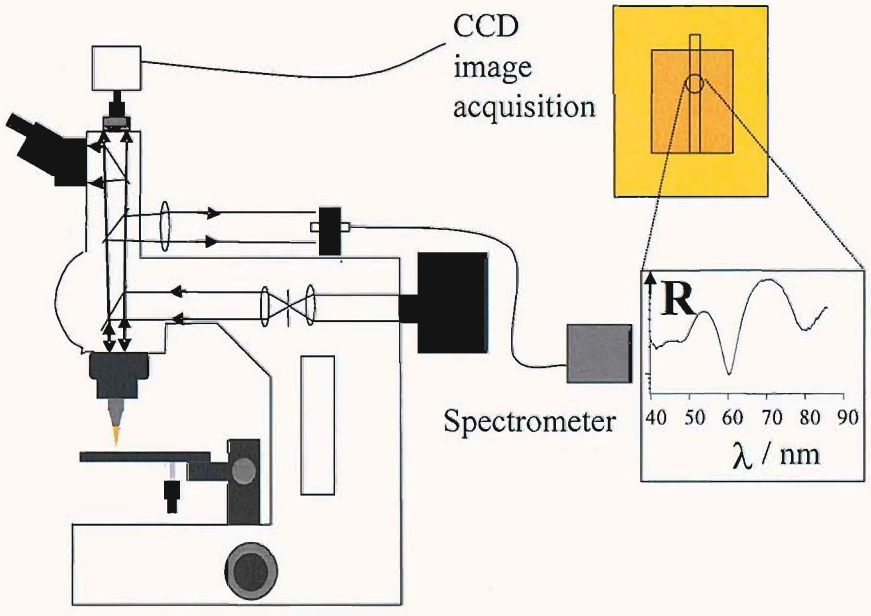

Figure 2.11 Schematic of experimental setup for recording reflectance spectra, after Bartlett *et al.* [1] The positions where the reflectance spectra are recorded are mapped for further SERS measurement.

2.6.2 Angle resolved

In this thesis angular reflectance data is presented which were collected in Prof. Jeremy Baumberg's group in the School of Physics, by his student Robin Cole. The data has been collected on a rig which allows the variation of the incident angle of the white light beam and the azimuthal angle in the plane of the substrate independently of each other. The reflected light is collected over a very small angle (numerical aperture: 0.01) ensuring that any contribution from scattering is eliminated. A schematic of the setup is shown below in Figure 2.12. The data presented in this thesis, unless mentioned otherwise, has been summed from 0 to 36 degrees to match the collection optics in a typical SERS measurement which utilized a 50x objective (NA:0.75).

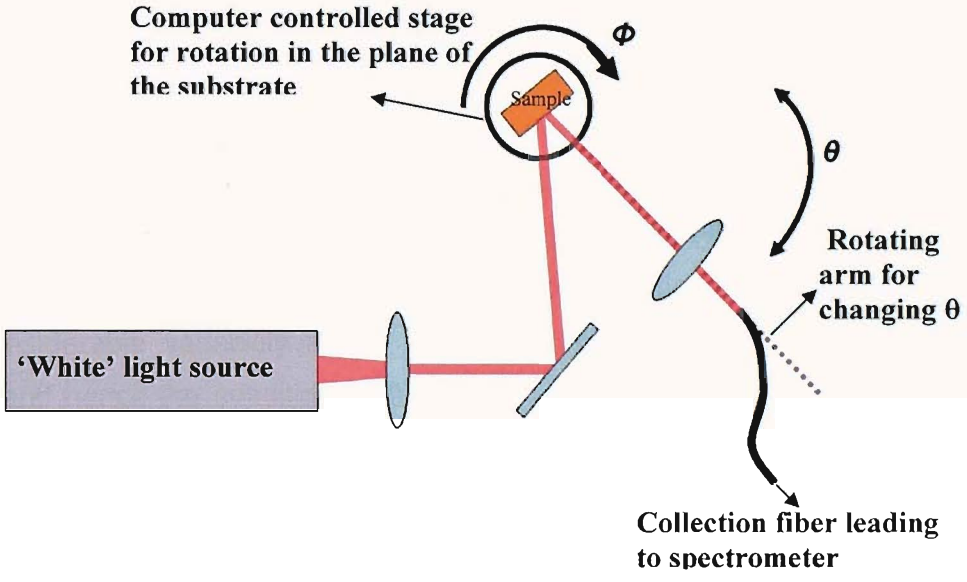

Figure 2.12 Schematic of the angle resolved reflectance measurement setup. Incident angle can be varied by changing θ while independently controlling Φ.

2.7 Raman measurements

2.7.1 In the near infrared with a 1064 nm laser

Raman measurements were made with a Perkin Elmer System 2000 FTIR spectrometer with an FT-Raman attachment equipped with a 1064 nm Nd:YAG diode laser. The laser spot size is 300 μm diameter. Raman spectra were recorded in the back-scattered geometry between 200 cm^{-1} to 3500 cm^{-1} wave-numbers shift using an Indium Gallium Arsenide (InGaAs) detector. A spectral resolution of 4 cm^{-1} was used with the incident laser power at the sample measured to be 250 mW. In general for SERS measurements 50 scans were averaged unless stated otherwise. A $BaSO_4$ standard was run at the beginning of

each experiment to check the calibration of the instrument and the power at the sample was determined by an analog laser power meter for 1064 nm radiation.

2.7.2 In the near infrared with a 785 nm laser

Raman measurements with a 785 nm laser were made using a Perkin Elmer RamanStation 400. The laser spot size is 50 μm in diameter. Raman spectra were recorded in the back-scattered geometry between 200 cm^{-1} to 3500 cm^{-1} wave-numbers shift using a Peltier cooled CCD detector. A spectral resolution of 4 cm^{-1} was used with the incident laser power at the sample measured to be 100 mW. In general 1 s exposures were recorded averaged over 5 or 10 scans for SERS measurements. The calibration of the instrument was carried out with a NIST standard supplied with the instrument.

2.7.3 In the visible with 633 nm laser

The bulk of the SERS data acquired in this thesis has been obtained with the 633 nm laser. Raman measurements were carried out on the Renishaw System 2000 confocal Raman Microscope equipped with a 633 nm He-Ne laser and a CCD detector. Typically, 50x short working distance (SWD) or 50x ultra-long working distance (ULWD) objectives were used for recording SERS spectra. There were considerable variability in the conditions employed for recording various spectra and hence the conditions will be stated when the results for the relevant experiment are discussed. Nevertheless, with this instrument, spectra can be recorded either in the extended scan mode or in the static scan mode. In the extended scan mode a spectrum can be collected from 200 to 3200 cm^{-1} or higher wave-numbers. The recommended minimum collection time is 10 s, though it is possible to override this. A scan with typical 10 s collection time takes about 2.5 min as the CCD detector is moved over the entire range of Raman shifted wavelengths. With a static scan collection times lower than 10 s can be set and the total scan time is approximately the same as the collection time though the range of collection spans only 520 wave-numbers. The laser power at the sample was typically measured by a digital laser power meter from Coherent Technologies and the grating was calibrated by measuring on a silicon wafer and adjusting the offset with respect to the peak at 520.6 cm^{-1}. The maximum power that could be obtained at the sample was 3 mW. Typically the laser power had to be turned to 1 % (3 μW) of the maximum for resonant SERRS measurements. The spectral acquisition conditions specific to the DNA work are mentioned in sub-section 2.8.7.

The confocality of the Raman microscope was determined under the spectral acquisition conditions (low resolution; slit width ≥ 50 microns) employed for the work carried out in this thesis. The vertical confocal distance was determined with the 20x and 50x short working distance objectives by measuring the intensity of the silicon peak at 520 cm^{-1}. The confocal depth is defined as the full width at half maximum (FWHM) of the intensity profile obtained by varying the vertical displacement (Z) of the substrate. Under the conditions of recording Raman spectra in this thesis the Raman microscope was operated with the slit width set to 50 μm or above. The confocality with the 20x objective was determined to be 53.2 μm while with the 50x objective it was found to be 12.7 μm, under the above-stated conditions. The intensity profiles as a function of vertical displacement from the focal point are shown in Figure 2.13. The plots show that under these conditions of low depth resolution all of the signal would be collected from thin films less than a few microns thick as in the case of the sphere segment void substrates discussed in this thesis.

Further with the Renishaw System there is an option to defocus the laser through the software to cover a large area with a diffuse spot. It is beneficial to have a diffuse spot in some cases to have lower incident power density resulting in less local heating and photochemical damage to the surface species, especially when SERS monitoring at the same spot is required. However, it is expected that owing to the fixed collection angle of the objective determined by its numerical aperture there would be a limit up to which this defocusing of laser allows collection of Raman signals without a loss in intensity. A plot showing the affect of defocusing the laser beam as a percentage of the initial focus on the intensity of Raman signal from a silicon wafer is presented in Figure 2.14. It is clear that beyond 50 % defocus the signal undergoes a drastic reduction in intensity and hence, work in this thesis was carried out within this limit.

The laser power can also be controlled by adjusting the settings with the software. It was verified that the power settings were linear as Raman signals are expected to be directly proportional to power. A plot showing the intensity of the 520 cm^{-1} peak of Silicon as a function of the percentage power settings of the spectrometer is presented in Figure 2.15. It shows that the Raman intensities recorded with the spectrometer are linear with the power settings made with software.

(a)

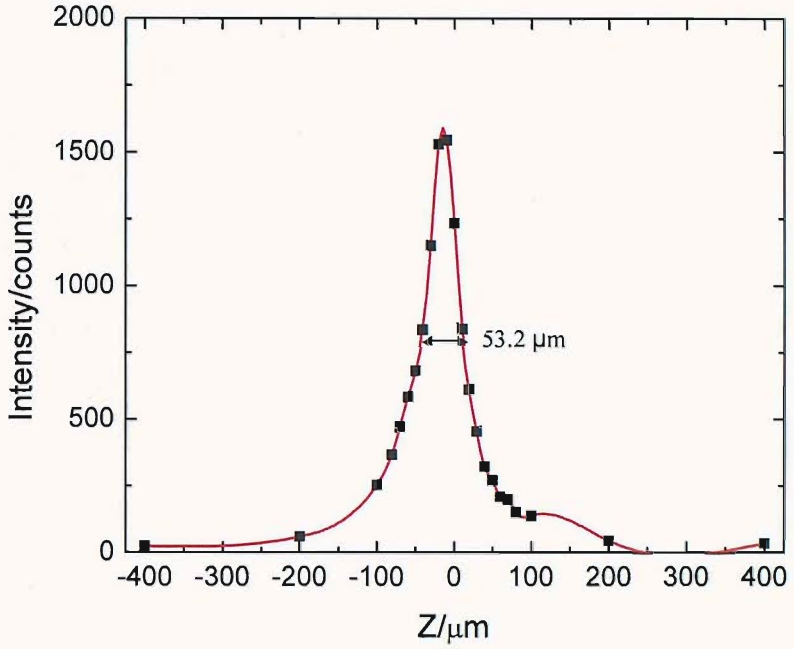

(b)

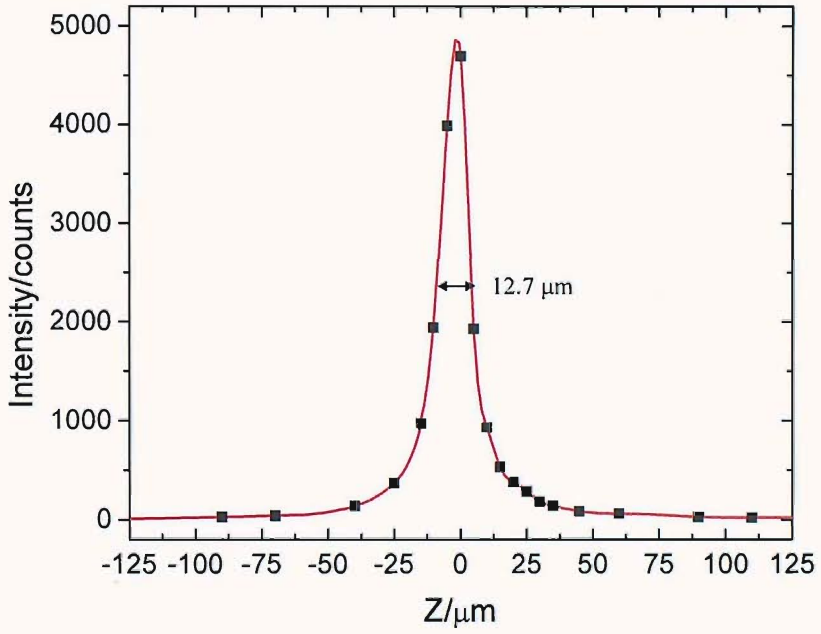

Figure 2.13 Confocal depth determination for the spectral acquisition conditions used in the thesis work with (a) 20x and (b) 50x objective. Intensity of the 520 cm^{-1} Si peak as a function of vertical displacement from the focal point is plotted.

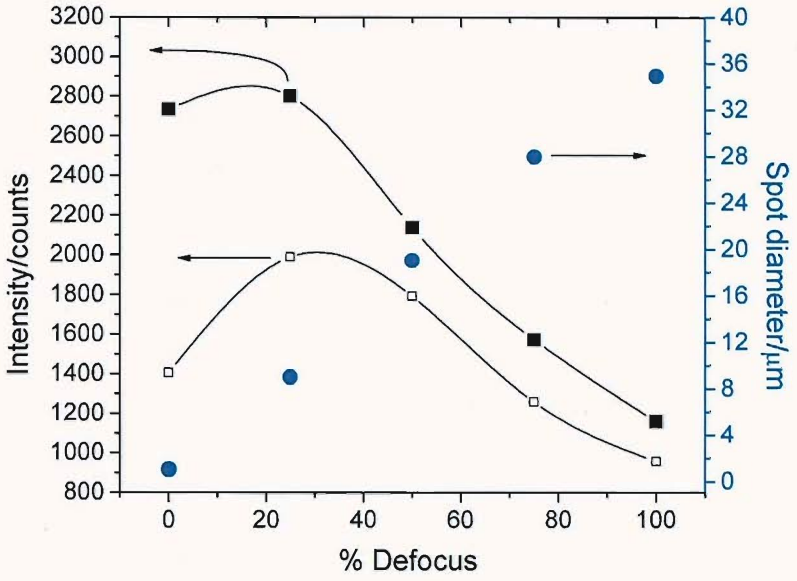

Figure 2.14 Affect of defocusing the laser on the Raman signal intensity. The 520 cm^{-1} peak of Silicon is plotted against % defocus for the 50x (■) short working distance (SWD) and (□) ultra-long working distance objective (ULWD). The (●) spot diameter read from its CCD image is also shown. 0 % corresponds to the fully focused condition.

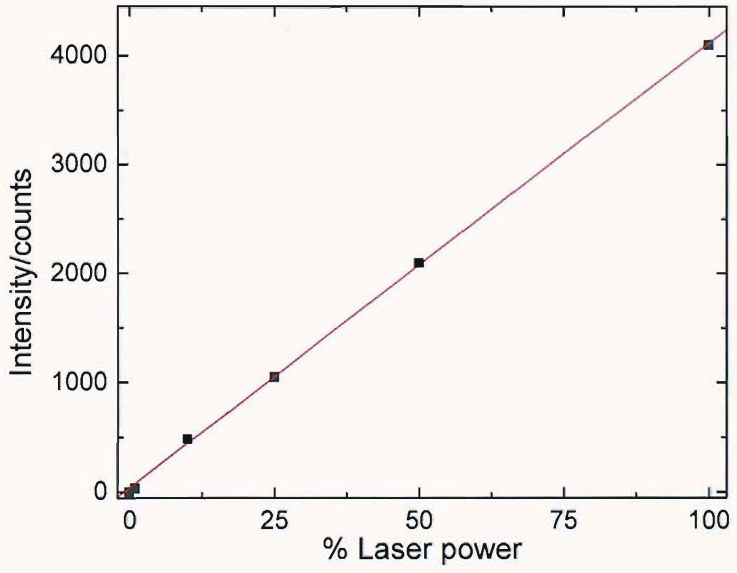

Figure 2.15 Intensity of Si peak at 520 cm^{-1} plotted versus percentage laser power to verify the corresponding settings on the spectrometer. The maximum (100 %) laser power was measured to be 3 mW at the beginning of this experiment.

2.8 DNA analysis

For DNA detection related work presented in this thesis synthesis of oligonucleotides, polymerase chain reaction (PCR) amplification and purification was carried out in Prof. Tom Brown's group by James Richardson and Noha Ben-Gaied.

2.8.1 Oligonucleotides synthesis

Standard DNA phosphoramidites, solid supports and additional reagents were purchased from Link Technologies Ltd, Sigma and Applied Biosystems Ltd. For 3'-labelling, C7-aminoalkyl synthesis columns were obtained from Link Technologies Ltd and Cy5 and dithiol phosphoramidites from Glen Research Inc. All oligonucleotides were synthesized on an Applied Biosystems 394 automated DNA/RNA synthesizer using a standard 0.2 or 1.0 μmole phosphoramidite cycles of acid-catalyzed detritylation, coupling, capping and iodine oxidation. Stepwise coupling efficiencies and overall yields were determined by the automated trityl cation conductivity monitoring facility and in all cases were >98.0%. All β-cyanoethyl phosphoramidite monomers were dissolved in anhydrous acetonitrile to a concentration of 0.1 M immediately prior to use. The coupling time for normal (A,G,C,T) monomers was 25 s and the coupling time for the Cy5 and dithiol monomers was extended to 360 s. Cleavage of oligonucleotides from the solid support and deprotection was achieved by exposure to concentrated aqueous ammonia for 60 min at room temperature followed by heating in a sealed tube for 5 h at 55 °C. Oligonucleotides labelled with 5'-Cy5 were prepared by adding a Cy5 phosphoramidite monomer at the final addition in solid-phase synthesis. The Cy5 chromophore is unstable to prolonged exposure to ammonia so 5'-Cy5 oligonucleotides were synthesized using fast deprotecting dmf-G and Ac-dC phosphoramidite monomers, cleaved from the resin by treatment with concentrated aqueous ammonia for 60 min at room temperature then deprotected for 1 h at 55 °C.3'-Dye-labelled oligonucleotides were synthesized by post-synthetic labelling of 3'-aminoalkyl oligonucleotides which were assembled using C7-aminolink solid support. These oligonucleotides were labelled with the NHS esters of Cy5 or Texas Red as described below.

To incorporate the Cy3, Cy5 or Texas Red chromophores at the 3'-end of C7-aminoalkyl oligonucleotide, 50-150 nmol of the oligonucleotide in 70 μL of 0.5 M $Na_2CO_3/NaHCO_3$ buffer (pH 8.75) was incubated for 4 h at room temperature with

1 mg of the succinimidyl ester of Cy3, Cy5 or Texas Red (Invitrogen) in 40 µL of DMSO. The crude oligonucleotides were purified by reversed-phase HPLC and desalted by NAP-10 gel-filtration according to the manufacturer's instructions (GE Healthcare). Reversed-phase HPLC purification was carried out on a Gilson system using an ABI Aquapore column (C8), 8 mm x 250 mm, pore size 300 Å. The following protocols were used: run time 30 min, flow rate 4 mL per min, binary system, gradient: Time in min (% buffer B);0 (0); 3 (0); 5 (10); 21 (40); 21(60)* 25 (100); 27 (0); 30 (0). Elution buffer A: 0.1 M ammonium acetate, pH 7.0, buffer B: 0.1 M ammonium acetate with 50% acetonitrile pH 7.0. **The % buffer B at 21 min was 40% for all oligonucleotides except those containing the hydrophobic Cy3, Cy5 and Texas Red dyes which required 60% buffer B.* Elution of oligonucleotides was monitored by ultraviolet absorption at 295 nm. Texas red oligonucleotides gave two product peaks corresponding to the 5- and 6- regioisomers of Texas red. The first peak (5-isomer) was collected and used in the SERS experiments described in this thesis and the second peak was discarded. After HPLC purification oligonucleotides were desalted using NAP-10 Sephadex columns (GE Healthcare), aliquoted into eppendorf tubes and stored at –20 ºC. All oligonucleotides were characterized by MALDI-TOF mass spectrometry.

For synthesizing the 3'-anthraquinone labelled oligonucleotides a modified phosphoramidite was used. The syntheses and their characterization has been published elsewhere [11].

2.8.2 PCR amplification

For the SERS-melting experiments with PCR amplicons a synthetic DNA template (50 ng) containing the wild type sequence or the ΔF508 mutation was amplified in a sample volume of 20 µL, containing 0.2 µM 5' Cy5 labelled forward primer, 0.05 µM reverse primer, 1 mM dNTPs (Promega, UK), 2.5 mM $MgCl_2$ and 1 unit hot start DNA polymerase (Eppendorf HotMaster®) in 1 × PCR buffer. The PCR reactions were performed using a thermocycler (Eppendorf Mastercycler Gradient) with a denaturation step of 95 °C for 2 min, followed by 15 cycles of 94 °C for 20 s, 54 °C for 45 s and 70 °C for 45 s. The sequences used and amplified along with that of the probe immobilized on the surface for detecting the amplicons are shown below in Table 2.3.

Table 2.3 Oligonucleotide sequences for PCR, the products and the probe used in the detection of amplicons.

Oligonucleotide	Sequence
Forward primer	**Cy5**-GTATCTATATTCATCATAGGAAACACC
Reverse primer	CATTGGAAGAATTTCATTCTGTTCTCAG
Wild type template	GCACATTGGAAGAATTTCATTCTGTTCTCAGTTTTCCTGGATTATG CCTGGCACCATTAAAGAAAATATCATCTTTGGTGTTTCCTATGATG AATATAGATACAGA
Mutant template (ΔF508)	GCACATTGGAAGAATTTCATTCTGTTCTCAGTTTTCCTGGATTATG CCTGGCACCATTAAAGAAAATATCATCGGTGTTTCCTATGATGAAT ATAGATACAGA
Wild type amplicon	**Cy5**-5'-GTATCTATATTCATCATAGGAAACACCAAAGATGATATTTTCTTTA ATGGTGCCAGGCATAATCCAGGAAAACTGAGAACAGAATGAAATT CTTCCAATG-3'
Mutant amplicon	**Cy5**-5'-GTATCTATATTCATCATAGGAAACACCGATGATATTTTCTTTAATG GTGCCAGGCATAATCCAGGAAAACTGAGAACAGAATGAAATTCTT CCAATG-3'
Probe for amplicons	$(Dithiol)_3$-3'-TCCTTTGTGGTTTCTACTATAAAAG-5'

2.8.3 Immobilization of probe oligonucleotides on the substrate

The dithiol modified oligonucleotides were diluted to 1 μM concentration with pH 8.1 phosphate buffer containing 0.1 M NaCl. It was extremely important that the substrates were clean. This was ensured by thoroughly cleaning them by sonicating in DMF for at least 3 h. Thereafter, they were immediately transferred to de-ionized water and sonicated for another 15 min. The substrates were preserved in water until used. For immobilizing the probe oligonucleotides, the substrates were dipped in the 1 μM solutions and kept in a refrigerator maintained at 6 °C for 48 h. After this the substrates were taken out and washed with pH 8.1 phosphate (0.1 M NaCl) buffer several times and dipped in 10 μM mercapto-hexanol solution prepared in pH 8.1 phosphate (1 M NaCl) buffer for 20 min. This ensured that any non-specific binding of the target oligonucleotides with the substrate was prevented. The substrates were taken out and rinsed with pH 8.1 phosphate (0.1 M NaCl) buffer several times and employed for detection or mutation analysis.

2.8.4 Surface coverage determination of probe on gold surface

The well known procedure of Steel *et al.* based on coulometry was employed to determine the coverage of immobilized probes on gold surfaces using $[Ru(NH_3)_6]^{3+}$ as the redox marker [12]. A 500 ms pulse from an initial potential of 0.1 V to -0.4 V *vs.* SCE was employed for reducing $[Ru(NH_3)_6]^{3+}$. Prior to the application of

potential pulse the solutions were deoxygenated by purging Argon through the solution for 20 min. and thereafter blanketed with Argon during the experiment. The electrode was allowed to equilibrate for 2 min. with the solution at each concentration of $[Ru(NH3)_6]^{3+}$ before recording the transient.

2.8.5 SERS-*T*melting procedure

The thermally induced melting experiments were carried out in custom designed micro-Raman cell (Version 1, Ventacon Ltd., www.ventacon.com). It utilizes a horizontal geometry for viewing under the Raman microscope maintaining a thin 150 micron thin liquid film on the substrate. It is possible to flow solutions over the substrate during an experiment without disturbing the position of the substrate. A heating element is provided in the body of the cell and can be controlled with a microcontroller circuit. Two thermocouple probes are incorporated, with digital display, for controlling and monitoring the heating temperature and the temperature of the substrate, respectively. In the thermal melting the temperature was ramped up from room temperature at 1 °C per minute to 60 °C or as appropriate in pH 8.1, 0.01 M phosphate buffer containing 0.1 M NaCl. The temperature of the substrate was recorded at the time the acquisition of each a Raman spectra was started.

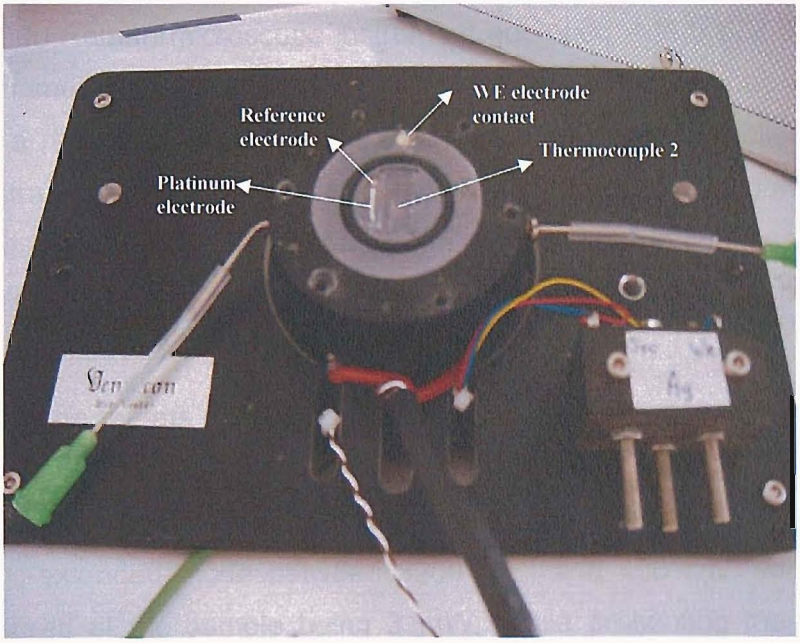

Figure 2.16 The first generation flow through micro-Raman cell for DNA detection and mutation discrimination studies. The top lid having the optical window has been removed to show the rectangular cavity where the substrate is placed. The cell cavity is made out of KelF in which a platinum counter and a Ag/AgCl electrode are embedded. It has an oven surrounding the cell as well as electrodes for electrochemical control. One thermocouple is placed near the heating element in the oven to control the temperature and the other is placed below the substrate (thermocouple 2) for monitoring its temperature. The connection to the substrate is made through a 50 micron platinum wire leading from the WE electrode contact to the top conducting surface of the substrate.

2.8.6 SERS-*E*melting procedure

The procedure for electrochemical melting was essentially similar to that used in *T*melting except that the temperature was held constant. The electrochemically induced melting experiments were carried out carried out in the same custom designed micro-Raman cell as for *T*melting experiments above (Ventacon Ltd., www.ventacon.com). For the *E*melting experiments the reference (Ag/AgCl) and counter (platinum wire) electrodes are placed on the side.

For a typical *E*melting experiment the substrates were dipped in pH 7, 10 mM TRIS buffer and the buffer was flushed over the substrates several times in the cell at open circuit potential. The experiments were carried out at room temperature. All electrochemical studies were carried out employing an EcoChemie μAutolab III potentiostat/galvanostat. A potential sequence was applied; typically, starting at -0.2 V then -0.4 V followed by 100 mV decrements until -1.3 V or less. The potential was held at each step for 300 s. Raman spectra were also recorded every 300 s with the first spectrum recorded 250 s after the beginning of the potential pulse.

2.8.7 Acquisition of SER spectra

Raman spectra were acquired using a ULWD 50x objective (NA: 0.5) on the Renishaw 2000 Raman microscope instrument equipped with a 632.8 nm He-Ne laser. The diameter of the laser spot was 1 micron. The Raman microscope system has a motorized stage with a precision XYZ stage controller. Typically, Raman spectra were acquired from a 4 μm x 4 μm or larger area on the substrate with the laser being moved 1-2 μm each time using the stage controller. This was done to avoid any bleaching effects of the dye and was aided by the fact that signals on our substrates are reproducible.

Typically, for the targets with Cy3 label, the spectra were acquired for 20-30 s; with Texas Red the spectra were acquired for 10 s and for Cy5 labelled oligonucleotides it was 2-10 s, either under static mode centred at 1400 cm^{-1} or 1450 cm^{-1} or extended mode between 3200 cm^{-1} and 400 cm^{-1} with the laser power measured at the sample being 3 mW. While presenting the results the spectra have been normalized by the laser power and the collection times to allow comparison between different measurements.

2.9 References

[1] P. N. Bartlett, J. J. Baumberg, S. Coyle, and M. E. Abdelsalam, Faraday Discuss. 125:117 (2004).

[2] P. N. Bartlett, in Biosensors: A Practical Approach (A. E. G. Cass, ed.), Oxford University Press, Oxford, 1990, p. 47.

[3] V. L. Colvin, MRS Bulletin August:637 (2001).

[4] N. D. Denkov, O. D. Velev, P. A. Kralchevsky, I. B. Ivanov, H. Yoshimura, and K. Nagayama, Langmuir 8:3183 (1992).

[5] A. S. Dimitrov and K. Nagayama, Langmuir 12:1303 (1996).

[6] K. Nagayama, Colloid Surface A 109:363 (1996).

[7] P. M. Tessier, O. D. Velev, A. T. Kalambur, A. M. Lenhoff, J. F. Rabolt, and E. W. Kaler, Adv. Mater. 13:396 (2001).

[8] Y. N. Xia, B. Gates, Y. D. Yin, and Y. Lu, Adv. Mater. 12:693 (2000).

[9] P. N. Bartlett, M. A. Ghanem, I. S. El Hallag, P. de Groot, and A. Zhukov, J. Mater. Chem. 13:2596 (2003).

[10] P. N. Bartlett, P. R. Birkin, and M. A. Ghanem, Chem. Commun.:1671 (2000).

[11] B. G. Noha and T. Brown, Tet. Lett. Submitted (2008).

[12] A. B. Steel, T. M. Herne, and M. J. Tarlov, Anal. Chem. 70:4670 (1998).

3 Improvement and Development of Substrates

3.1 Overview

In this chapter work related to improving the quality of our sphere segment void substrates is first presented and discussed. As described in the previous chapter SSV substrates are fabricated employing self-assembled colloidal crystal templates on flat gold coated slides. The electrodeposition through the template results in an inverse replica of the assembled spheres. Therefore, the quality of the substrate in terms of the close packed arrangement of the voids will be limited by the quality of the template. Therefore, chemical treatment of the gold coated substrate will affect the quality of the template and hence, the structured substrate. This was assessed systematically and a quantitative parameter as an indicator of the quality of substrates was developed based on analysis of their SEM images. Thereafter, some new developments employing self-assembled sphere templates for obtaining inter-penetrating voids and patterned wires are presented.

3.2 Effect of chemical treatment on assembly

3.2.1 Introduction

Colloidal sphere templating has become an important means of fabricating ordered metal films on the nano- and micro-scale with interesting structural and optical properties [1-3]. Since the first report of electrochemically deposited nanostructured films for photonic crystals [4] our group has led the development of electrochemically deposited metal films using colloidal nanosphere templates [5, 6]. However, the utilization of these two-dimensional (2-D) films in various applications requires the formation of a high quality defect-free colloidal crystal template.

Various methods like surface modification, modification of viscoelastic properties [7] or electrophoretic assembly [8] have been tried by researchers to improve the assembly of 2-D colloidal crystals. Yet defects abound in colloidal crystal films reported in literature though their quantification has not been carried out.

In the method developed in our group, as outlined in the previous chapter on experimental methods, cysteamine is used to treat the plain gold surface before assembly of spheres [9, 10]. Though the method worked reasonably well a study was required for optimization of the parameters like treatment time and to

investigate the nature of its effect on the gold surface to seek methods for improving the assembly (less defects). The need for improving the quality of the template warranted a systematic study of various chemical treatments on the assembly of colloidal spheres on gold. Since, traditionally, thiols have been used

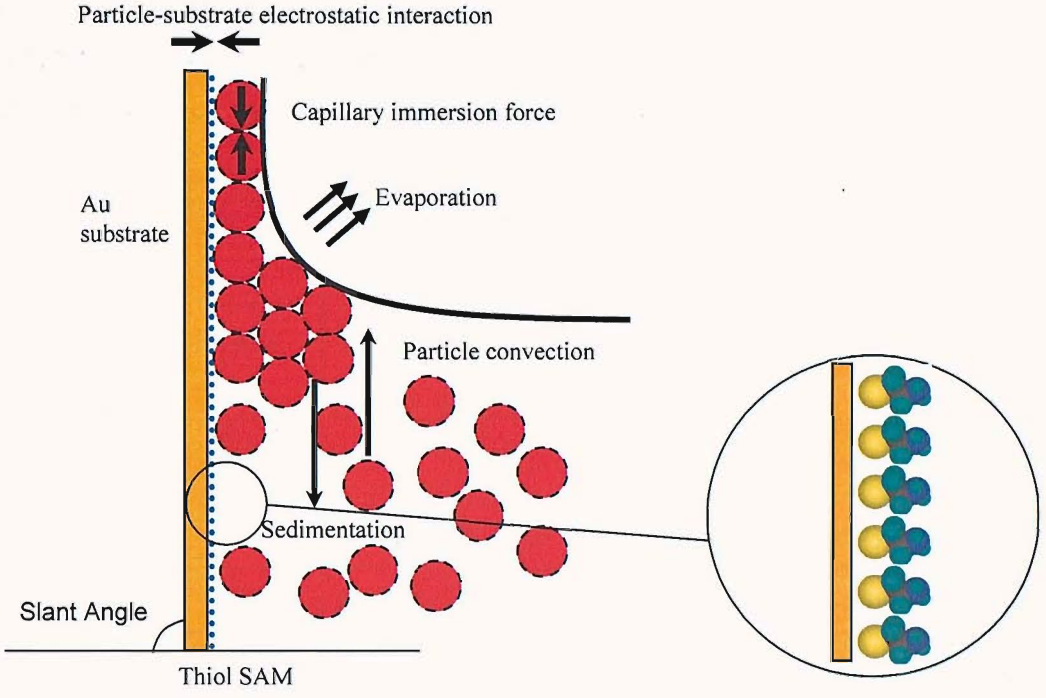

Figure 3.1 Schematic showing the self-assembly of colloidal spheres on a planar surface showing the processes and interactions involved. Surface modification affects the particle-substrate electrostatic interaction. The inset shows schematic of cysteamine molecules (where the atoms are colour coded with yellow: sulfur; cyan: hydrogen; blue: nitrogen; grey: carbon) attached to the gold surface.

for chemical modification of gold surfaces due to the strong metal-sulfur bond formed [11-13] it was decided to study the effect of thiols with different terminal groups. The different thiols chosen in this study were cysteamine, 3-mercaptopropionic acid (3-MPA), 1-propanethiol (PT) and 3-mercapto-1-propanol (MP). Thiols attach to the gold surface through the thiol functional group resulting in a metal-sulfur bond leaving the other functional groups to interact with the environment. Thus, in principle the surface properties will be governed primarily by the terminal moiety of the surface attached species. Hence, the four different kinds of surface modification will result in positively charged hydrophilic, negatively charged hydrophilic, uncharged hydrophobic and uncharged hydrophilic surface in deionized water (DI), pH ~6, from the amino, carboxy, alkyl and hydroxyl terminal groups on these compounds, respectively. The surface of the polystyrene spheres has residual sulphate groups resulting from the initiator ($K_2S_2O_8$) used during their emulsion polymerization. Hence, different types of electrostatic interaction are expected between the spheres and the chemically modified surface.

3.2.2 Contact angle measurements

Gold coated glass slides were cleaned by sonication in isopropanol for 90 min and then soaked in 10 mM solutions of the respective thiols, stated above, for various time durations increasing from a few min. to more than a month. The effect of this surface treatment was monitored with respect to different treatment times by monitoring the contact angle of the surfaces with deionized water under static conditions. A drop volume of 1 µl was employed in the experiments.

Table 3.1 Contact angle measurements (static mode) on gold surfaces for different surface modifiers after various time durations of treatment.

Treatment time / Surface treatment	Mean Contact Angle ± Std. Deviation (n=5)						
	5 min.	30 min.	2 hours	12 hours	48 hours	1 week	> 1 month
IPA	80.1±1.5 (only cleaned)						85.4±0.6
Cysteamine	44.7±4.9	39.5±4.6	37.3±1.5	34.7±2.5	35.2±1.5	35.4±2.1	34.9±2.2
3-MPA	35.9±1.5	33.7±1.7	13.9±1.6	15.1±1.5	15.4±2.5	45.6±4.1	71.6±0.8
PT	88.8±1.7	90.4±0.8	92±0.8	93.0±0.7	93.1±1.0	92.3±0.9	92.7±0.5
MP	16.1±1.9	18.8±2.8	17.0±2.1	16.6±1.3	18.3±1.6	18.7±2.5	19.5±2.8

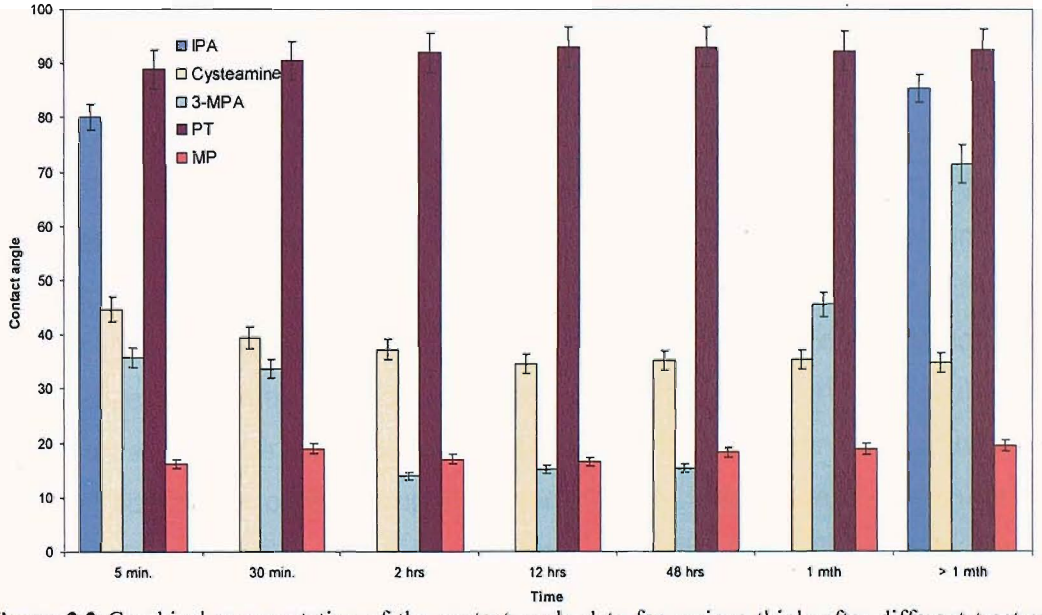

Figure 3.2 Graphical representation of the contact angle data for various thiols after different treatment times. IPA: isopropanol, 3-MPA: 3-mercaptopropanoic acid, PT: 1-propanethiol and MP: 3-mercaptopropan-1-ol.

From the above results we can see that the contact angle does not vary much after treatments beyond 48 hours except in the case of 3-mercaptopopropionic acid. It is noted that the contact angle with 3-mercaptopropionic acid first

decreases slowly to a minimum probably due slow reaction of 3-mercaptopropionic acid with the surface, which can be due to the strong electron withdrawing nature of the carboxy group making the displacement of hydrogen difficult to form the metal-sulfur bond. Thereafter, after reaching a minimum, the contact angle with 3-mercaptopropionic acid increases again on prolonging the treatment time beyond 48 h. A possible explanation for the inversion of surface hydrophilicity could be due to esterification of carboxy terminal group of the thiol with ethanol in the solution. Nevertheless, for all surfaces, as one would expect the nature of the surface followed the characteristics of the terminal group of the thiol employed.

The effect of this surface treatment on the assembly of colloidal spheres was further examined by carrying self-assembly of 600 nm diameter spheres using our controlled confined convective assembly method described in the experimental methods chapter. All steps involved in the whole process were identical except the surface treatment carried out after cleaning of the gold coated slides with isopropanol.

Templates were fabricated using the cleaned gold coated slides after 48 hours, 1 week and 1 month of treatment by the different thiols. With 3-mercaptopropionic acid and propanethiol treatment for 48 hours either the spheres did not adhere well to the surface, got re-suspended on dipping in the gold plating electrolyte or the assembly did not take place at all. Also, there was no perceptible difference in the electrodeposition characteristics for the different surface treatments. Cysteamine and 3-mercapto-propan-1-ol did result in colloidal sphere templates though the quality and reproducibility, especially with the latter were poor. After one week of chemical treatment, those gold slides modified with cysteamine and 3-mercapto-propan-1-ol gave the most uniform and robust templates. However, the best results were obtained, in terms of visual quality (fewer defects, large domain size) as examined under with the SEM, with those surfaces incubated for more than a month in the thiol solutions. Further, it was observed that the quality and the robustness of the templates were largely independent of the chemical treatment for incubation times longer than a month. Even those gold surfaces soaked in isopropanol for more than a month formed decent templates while those just cleaned with isopropanol did not. It was clear that the effect of surface treatment over prolonged periods was not detected by the contact angle measurements which changed very little after 48 h except in case of 3-

mercaptopropionic acid. Hence, this improvement in templates was not entirely due to the wettability characteristics of the surface.

3.2.3 Quantification of quality

Before proceeding to investigate the effect of prolonged chemical treatment on the surface it was necessary to develop a parameter which quantifies the quality of the substrates in terms of the defects. Since, the structured substrates are inverse replicas of the templates; this quality parameter would in effect be a reflection of the quality of the templates obtained.

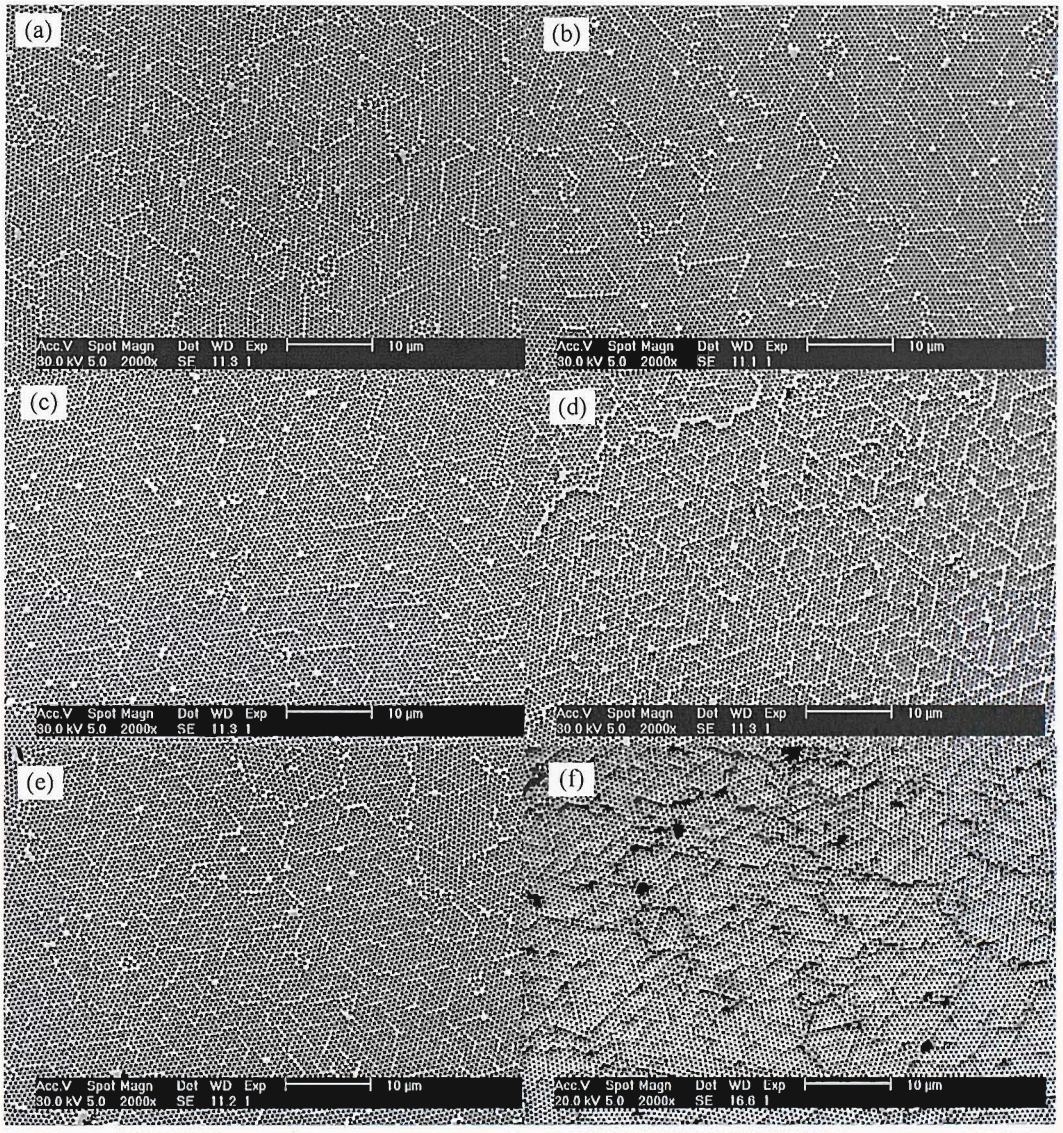

Figure 3.3 SEM images of gold films grown to half-sphere diameter using 600 nm polystyrene sphere templates formed by using substrates subjected to chemical treatment for > 1 month using (a) IPA, 10 mM ethonolic solutions of (b) cysteamine (c) 3-mercaptopropanoic Acid (d) propanethiol and, (e) 3-mercapto-1-propanol and that for (f) 48 hrs treatment with cysteamine. Scale bar is 10 µm for the images.

To quantify the quality of the templates, wherever possible, they were utilized for electrodeposition to give sphere segment void structures up to half-sphere height. This also evaluated the stability of the templates in the electroplating bath and hence, the strength of chemical interactions between the spheres and the surface.

Large area SEM images were acquired with the Philips XL030 Environmental Scanning Electron Microscope and images at low magnifications such that the voids and the area occupied by the metal remained distinguishable. The SEM images of the metal films generated are shown in Figure 3.3. The dark areas are the voids. The defect areas appear brighter than the rest of the structured metal due to the presence of excess metal. Comparing figure 3 (b) and 3 (f) it can be readily seen that the structured film prepared with cysteamine treatment for a month is distinctly better than that prepared with just 48 h treatment. In particular, it is noted that the domain size is smaller for the 48 h treated sample than those

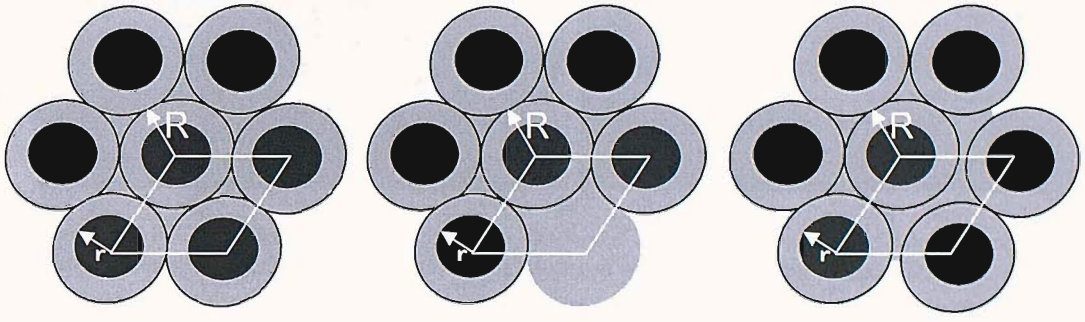

Figure 3.4 Schematic showing a plan view of an (a) ideal hexagonal close packed arrangement of metallic voids with pore radius 'r' in structured substrates templated by spheres with radius 'R', and common defects such as (b) a missing sphere and (c) a dislocation. The black outlines are guides to the eye showing the position of the spheres in the template. The solid black circles indicate the voids in the substrate and the grey areas represent the electrodeposited metal.

treated for longer times. However, with treatment times of a month the quality of the substrates is largely independent of the thiol used for chemical modification. To develop a parameter for differentiating the quality of even such visually similar films a scheme was developed based on comparing the area occupied by the metal and voids from the SEM images with the ideal case. In the ideal case the spheres are hexagonally close packed leading to voids in the structured film and a periodicity determined by the sphere size used for the formation of the template as shown schematically in Figure 3.4. In practice however a structured film templated by colloidal crystal spheres would have point defects (missing spheres) and line defects (plane dislocations) in addition to other non-idealities such as the periodicity being slightly higher than the sphere diameter of the template (see SEM image of template in Figure 3.6). Hence, a measure of the area occupied by the metal excluding the pores would include the area occupied by all kinds of defects. Comparing this with the area which should be occupied by the metal in the ideal case would be an indicator of the quality of the film in terms of defects. Thus, for practical cases in general the ratio of actual to ideal area would be expected to be more than unity. Similarly, the packing efficiency can be investigated wherein the

voids present in a particular area in the actual structured film are compared with the ideal (based on hexagonal close packed arrangement) number of voids which should be present in the same stipulated area. Thus, the packing efficiency would normally be expected to be less than unity.

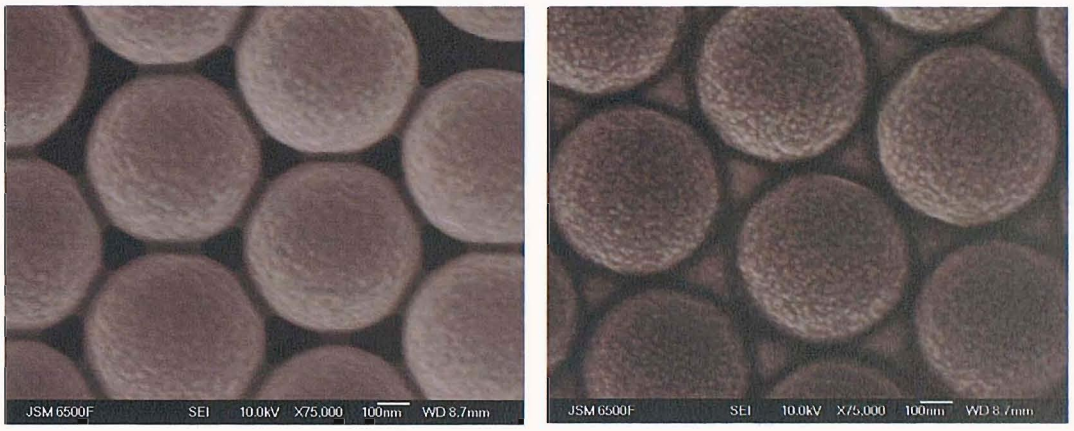

Figure 3.6 FEGSEM images of the (a) template fabricated with 600 nm spheres and (b) structured film with spheres still intact. The samples have been sputtered with 10 nm of gold before imaging.

Based on the scheme outlined above an image analysis was carried out on the structured gold films shown in Figure 3.3 employing ImagePro™ version 3.02. Two kinds of measurements were carried out; in the first case the area occupied by the bright objects (metal) was measured after appropriate calibration (using the scale bar of an SEM image) and in the second case dark objects were counted and various parameters such as their width, diameter etc. by particle fitting along with

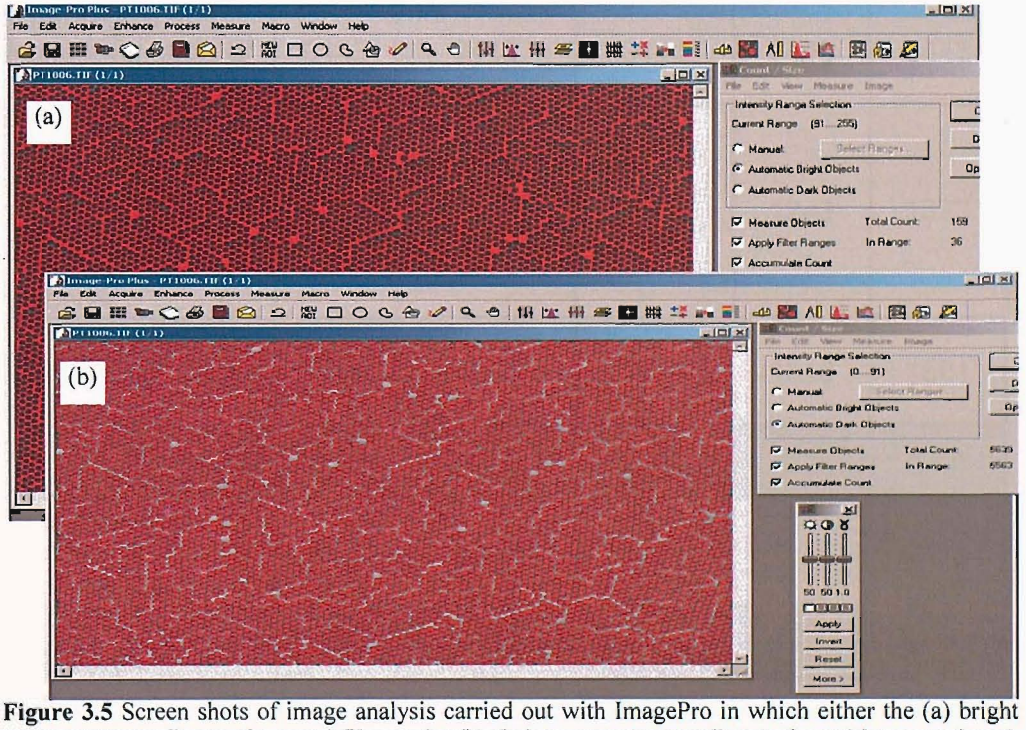

Figure 3.5 Screen shots of image analysis carried out with ImagePro in which either the (a) bright areas corresponding to the metal film or the (b) dark areas corresponding to the voids are analyzed. The analyzed area is shown in red.

the total area occupied by the voids. Typical screen shots of the two types of analysis are shown in Figure 3.5.

The total area of the dark areas (voids), the area of the bright areas (metal) and average particle (void) diameter was obtained from this analysis. The total area and the average diameter were used to arrive at the actual number of voids in the image area. Direct counting by the software was sometimes ineffective as many voids got counted as one and the software was unable to resolve them separately due to variable contrast on the film. The average particle (void) diameter along with the template sphere radius, 'R' was used to find the theoretical parameters in the image area. A summary of the results corresponding to the images shown in Figure 3.3(a)-(e) for each chemical treatment used during fabrication of the template is presented in Table 3.2.

Table 3.2 Image analysis data presented as an average for three different SEM images of the metal film for each different chemical modifier treated over 1 month. (IPA: isopropanol, 3-MPA: 3-mercaptopropionic acid, PT: propanethiol, MP: 3-mercaptopropan-1-ol)

	IPA	Cysteamine	3-MPA	PT	MP
Total area of voids $(\mu m)^2$	1460	1412	1340	1428	1353
Average Void Diameter (μm)	0.47	0.46	0.46	0.48	0.46
Template Sphere Diameter (μm)	0.60	0.60	0.60	0.60	0.60
Area of each SEM image $(\mu m)^2$	2944	2944	2944	2944	2944
Theoretical no of spheres in area of SEM	9443	9443	9443	9443	9443
Theoretical area of metal using the average void diameter & theoretical no. of spheres	1317	1391	1391	1243	1373
Actual area of metal $(\mu m)^2$ from ImagePro	1484	1532	1604	1516	1591
Actual/Theoretical Area Ratio	**1.14**	**1.11**	**1.17**	**1.23**	**1.16**
Standard deviation (n=3 different regions)	0.03	0.09	0.08	0.27	0.03
Packing efficiency	**0.89**	**0.91**	**0.86**	**0.83**	**0.85**

From the above table it is obvious that that even over long term surface treatment times, cysteamine results in lower actual/theoretical ratio and a higher

packing efficiency compared to other solutions. Also it is clear that for a month long treatment isopropanol as well as 3-mercaptopropan-1-ol result in decent characteristics while propanethiol is the worst. Nevertheless, in spite of the difference in quantitative parameters obtained above, it has to be pointed out that all the treatments over long period resulted in an improved quality of templates and hence, of the structured films, compared to those obtained with short term treatments. It was postulated that over long term periods the surface itself might be undergoing some changes under the influence of the thiols. Therefore, we examined the surface with high resolution SEM and AFM.

3.2.4 Surface characterization

High resolution images were taken with a Jeol 6500F Field Emission Scanning Electron Microscope (FESEM) to see the effect of surface modification on the

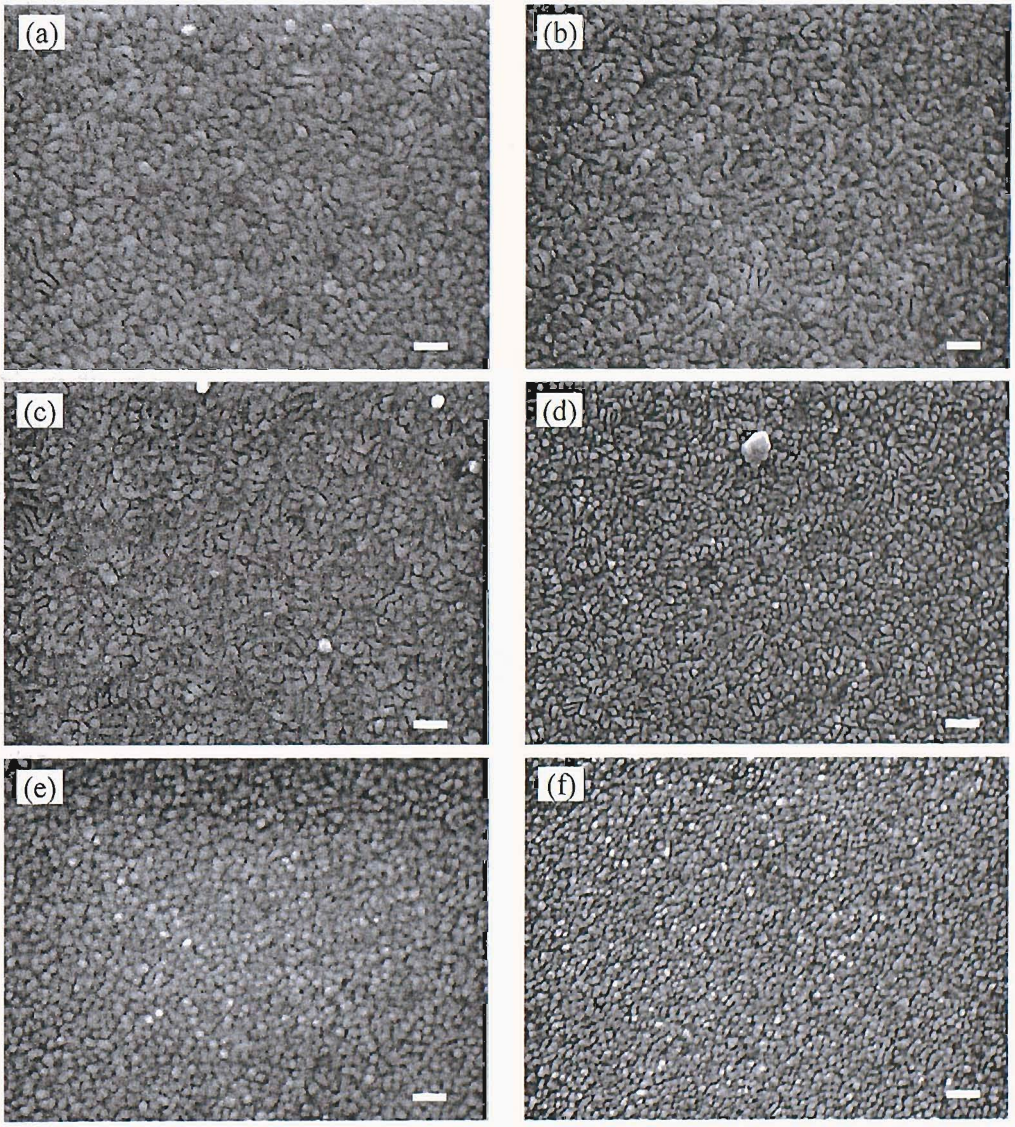

Figure 3.7 FESEM images of gold coated (~300 nm) glass substrates subjected to (a) cleaning in IPA, treatment with cysteamine for (b) 48 hours, (c) ~ 1 week, (d) ~ 2 weeks, (e) > 1 month and, treatment with 3-mercaptopropan-1-ol for (f) > 1 month. The scale bar for the images is 200 nm.

microstructure of the evaporated gold films which served as substrates for the self-assembly process. Images of the variously treated gold coated glass slides taken from the same batch (corresponding to thermal vapour deposition of gold) but incubated with different solutions and for different lengths of time are presented in Figure 3.7.

The evolution of the grains with time is evident from the images. Compared to the isopropanol cleaned surface the grain size progressively become smaller with increasing soaking time for the surfaces treated with thiols. The metallic islands decrease from about 100 nm to less than 50 nm. Over prolonged periods, treatment with any of the thiols or even IPA produces the same effect of decreasing the surface roughness.

To conclusively establish this smoothening effect with prolonged treatment of thiols AFM studies were carried out and the surface roughness of the treated gold substrates was determined. Surface roughness was evaluated using a Topometrix AFM Explorer™ in the contact mode. 5μm x 5μm scan areas were imaged after optimizing the PID (proportional, integral & differential) feedback values for each sample at a scan rate of 10 μm/s. Root mean square (RMS) roughness values were recorded for the whole area of the image after fitting a second order plane for levelling the images using the Topometrix SPMLab NT Version 5 analysis

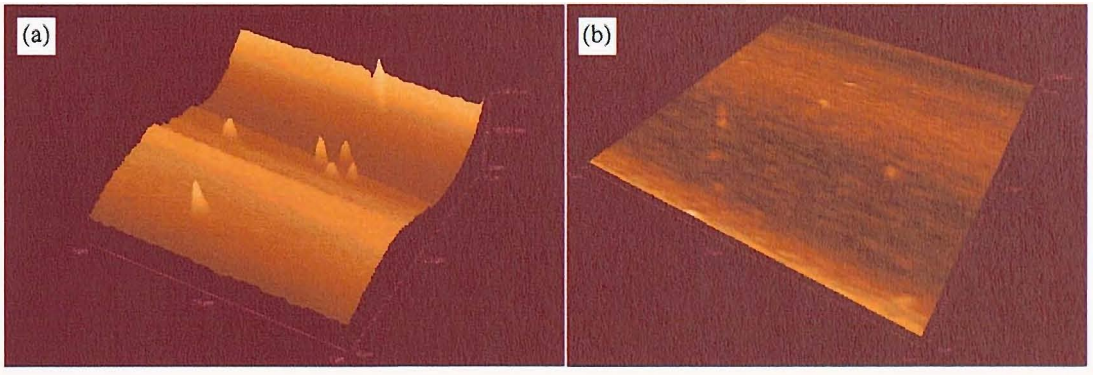

Figure 3.8 AFM images in contact mode for (a) untreated -only cleaned with isopropanol and (b) treated with 10 mM Cysteamine solution over a month with the same y-scale. Scan area 5 μm x 5 μm, scan speed 10 μm/s.

software. Two representative images are presented in Figure 3.8 showing the effect of surface treatment with thiols over prolonged periods. It can be readily seen that the spikes seen in the AFM image of untreated surface are clearly reduced compared to the surface soaked in cysteamine solution over a month. This confirms the earlier observation that there is indeed an etching type effect by the thiols which is also reducing the surface roughness of the evaporated gold

substrates. The undulation of the surface itself (in Figure 3.8a) is attributed to that in the ordinary glass slide used as the base substrate.

This etching effect of neat thiols termed 'digestive ripening' has been demonstrated by Prasad and coworkers [14] in a different study for reducing the size of their gold nanoparticles. In addition to the digestive-ripening effect of thiols they have found the following series on the effectiveness of various ligands towards reducing the size of gold nanoparticles: RSH ≈ RNH_2 ≈ R_3P ≈ $RSiH_3$ > RI > ROH ≈ RBr. Besides providing a possible explanation of the reduction in grain size and surface roughness by thiol solutions over prolonged periods this also could be the basis of the effectiveness of cysteamine solution. Other than altering the wettability of the substrate leading to better self-assembly of colloidal spheres cysteamine is the most effective as it possesses both the mercapto- and the amino- groups among the various chemical modifications examined in this work. Therefore, it smooths the surface much more effectively than the others thus aiding the assembly and leading to an improvement in the quality of the structured substrates. The digestive ripening effect also helps explain the behaviour observed with other thiol solutions used in this study and isopropyl alcohol over prolonged periods. Probably they all etch the surface though to various degrees and reduce the surface roughness and therefore increase the domain size of the assembled spheres. The decrease in surface roughness probably helps the meniscus sweep over the surface more smoothly or the rough surface disturbs the packing of the spheres and hence, improves the ordered assembly of spheres.

Utilizing the above discussed affect it was imperative to find an improved (faster) way of treating the surface in order to achieve the same effect of reduction in surface roughness observed over prolonged treatment with thiol solutions. Prasad and coworkers in their study have used reflux with neat thiols such as decanethiol to reduce the dimensions of gold nanoparticles [14, 15]. It was found that refluxing the gold coated substrates with a 10 mM solution of decanethiol in ethanol produced a similar effect. The root mean square (RMS) surface roughness values obtained with this decanethiol treatment using AFM are tabulated below along with those obtained with untreated and cysteamine treated substrates.

Table 3.3 RMS roughness values obtained with contact mode AFM with various chemical treatments of gold coated glass slides.

Treatment	Only cleaned with isopropanol	10 mM Cysteamine for 56 hrs	10 mM Cysteamine for > 1 month	Refluxed with 10 mM decanethiol for 48 hrs
RMS values/nm	30.2±3.3	27.16±5.1	10.1±4.0	11.6±2.8

However the substrate, though reduced in surface roughness, did not result in any assembly of the polystyrene colloidal spheres due to the extremely hydrophobic nature of the surface. Hence, instead of employing decanethiol the same methodology of reflux was utilized with a 50 mM solution of cysteamine in ethanol over 24 hours. A RMS roughness of about 12 nm was obtained with this treatment and with proper wettability enabling fabrication of good quality templates on a much faster timescale.

However, during the course of this thesis work, subsequent to this study, gold coated glass slides were left to 'pickle' (soak) in 10 mM cysteamine in ethanol solutions for ≥1 month durations. Only a few times, for making some structured surfaces in large quantities at short notice, was this reflux methodology used for getting good quality substrates. The results from both the procedures appeared to be indistinguishable. An SEM image of one such structured substrate prepared with the 24 h reflux method for surface preparation is presented in Figure 3.9.

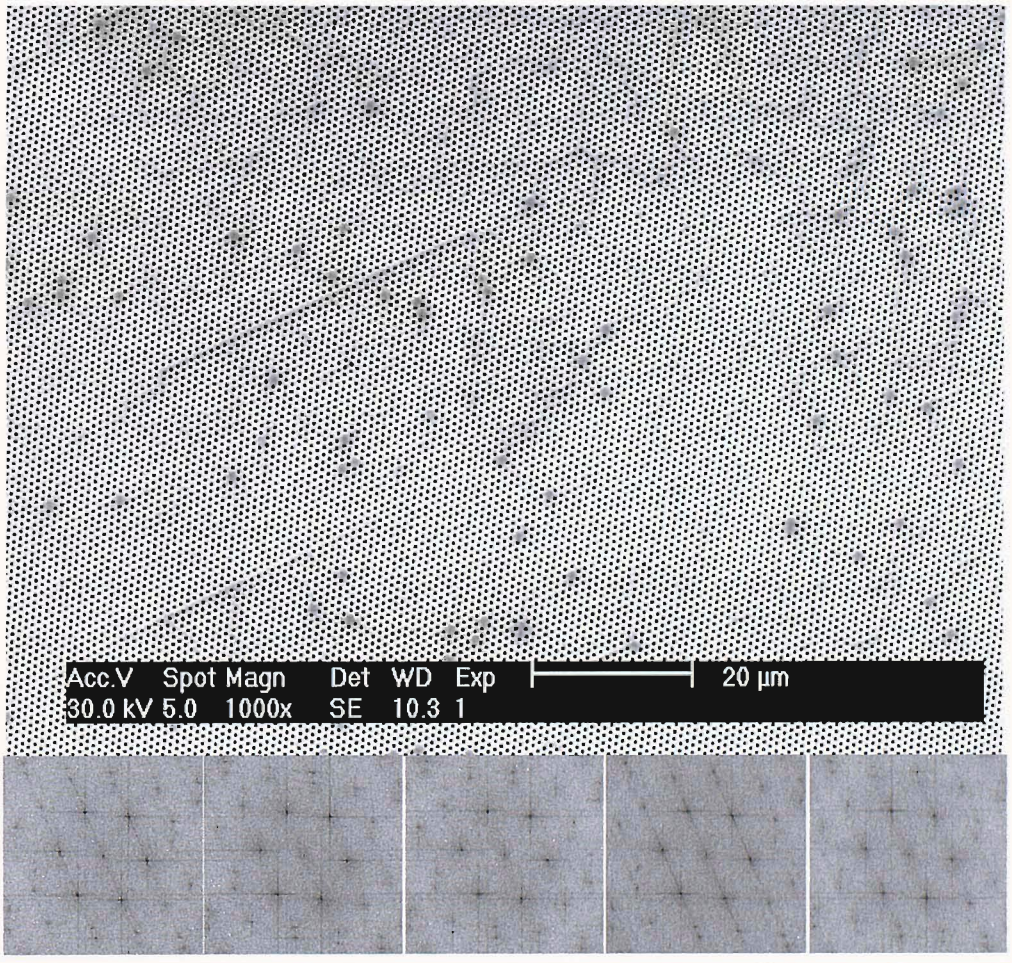

Figure 3.9 A large area SEM image of a structured gold substrate templated with 900 nm spheres. Below the SEM image FFT analysis of the image is shown at five different locations at the corners and in the middle (beginning at the top left hand and going clockwise) corner using a square area of 45.31 µm x 45.31 µm.

Though there are still some defects yet the whole area is essentially a single crystal; the arrangement of lattice points is continuous and there are no grain boundaries. That it is a single domain is confirmed by an FFT analysis of the image at five different places on the image using 256x256 pixels square (45.31 μm x 45.31 μm). Deviation in one crystal direction is found to be less than 3 degrees. The amount of area occupied by missing sphere and line defects as a percentage of the total area were found to be 2.4% and 0.9%, respectively. The numbers have been obtained by physical measurement from the image. This has to be seen in perspective of the fact that the polydispersity of the spheres itself is 1.3 %. Thus, the quality of the substrates with this method is significantly improved without the use of any gelling/viscoelastic agent etc. added to the colloidal sphere solution [16].

3.2.5 Summary

From the foregoing discussion it is evident that control over the surface wettability and the electrostatic interaction is important to improve the assembly of colloidal crystals. In the current study cysteamine was the most effective over short treatment times due to its benevolent effect on the wettability of the surface. The contact angle, which indicates the wetting property of the substrate, needs to be around 35-45 degrees; therefore 3-mercapto-1-propanol and cysteamine give better results than other surface treatments. The contact angle also has an effect on the meniscus shape at the drying edge of the colloidal solution. The movement of the meniscus is determined by the surface roughness while particle-particle and particle-surface interactions are determined by the pH and surface treatment, respectively, and play a role in the packing of the crystals. All these combine in surfaces treated with cysteamine over long durations and used with polystyrene sphere colloidal suspensions (~pH 6) to give the best self-assembly conditions. Nevertheless, macro surface parameters like cleanliness and smoothness of the surface are primary to the get high quality 2-D colloidal templates. The decrease in surface roughness due to prolonged treatment with various thiols and isopropanol led to a general improvement in the quality of the templates obtained though cysteamine still gave the best results among the chemical modifications examined. A process to decrease the surface roughness without resorting to expensive methods for flat substrate preparation and on faster timescale was also found.

3.3 Interpenetrating voids

Abdelsalam *et al.* have earlier used **double templating method** to generate non-close packed spherical void substrates using the colloidal sphere templating method [17]. While working with this method to obtain various non-close packed spherical cavity substrates another new class of substrates were discovered. These are termed interpenetrating sphere segment void substrates that consist of two hexagonally close packed arrangements of spherical cavities. In the double templating method described by Abdelsalam *et al.* [17] an assembly of large spheres is first carried out, then the films are grown and the spheres removed; this is followed by assembly of smaller spheres using the structured surface as the substrate. With the pre-patterned heights mentioned in the previous work carried in our group ($\geq 0.3\ D$) the smaller spheres assemble inside the preformed voids and this is dependent on the ratio of the sphere sizes. Further electrodeposition and dissolution of the template leads to non-close packed voids whose size is determined by the smaller spheres while the periodicity **is determined by the** large spheres used to form the initial template (see Figure 3.10a). In the work described here the height of the first patterned layer has been found to have an effect on the

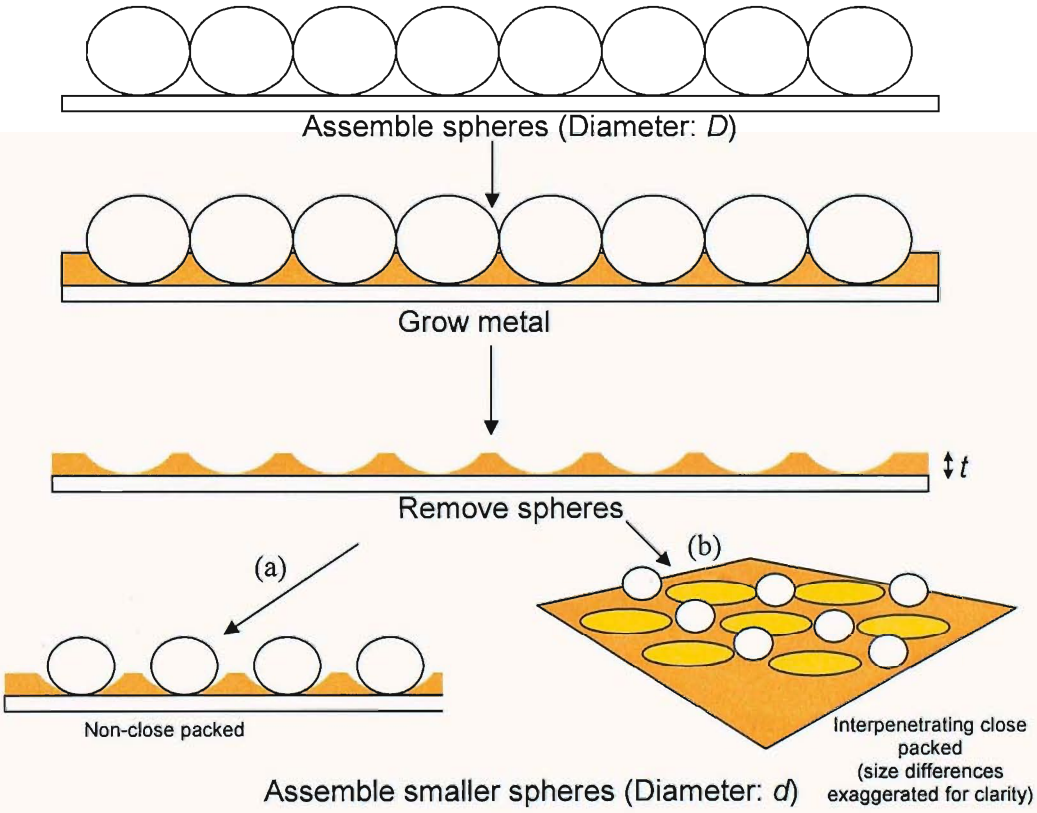

Figure 3.10 Twin templating using two sizes of spheres. In (a) $t \geq 0.4\ D$ leads to assembly of smaller spheres inside the voids while in (b) $0.2 \leq t < 0.3\ D$ leads to assembly of spheres on top of the metal interconnect between the voids. D is the diameter of the spheres used in the first templating step. t is the normalized height (=height/D).

assembly of the second layer of spheres.

For obtaining the interpenetrating type of substrates a similar procedure works with only slight modification that instead of growing the electroplated layer to 0.3 or higher of the sphere diameter, the film is electrodeposited to 0.2 of the sphere diameter. In such a case the second layer of smaller spheres assembles on the top of metal connecting the voids rather than in the voids themselves. Larger area is available at the junction between three voids compared to the area between adjoining voids on the hexagonally arranged cavities formed from the initial template. Hence the second layer of spheres assembles in a hexagonal array using the former as the array sites. Figure 3.10 gives the scheme for this fabrication methodology. The spheres in the case of Figure 3.10b assemble in between the voids probably due to their depth not being enough to create enough surface tension force to overcome the attractive capillary force existing between the spheres. Obviously, whether the smaller spheres stay on the top or fall into the voids or both will also depend on the ratio of spheres being employed in the twin templating process; however, this possibility was not tested in the current work.

Using this scheme interpenetrating structures were fabricated using 900 nm diameter spheres for the first templating step. Gold electrodeposition was carried out to obtain a film thickness of around 180 nm and the spheres were dissolved in DMF. An SEM image of this surface is shown below in Figure 3.11.

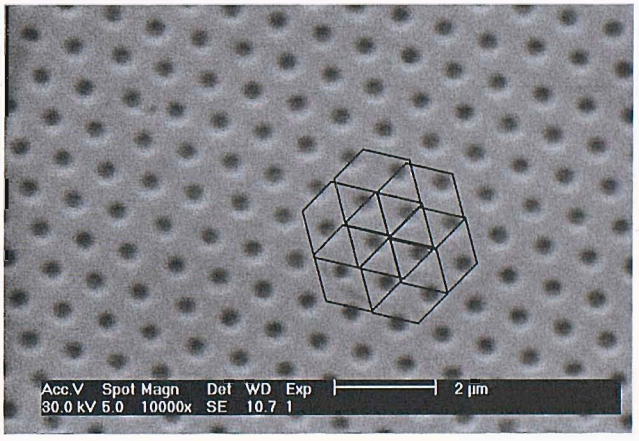

Figure 3.11 A SEM image of patterned surface templated with 900 nm spheres and having a film thickness of 0.3 *D* used for the second step in twin templating.

Thereafter, the cleaned substrate obtained above was soaked in 10 mM cysteamine solution for a week and then 700 nm diameter spheres were assembled using the above patterned substrate. A representative SEM image showing that the second step in this case of twin templating leads to assembly of spheres on the top metal between surrounding the voids is shown in Figure 3.12.

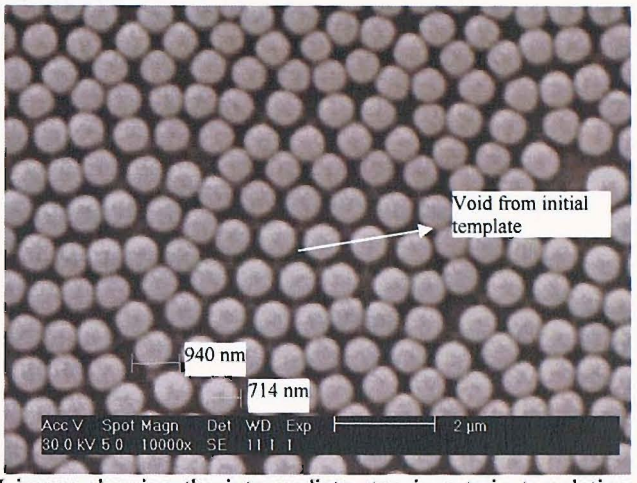

Figure 3.13 A SEM image showing the intermediate step in a twin templating process for generating interpenetrating structures wherein 700 nm spheres assemble on the structured metal film rather than in the voids.

The underlying patterned void layer is visible through the 700 nm diameter assembled spheres on the area between the voids.

After the assembly of 700 nm spheres on the 900 nm templated substrate, further electrodeposition can be carried out in steps to yield a sample with graded film thicknesses or a fixed film thickness. However, the twin templated structures appear most interesting up to a height of about ~0.4 *D* corresponding to the second electrodeposition step. SEM images corresponding to 0.1 and 0.2 *D* thicknesses for the second templated electrodeposition step is shown in Figure 3.13. The distances between the smaller and large spheres clearly suggest that

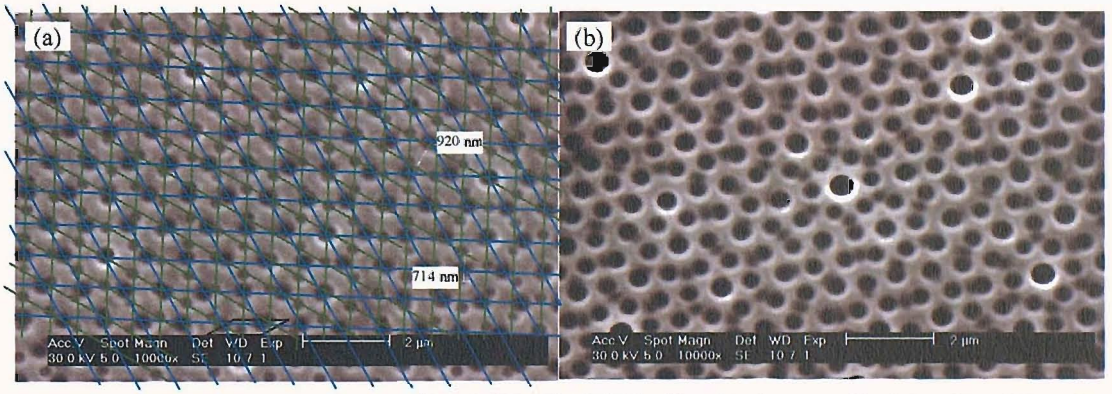

Figure 3.12 SEM images of (a) 0.1 *D* and (b) 0.2 *D* thick film for the second electrodeposition step showing the two hexagonal packed void arrays templated with 700 nm diameter spheres on a surface patterned with 900 nm diameter spheres.

both the voids are a result of close packed templates both for the initial and the second assembly step.

As a result of two separate interspersed arrays with a periodicity of 700 nm and 900 nm, respectively these structures were found to have hybrid optical properties possessing a combination from their constituting components. For comparison

with the geometry shown in Figure 3.12a, reflectance spectra were recorded on a 0.2 *D* thick 900 nm diameter sphere templated gold film and a 0.1 *D* thick 700 nm diameter sphere templated film. The reflectance maps showing the energy distribution of reflectance as a function of incident angle are shown in Figure 3.14 for the aforementioned films along with that obtained for the interpenetrating structure shown above in Figure 3.13. In the contour plot, blue indicates strongest reflection while red means strongest absorption. This absorption is indicative of the existence of plasmons.

As mentioned in Chapter 1 that the Bragg plasmons are strongly angle dependent and follow the principles of diffraction. The periodicity of the assembled spheres determines the distance between the diffraction planes in the hexagonal array. Hence, this determines the energy of Bragg type plasmons which are observed when the samples are thin and the SSV structure takes the form of a hexagonally arranged array of voids. The dispersion plots presented in Figure 3.14a & b are typical of Bragg plasmons observed with sphere segment voids for 900 and 700 nm periodicities, respectively, at these relative thicknesses [18]. Plasmon maps are discussed later in Chapter 4 and are therefore not described in detail here.

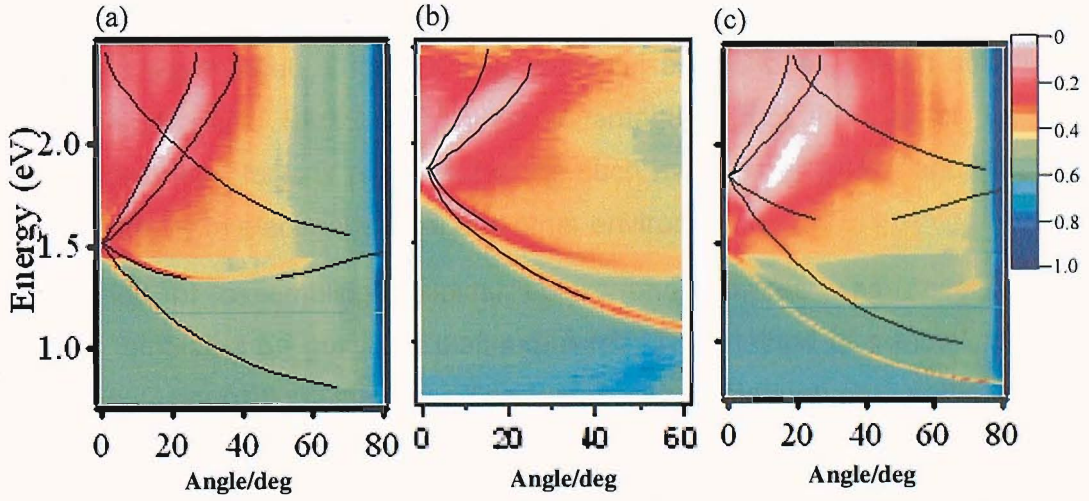

Figure 3.14 Reflectance maps showing the angular distribution of the energy absorbed by the gold structured surfaces for (a) 0.2 *D* thick film templated with 900 nm spheres, (b) 0.1 *D* thick film templated with 700 nm spheres and (c) an interpenetrating structure film with 0.1 *D* thick 700 nm templated film on a 0.2 *D* thick 900 nm sphere templated surface. Blue indicates weakest and red indicates the strongest absorption. The black lines show the theoretical dispersion of plasmons.

Nevertheless, from the above reflectance maps it can be seen that the Bragg plasmon (the black overlaid lines are the theoretically predicted dispersions) for the 700 nm spaced voids crosses at 1.85 eV (675 nm) at 0 deg (Figure 3.14a) while for the 900 nm spaced voids it crosses at 1.5 eV (829 nm) at 0 deg (Figure

3.14b). For the interpenetrating structure of 700 nm templated voids on a 900 nm templated surface shows the Bragg plasmon distribution for both the individual cases with a branch emanating at 1.85 eV and another at 1.5 eV. This suggests that the Bragg scattering effect is additive as expected from diffraction theory, even for the case of plasmons generated here. Though an application for these interpenetrating void substrates was not attempted, these could be interesting to study for a variety of purposes including studying tesselations or tiles and mathematical analysis. Voronoi analysis can be carried out where the plane is partitioned with *n* points (called Voronoi sites or generating points) into convex polygons such that each of the polygons contains exactly one generating point and that every point on the polygon is nearest to its generating point than to any other. Nevertheless, not only are these structure novel, the reflectance study demonstrates that it is possible to combine the properties of two different optical active surfaces using such an interpenetrating structure fabrication methodology.

3.4 Patterned wires

In the literature as well as in our group, colloidal crystal assembly has carried out primarily on planar surfaces. For practical applications in a host of fields ranging from optoelectronics to biology one can envisage that there is a great potential for patterning non-planar surfaces. Such patterning, especially of wires would be particularly advantageous for studying electrical effects due to such structuring and electrochemical SERS. The other advantage is that the use of the wire obviates the need for any planar substrate such as glass or silicon and thus can be used directly in electrochemical and other environments.

A method of assembling colloidal polystyrene spheres was developed to fabricate templates on gold and platinum wires. The method is a modification of the vertical deposition method. The wires were cleaned by sonicating in isopropanol for 90 min and then soaked in 10 mM cysteamine for at least a week. Thereafter, the wires were rinsed with water and soaked in a 0.025% solution of the colloidal solution prepared in de-ionized water and held in a holder as shown in Figure 3.15. The holder was made out of Parafilm™ and cut pipette tips were embedded in it for holding the wires vertical in the vial. This holder was kept in a 20 ml glass vial and the whole system placed in an incubator maintained at 25 °C.

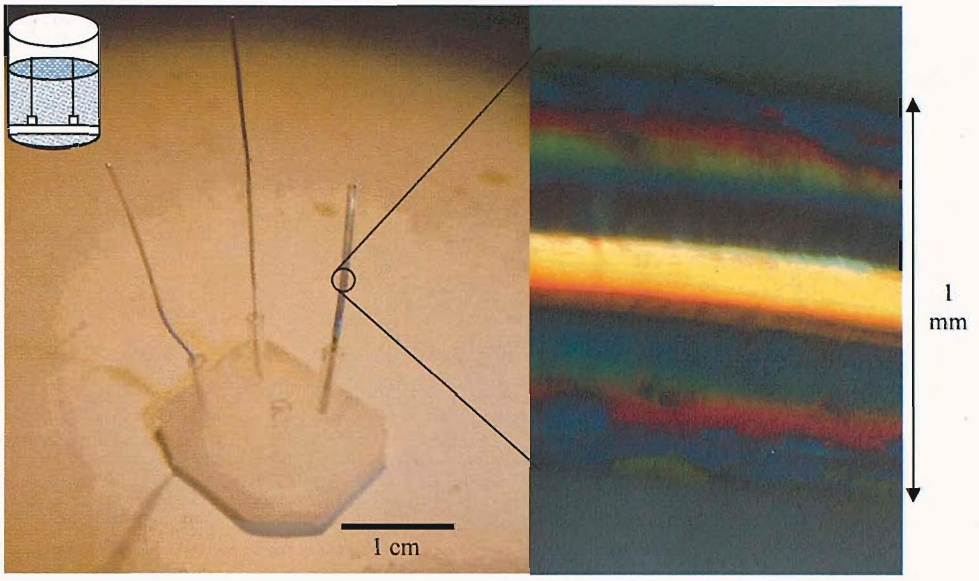

Figure 3.15 Assembled polystyrene spheres on different diameter (0.5 mm & 1 mm) Pt wires held vertically on a holder (a schematic of the cell employed with 2 wires held vertically is shown in the inset) and close-up of a 1 mm diameter patterned wire observed using an optical microscope with a white light source

This assembly resulted in a monolayer of the colloidal spheres deposited on the wires. The method worked equally well with gold wires. These colloidal crystals served as a template for fabricating sphere segment void structures on the wires. Rhodium and gold structures were successfully fabricated. A patterned wire templated with 600 nm spheres and grown to 450 nm thickness is shown in Figure 3.16.

Rhodium has a very high melting point (1964 ^{o}C) and can be heated to give black body emission. It is expected that with the patterning the emission will be modulated due to the structure. Wires with structured rhodium fabricated using sphere templated electrodeposition were tested for black body emission in a vacuum cell with the wire heated electrically by passing a current through it. The experimental arrangement used in the School of Physics is shown in Figure 3.17.

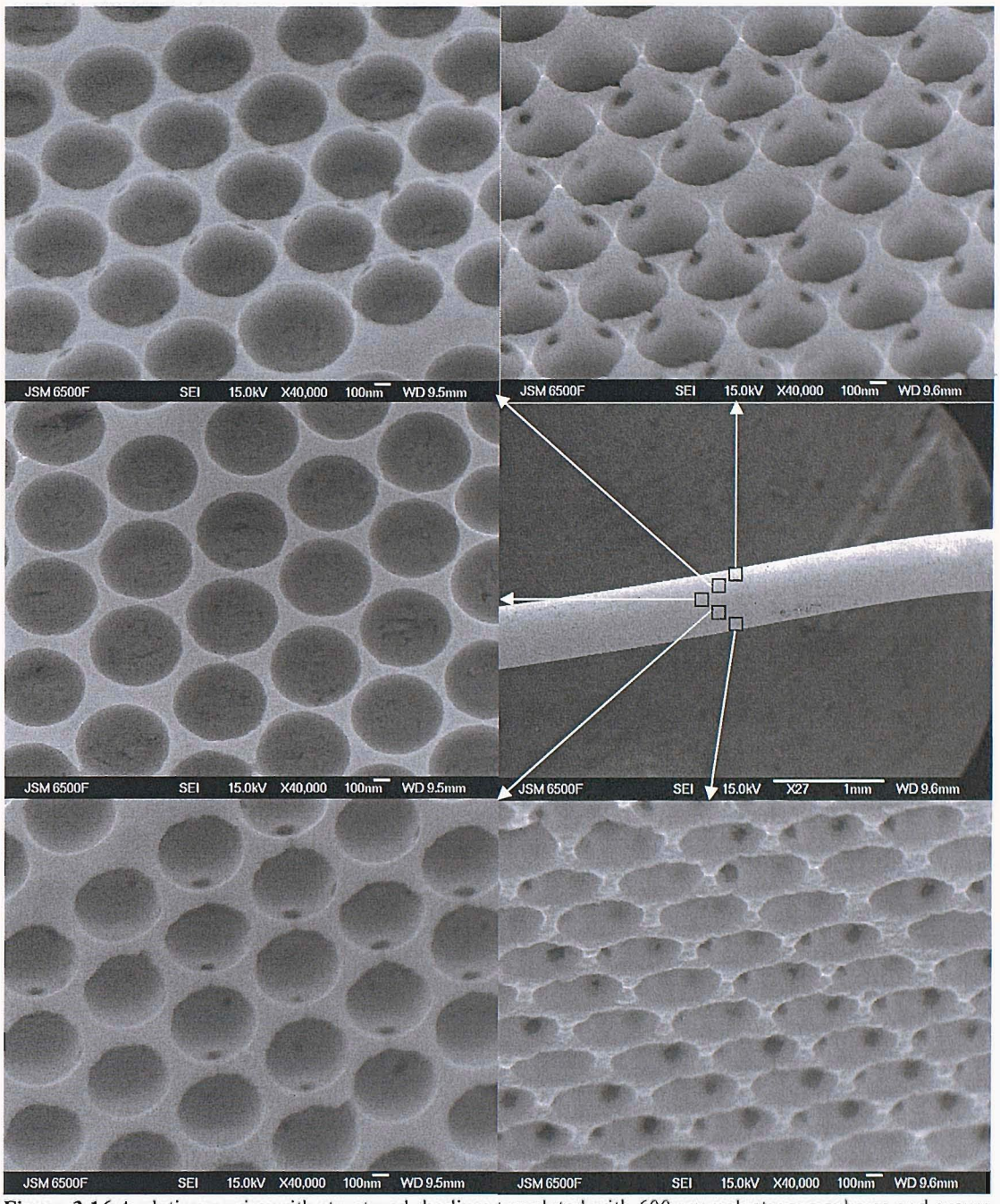

Figure 3.16 A platinum wire with structured rhodium templated with 600 nm polystyrene spheres and grown to 0.75 *D*.

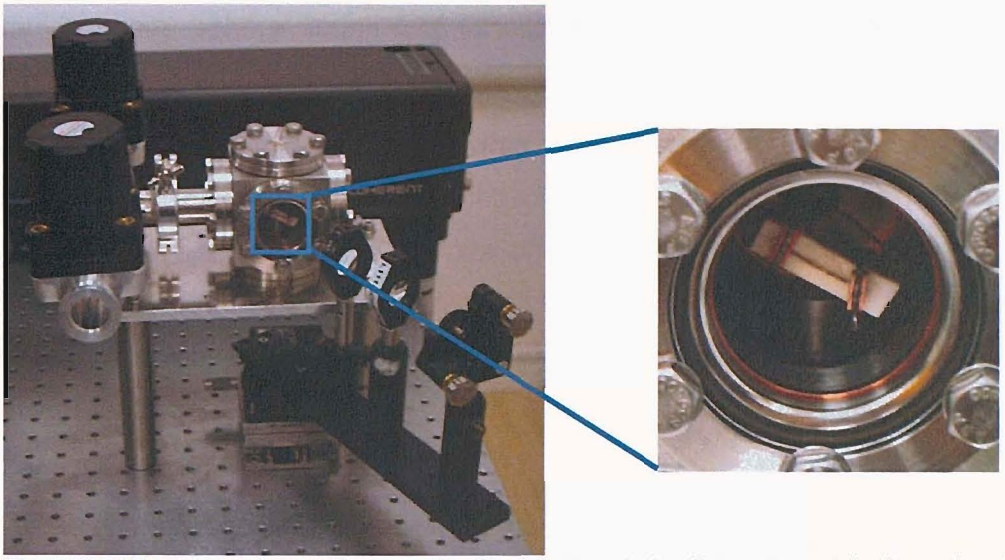

Figure 3.17 Experimental setup for measuring black body emission from patterned rhodium wires. The wire is held against a ceramic plate pinned down with the electrical contacts. Heating is carried out by increasing the current in the vacuum cell.

Results from preliminary emission experiments are shown in Figure 3.18. In this case the structured rhodium was patterned using 600 nm spheres and electrodeposited to 480 nm; correspondingly for a control experiment the electrodeposition was carried out to the same thickness without the template. Emission recorded from a patterned rhodium wire shows a clear difference compared to the flat rhodium coated wire. The normalized emission from the patterned rhodium wire drops at lower wavelengths on account of modulation by

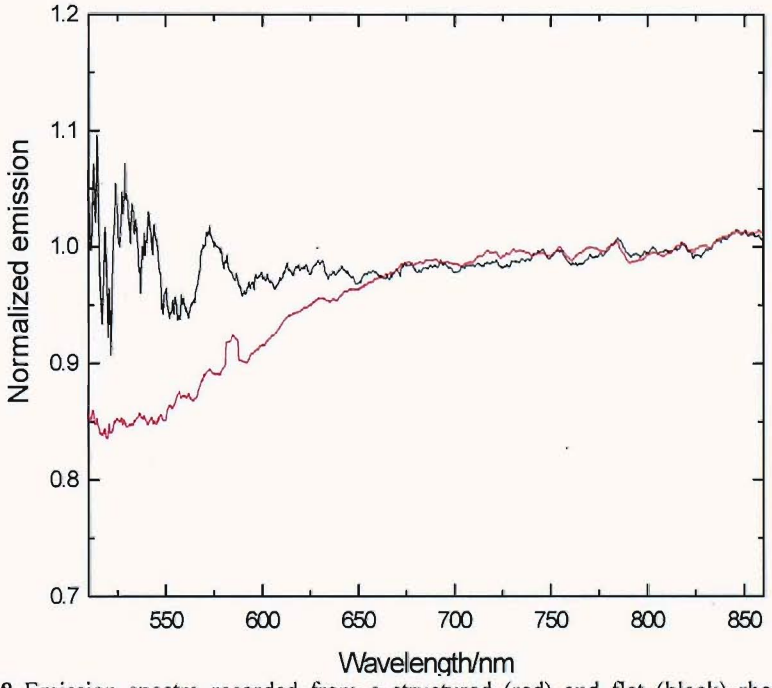

Figure 3.18 Emission spectra recorded from a structured (red) and flat (black) rhodium coated platinum wire at a temperature of 1201 °C and 1315 °C, respectively, as determined by the respective black body fits. The intensities have been normalized by the corresponding theoretical black body emission intensity at that particular wavelength.

the 600 nm sphere templated structure compared to the flat film. Further experiments are under way.

In addition, the gold patterned wires were tested for SERS using the micro-Raman Renishaw system. Benzenethiol was used as the probe molecule. The wire worked well and SERS spectra of similar quality to those observed from a sphere segment void structure on a flat substrate were obtained. A representative SERS spectrum of benzenethiol is shown in Figure 3.19 without discussing its salient features. SERS spectra including those from benzenethiol are discussed in detail in Chapter 4.

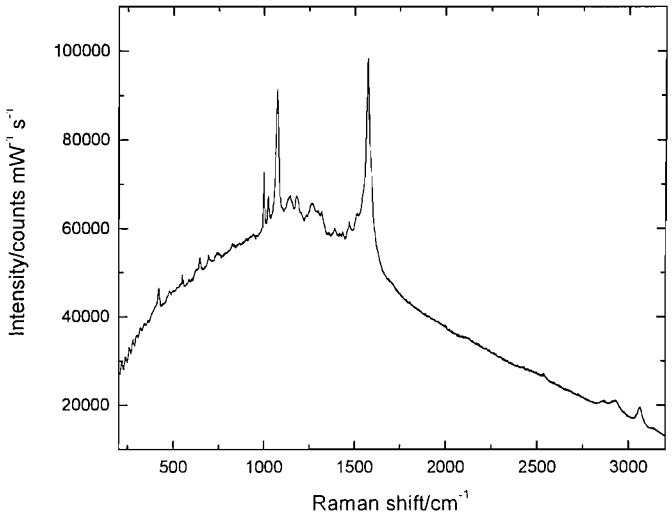

Figure 3.19 A spectrum of benzenethiol on a patterned wire gold substrate templated with 600 nm spheres having a thickness of 480 nm. Laser: 633 nm; Power: 3mW, single 10 s extended scan; 50x objective (NA: 0.75).

For SERS applications the patterned wire obviously shows similar characteristics as the planar substrates further described in this thesis in Chapter 4 and doesn't present any significant advantage other than obviating the need for evaporating/depositing a layer of conductive material on a planar surface such as glass slide). However, for electrochemical applications the wire geometry might prove much more useful as it avoids the problem of making the contact from the top as in the case of gold coated glass slides and is easier to use in complex cell geometries without the need for any special modifications of the cell. Another significance of this method of obtaining patterned wires is that it has the potential of being scaled up very easily and could lead to a mass manufacturing method for fabrication similar to that extruding wires in a continuous assembly line, if desired.

3.5 Conclusions

In this chapter the material related developments have been described. With regard to the systematic study on the effect of chemical modification of the surface

on the assembly and hence the quality of the substrates, the most significant finding was the long term affect of thiols on the surface. It was found that cysteamine was the most effective both over short term and long term treatments on account of the creating proper wettability and reducing surface roughness. The best results for the self-assembly of polystyrene spheres were obtained with surfaces treated with 10 mM ethanolic solutions of cysteamine for a month. It was also shown in this chapter that control over assembly through twin templating could be tuned to obtain a new type interpenetrating void structures which possessed mixed optical properties. Lastly, the technique of templated electrodeposition through colloidal spheres was successfully applied to pattern curved surfaces. It is postulated that this might present a significant technological advance and may lead not only to novel applications but also could be scaled up and used in mass production as a SERS substrate or other applications.

3.6 References

[1] P. N. Bartlett, J. J. Baumberg, S. Coyle, and M. E. Abdelsalam, Faraday Discuss. 125:117 (2004).

[2] S. Cintra, M. Abdelsalem, P. N. Bartlett, J. J. Baumberg, T. Kelf, Y. Sugawara, and A. E. Russell, Faraday Discuss. 132:191 (2005).

[3] J. C. Hulteen, D. A. Treichel, M. T. Smith, M. L. Duval, T. R. Jensen, and R. P. Van Duyne, J. Phys. Chem. B 103:3854 (1999).

[4] P. V. Braun and P. Wiltzius, Nature 402:603 (1999).

[5] P. N. Bartlett, P. R. Birkin, and M. A. Ghanem, Chem. Commun. 671 (2000).

[6] M. A. Ghanem, P. N. Bartlett, and P. R. Birkin, Proceedings - Electrochemical Society 2000-25:180 (2001).

[7] M. H. Kim, H. K. Choi, and O. O. Park, Appl. Phys. Lett. 88:143127/1 (2006).

[8] H. J. Schoepe, J. Phys.: Condens. Mat. 15:L533 (2003).

[9] P. N. Bartlett, J. J. Baumberg, P. R. Birkin, M. A. Ghanem, and M. C. Netti, Chem. Mater. 14:2199 (2002).

[10] A. A. Zhukov, A. V. Goncharov, P. A. J. de Groot, P. N. Bartlett, and M. A. Ghanem, J. Appl. Phys. 93:7322 (2003).

[11] H. A. Biebuyck, C. D. Bian, and G. M. Whitesides, Langmuir 10:1825 (1994).

[12] A. Badia, S. Singh, L. Demers, L. Cuccia, G. R. Brown, and R. B. Lennox, Chem. Eur. J. 2:359 (1996).

[13] E. Delamarche, B. Michel, H. A. Biebuyck, and C. Gerber, Adv. Mater. 8:719 (1996).

[14] B. L. V. Prasad, S. I. Stoeva, C. M. Sorensen, and K. J. Klabunde, Chem. Mater. 15:935 (2003).

[15] B. L. V. Prasad, S. I. Stoeva, C. M. Sorensen, and K. J. Klabunde, Langmuir 18:7515 (2002).

[16] M. H. Kim, H. K. Choi, and O. O. Park, Appl. Phys. Lett. 88:143127 (2006).

[17] M. E. Abdelsalam, P. N. Bartlett, J. J. Baumberg, and S. Coyle, Adv. Mat. 16:90 (2004).

[18] T. A. Kelf, Y. Sugawara, J. J. Baumberg, M. Abdelsalam, and P. N. Bartlett, Phys. Rev. Lett. 95 (2005).

Chapter 4

4 Plasmons and SERS on SSV substrates

4.1 Introduction

Sphere segment void (SSV) substrates generate intense absorptions under illumination by white light. These are due to surface plasmon polaritons (SPPs), hereafter referred to as plasmons, generated on the surface. Plasmons result in a large increase in the local electric fields and therefore are expected to enhance all near field phenomena, such as SERS. It has been demonstrated that SSV substrates give intense SERS [1]. However, systematic correlations between plasmon resonances and SERS signals need to be established. This would facilitate the optimum design of substrates suited for a particular laser excitation, which can prove very important especially for detecting trace analytes. There is also a genuine requirement for substrates which are not only reproducible but at the same time have the flexibility to be tuned to obtain huge SERS enhancements with either visible or near infrared (NIR) laser excitations. The latter is particularly beneficial for studying large biomolecules, resulting in low auto-fluorescence and photolytic damage [2].

Furthermore, the plasmonics as well as SERS has traditionally been studied on metals such as gold and silver. The colloidal crystal templated electrodeposition methodology enables the fabrication of structured surfaces with a variety of materials such as transition metals [3], semiconducting oxides [4] and conducting polymers [5] apart from traditional SERS materials. Transition metals such as nickel, platinum and palladium display weak plasmonic properties and hence, weaker SERS than gold and silver. Nevertheless, they are important materials useful in catalysis and other applications. Therefore, monitoring surface reactions utilizing SERS on them could prove extremely valuable for understanding the mechanism and hence, design of better materials.

Apart from finding the substrates best suited for SERS, there are many unresolved fundamental issues regarding understanding the SERS process itself. One of them is regarding the origin of the broad continuum called the background [6] observed in all SERS experiments. Researchers around the globe have tended to simply ignore it and resort to background subtraction methods. This practice continues as it undoubtedly improves the quality of the spectra and does not affect

the analysis. SERS peaks can easily be about 10-50 times smaller than the background observed in a spectrum. Hence, a fundamental understanding of the background can improve the sensitivity of analysis by enabling the design of better and improved substrates.

4.2 Overview

In this chapter first results are presented for the plasmonics of SSV substrates as studied through reflectance measurements with a microscope as well as in the angle resolved mode using an automated goniometer. It is shown that this strategy yields information on plasmonic absorptions and their variation with both the template sphere diameter and film thickness. It is demonstrated that this can be carried out not only for gold but also for nickel, platinum and palladium substrates. Thereafter, representative SERS results are presented for gold, platinum and palladium SSV substrates. This is carried forward to demonstrate the strong correlation between SERS and plasmon absorptions on the substrates, which helps in establishing our plasmon engineering strategy for optimizing SERS substrates for different laser wavelengths. In particular, it is demonstrated that using this strategy we can optimize substrates for SERS with visible laser excitations both in air and in water; this also shows the effect of tuning plasmons with a change in dielectric media and the necessity of matching resonances. Thereafter results are presented for optimizing SERS substrates with a near infrared 1064 nm laser. Finally in this part results obtained are collated together to establish correlations between SERS intensities and the plasmons generated on SSV substrates.

In the last section of this chapter, the issue of the background observed in SERS on SSV substrates is addressed. Results are presented which show that the background is coupled and enhanced by plasmons generated on the substrates. It is demonstrated that it is linear with power. Further it is shown that the background is dependent on the nature of the molecule adsorbed on the surface, the ionic strength of the solution and electronic excitation of the molecule. Finally, a model for understanding the background is presented which fits with our observations. This model is tested by carrying some anti-Stokes SERS on the substrates proving the robustness of the model.

4.3 Plasmons and SERS

4.3.1 Terminology used for SSV substrates

The terminology for describing the geometry of SSV substrates was briefly mentioned in Chapter 1. This terminology permits easy referral and identification of the fabricated geometry (sphere diameter and thickness) of sphere segment void (SSV) substrates and is described in detail here. The sphere diameter used for templating the SSV substrates is referred as *D* and a substrate fabricated by a template of say, 700 nm diameter spheres is called a D700 sample. The film height is quoted in terms of the normalized thickness (*t*) which implies that the thickness of the electrodeposited film has been divided by the sphere diameter (t= film height/sphere diameter); hence, if the substrate has been fabricated with a template sphere size of 600 nm diameter and the normalized thickness is quoted as 0.5 *D*, it means that the thickness of the film is half of the sphere diameter, that is, 300 nm or in other words $t = 0.5$. This terminology helps visualize the structure as substrates fabricated with different sphere diameters would show the same morphology at a particular normalized thickness, though scaled by the size.

Further, a combinatorial approach has been adopted for studying the optical properties (plasmonics) and carrying out the SERS optimization. As described in the experimental methods chapter, using a single template a sample can be fabricated which has a number of film thicknesses, most often from 0 to 1 *D*, allowing the study of reflectance as well as SERS as a function of thickness of the film. Such a sample, say, fabricated with a template consisting of 600 nm diameter spheres, is called a *D*600 'graded' sample as it would have a gradation of film thicknesses, ranging from $t = 0$ (or 0 *D*) to $t = 1$ (or 1 *D*), unless stated otherwise, in equally spaced steps from one end (thin) to the other (thick). A uniform height (with only one film thickness) sample, say, fabricated with 1000 nm diameter sphere template and electrodeposited to 750 nm is just quoted as *D*1000, $t = 0.75$ (or 0.75 *D*) substrate.

4.3.2 Optical properties of the substrates

SSV substrates display different colours depending on the diameter of the sphere used for templating the structures and the thickness of the film. These colours are distinguishable even with the naked eye. To first study the optical properties of these substrates by reflectance measurements a microscope coupled with an Ocean Optics spectrometer (either visible or near infrared) was employed. The microscope spectra presented in this chapter have been recorded with a 20X microscope objective with a numerical aperture (NA) of 0.4 (or 0.46 for NIR). Therefore, strictly speaking, the reflectance measurements sum up over incident and collection angle of ~24 degrees (NA = $n\sin\theta$; where n is the refractive index, equal to 1 for air).

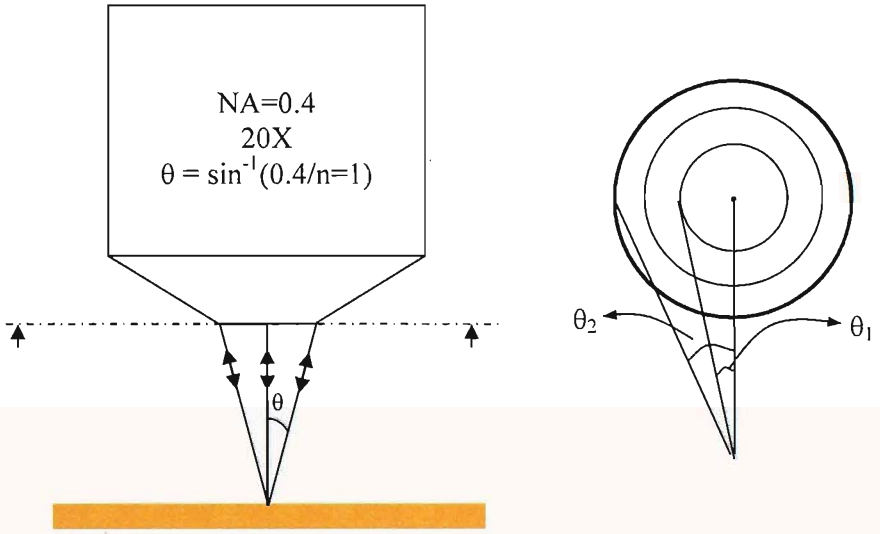

Figure 4.1 Schematic showing the ray optics with a microscope objective employed for recording reflectance spectra. The incident and collection angles vary from 0 to θ, determined by its numerical aperture (NA). A section view shows the distribution of angles across the aperture of the objective. The weighting (width of the annular ring) increases with the angle scaling in favour of larger angles.

The microscope also has a CCD camera mounted on it which enabled recording images of the samples. These images also helped as a reference so that SERS spectra could be acquired from the same locations on the substrates. Optical images recorded with a 5X objective for D400, D800, D900 and D1000 sphere templated gold substrates are shown in Figure 4.2.

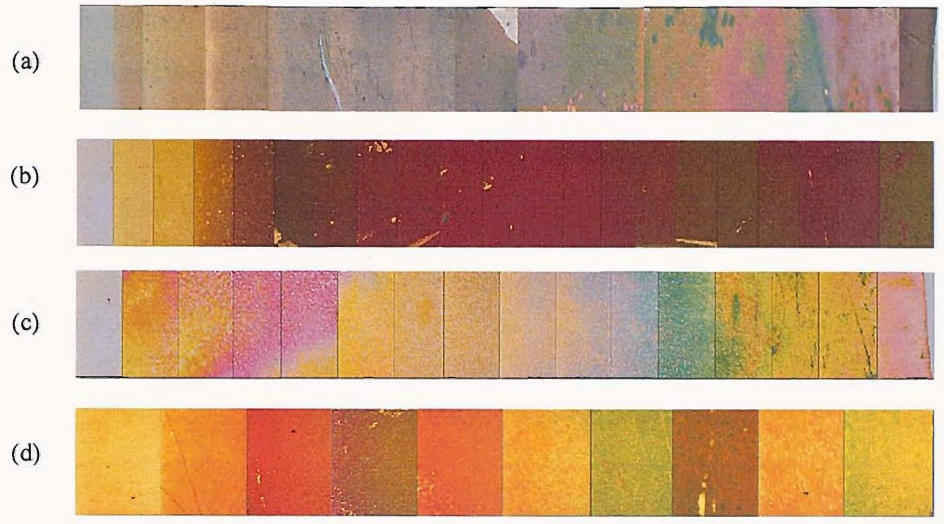

Figure 4.2 Optical images of (a) D400, (b) D800, (c) D900 and (d) D1000 SSV gold substrates. The images show the variation in colour with the thickness of the electrodeposited film. The film thickness increase from 0 to 1 *D* for (a), 0 to 0.8 *D* for (b) and (c) and 0.1 to 1 *D* for (d) in equally spaced steps from left to right. The area of each image is 700 μm x 500 μm.

4.3.2.1 Reflectance spectra and plasmon maps

Reflectance measurements carried out with the microscope or the goniometer yield spectra such as those given in Figure 4.3a. The only difference being that with the microscope data the intensities observed are summed over a solid angle determined by the numerical aperture of the objective used for the measurement while with the goniometer (NA: 0.01) individual angles are sequentially scanned, which may or may not be later summed. Representative spectra from the microscope recorded in the near infrared at the specified thicknesses for a *D*800 graded sample are shown in Figure 4.3. The dips observed in a reflectance spectrum correspond to the extinction on the surface. It has been shown earlier by Baumberg *et al.* that the extent of scattering by such structures is minimal (less than 1 %) when mapped in the far field [7]. Hence, the extinction (total attenuation of radiation) observed on the surface can be attributed almost entirely to absorption due to the plasmon resonances resulting from white light illumination of these surfaces. Further, if these reflectance spectra are recorded on a graded sample as a function of thickness they can be converted to contour maps (hereafter called plasmon maps) of the intensity of absorption as a function of wavelength and thickness of the film. Such an example of a plasmon map for a *D*800 sample derived from its constituent spectra is shown in Figure 4.3(b). The intensity of absorption is normalized with the reflectance recorded on a flat gold (evaporated gold on a glass slide). Thus a plasmon map essentially gives the

absorptions due to the structuring of SSV substrates. The maps presented for full graded (0 to 1 *D*) samples in this chapter have been constructed using at least 10 or more reflectance spectra.

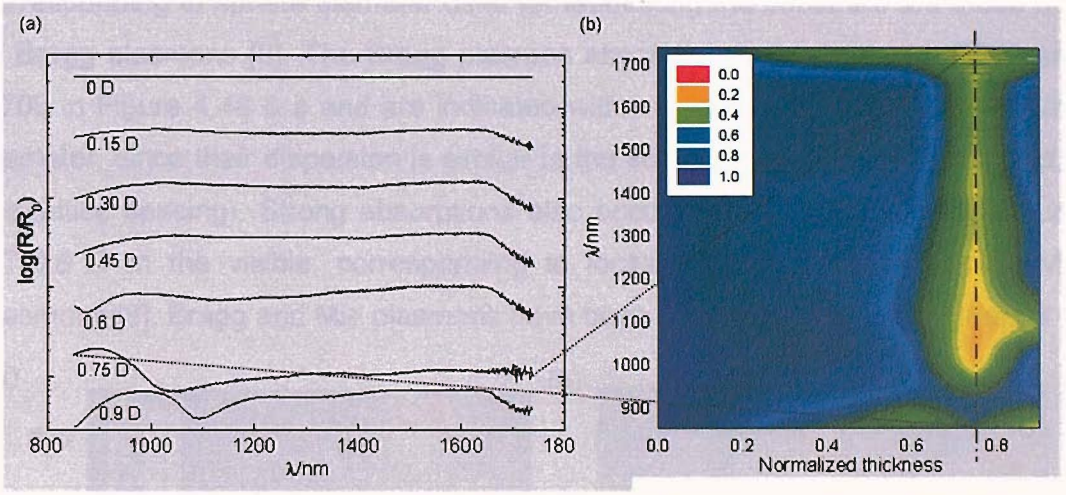

Figure 4.3 Reflectance spectra and relation with a plasmon absorption map. Data obtained from reflectance measurements in the near infrared at different film thicknesses on a graded gold film is converted to an extinction intensity map. In (a) reflectance spectra recorded at different film thicknesses on a graded gold film templated with 800 nm spheres are shown. They are offset for clarity. The film heights in the figure, shown under each spectrum, increase from top to bottom. R and R_0 are reflection intensities obtained from the nanostructured film and flat gold, respectively. The corresponding extinction intensity contour map is shown in (b). The reflection intensity is normalized with respect to flat gold. Red indicates maximum absorption and violet stands for complete reflection (= 1) with respect to flat gold. The dips in the spectra correspond to the bright areas in the extinction map and indicate the plasmonic absorptions on the substrate as a function of normalized thickness (t).

4.3.3 Reflectance mapping of gold SSV substrates

4.3.3.1 Visible region

Utilizing reflectance measurements as stated above plasmon maps in the visible wavelength range are presented for gold SSV substrates for *D*600, *D*700, *D*900 and *D*1100 graded samples in Figure 4.4. The reflectance spectra for generating these plasmon maps have been recorded using the microscope with an objective (20X, NA: 0.4) and a visible range spectrometer. All of the reflectance maps shown in Figure 4.4 have been plotted on the same intensity scale. Comparing the plasmon map for D600 in Figure 4.4(a) with that of D700 graded sample, it can be seen that the plasmonic absorptions red shift by about 100 nm with an increase in the sphere diameter from 600 to 700 nm (compare the position of the + sign). The red shifts increase further with the D900 and D1100 graded samples with both of them heavily absorbing in the visible wavelength region for 0.5 *D* and above film thicknesses. It has to be borne in mind that the absorptions observed through the microscope objective, since it sums over a range of angles, are probably due to contributions by several plasmon modes. Hence, the absorptions become

widespread and not well defined, though similar features can be identified (marked with an X) and are found to red shift between *D*900 and *D*1100. The absorptions for the thin part of the substrates, below 0.5 D, at around the wavelength corresponding to sphere diameter used for fabricating the substrate are those due to Bragg plasmons [8]. The Bragg plasmon absorptions are visible for D600 and D700 in Figure 4.4a & b and are indicated with • and they scale linearly with the diameter, since their dispersion is similar to the scattering relation ($\lambda = nd\sin\theta$; d is the lattice spacing). Strong absorptions also occur above 0.5 *D* , usually around 0.7-0.8 *D* in the visible, corresponding to localized void plasmons called Mie plasmons [8]. Bragg and Mie plasmons have been described in detail in Chapter 1.

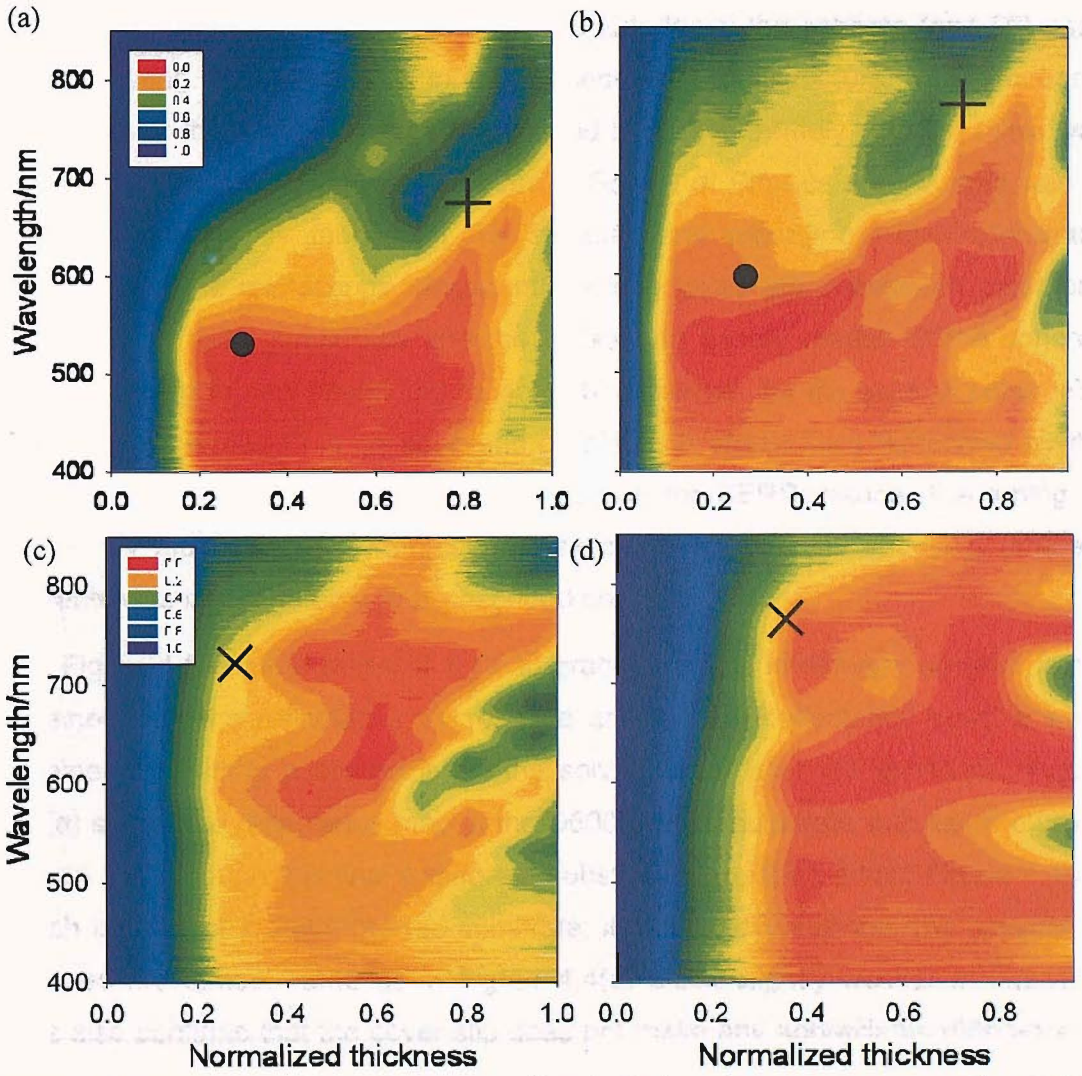

Figure 4.4 Plasmon maps obtained using spectra collected with the reflectance microscope with a visible range spectrometer for (a) D600, (b) D700, (c) D900 and D1100 graded samples. The + and • signs correspond to the same plasmonic feature for *D*600 and *D*700. Similarly the X mark shows similar plasmon features on *D*900 and *D*1100 graded substrates. Red indicates strongest absorption while violet shows complete reflection.

The theoretical scaling of plasmon mode energies with sphere diameter for SSV structures however, is almost linear for lower order (dipolar) localized void

plasmons while for higher order (multi-polar) resonances the scaling becomes non-linear [9]. Simplistically, this can be understood by the concept that for a plasmon fitting in the void with just a single wavelength (such that $\pi D = \lambda_{plasmon}$) will scale linearly with the diameter while others will have more complex dependence. Further complexities arise due to the different nature of plasmons generated in the void cavity, on the rim and on the top surface and the interaction between them and their different angular dependences [8]. Some of these effects are discussed later in the chapter.

A possible way of tuning the plasmon absorptions observed on SSV substrates is to change the dielectric medium surrounding the voids. The easiest and obvious method to see the effect of this modulation is to leave the spheres (n=1.56) used for templating SSV substrates intact, embedded in the structure. The plasmonic properties of these structures get modulated but are extremely complex. This was investigated further by our collaborators in School of Physics and my role was to initiate the study by fabricating the samples and recording initial reflectance spectra with the microscope. Apparently mixing takes place between plasmons generated by SSV substrates and the whispering gallery modes of the spheres occurs leading to new interesting modes [10]. However, for the sake of coherence the present discussion is concentrated on plasmon absorptions generated by the SSV substrates with a view to their utilization for SERS; hence, the tuning of modes by modulating the refractive index of the medium by choosing different solvents was investigated and is described below.

In Figure 4.5 contour maps of a D600 graded sample in different solvent media obtained with the reflectance microscope are shown. Reflectance spectra were obtained by putting a cover-slip on the solvent layer over the substrate. Figure 4.5(a) shows the reflectance map of the D600 graded substrate with just the cover slip on top. Though this was a different substrate comparing it with Figure 4.4(a), which is also for a D600 graded substrate; it can readily see that the absorption features are almost same as in Figure 4.4(a) albeit slightly weaker in intensity. This also confirms that the cover-slip does not make any appreciable difference to the reflectance map and observation of plasmon absorptions. Further, the reflectance maps with water, hexane and isopropanol as the solvent medium covering the SSV substrate are shown in Figure 4.5(b), (c) and (d) respectively.

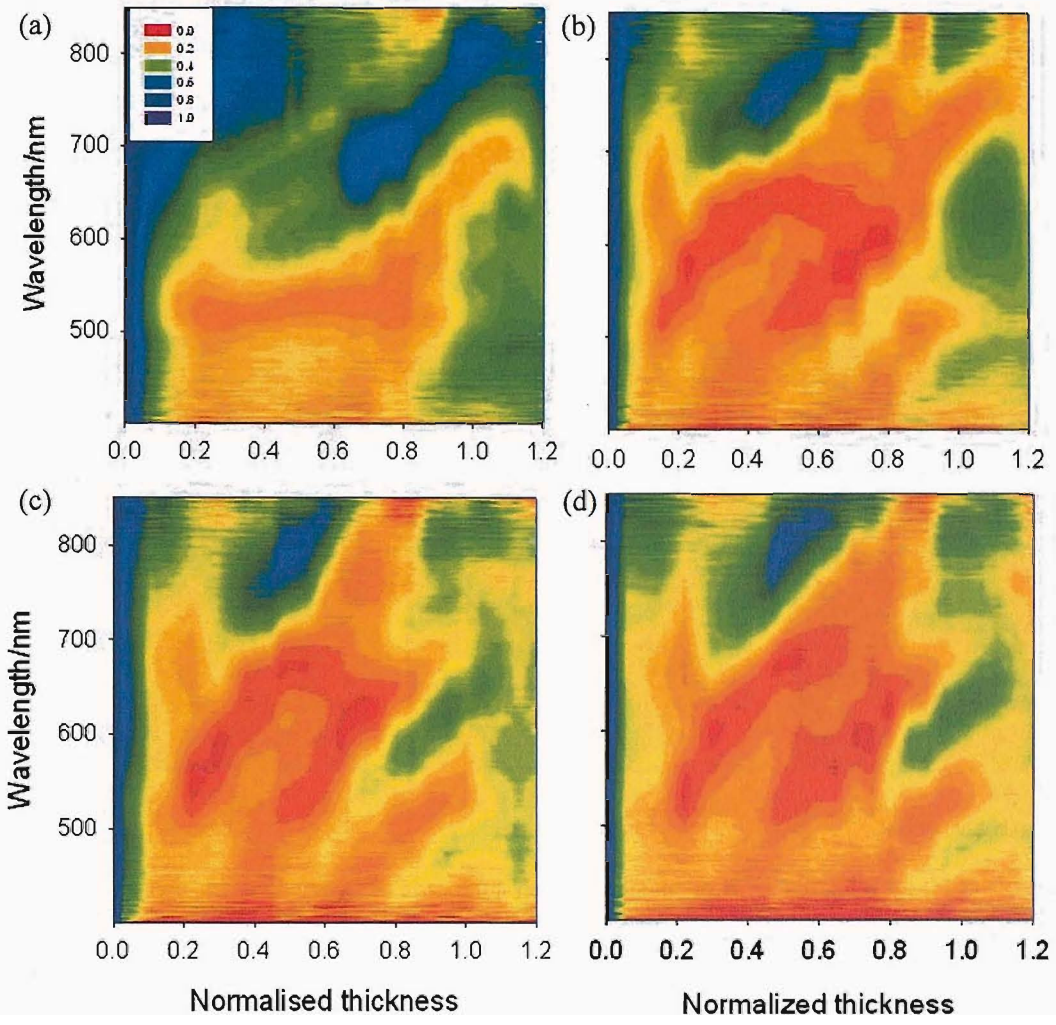

Figure 4.5 Reflectance maps of a *D*600 sample recorded with a cover slip on top in (a) dry condition soaked in (b) water, (c) hexane and (d) isopropanol. Red indicates strongest absorption while violet shows complete reflection.

Again from the plasmon absorption maps it can be observed that the wavelength of similar features red shifts to higher wavelengths with an increase in refractive index. The refractive index of water is 1.33 (at 25 °C) and the absorptions scale exactly with it compared to that in air. The refractive index of hexane and isopropanol are 1.372 and 1.375. From the respective reflectance maps it is clearly seen that the change of solvent from hexane to isopropanol doesn't significantly alter the plasmonic properties of the substrate though there is a slight change compared to water. Also, though there will be slight changes in the incident and collection angles in the medium, the effect appears to be insignificant to have an affect on the plasmon maps obtained. Nevertheless, these examples show that the substrates are stable in a number of different media including water and organic solvents. It also demonstrates that the plasmon absorption wavelengths get scaled (increased or decreased) by the refractive index of the medium and are not affected by the nature of the solvent itself.

4.3.3.2 Near infrared region

Similar to plasmon absorption mapping in the visible wavelength regime reflectance measurements were carried out in the near infrared (NIR) with the microscope arrangement, as described earlier. Instead of a visible spectrometer the optical fibre from the reflectance microscope is coupled to a NIR spectrometer.

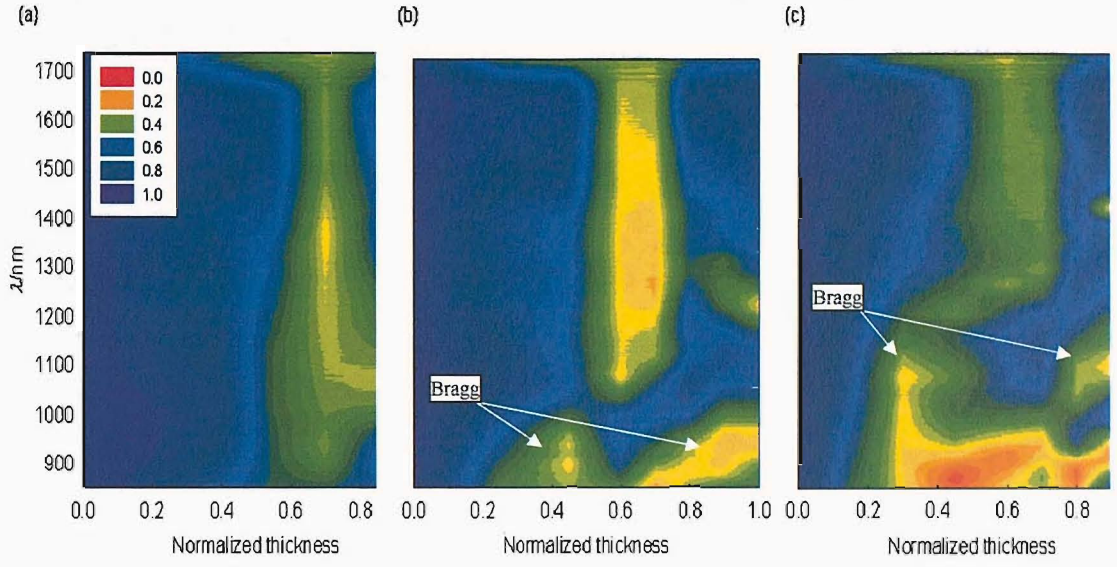

Figure 4.6 Contour maps showing the absorption due to plasmons in NIR for (a) D700, (b) D900 and (c) D1100 gold SSV substrates. All maps are colour coded using the same spectrum scale of 0 (violet: weakest absorption) to 1 (red: strongest absorption). The film heights are normalized with the respective sphere diameters.

As mentioned above, the void plasmons on SSV substrates are found to scale with the sphere diameter, it was expected that to generate strong plasmon absorptions in the near infrared (NIR), templating with sphere sizes larger than 700 nm diameter would be required. Plasmon absorption maps obtained with reflectance spectroscopy in the NIR range of 850 to 1800 nm were obtained for graded gold SSV films templated with 700 nm, 800 nm, 900 nm, 1000 nm and 1100 nm diameter spheres and the maps for (a) D700, (b) D900 and (c) D1100 nm graded gold films are shown in Figure 4.6. Localized plasmons have been shown to exist at ~0.6 D for gold SSV substrates [8]. This appears as a weak band for the 700 nm SSV film as evident in Figure 4.6a. This band undergoes a red shift on increasing the sphere size to 900 and 1100 nm (Figure 4.6b and c). The extent of absorption is largest for D900 SSV substrate compared to the 700 nm and 1100 nm substrates. Plasmon maps with 800 and 1000 nm sphere templated films display the same trend and hence, have not been included in this figure. One can also see Bragg plasmons emerging in the NIR region, centred around 900 nm and 1100 nm in Figure 4.6b and c, respectively, corresponding to the grating like behaviour of shallow dishes. Representative SEM images at different film heights

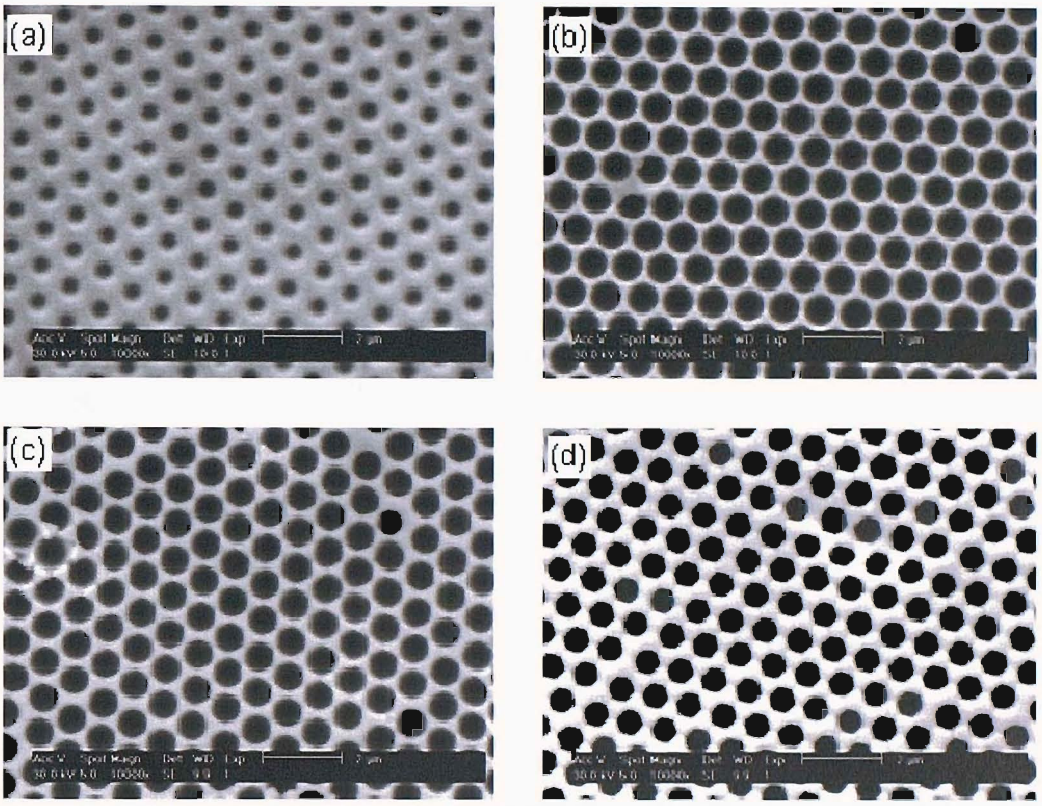

Figure 4.7 SEM images of a graded gold film fabricated using 900 nm diameter (*D*) sphere template recorded at various film heights. Images corresponding to film thicknesses of (a) 0.25 *D* (b) 0.45 *D* (c) 0.7 *D* and, (d) 0.9 *D* are shown. All images were obtained under 10000 magnifications. The scale bar for the images is 2 μm.

for D900 gold SSV substrate are shown in Figure 4.7. They demonstrate the well ordered arrangement of the voids and the variation of the morphology with film thickness.

4.3.4 Reflectance mapping on nickel, palladium and platinum SSV substrates

Reflectance spectra were recorded on graded nickel, palladium and platinum substrates similar to that on gold substrates using the microscope setup. The absorption corresponding to the dips in the spectra observed on SSV substrates of these transition metals were weaker in strength compared to gold. The geometry of substrates is responsible for the occurrence of the systematic absorptions while the nature of the metal determines their strength. In nickel, palladium and platinum the d-orbital mixes with the conduction band. Consequently, inter-band absorptions occur in the visible region leading to weak excitation of plasmons. Further, the band structure becomes more elaborate from Ni to Pt and consequently the energy losses in increase in the same order. Therefore, plasmon strengths decrease in the same order and will be weakest in Pt among these.

Reflectance spectra recorded on a D600 graded nickel SSV substrate are shown in Figure 4.8. The normalization has been carried out with respect to a flat electrodeposited nickel film. The figure also shows optical images of the substrate at various film heights corresponding to the reflectance spectrum starting with that at 0.2 *D*. The trend for the absorptions is similar to that for gold substrates and hence, the assignments for the different modes are based on observations on gold and detailed studies using angular resolved data. A Bragg mode observed for the thin part of the substrate gradually shifts red until t = 0.4, where it vanishes and instead gives way to localized Mie plasmons in the void. The Mie modes are split into two from their beginning at t = 0.5 and each of them red shifts as the thickness increases while higher order Mie modes around 400-450 nm can be seen at t = 0.8 and above. All Mie plasmons continue to decrease in energy till 1 *D*.

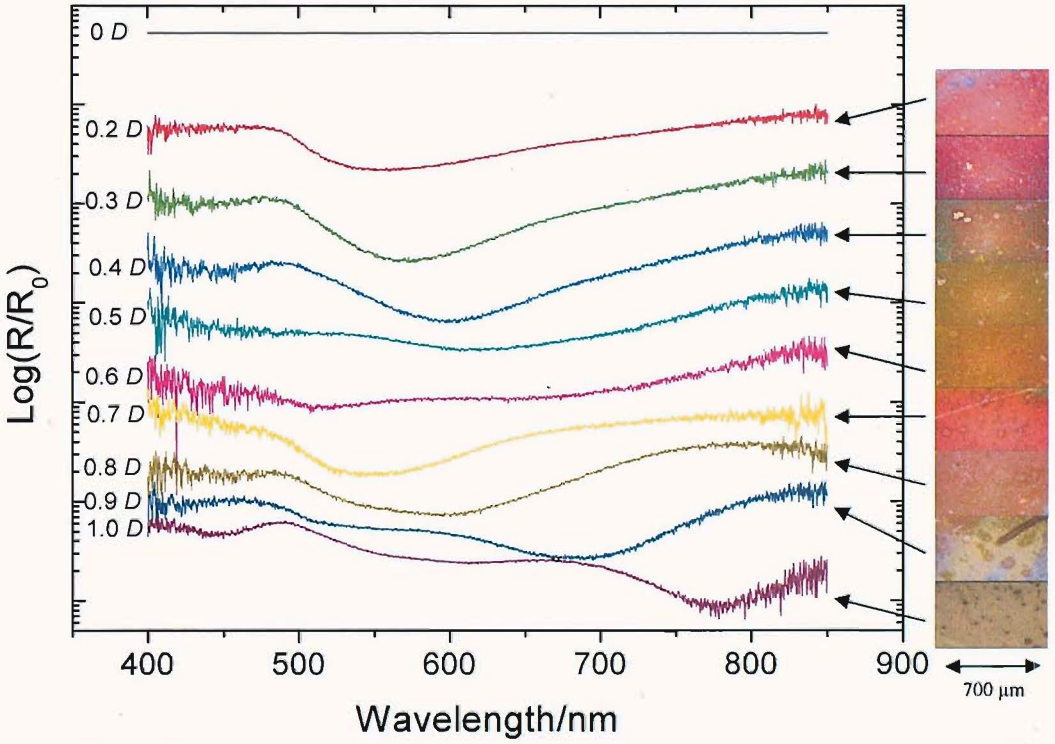

Figure 4.8 (a) Spectra recorded on *D*600 graded nickel substrate at different film heights obtained with the reflectance microscope. The spectra have been offset for clarity. (b) Shows different colours of the substrate corresponding to the film heights at which the reflectance spectra have been recorded.

Reflectance spectra are presented in Figure 4.9 for D600 graded sample for palladium along with optical images of the film at different film heights corresponding to the spectra. In this case the structured substrate was fabricated on a palladium coated glass slide. The spectra have been normalized to flat palladium to highlight the changes due to the structured geometry.

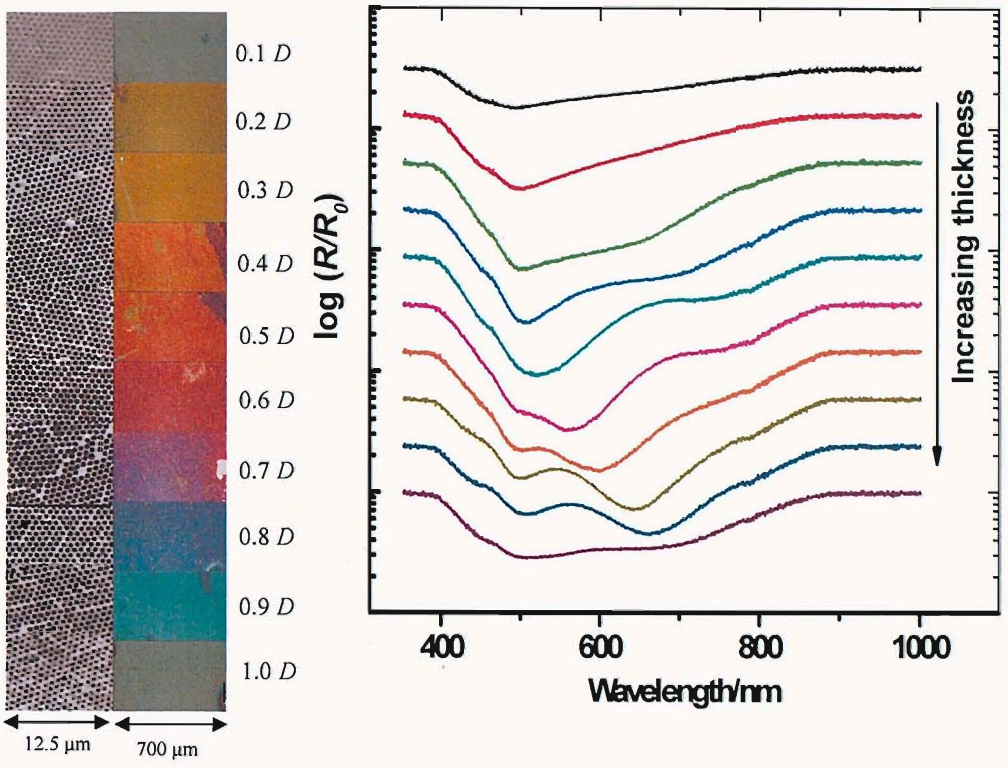

Figure 4.9 Reflectance spectra acquired with the microscope arrangement for a stepped, structured palladium SSV film grown through a 600 nm sphere diameter template together with the corresponding SEM and optical shown on the right. The film heights are indicated alongside the optical images. The spectra are off-set for clarity.

Platinum SSV substrates were also fabricated successfully using templated electrodeposition. The structured substrates were again fabricated on palladium coated glass slides (prepared by Alistair Clark) since it was not possible to evaporate platinum due to its high melting point (1768 °C) with the available physical vapour deposition system. Reflectance spectra are presented for D500 and D600 platinum SSV graded substrates in Figure 4.10. By varying the sphere diameter used for templating the optical properties can be modified and this is clearly visible even for platinum substrates. The optical images at different heights between D500 and D600 are distinctly different and spectacular in colour compared to other metal substrates discussed in this thesis. The various features are as described for other metals and a similar trend is observed that with a decrease in the sphere diameter all the plasmon energies shift to higher energies. Thus Bragg plasmons only begin to emerge in the visible at around 0.3 *D* and split into Mie modes. Only one localized mode is visible and the other Mie mode appears later at 0.7 *D*. As shown earlier all the Mie plasmon modes continue red shifting as expected with increasing thickness. The discussion on the reflectance spectra presented here for palladium and platinum is limited since they were

primarily obtained for drawing correlations between plasmon absorptions and SERS; hence, they will be discussed later in the chapter in that context.

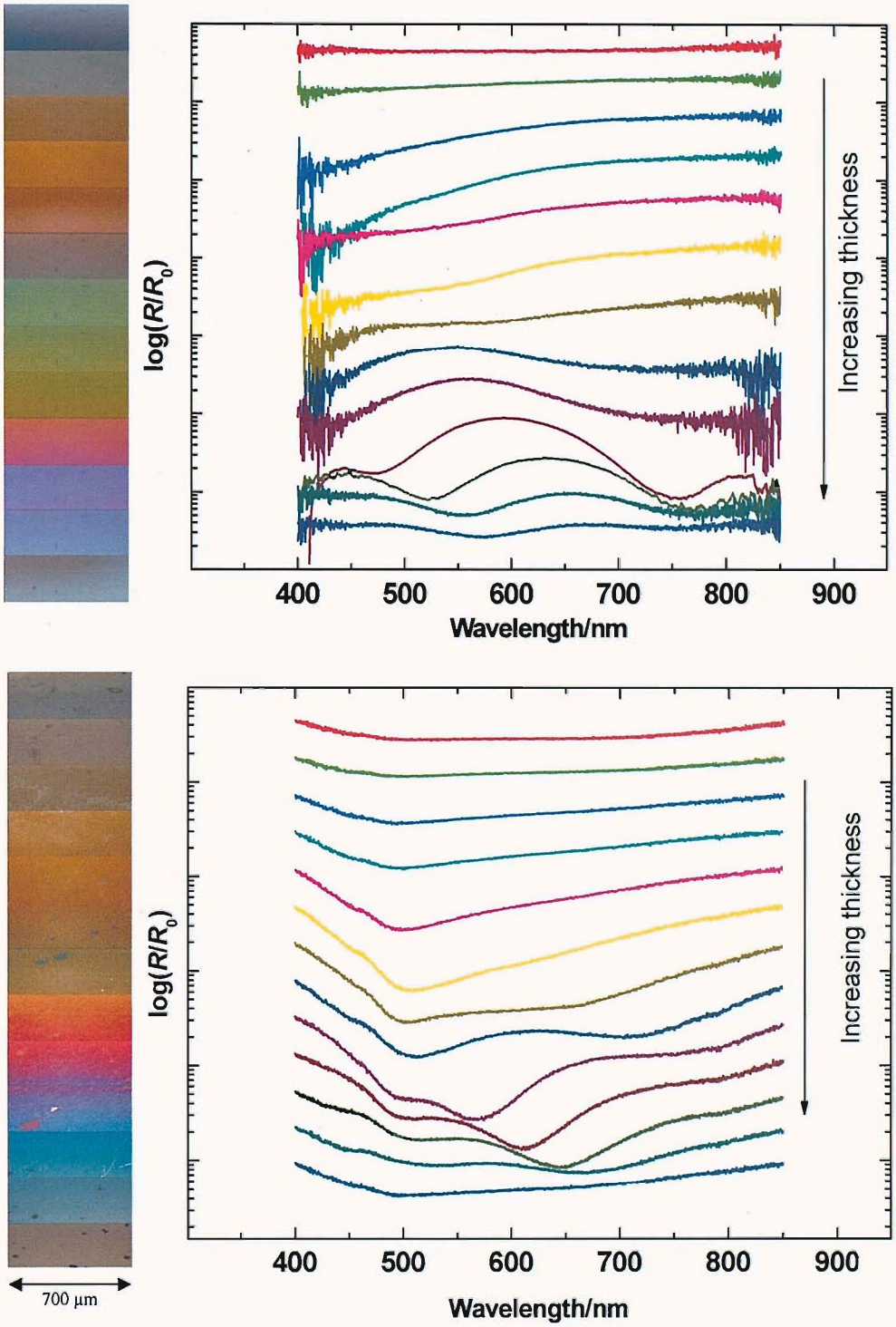

Figure 4.10 Reflectance spectra on *D*500 and *D*600 graded platinum substrates along with the corresponding optical images of the samples at different film heights.

4.3.4.1 Plasmon maps with goniometer (angle resolved)

Similar to reflectance mapping with the microscope setup; plasmon absorption mapping was carried out with the automated goniometer arrangement permitting angle resolved reflectance measurements as described in Chapter 2. This system

allows monitoring reflection as a function of angle of incidence (θ) and planar orientation (Φ) enabling the study of the angular dependence of the different types of plasmons. All of the results discussed in this thesis are for an arbitrary planar orientation. Orientation in the plane of the substrate does not significantly affect the intensity patterns in the plasmon maps described here. The other advantage of using the goniometer arrangement for plasmon mapping is that since it collects light over a very small angle (NA: 0.01) this arrangement virtually eliminates any

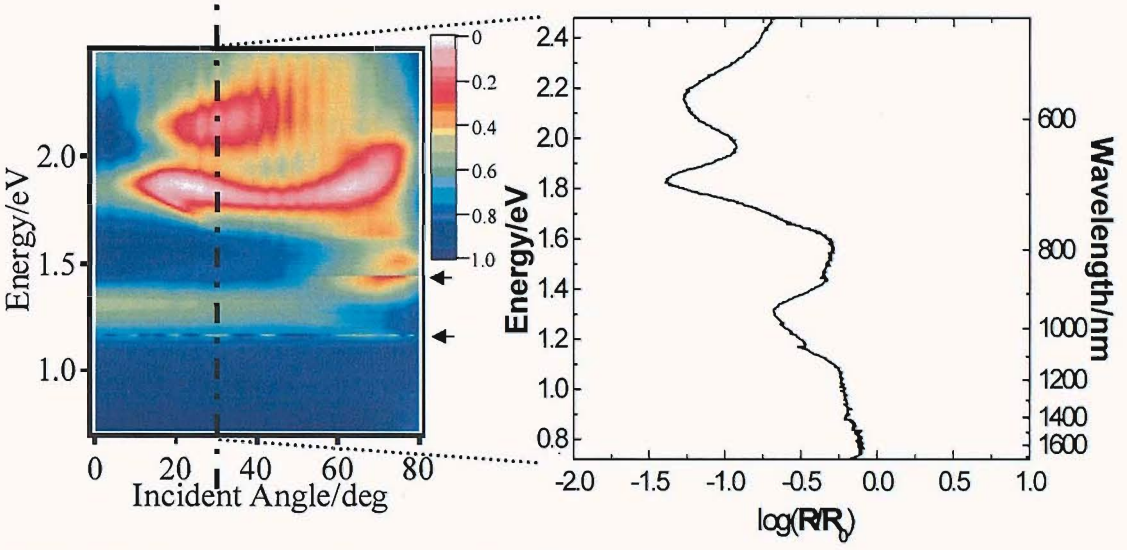

Figure 4.11 Angle resolved reflectance map of a D600, t = 0.9 substrate. Each vertical section is a spectrum where the dips in reflectance correspond to absorption due to plasmons generated on the surface. Here a section is taken at 30 deg and the corresponding spectrum is shown in (b). The energy scale relates reciprocally to the wavelength scale. The intensity scale in both the map as well as the spectrum is the normalized reflectance, where R is the reflectance recorded on the SSV substrate and R_0 is the reflectance recorded on flat gold. In the reflectance map violet implies weakest reflection and whitish red means strongest absorption. The artefacts generated in the plasmon map due to a change in detectors are indicated by the position of the arrows.

scattering contribution in the plasmon maps. Therefore, though for preliminary understanding and simplicity of usage the microscope setup is preferable, the goniometer arrangement is necessary for measuring the angular dispersions of plasmons, which enables their classification and subsequent detailed analysis. Reflectance spectra are collected varying the incident angle of the illuminating white light beam every 0.5 degree till 80 degrees at a particular point on the sample; the collecting arm is correspondingly moved by $2\Delta\theta$ for recording the reflected light. These reflectance spectra are plotted in an intensity contour map similar to that described for the microscope setup. A typical angular map of a D600, t = 0.9 substrate is shown in Figure 4.11, where each vertical section is a spectrum recorded at that particular incident angle. The spectrum is shown with

the y-axis showing the energy/wavelength[1] and the x-axis showing the normalized reflectance. Hence, the dips correspond to absorptions due to plasmons.

Reflectance maps showing angular dependence at a particular normalized thickness on SSV substrates are useful to decipher the nature of the plasmon mode; whether it is Bragg or Mie type (described in Chapter 1). However, to recall Bragg modes are propagating type plasmons and show an angular dependence of energy while the Mie modes being localized are less angular dependent in their energy profiles. Since, the study of plasmons on SSV substrates was not the primary aim of this thesis and since this is being pursued by our collaborators in Physics, the discussion on this aspect is limited to Figure 4.12 which shows an example of the variation of angular dependent energy profiles of the various types of plasmons for different thicknesses for SSV substrates. One can observe that till about t = 0.35 the reflectance maps show only Bragg modes, which are essentially plasmons propagating on the top surface connecting the shallow dishes and getting scattered off the rims of the voids. The voids on the substrates are hexagonally packed with 6-fold symmetry. However, only 4 Bragg modes are observed, due to two of them being degenerate with the others [8]. After t = 0.35 mixed modes due to interaction between the Bragg and Mie modes are formed, this can be visualized as the propagating plasmons flowing into the voids, where they get localized, due to the top surface being broken into islands. The localization of modes continues, developing more Mie character till t = 0.70 when the top surface again becomes continuous, permitting the generation of Bragg plasmons. However, due to a well developed spherical cavity the localized modes continue to exist and interact with the developing Bragg modes, through the rim of the cavity, leading to very strong modes from t = 0.7 to t = 1. At $t \geq 1$ the spherical cavities are almost encapsulated such that very little light can couple into the voids. Hence, the Mie modes become weaker and Bragg modes are seen again above this height.

[1] Energy (eV) $\approx$ 1241/Wavelength (nm); this is derived from $E = hc/\lambda$ where E is the energy, h is the Planck's constant, c is the speed of light and λ is the wavelength, respectively expressed in SI units and utilizing the conversion factor that 1 eV = 1.602×10^{-19} J.

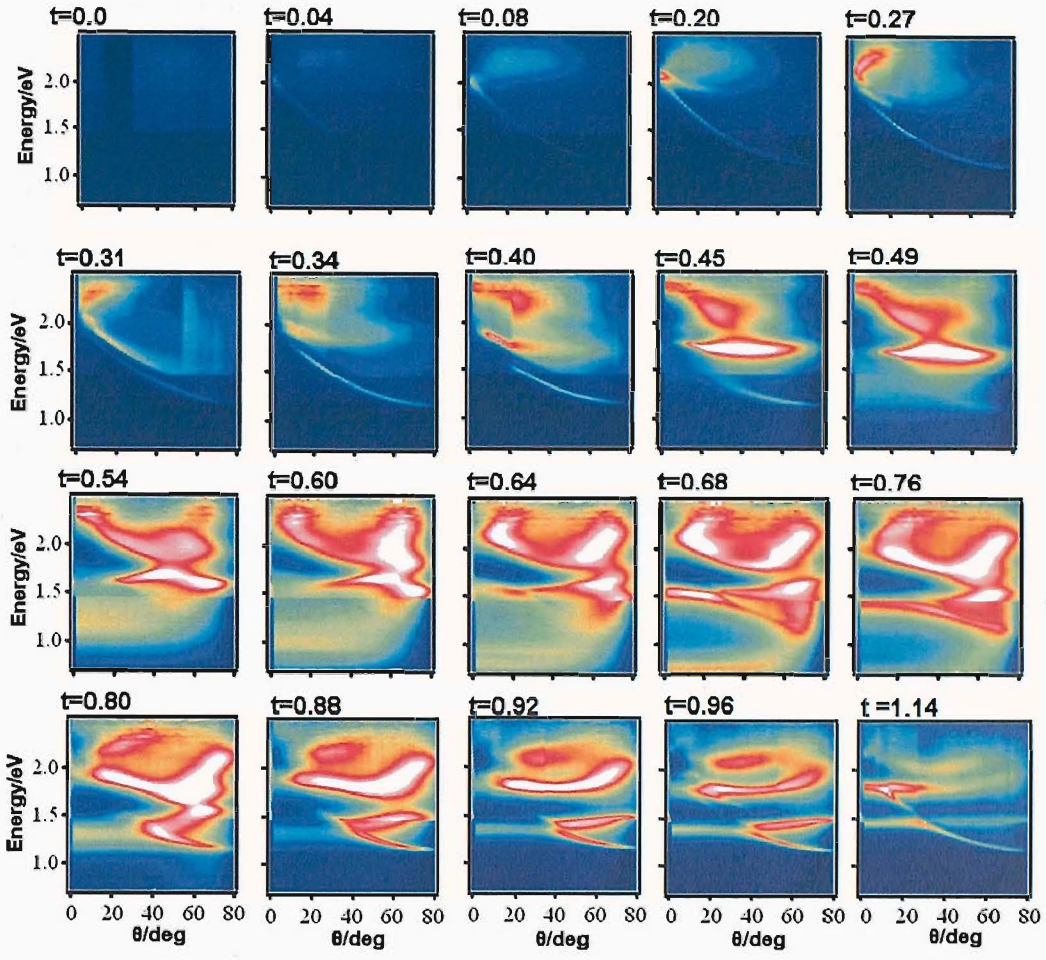

Figure 4.12 Angle resolved reflectance mapping of a D600 substrate at different thicknesses. The normalized thickness is mentioned above each intensity contour map. Violet indicates strongest reflection while reddish white indicates strongest absorption. All maps are on the same intensity scale.

As shown above angular reflectance mapping is a very powerful technique for studying plasmons. Nevertheless, for the purposes of optimizing substrates for SERS, where we want to study the thickness and diameter dependence of SSV substrates for a particular laser excitation and the correlation between the SERS signals and plasmon absorption, position maps for graded substrates can be developed such as that shown in Figure 4.13. The figure shows plasmon energy dispersion as a function of film height on a D600 gold SSV substrate at normal incidence and at an angle of 40 deg. It can be readily seen that at different incident angles the absorptions due to plasmons are different as a function of the thickness of the film. The difference arises due to the angular dependence of the plasmons discussed above. Nevertheless, it can be inferred that the plasmon energies depend on the thickness of the film, with the Bragg plasmons increasing in energy

with thickness till they get mixed with Mie modes. These modes display complex behaviour as a function of film height which is described below.

Plasmon modes in a fully enclosed spherical cavity are modelled using the Mie theory and the solutions are mathematically identical to hydrogen atom wave-functions based on spherical harmonics [11]. Thus, they can be described by azimuthal (S, P, D. F) and magnetic (0, 1, 2...) quantum numbers. In SSV substrates where the cavities are truncated rather than fully encapsulated certain modes are not allowed due to a break in symmetry. The S mode requires full spherical symmetry hence, is not observed. The ^{0}P is not forbidden but is not observed in experiment. From theory its electric field orientation is predicted to be in the z-axis direction and requires symmetry along the x-y plane (for top and bottom lobes analogous to that in a p_z orbital). The reasons for it not being observed can be due that 1) it is coupled at high angles and has a narrow line width, so is not easy to detect in experiment; 2) currently in the modelling the interaction between modes in neighbouring cavities is ignored so maybe ^{0}P is

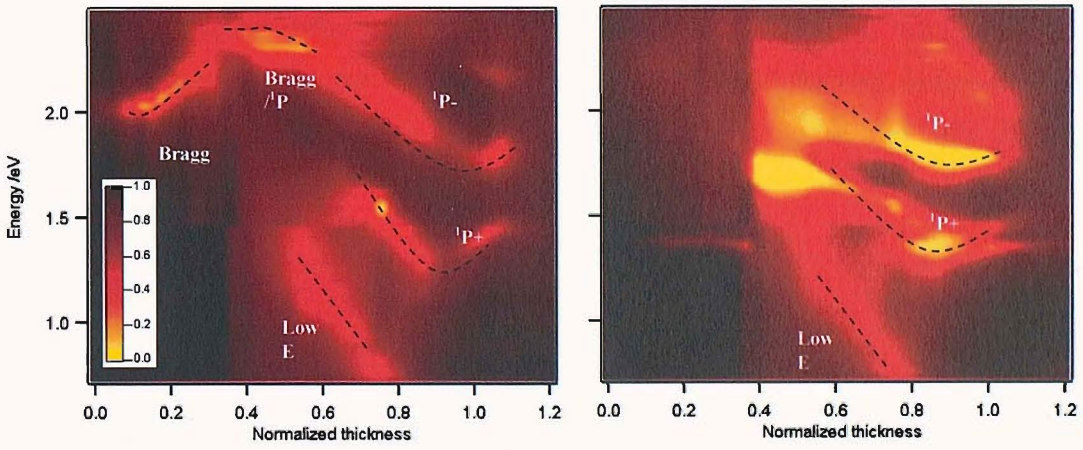

Figure 4.13 Reflectance maps at fixed angle of incidence of (a) 0 and (b) 40 degrees across a D600 graded sample. The bright areas (yellow) indicate the strongest absorption while the dark areas (black) indicate strongest reflection. The dashed lines are guides to the eye and the labels above the lines are the classification of the plasmons.

strongly affected by this; 3) windows form between neighbouring cavities due the close packed spheres touching each other in the template. This means that there may be not enough surrounding metal to support the ^{0}P mode

Further, there exists a rim mode at the edge of the cavity with which the Mie modes such as the ^{1}P (same as p_x and p_y) can hybridize [12]. The plasmon hybridization concept is similar to the hybridization of interacting atomic states into molecular orbitals in a diatomic molecule [13]. Thus, mixing of two plasmons results in an 'anti-bonding' (high energy; anti-symmetric) and a 'bonding' (low

energy; symmetric) plasmon [13]. Hence, the ^{1}P mode on hybridizing with the rim mode forms the ^{1}P- and the ^{1}P+ plasmons, respectively. These modes (^{1}P+ and ^{1}P-) decrease in energy as the thickness of the film increases before finally rising to their Mie solution limit. The low energy mode is currently presumed to arise due to the circular interconnection between the voids and is currently under investigation. These modes are marked on Figure 4.13 for clarity. For further details regarding the current understanding on plasmons the reader is directed to published work [12].

At this juncture it is pointed out that the SERS spectra presented in this thesis have primarily been acquired with a microscope, hence have an angular distribution for incident and collected radiation determined by the aperture of the objective employed. It can be easily seen that plasmon maps at a fixed angle of incidence would give an incomplete picture of the total plasmonic absorption. It can also be now realized that for drawing correlations between SERS and plasmon absorptions, reflectance maps with the microscope are directly useful but for pin pointing the actual mode and deciphering the nature of plasmons on SSV substrates, angular resolved mapping is essential. Therefore, for utilizing the angular resolved maps for the purposes of drawing correlations between SERS intensities and plasmons, the absorption intensities were numerically summed

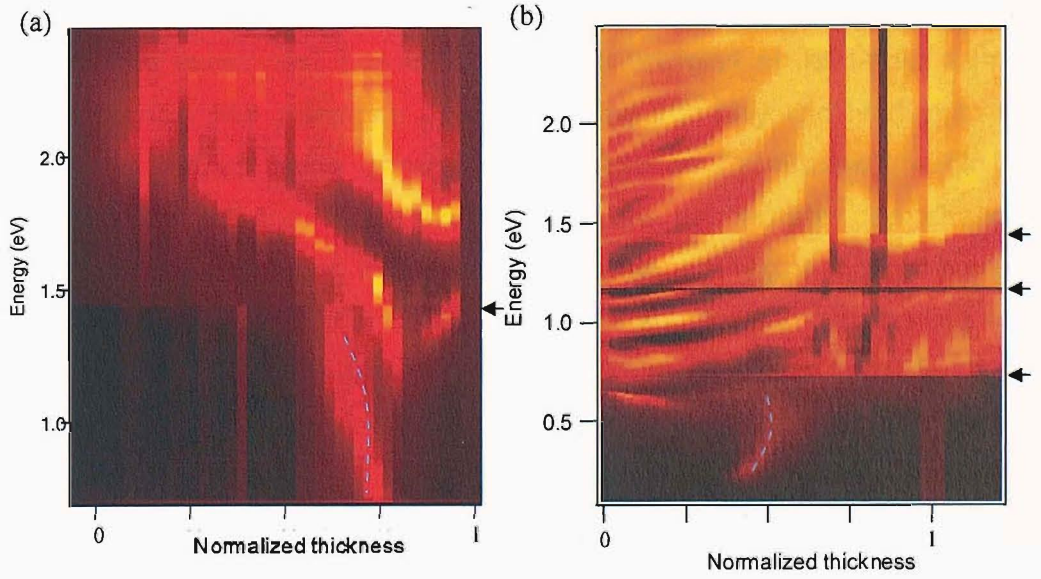

Figure 4.14 Reflectance maps acquired with the angle resolved setup but summed over 0 to ~40 degrees to match the numerical aperture of the SERS spectrometer. The data from three different spectrometers is stitched together at the energies indicated by the arrows. Here plasmon absorption with (a) D600 and (b) D1600 graded gold SSV substrates are shown. The dashed line corresponds to the low energy mode which scales into infrared on increasing the sphere diameter to 1600 nm.

over the angles of incidence to match the optical angle determined by the microscope objective in a SERS experiment. Due weighting of the absorptions was given due to the annular geometry of incident and collection angles in a microscope objective (refer Figure 4.1); the rays coming from the edge of the objective will emanate from a larger area than those from the middle of the objective. Two such plasmon maps for D600 and D1600 graded samples are shown in Figure 4.14. The intensities recorded from angle resolved spectra are

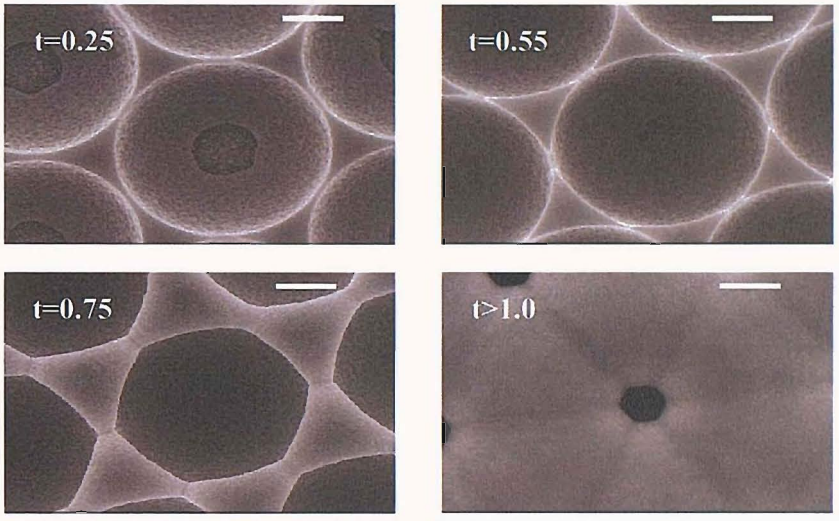

Figure 4.15 FESEM images of D1600 gold substrate at different film heights. Scale bar is 500 nm for the images.

summed over 0 to 40 degrees. As can be seen from the two maps the number of plasmon modes increases with the increase in sphere diameters used for templating the substrates. This is due to lower energies of the larger azimuthal quantum number Mie plasmons (D, F...) coming into play and leading to many higher order modes being generated due plasmon hybridization within large cavities. Breaks in the maps indicated by the arrows are due change of spectrometers for recording in the different wavelength regimes. High resolution electron micrographs for the D1600 gold SSV substrate corresponding to the plasmon map in Figure 4.14(b) are shown in Figure 4.15 at different film heights showcasing the development of void geometry as the thickness of the film increases.

In the next section SERS data acquired on different substrates with three different lasers is presented. Thereafter for drawing correlations either integrated (to match the SERS collection optics) plasmon maps obtained with the goniometer or reflectance data acquired using the microscope are utilized.

4.3.5 SERS on SSV substrates

For SERS substrate optimization studies benzenethiol was chosen as the probe molecule, since it attaches on the metals investigated in this thesis, forms monolayers on the surface and gives unambiguous strong signals. Furthermore, benzenethiol is a good model molecule as its major peaks are around 1000 cm^{-1} and 1500 cm^{-1}, which is the middle of the 'fingerprint' region (500-2000 cm^{-1}) for

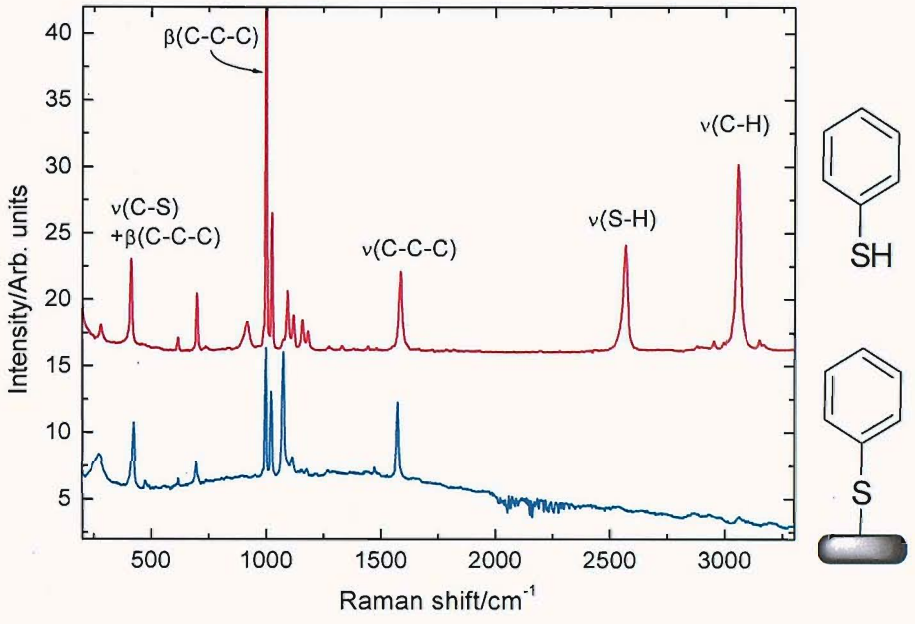

Figure 4.16 Raman (top) and SERS (bottom) spectrum of benzenethiol showing its salient peaks. Laser excitation: 1064 nm, 50 accumulations at 250 mW laser power.

organic molecules. Benzenethiol was adsorbed on substrates by soaking them in 10 mM ethanolic solutions for at least 1 h. A typical Raman and SERS spectrum of benzenethiol is shown in Figure 4.16. The SERS spectrum is acquired in air after washing the surface with ethanol and drying under a stream of compressed air. The peak positions of the prominent benzenethiol peaks and their assignment are listed in Table 4.1. The absence of S-H stretching as well the S-H bending vibration in the SERS spectrum clearly shows that the molecule is chemisorbed on the surface by displacement of the hydrogen forming a thiolate bond and that there is only a monolayer of molecules on the surface [14, 15]. Among all the vibrational modes observed, the ring stretching and breathing (υ_{C-C} & β_{C-C-C})[2] are the strongest in both Raman and SERS; aromatic C-H stretch though strong in Raman is usually weak in SERS; probably due to additional surface selection rules [16] for SERS over Raman or due to weak overlap of orbitals with the surface (often given as an evidence of the chemical effect in SERS [17]). Further, there are differences

[2] υ- stretching, β – in-plane bending, δ-deformation, γ - out of plane bending, ω - wagging, τ - twisting, ρ-rocking

between the positions of the major peaks due to the fact that the Raman spectrum in this case has been acquired from neat benzenethiol while the SERS spectrum is from the surface attached species. The most prominent shifts in position are for the ring ($\beta_{C-C-C}+\nu_{C-S}$ and ν_{C-C}) modes. The aforementioned differences are attributed to a change in the chemical environment of the molecule and due to the surface selection rules [16].

Table 4.1 Raman and SERS peak positions for benzenethiol and their assignment [15].

Vibrational modes	ν_{C-S} + β_{C-C-C}	β_{C-C-C} + ν_{C-S}	β_{S-H}	β_{C-C-C}	β_{C-H}	β_{C-C-C} + ν_{C-S}	ν_{C-C}	ν_{S-H}	ν_{C-H}
Raman	414	699	921	1001	1026	1093	1583	2566	3056
SERS	416	689	-	997	1023	1074	1570	-	3058

In the rest of this section SERS spectra of benzenethiol are presented as recorded on graded SSV substrates. Since the objective was to optimize the geometry for a particular laser excitation, SERS mapping was carried out as a function of film height fabricated with a series of sphere diameter templates. During the course of this thesis work uniform large area templates could be obtained from 200 nm to 1600 nm sphere diameter using the methods described in Chapter 2. However, in this section representative results are presented for substrates fabricated with sphere templates having diameters from 400 to 1100 nm only.

4.3.5.1 With a visible laser at 633 nm on gold SSV substrates

SERS data are presented for D400, D700, D900 and D1100 gold SSV substrates as a function of the film thickness for each sphere templated film in Figure 4.17. The trends shown in the figure are repeatable and have been checked with at least two replicate samples. Also, on the same substrate the signals are reproducible from place to place at a given film thickness with less than 10 % variation. From the plots it is evident that SERS spectra are not only dependent on the sphere diameter of the SSV substrate but also on the film height. However, it is noted that this effect is not limited to that on the intensity of the peaks but also affects the nature of the broad spectral continuum (called the background) observed on which the SERS peaks are superimposed. For analysis of SERS data the peak intensities were extracted by subtracting the background and curve fitting using WiRE 9.0 software where possible. The intensity of peaks

was plotted as a function of thickness of the film and these graphs enabled comparison between the enhancement capabilities of different sphere diameter templated substrates.

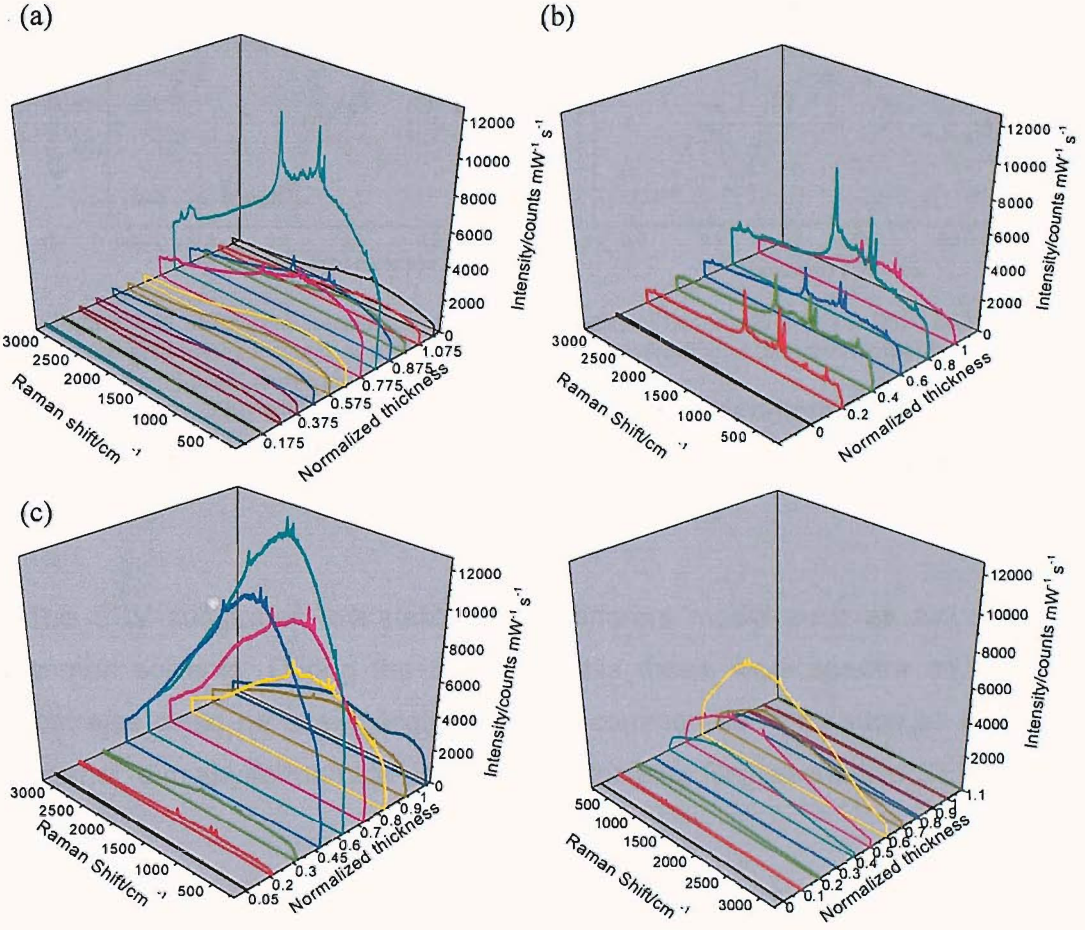

Figure 4.17 SERS spectra of benzenethiol with 633 nm laser on (a) D400, (b) D700, (c) D900 and (d) D1100 gold SSV substrates at different film heights. The intensity has been normalized to collection times and laser power and the film height has been normalized to the sphere diameter employed in the fabrication of the substrate. Spectral acquisition was carried at 3 mW laser power and 10 s collection time; the power was turned down to 1.5 mW or 0.75 mW if the detector saturated or some photodegradation was observed.

SERS intensity profiles for benzenethiol peaks after background subtraction are presented in Figure 4.18 for a D600 and D900 gold SSV substrate. The peak intensities show a maximum at different thicknesses for the two substrates, at ~0.8 *D* and ~0.6 *D* for the 600 nm and 900 nm sphere templated substrates, respectively. The maximum intensity obtained at both these geometries is almost similar between D600 and D900. The explanation behind this should be provided by the dependence of SERS on plasmon absorption. The relation between plasmons and SERS will be discussed in section 4.3.6. The profiles for three peaks (marked on the Raman spectrum shown in the inset) at 416, 1074 and 1570 cm^{-1} have been plotted together on the graphs. Again the intensity variation with thickness of the three peaks considered here is quite similar to each other though

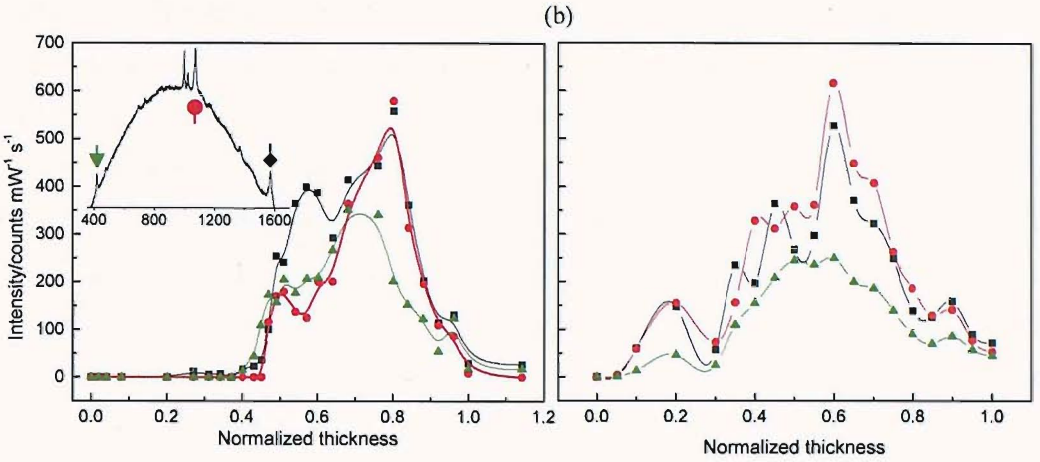

Figure 4.18 SERS peak intensity profiles of three peaks of benzenethiol on (a) D600 and (b) D900 graded gold SSV substrates as a function of thickness of the film. A spectrum with the 1570, 1074 and 416 cm^{-1} peaks marked is shown in the inset.

not coincident. The slight differences may be due to the difference in enhancement as a function of wavelength, which might depend on the energy dispersion of the plasmon.

The SSV substrates are stable under different media such as air, water and common solvents. During the course of this thesis work spectra on gold SSV substrates could be easily acquired under common solvents such as ethanol, 2-propanol, dimethylformamide and even acetonitrile. Representative SERS spectra

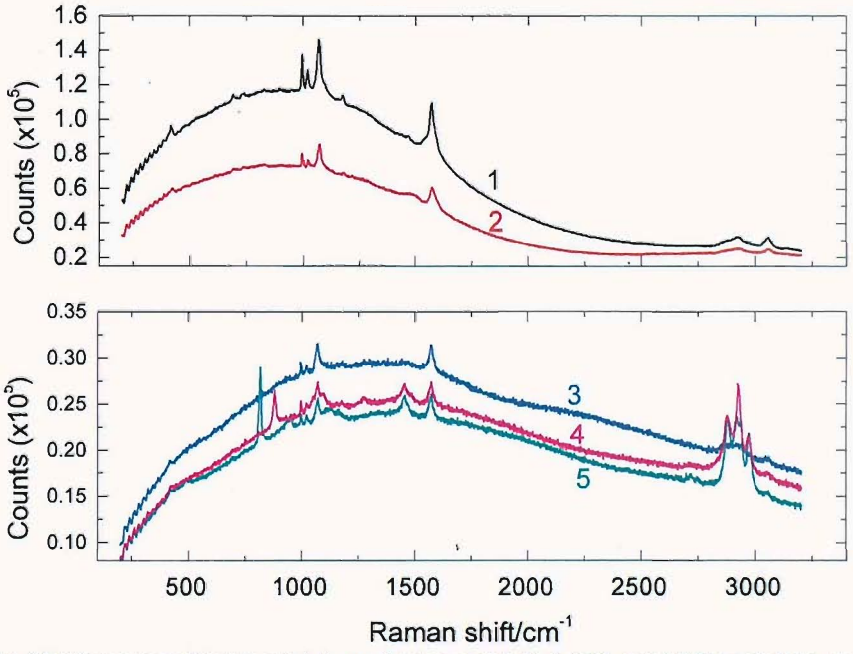

Figure 4.19 SERS spectra of benzenethiol attached on a 0.8 *D*, D600 gold SSV substrate under different media. Top shows spectrum in 1. Air 2. Air and ordinary cover glass placed on the substrate. Bottom shows spectrum with cover glass placed on top in 3. water, 4. ethanol and 5. isopropanol. Spectra acquired with 633 nm laser; 2 mW power, single accumulation of 10 s.

are shown in Figure 4.19 in different media. Though there is some attenuation due to the ordinary glass cover slip placed over the medium on the substrate, clear peaks can be seen well over and above the Raman peaks of the bulk solvent. The decrease might be attributable to a change of the optical properties of the substrate due to the surrounding dielectric medium as mentioned earlier in this Chapter in section 4.3.3. However, the affect of change of medium surrounding the structured substrate on the SERS enhancements will be presented later in section 4.3.6 wherein the SERS signals in air and water are compared and discussed in the context of the tuning of plasmons by the different media.

4.3.5.2 With a near infrared laser at 785 nm on gold SSV substrates

SER spectra of benzenethiol were acquired on a graded D600 gold SSV substrate with a 785 nm laser. The peak intensity for the 1570 and 1074 cm^{-1} bands was calculated after background subtraction and their profiles with variation in film thickness are plotted in Figure 4.20. Again it is observed that the intensities show a maximum around t= 0.7-0.8 for the D600 SSV film even with a 785 nm

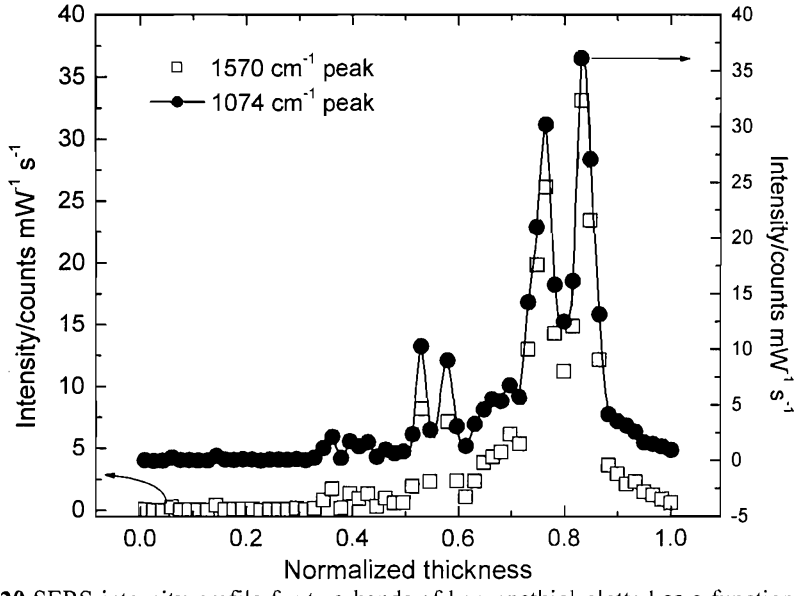

Figure 4.20 SERS intensity profile for two bands of benzenethiol plotted as a function of film thickness. The profiles have been offset for clarity as they are very similar to each other. Intensity of the peak is calculated after background subtraction; spectra recorded with 785 nm laser, 100 mW laser power, 1 s collection time, 10 accumulations.

laser excitation. However, compared to the profile obtained with the 633 nm laser shown in Figure 4.18 in the previous sub-section, the maxima are much sharper and do not occur over a broad range of film heights. With the 633 nm excitation the peak intensities gradually increase above 0.5 *D* and show a maximum at 0.8 *D* while with the 785 nm laser, apart form the small blips observed around 0.5 *D*, the intensities rise sharply only after 0.7 *D*.

Another experiment was carried out to show that the SERS peak intensity profile such as that in Figure 4.20 is reproducible across the substrate. This is demonstrated in Figure 4.21 showing SERS data recorded on a graded substrate. A total of 300 spectra were recorded, one every 200 microns, on 12000 μm x 800 μm area of a D600 graded gold SSV substrate. The peak intensity of the 1570 cm^{-1} band of benzenethiol has been plotted on the map after automatic background subtraction between 1540 and 1600 cm^{-1} using SpectrumImage software provided by Perkin-Elmer with the RamanStation spectrometer. Except for some odd spots, signals are quite uniform across the width of the sample (some of the noise could have been generated to the automatic background subtraction method).

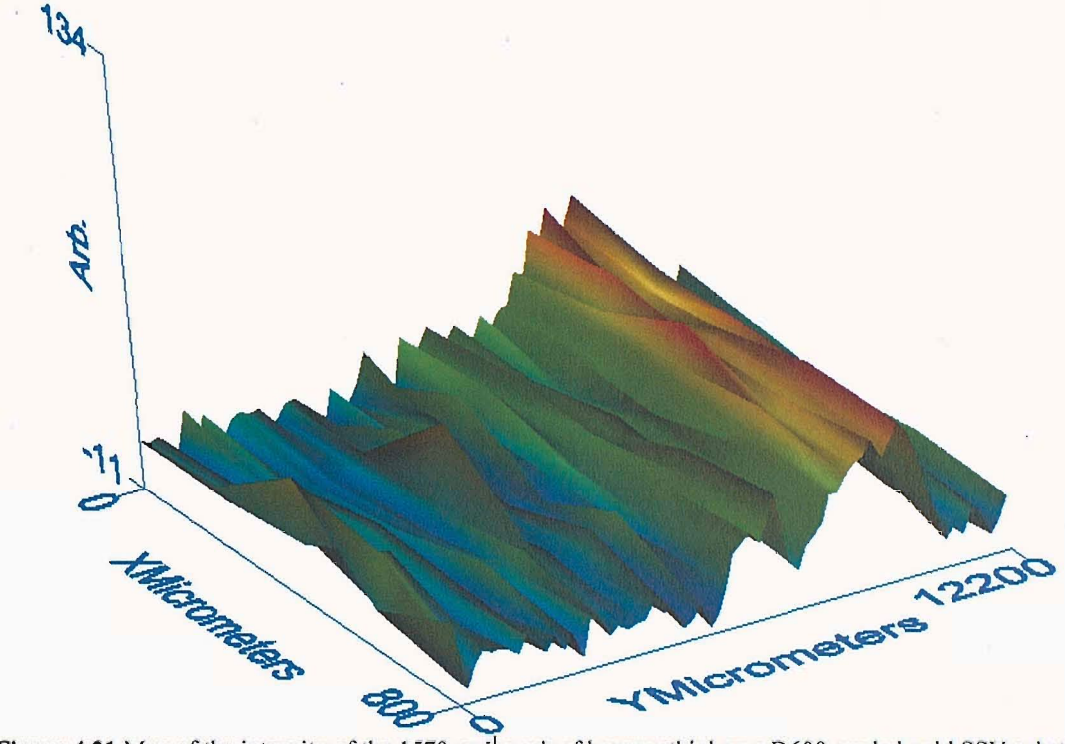

Figure 4.21 Map of the intensity of the 1570 cm^{-1} peak of benzenethiol on a D600 graded gold SSV substrate 800 microns wide and 12000 microns long. 60 spectra have been recorded along the length of the substrate in parallel lines 200 micron apart. The thickness increases from 0 to 1 *D* from left to right. The y-axis shows the background corrected intensity of the 1570 cm^{-1} peak.

4.3.5.3 With a near infrared laser at 1064 nm on gold SSV substrates

SER spectra of adsorbed benzenethiol were obtained as a function of film height for a series of gold substrates templated with 700 nm to 1100 nm spheres. Smaller sphere sizes were not chosen since it was expected that the plasmon resonances around 1064 nm would be obtained with large sphere (> 700 nm diameter) templated substrates. SERS spectra with respect to film height for 900 and 1100 nm sphere templated substrates are shown in Figure 4.22. The intensity of peaks in the SERS spectra exhibit a strong dependence on the thickness of the film as well as the sphere diameter used for templating the structure. The maximum

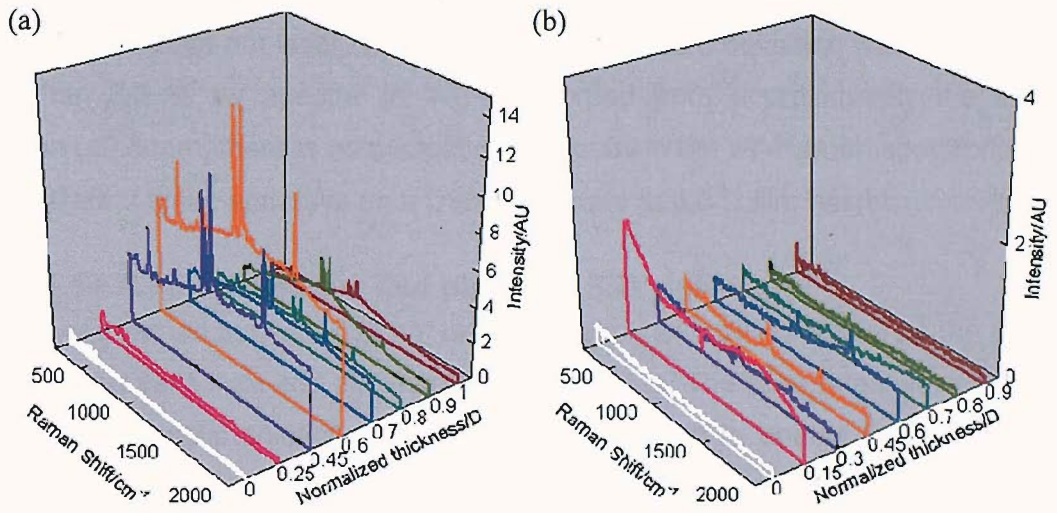

Figure 4.22 SERS spectra of benzenethiol on (a) D900 and (b) D1100 gold SSV substrates with a 1064 nm laser excitation as a function of film height are shown.

enhancements for the substrates in Figure 4.22 occur between 0.4 and 0.7 D though the peaks are much reduced for the D1100 substrate compared to D900. The SERS enhancement factors were determined by comparison to the spectrum of neat benzenethiol and assuming the formation of a compact monolayer as described previously [18]. The fractional coverage for SSV substrates was found to be 0.29 determined using cyclic voltammetry (reductive desorption in 5M KOH) compared to a theoretical maximum of 2.3 nmol cm^{-2} [19]. Using this, the number of molecules in the area illuminated by the 300 micron laser spot on the surface was calculated. Then from the Raman measurement with the neat benzenethiol solution, the number of molecules in the cylindrical volume illuminated by the laser spot and the path length of the cell was determined. The peak intensities after background subtraction were used to find the enhancement ratio between the substrate and the pure liquid. This method of obtaining enhancement factors is similar to that of Tian *et al.* [20]. Further it is pointed out that the enhancement factors stated here are averaged over the entire laser spot area. Among all the samples the greatest SERS enhancements were obtained with the 900 nm sphere templated nanovoid film at around ~0.6 D. The enhancement factor was calculated to be 3 x 10^6, which was the highest among the substrates in this study. The 800 nm sphere templated film showed a SERS enhancement profile similar to that of the 700 nm sphere templated film, with the maximum signal being obtained at ~0.75 D albeit with much higher intensities. The enhancement factor for the 800 nm nanovoid film at ~0.75 D thickness was only slightly lower than that obtained for D900 nm film at ~0.6 D. The 1000 nm nanovoid film behaved very similar to the 1100 nm sphere templated film and showed very little SERS enhancement.

The signals from the substrates were again found to be stable and repeatable even with the 1064 nm laser. To exemplify, the standard deviation was found to be less than 6.3 % for spectra (n = 14) recorded from approximately the same position (±0.5 mm, there is no microscope to focus in the FT-Raman spectrometer) over different times and days on a D900 substrate at 0.6 D film height.

4.3.5.4 SERS on palladium and platinum SSV substrates

SERS was carried out with 633 nm laser excitation with benzenethiol as the probe molecule on palladium and platinum SSV substrates. The substrates were soaked in 10 mM ethanolic solutions of benzenethiol for 24 h to enable the adsorption. Benzenethiol forms a monolayer on palladium and platinum similar to that on gold [21]. The effect of film thickness on the SERS intensity for 400, 500, 600 and 700 nm diameter sphere templated Pd SSV substrates is shown in Figure 4.23 and correspondingly for Pt SSV substrates in Figure 4.24. It is again clearly evident

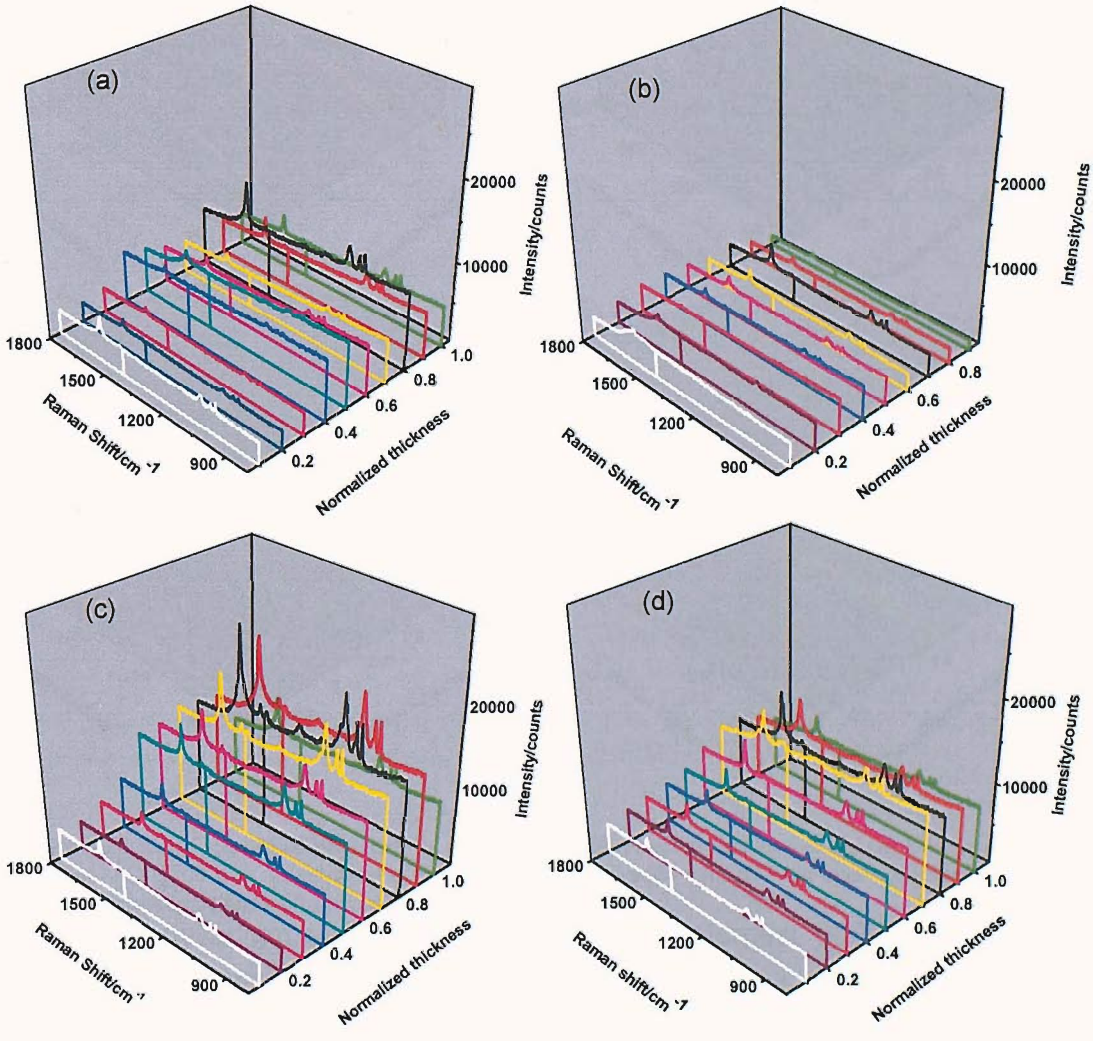

Figure 4.23 SERS spectra of benzenethiol recorded at different film thicknesses for (a) D400, (b) D500, (c) D600 and (d) D700 sphere templated SSV Pd films. The spectra were recorded with 633 nm laser excitation, 3 mW laser power, employing a single 60 s accumulation.

that the SERS intensity varies with the film thickness and the template sphere size indicating that the precise geometry of the structured film is an important factor in determining the enhancement. The results for palladium and platinum agree well with results presented for gold SSV substrates earlier. For SERS with 633 nm laser excitation on palladium and platinum surfaces fabricated using various sphere size templates the maximum enhancement always occurs between 0.7 and 0.9 *D*, the precise value depending on the template sphere diameter. In general the largest enhancements were obtained on D600 and the smallest on D500 SSV films.

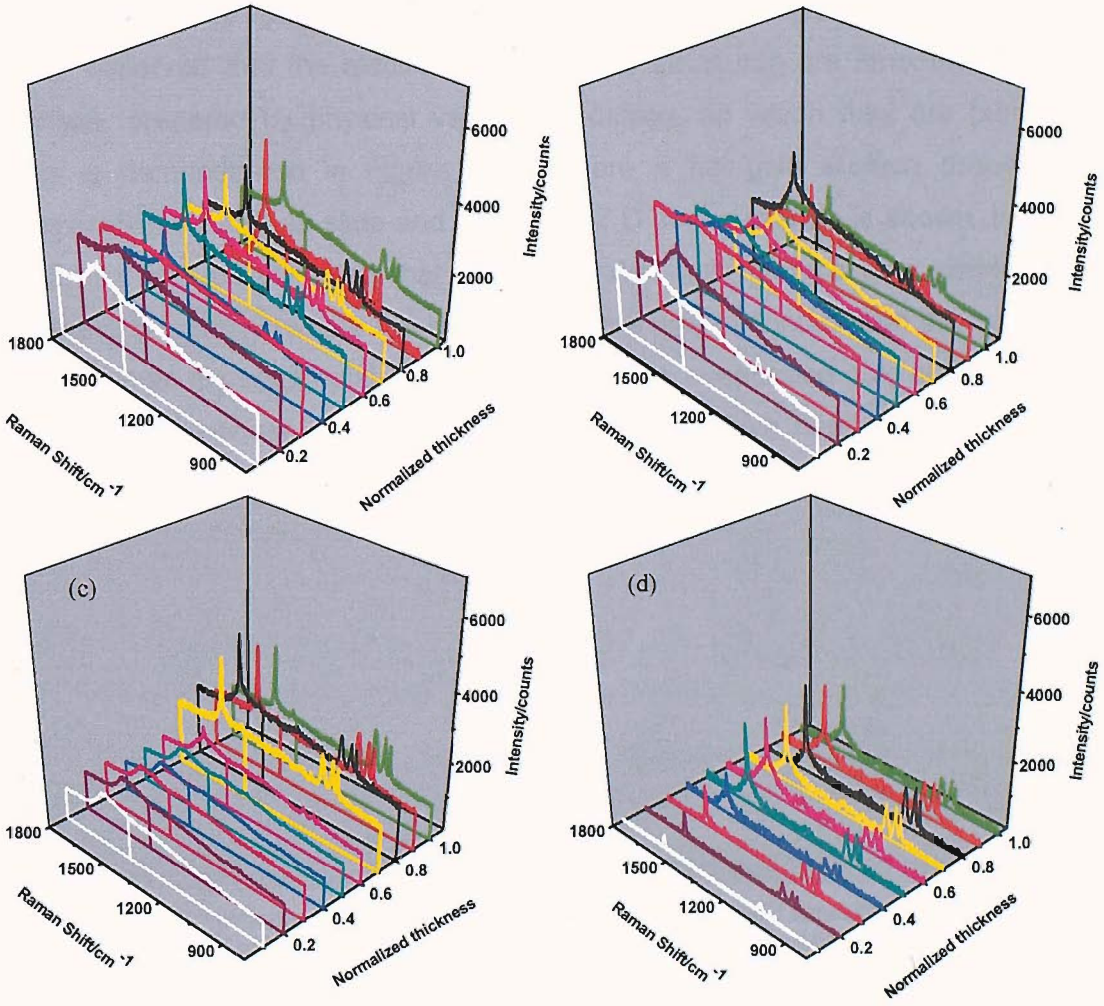

Figure 4.24 SERS spectra of benzenethiol recorded at different film thicknesses for (a) D400, (b) D500, (c) D600 and (d) D700 SSV Pt substrates. The spectra were recorded with 633 nm laser excitation, 3 mW laser power, employing a single 60 s accumulation.

For both palladium and platinum substrates the largest SERS enhancements were obtained with 600 nm sphere-templated nanovoid film at around 0.8 *D*. Enhancement factors were calculated at this geometry for both palladium and platinum films using the method described in the literature assuming a surface coverage of 0.45 nmol cm^{-2} for benzenethiol on platinum [20, 22] and using

calculated surface area of the voids determined by the morphology (3 times the flat area)[3]. The calculated values of the enhancement factors for palladium and platinum were found to be 1800 and 550, respectively.

4.3.5.5 Discussion on SSV SERS substrates

In the previous section it has been demonstrated that SSV substrates provide a stable, reproducible platform for obtaining SERS. The SERS enhancements can be engineered for a particular laser excitation or in a specific medium by the control over film height and the sphere diameter. This approach marks a departure from the approach of generating random hot spots for SERS such as with electrochemically roughened surfaces, cold deposited films and the like. It has been observed that the electrodeposited SSV structures are smoother than the surface, prepared by physical vapour deposition, on which they are fabricated. This is demonstrated in Figure 4.25, where a flat gold surface prepared by evaporation on a glass slide and a D900, 0.7 D gold substrate is shown. In Figure 4.25(b) it can clearly seen that the evaporated gold surface also visible in the centre of the cavity (where the template sphere was in contact with the surface) is rougher than the electroplated structure itself. The evaporated gold surface as well as the plain (non-templated) electrodeposited films give negligible SERS and it

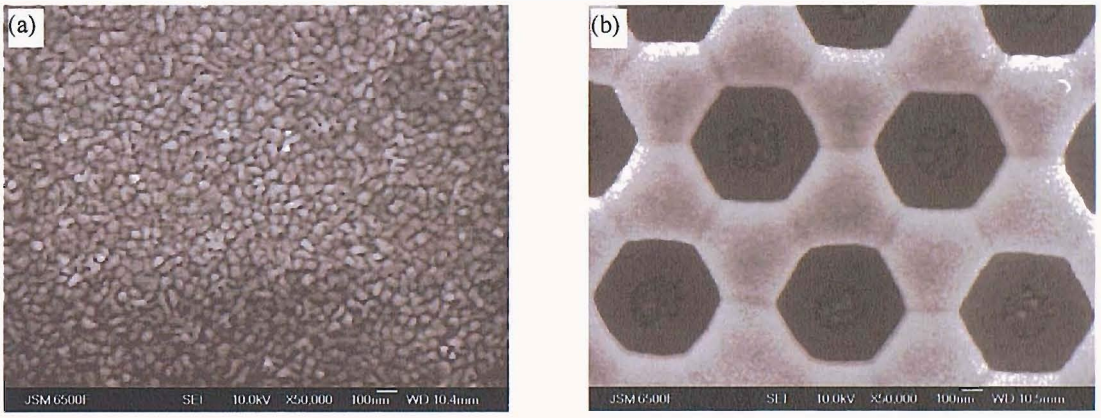

Figure 4.25 FESEM images showing the smoothness of (b) electrodeposited structured film compared to (a) flat evaporated gold used as substrate. Evaporated gold also visible in the middle at the bottom of the voids is clearly rougher than electrodeposited structured gold film. The voids shown in (b) correspond to a film height of 0.7 D templated with 900 nm spheres. The images are recorded under a magnification of 50000 and the scale bar is 100 nm

has been demonstrated that SSV substrates generate reproducible and higher SERS signals compared to electrochemically roughened surfaces [1]. This lends credence to the assertion that it is the tunable plasmonic properties of the SSV substrates which produce high SERS enhancements on them. Ample proof of this is provided in the next section.

[3] For calculation of surface area of sphere segment voids see Appendix I

4.3.6 Plasmon resonance matching for maximum SERS

In this section the plasmon absorptions and SERS signals measured on the same substrates are collated to draw correlations between them. This has been carried out primarily for two reasons, 1) to understand the origin of the SERS enhancement properties of SSV substrates and 2) to develop a holistic approach for engineering these tuneable plasmonic substrates to give maximum SERS enhancement with a desired laser in the required medium.

The SSV substrates discussed in this thesis support a wide variety of plasmons which can be engineered for high local fields, strong coupling strength and wavelengths tuneable from UV to IR. Dual control of the morphology is provided by the choice of sphere size employed for the template formation and by the thickness of the film provided by electrodeposition. However, a single graded SSV substrate can exhibit intense SERS enhancements over a wide range of

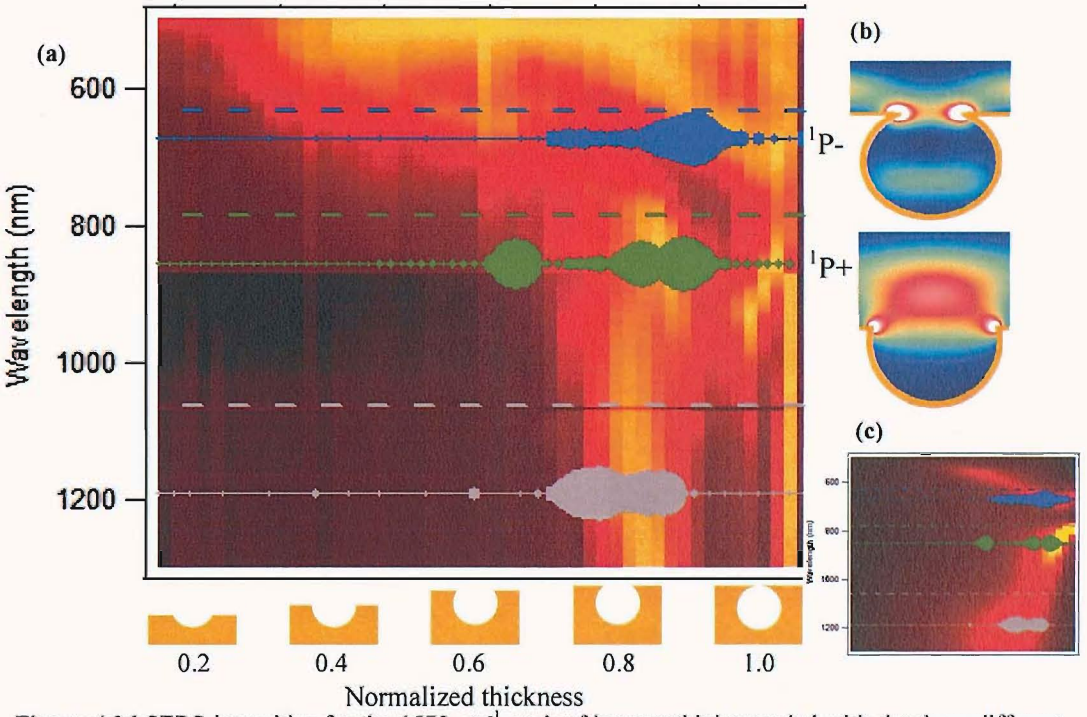

Figure 4.26 SERS intensities for the 1570 cm^{-1} peak of benzenethiol recorded with the three different lasers overlaid on the plasmon map for the same substrate. The peak intensities have been extracted after background subtraction. The diameter of the circles is proportional to the intensity recorded with a particular laser wavelength. The laser lines at 633 nm (blue), 785 nm (green) and 1064 nm (grey) are shown in the same colour along with the scattered wavelengths at 703 nm, 895 nm and 1277 nm, respectively, corresponding to the 1570 cm^{-1} band. The electric field distribution for the ^{1}P- and ^{1}P+ modes (b) and their dispersion with film height obtained by modelling (c) carried out by our physics collaborators is shown alongside. Bright colours indicate plasmonic absorptions.

wavelength excitations at the same or different locations on the substrate, directed by the surface morphology. An example of SERS measurements of benzenethiol adsorbed on a single graded substrate templated with 600 nm spheres (D600) carried out with 633 nm, 785 nm and 1064 nm laser excitations as a function of

thickness of the film is shown in Figure 4.26. The intensity of the 1570 cm^{-1} Raman scattered peak, corresponding to the ring stretching mode of benzenethiol, is extracted after background subtraction and plotted for each laser wavelength on the corresponding plasmon map of the substrate. The size of the circles is proportional to the SERS intensity acquired with a particular laser. It is difficult to normalize between the three sets of SERS data as they were acquired on three different instruments with different detector and collection efficiencies. However, it is strikingly clear that there is near coincidence of the maximum SERS intensity observed and the optical absorption observed on the substrate at every laser wavelength investigated. The ingoing laser lines are indicated above the SER scattered peak positions, here plotted in terms of their absolute wavelength. The SERS intensity increases when there is resonance between the laser or scattered radiation and a plasmon mode supported by the structured substrate. However, not only the strength of the plasmon absorption but also its nature affects the SERS enhancements.

The localised modes such as the ^{1}P- and ^{1}P+ modes are identified to be responsible for SERS enhancement with the 633 nm and 785 nm laser, respectively, as shown in Figure 4.26. The ^{1}P- Mie mode has most of the electric field in the middle of the cavity rather than on the metal and hence, produces very little SERS before 0.7 D, after which thickness it becomes very strong and hence, we speculate it has enough field strength on the metal to lead to SERS on resonance with the 633 nm lasers. Due to interaction with the rim mode, the ^{1}P mode forms a lower energy mode (^{1}P+) which has the bulk of its field located on the metal and hence produces SERS 0.5 D upwards with the 785 nm laser. On this particular substrate enhancement of SERS is also observed when the 1064 nm laser matches the low energy absorption at 0.8 D. It is currently speculated that this arises from the windows (as shown in Figure 4.27) between neighbouring voids, which form tips as they close up around 0.7 D which may support this low energy mode. This mode rapidly tunes into the NIR as the tips close up.

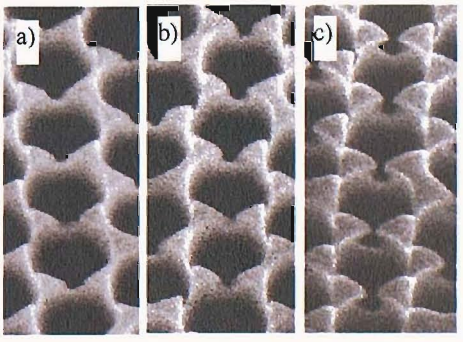

Figure 4.27 SEMs showing the growth of electrodeposited Au film around the interconnection between voids for a D600 film for (a) $t \approx 0.4$, (b) $t \approx 0.5$ and (c) $t \approx 0.6$.

From Figure 4.26(c) it can be seen that the ^{1}P- mode has been properly simulated but the dispersion of the ^{1}P+ mode with film thickness leaves much to be desired especially below 0.6 D. The modelling of the modes is currently limited to a single cavity and ignores the neighbouring interactions. Also, the interconnection between the voids (windows) needs to be taken account in the model of the void itself.

Nevertheless, qualitatively, it can be seen that the SERS peak intensities increase when either the ingoing laser or the outcoming scattered radiation matches with a plasmon resonance on the substrate. The current theory allows us to identify the position of fields in the cavities; however a full theory which can take account of all the features of the experimentally realised structures is still awaited.

4.3.6.1 Plasmon resonant SERS with 633 nm laser

As mentioned earlier, the properties of our substrates vary controllably as a function of sphere diameter and the film height. Hence, using our combinatorial approach with graded SSV substrates it was possible to find the best structure suitable for SERS at a particular excitation. SERS was recorded for benzenethiol adsorbed on these substrates in air and water. Results are presented in Figure 4.28 wherein the extracted SERS peak intensity of the 1571 cm^{-1} band of benzenethiol recorded with a 633 nm laser is plotted as a function of thickness of the substrates templated with 400, 500, 600 and 800 nm diameter spheres. Again an obvious conclusion from the SERS peak intensity and the absorption profiles is the clear coincidence of their respective maxima for each of the graded samples in either medium. Further, qualitatively it can be seen that both the ingoing and outcoming resonances are important for obtaining maximum SERS. For example, with D400 in air both the laser and the scattered radiation are in resonance with the ^{1}P+ mode and therefore SERS intensity is the highest. In water the resonances are with the ^{1}P- mode and also lead to high SERS. In both cases, the highest SERS is obtained around t = 0.75. However, with the D800 sample the ingoing resonance seems to be more important in air while in water the outcoming resonance appears to cause the SERS enhancement.

It is predicted that the SERS enhancement depends on the coupling of ingoing and outcoming radiation [23, 24] as they occur at different energies. Nevertheless, it is often ignored. However, the hypothesis that plasmon resonance matching with the ingoing or outcoming leads to SERS intensity appears justified even with a change in the dielectric media surrounding the substrate. Further, the sizes of the

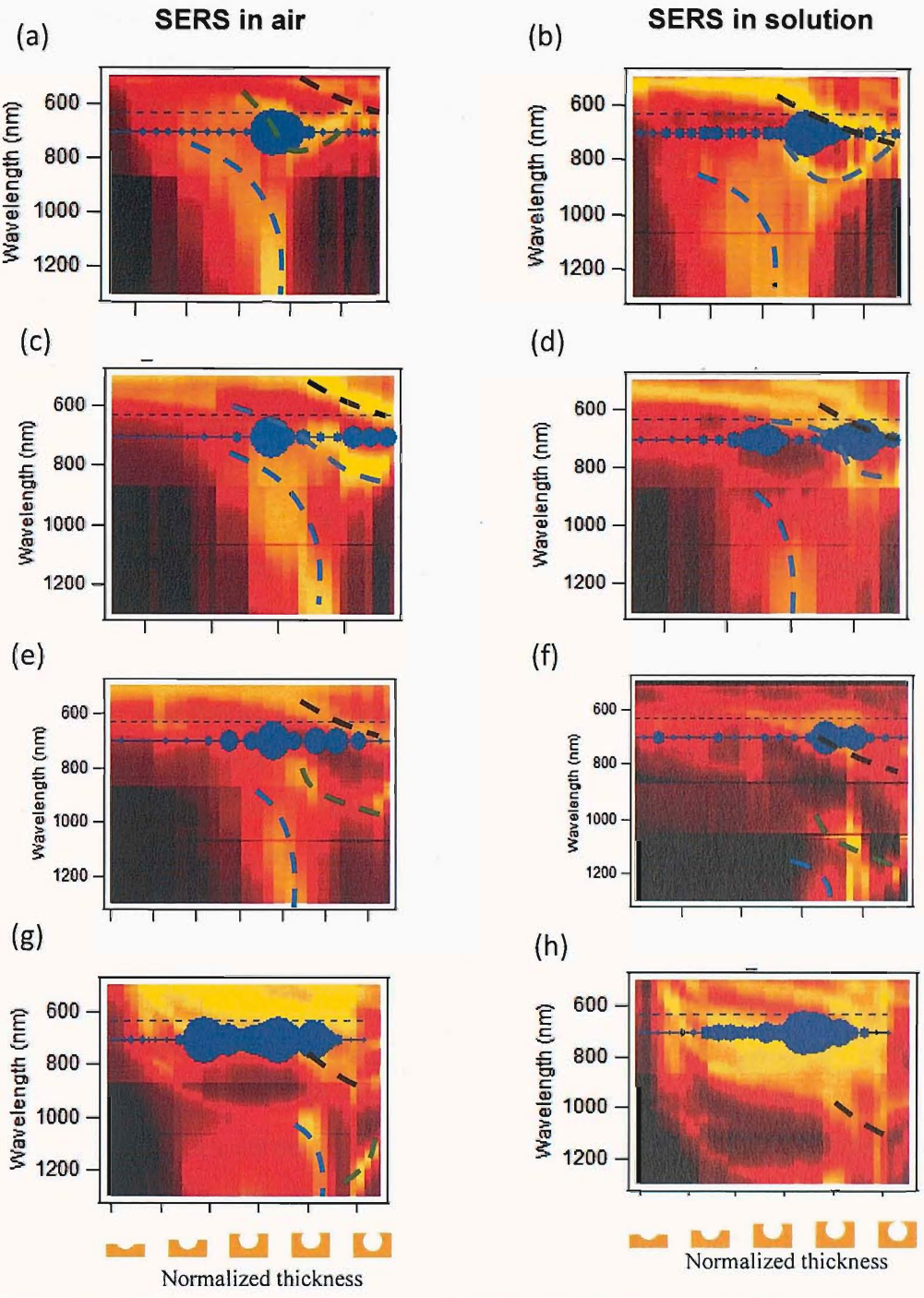

Figure 4.28 SERS intensities (in blue) overlaid on plasmon maps. Spot size corresponds to SERS enhancement for D400 voids in (a) air and (b) solution; D500 in (c) air and (d) solution; D600 in (e) air and (f) solution; D800 in (g) air and (h) solution. The ingoing laser is at 633 nm and the outcoming scattered radiation (for the peak corresponding to the 1570 cm^{-1}) band of benzenethiol is at 703 nm. The intensity of the peak after background subtraction is indicated by the size of the circle. The dashed lines are guides to the eye showing plasmon modes (– –: ^{1}P-, – –: ^{1}P+ and – –: Low E) and their tuning with change in template sphere size and refractive index of the medium.

circles representing SERS intensities are relative to each other. Hence, it shows that it is not just a single type of plasmon mode which could lead to SERS but a number of them which can be manipulated by the choice of sphere diameter and film height to give comparable SERS. For example, with the 400 nm diameter sphere templated graded sample the ^{1}P+ plasmon mode leads to SERS

enhancements while for D800 it is the ^{1}P- plasmon mode which resonates with the 633 nm laser. However, it is pointed out that the SERS intensities observed with the substrates in water are 5 to 10 smaller than in air and this could be due to attenuation by water or the cover glass placed on top of the water layer on the substrate and similar weakening of plasmon absorptions was observed and was mentioned under section 4.3.3. It is also possible that the high dielectric constant of water weakens the fields on the surface.

4.3.6.2 Plasmon resonant NIR-SERS

As mentioned in section 4.3.5.3, SSV substrates give high enhancements even with a 1064 nm laser. The SERS intensities were profiled on D700 to D1100 nm substrates and plasmon maps obtained on the same substrates. Not only were the SERS intensities dependent on the sphere diameter and the film thickness, the enhancement was higher at those film thicknesses where the existence of a plasmon mode was indicated on the plasmon map compared to those where weak, or no, plasmonic interaction was observed. However, the effect is more subtle than this. On overlaying the SERS intensities corresponding to 420 cm^{-1}, 997 cm^{-1} and 1570 cm^{-1} Raman bands of benzenethiol at the appropriate outcoming wavelengths on the absorption maps along with the ingoing excitation laser, again a clear correlation can be observed (Figure 4.29). Wherever, both the ingoing and outcoming wavelengths match with strong plasmon absorption on the substrate, a large enhancement in SERS can be seen. For example, in Figure 4.29b and c, the ingoing and outcoming radiation match with the plasmon resonance on the surface at ~0.8 *D* and ~0.6 *D*, respectively and hence, high SERS intensities can be seen. However, in Figure 4.29d & e at 0.6 *D* the laser is not able to couple into a plasmon resonance and hence, very little SERS intensities are observed. For the 700 nm sphere templated film, Figure 4.29a, the plasmon resonances are not strong enough in the NIR; consequently, they do not contribute to large NIR-SERS enhancement.

The matching of wavelengths corresponds to the desired resonance coupling between the laser excitation as well as scattered radiation with the plasmons generated on the structured surface and hence, a large increase in SERS is expected. Existence of plasmon modes on the structured substrates not only helps in coupling of energy between ingoing radiation and the molecule adsorbed on the surface but also assists in coupling of scattered radiation back from the surface.

Hence, resonance between ingoing excitation and outcoming scattered radiation with plasmon modes on the surface is critical for optimization of SERS [6, 23, 24].

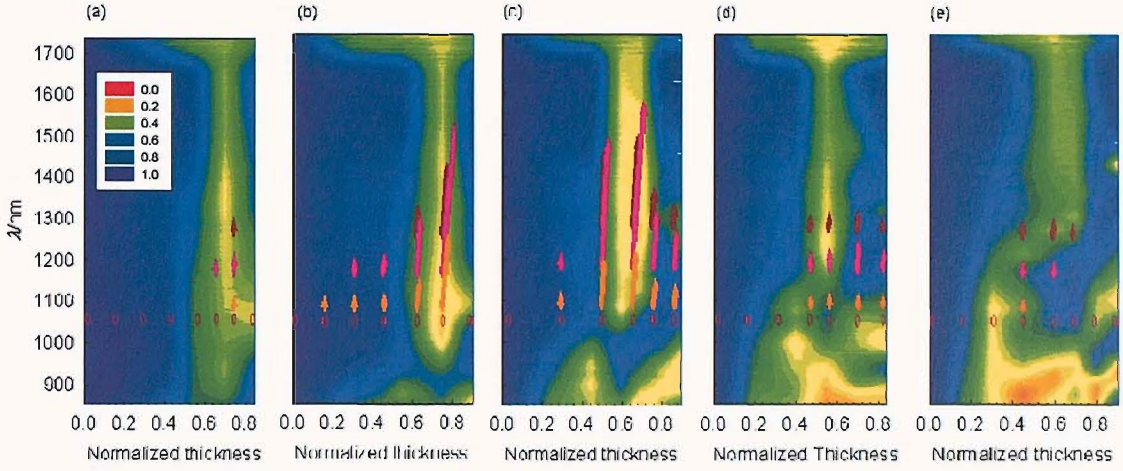

Figure 4.29 Plasmon maps superimposed with Raman scattering peak intensities for gold substrates templated with (a) 700 nm, (b) 800 nm, (c) 900 nm, (d) 1000 nm and (e) 1100 nm spheres. (0) denotes the ingoing laser excitation at 1064 nm in the NIR-SERS experiment. (▲), (▲) and (▲) represent the outcoming radiation at 1114 nm, 1191 nm and 1277 nm corresponding to 420 cm^{-1}, 1000 cm^{-1} and 1570 cm^{-1} Raman bands of benzenethiol, respectively. The lengths of the arrows indicate the intensity of the scattered radiation (on a scale of 0 to 8.5 AU). The plasmon maps have been acquired with the microscope setup. The scale shows normalized reflectance with respect to flat gold. Thus, 0 means the strongest plasmonic absorption while 1 indicates maximum reflection (no absorption with respect to flat gold).

4.3.6.3 Plasmon resonant SERS with Pd and Pt SSV substrates

In the above discussion it has been shown that for gold SSV substrates plasmon resonance matching is necessary to obtain the maximum SERS enhancements. It has been shown earlier that with Pd and Pt SSV substrates also the SERS signals are dependent on the sphere diameter and film height of the substrate. To relate this dependence of the SERS enhancement to the geometry of the structured film, reflectance spectra were recorded for the palladium and platinum surfaces as a function of film thickness at the same positions on the graded substrates at which SERS was measured. In sub-section 4.3.5.4 SERS data has been presented for different Pd and Pt SSV substrates. The SERS enhancement observed for D500 Pd films is the smallest among them and maximum for the D600 substrate. This is rationalized by the principle of plasmon resonance matching that the SERS enhancement depends on the matching of the incident and outcoming radiation with plasmons on the substrate in Figure 4.30 by comparing their reflectance spectra. The wavelengths corresponding to the laser excitation, 633 nm (red line), and Stokes scattered photons for the 1571 cm^{-1} SERS peak at 703 nm (blue line), are shown in Figure 4.30. As can be seen, for the 600 nm sphere templated films both the wavelength of the excitation laser and the Stokes scattered photons

overlap with a strong plasmon absorption feature in the reflectance spectra for the thicker film leading to a large SERS signal. For the 600 nm sphere templated film maximum overlap is obtained for a film height of ~0.8 *D*. In contrast, in the case of the 500 nm sphere templated films the incident and Stokes scattered radiation do not match well with the strong plasmon absorptions in the spectra, consequently these surfaces produce much smaller surface enhancements. Further it is noted that the magnitude of SERS signals observed on these surfaces is much weaker than those observed for gold substrates as the plasmon strength is smaller in Pd and Pt than on Au.

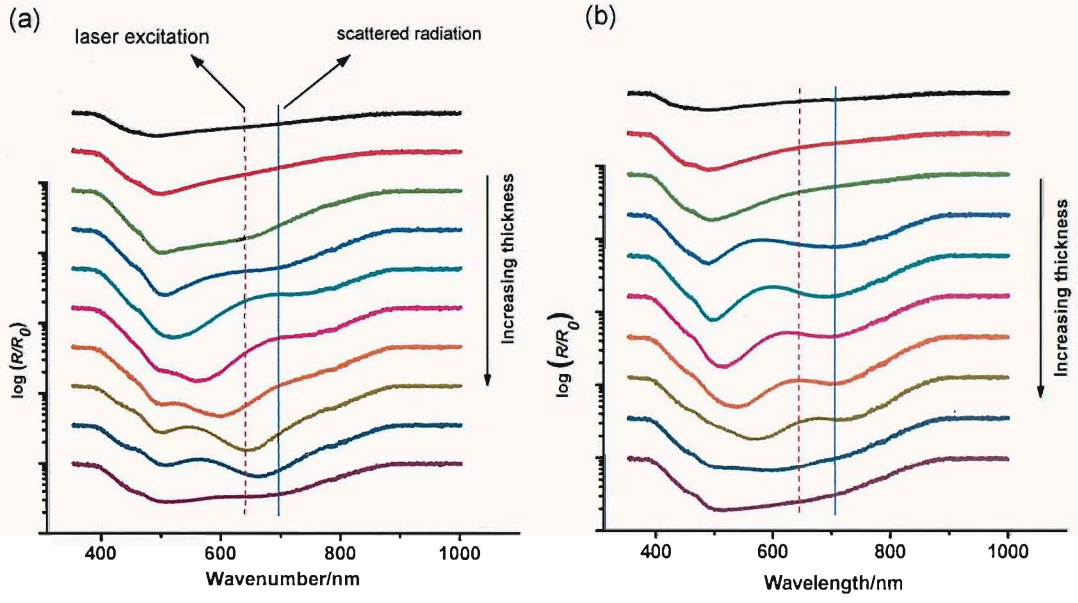

Figure 4.30 Reflectance spectra of graded in thickness palladium substrates made using (a) 600 nm and (b) 500 nm template spheres. The dashed red line denotes the ingoing laser excitation at 633 nm and the solid blue line denotes the out coming radiation at 703 nm corresponding to the 1570 cm^{-1} SERS band of benzenethiol.

4.3.7 Summary

In this chapter so far it has been shown that SSV substrates, with a variety of metals, display interesting optical properties which can be tuned by variation of sphere diameter and film height. Suitability for SERS has been established for gold, palladium and platinum SSV substrates. It has also been demonstrated that SSV substrates can be tailored for used with different lasers and in different media. Plasmon resonance matching appears to be the key to obtain high SERS enhancements. The theory developed for understanding the plasmon resonances observed on the substrates has led to identify the modes responsible for the high SERS enhancements observed on them and their consequent optimization.

4.4 Continuum observed in SERS

4.4.1 Introduction

A broad continuum called the background is always observed in a SERS spectrum on top of which the peaks are superimposed. Vigorous investigation into the mechanism of enhancement in SERS has been carried out over the last 34 years; similarly theories have been discussed in literature trying to explain the background continuum which accompanies SERS. Most researchers consider it to either arise due to inelastic scattering induced by the surface roughness [25, 26] or due to luminescence [27] due to the molecule. Among the most prominent earlier theories also discussing the background, those by Gersten *et al.* [28] (GBL model) and Burstein *et al.* [29] (BCCLT model) stand out. These have been critically reviewed by Furtak and Reyes [30]. There appears a consensus that electron-hole pair excitations initiate the process, however, current theories fall short of providing a comprehensive explanation of all the observations by various researchers [31]. Undoubtedly there is a chemical (molecular) effect on the observation of the background but there is ample proof that there is also an electromagnetic component. A brief summary of the developments in understanding regarding the continuum observed has been provided by Moskovits in his reviews on SERS [6, 23]. Similar to the debate regarding the mechanism of SERS enhancement, confusion abounds regarding the generation of the background and most of it could be ascribed to lack of reproducible SERS substrates with well defined geometry which enable systematic studies. Furthermore, in the quest for applications of SERS, in the last two decades researches have tended to ignore the background, regarding it as a necessary evil and have simply subtracted it, concentrating on the peaks instead. However, there seems to be renewed interest and new observations such as the possibility of plasmon coupled emission, which might help in a more elaborate understanding on the background [32-34]. These are taken into account in developing our model for the background.

In this section the background as observed on SSV substrates is analysed and its correlation with various physico-chemical parameters such as the strength of plasmons and the nature of molecule is demonstrated. Utilizing these observations a model for the origin of this background is postulated and discussed. Thereafter, the model's robustness is tested by discussing the case of resonantly enhanced molecules (SERRS) and anti-Stokes SERS.

4.4.2 Background studied on SSV substrates

SERS peaks sit on a broad continuum whose shape depends on the structure of the SSV substrate. This can be readily seen in section 4.3.5 on SERS. Most often the background has one prominent broad maximum; sometimes, however, close observation revealed small features which were found to vary systematically with thickness and thus altered the overall shape of the continuum. In Figure 4.31 spectra at 0.52 and 0.6 D for 600 nm sphere templated gold substrates on which benzenethiol had been adsorbed are shown. These spectra show another feature in the background apart from a broad overall maximum. The position of the overall maximum and the next most prominent feature are marked by arrows and to determine their positions a curve-fitting was carried out using WiRE 9.0 software provided by Renishaw. The position of the smaller feature also shows a red-shift (higher Stokes shifted wave-number) with increasing film-height; compare the positions indicated by orange and green arrows in Figure 4.31a & b, respectively. In Figure 4.31a & b spectra recorded at the same location on the substrate are plotted at different incident laser powers. The power dependence of the absolute intensity at the position of the maximum (indicated by black and blue arrows) and the side feature (indicated by orange and green arrows) of the spectra shown in Figure 4.31a & b are plotted in Figure 4.32. Clearly a linear dependence is seen not merely for the intensity of the overall maximum in the background but also for the smaller features observed on it. This confirms that the background emission is not due to a two photon process such as second harmonic generation or supercontinuum generation or a two-photon excited photoluminescence as these

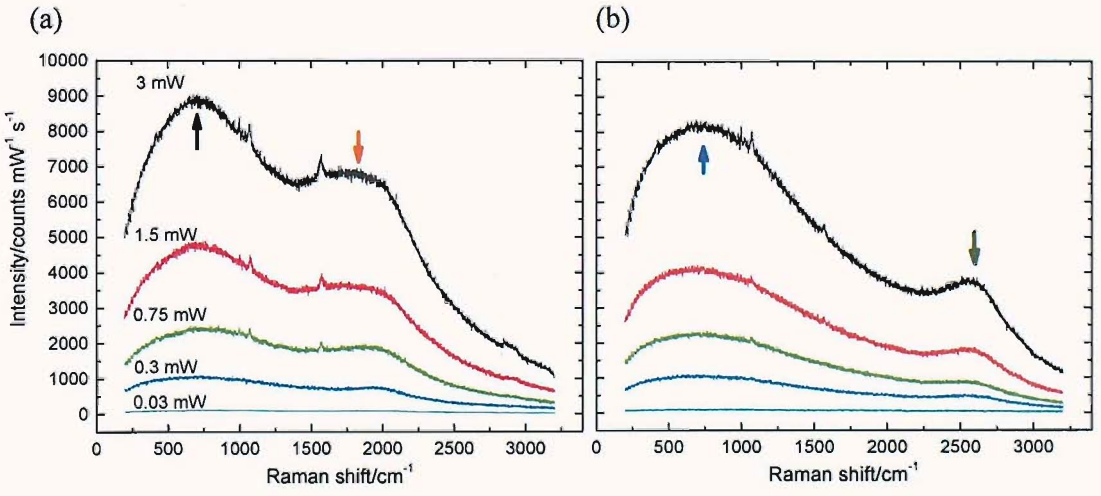

Figure 4.31 Spectra recorded with a 633 nm laser at (a) 0.52 *D* and (b) 0.60 D on D600 gold SSV substrates are shown as a function of laser power incident on the sample. The laser powers are indicated on top of each spectrum in (a) and the same sequence is followed in (b). The position of the overall maxima of the background and that of the next most prominent features are indicated by black & blue and orange & green arrows, respectively.

would cause the background to be non-linearly dependent on incident laser power.

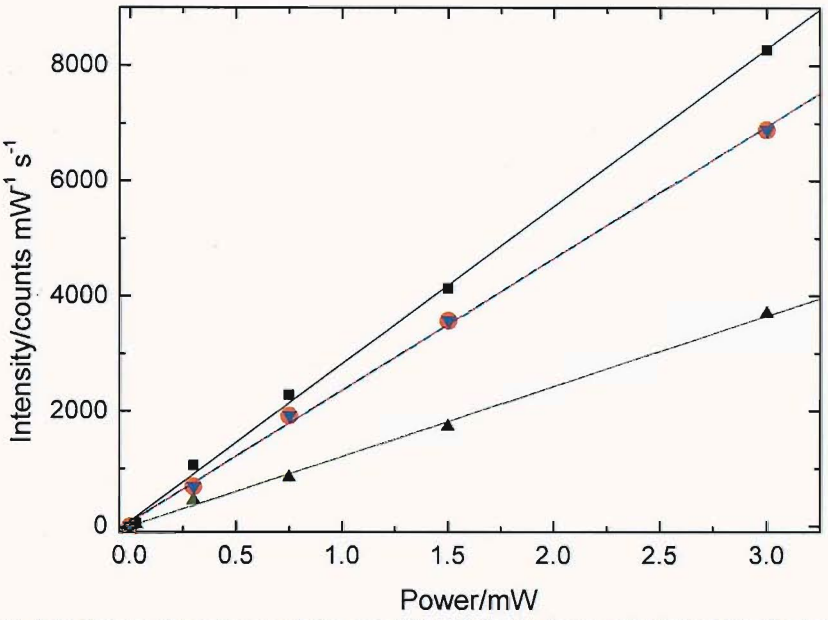

Figure 4.32 Power dependence of the intensity of the background plotted for the overall maximum (■ and▼) and the second feature (● and ▲) corresponding to spectra presented in Figure 4.31a & b (indicated by arrows of the respective colour). The lines drawn through the origin are guides to the eye.

4.4.2.1 Plasmon dependence

As also seen in the previous section some of the features on the background were observed to vary systematically with the film height of SSV substrates. This prompted the investigation of their dependence on the plasmonic absorption of the substrate, since plasmons also show a systematic (now fairly well understood) variation as a function of thickness of SSV films. Hence, the position of the overall maximum as well as that of any side features observed were extracted from the SERS spectra using curve fitting with WiRE 9.0 software provided by Renishaw. This was carried out as a function of film thickness on a series of graded substrates such as those utilized in section 4.3.5. The Raman shift position was converted to its absolute energy (wavelength) corresponding to the Stokes scattered radiation and overlaid on the integrated plasmon map of the same substrate. This is shown for D400, D600 and D800 graded gold substrates in Figure 4.33. The corresponding intensities relative to each other are also indicated by the size of the circle plotted for each point.

It can be observed that both the position of the broad maximum and that of the smaller side feature, if present, are closely related to the dispersion of plasmon modes across the thickness of the substrates. This is especially true more for the side feature which coincides closely with plasmon modes (Figure 4.33b & c) The position of the broad maximum is always red-shifted by about 0.15-0.2 eV with a

bit of variation compared to the laser excitation. The laser is indicated by the red dashed line in the maps. However, the most significant aspect is that the background shows a distinct maximum at the same locations as strong plasmonic absorptions on the substrates either matching with the laser excitation or the emitted radiation. Moreover, this enhancement profile is almost exactly same as that observed for SERS peaks shown in Figure 4.28. Hence, this confirms that the background is either a luminescence or a scattering process which is enhanced on being coupled with plasmons. Further, the red shift, though slightly variable, of the main background continuum with respect to the laser line suggests a non-radiative loss in energy. The variability in the position indicates that this loss involves the metal rather than the molecule because the metal has a continuum of states rather than discrete levels such as in a molecule. The breadth of the spectral continuum also suggests the involvement of metal in its generation. Nevertheless, the strong correlation of the background intensity with SERS points to a coupled or co-occurring process.

Furthermore, from the near infrared SERS experiments it was found that the background was present and does not vanish completely in NIR. Though the signal to background is much higher for the 1064 nm laser than with the 633 nm laser the broad continuum is seen nevertheless. Thus, it cannot be luminescence from the molecule as a 1064 nm laser would be unable to excite such a process. Again in the NIR it is seen that the highest background and SERS peaks are observed when the laser and the outcoming radiation coincides with strong plasmon absorption on the substrate as seen for SERS in Figure 4.29 confirming the involvement of plasmons in the enhancement of the background. The plasmon dependence is further evident with the observation of low backgrounds on Pd and Pt, which are weaker plasmonic metals than gold.

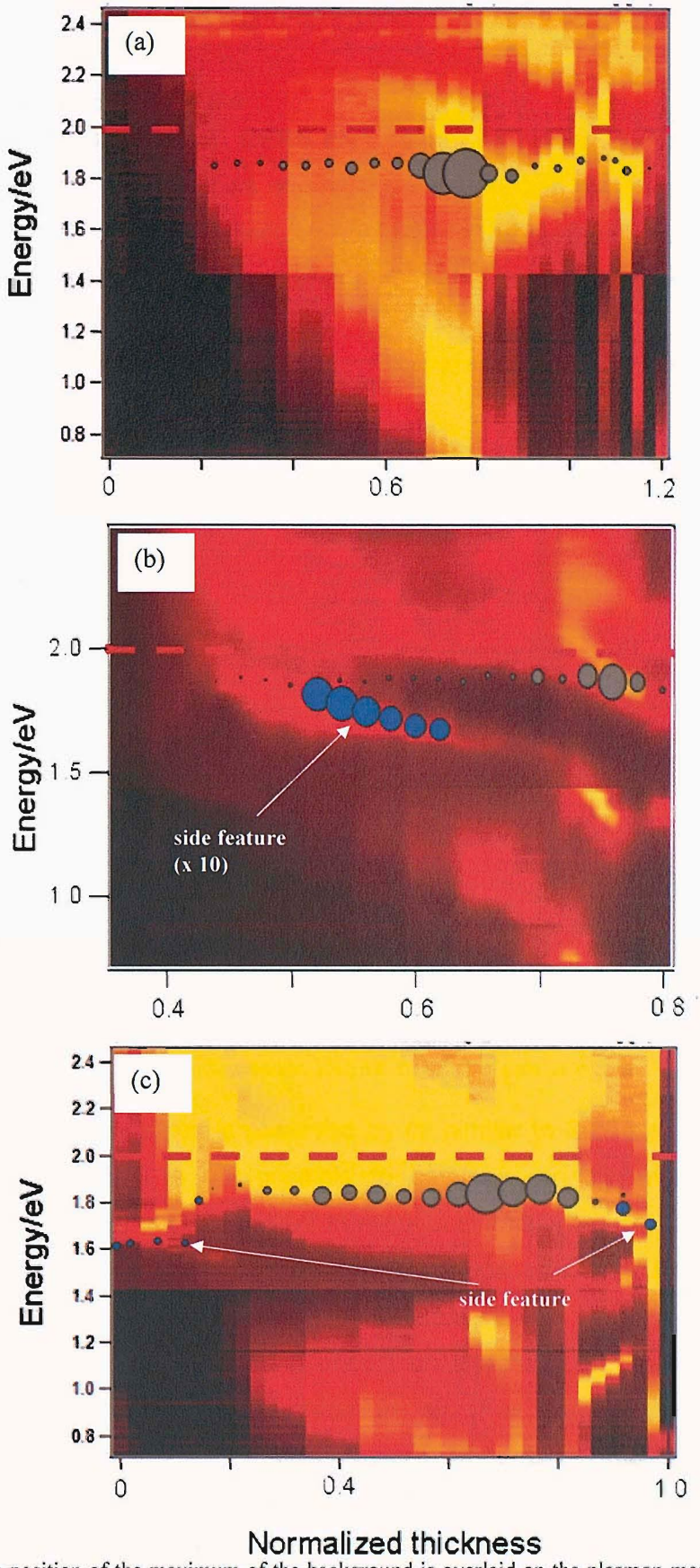

Figure 4.33 The position of the maximum of the background is overlaid on the plasmon maps for (a) D400, (b) D600 and (c) D800 graded substrates. The size (diameter) of the grey circles is proportional to the intensity of the background and is comparable between the three plots. The smaller blue circles represent the position and relative intensity of the next most prominent feature (marked by the white arrow in (b) & (c) above) observed in the background. The red dashed line represents the laser excitation with 633 nm laser.

4.4.3 Chemical dependence

The background observed in SERS also cannot be luminescence or scattering solely from the metal as it shows chemical dependence in that it is modulated by the presence or absence of molecules attached to the surface, as observed both in air and in solution. A strong correlation of the background with molecules

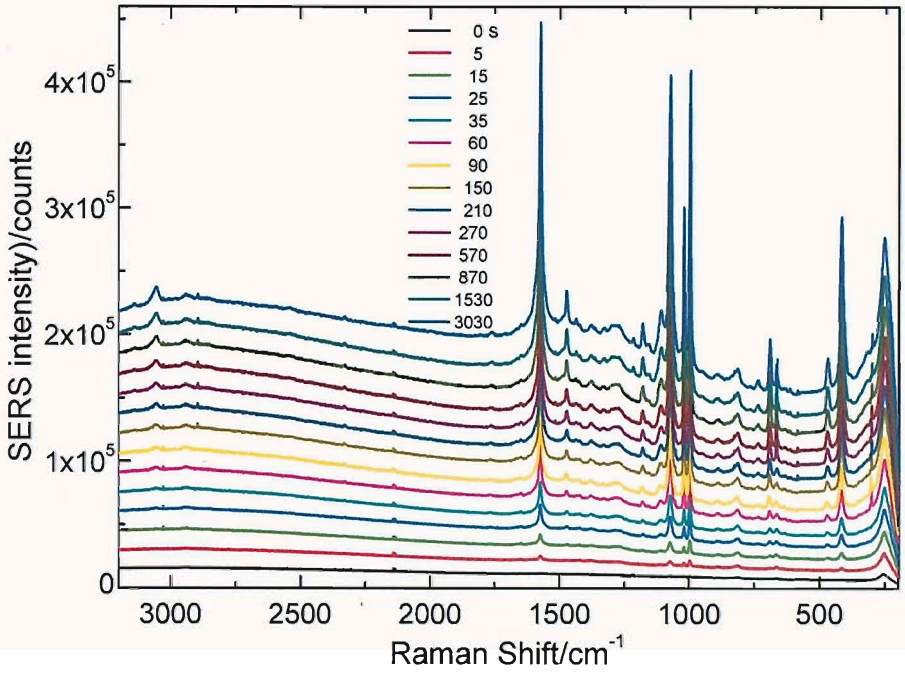

Figure 4.34 SERS spectra recorded on a silver SSV substrate after soaking the substrate in a 10 mM benzenethiol solution for different times (immersion times stated in the legend). After the specified time the substrate was washed with ethanol and dried under a stream of nitrogen. Spectra recorded with a 633 nm laser at 3 mW laser power with a single scan of 10 s. This data is credited entirely to M. E. Abdelsalam in our group.

adsorbed on SSV substrates is observed by us similar to SERS studies by other researchers [35, 36]. It is not possible to comment on the existence of the background with or without SER active molecules chemisorbed on SSV substrates since that necessitates experiments under ultra-high vacuum (UHV), for which experiments need to be carried out. Nevertheless, it has been observed that a dramatic increase in the background occurs on attaching SER active molecules such as benzenethiol on the surface in air. For example, on adsorbing benzenethiol on silver substrates for increasing amounts of time the background increases along with the SER peaks as shown in Figure 4.34; the sample was soaked in a 10 mM ethanolic solution of benzenethiol for a specified time, taken out and immediately rinsed thoroughly with ethanol and dried under nitrogen.

Apart from the above many experiments show that the background is correlated with the SERS on SSV substrates. However, the experiments in air have an uncertainty in that the metal-environment interface is less clear, for example, the reason why low background is observed on bare (without chemisorbed molecules such as benzenethiol) could be due a physisorbed water/solvent molecules used for cleaning etc. which are weak scatterers. Hence, the conclusion that a strong SER scatterer produces a high background is tempting but deferred to a later

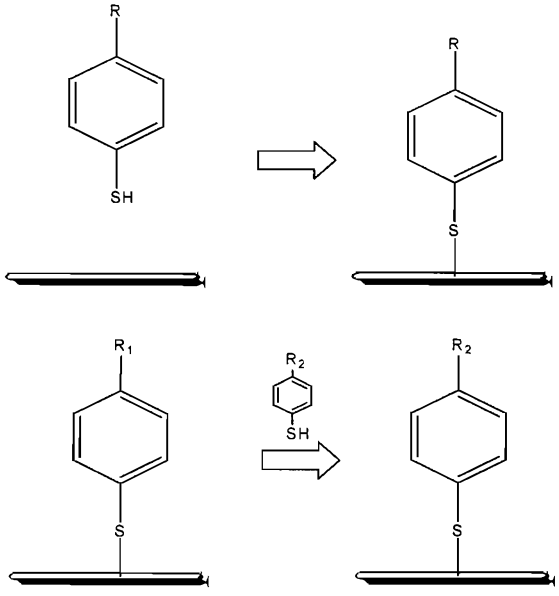

Figure 4.35. Scheme for studying the adsorption of thiols and their exchange on SSV substrates. Scheme depicted was used for monitoring the adsorption of thiols with SERS (top) and their exchange (bottom) using SERS. This allowed the study of the effect of adsorption of molecules and the nature of substituent (R_1 and R_2) on the background observed in SERS spectra. R1 and R2: H, -NO_2, -COOH, -OCH_3.

discussion in this section. For further confirmation of the correlation of the background with SERS active molecules on SSV substrates such that the interface is well defined, experiments were carried out in solution. To reduce any uncertainties arising out of adsorption of ions, the experiments were carried out in deionized water. Also, to negate the affect due to any luminescence from the molecule itself SERS was obtained with a 785 nm laser. The system of thiol adsorption and exchange shown in Figure 4.35 was chosen because of its simplicity and well defined SER spectra of the molecules. The experiment was carried out in a traditional electrochemical SERS cell with the substrate near the optical window facing the laser [37]. The volume of water was fixed at 30 mL. 100 microlitres of a 30 mM thiol solution in water, where possible, or ethanol was introduced at a distance of ~5 cm behind the surface thus, allowing the molecules to slowly diffuse towards the surface and become adsorbed, while spectra were cquired in the kinetic mode every 30 s. Two representative sets of spectra are

shown in Figure 4.36a and b for adsorption of nitro-benzenethiol and exchange of the adsorbed *p*-nitro-benzenethiol by *p*-methoxy-benzenethiol, respectively on gold SSV substrates. The intensity for the maximum of the background or at a particular wave-number (well clear of peaks) was plotted against the extracted intensity of prominent and characteristic SERS peaks for the molecule being adsorbed or displaced.

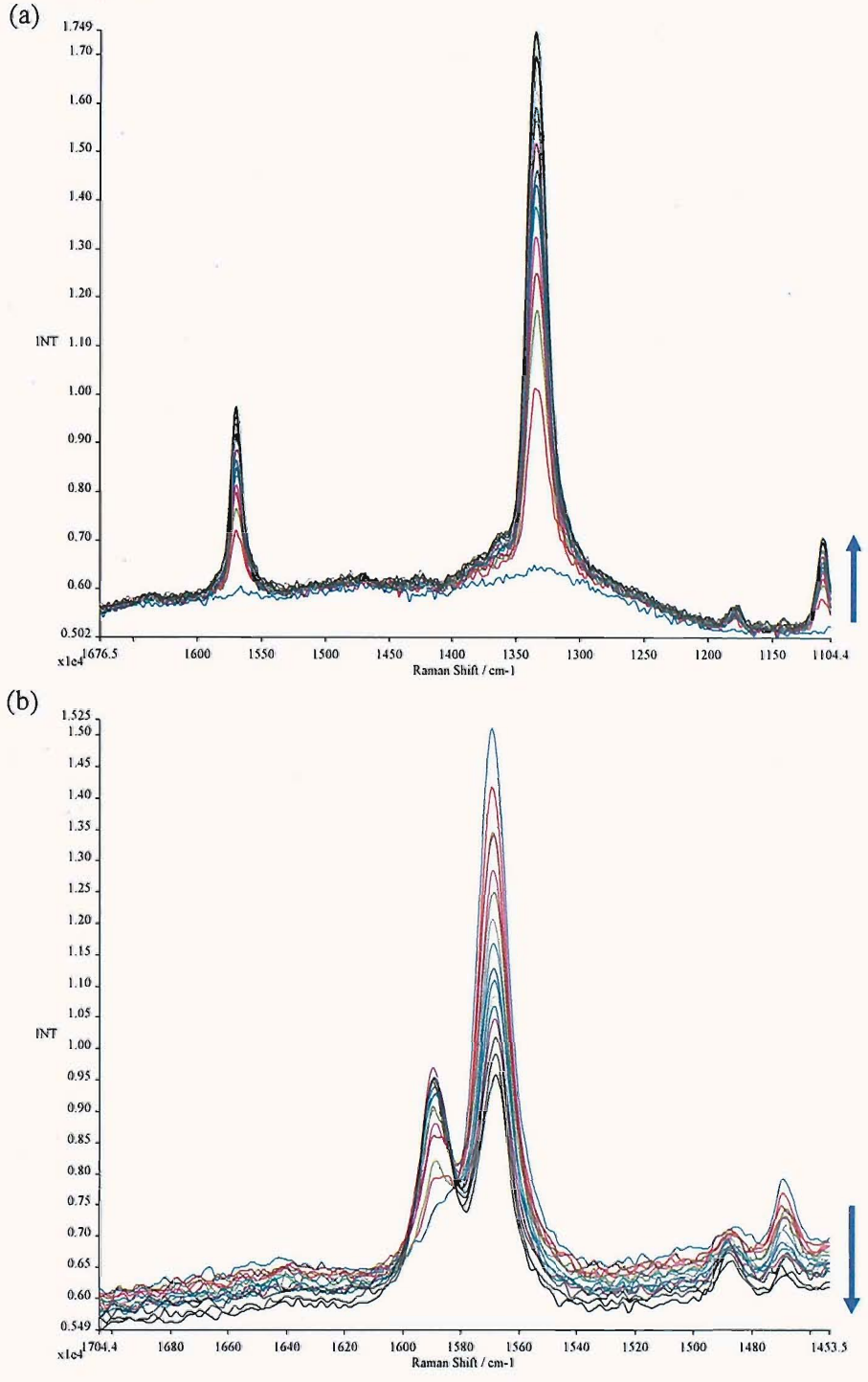

Figure 4.36 SER spectra on gold SSV substrates recorded every 30 s for (a) adsorption of nitro-benzenethiol and (b) exchange of adsorbed *p*-nitro-benzenethiol by *p*-methoxy-benzenethiol in water. Laser: 785 nm, 100 mW, 10 accumulations of 1 s exposure. The blue arrow indicates the progress of experiment beginning at *T* (time) = 0

4.4.3.1 Direct adsorption

With experiments studying the adsorption of thiols from their solutions in water on gold SSV substrates the magnitude of the SERS peaks for the species being chemisorbed on the surface slowly changed with time. However, instead of a monotonic increase, the concomitant background either decreased or increased depending on the molecule. To exemplify, with adsorption of nitro-benzenethiol the background was found to increase while with benzenethiol the background was found to decrease during adsorption from an aqueous solution. This is presented in Figure 4.37. The correlation of the background with molecules is very clear.

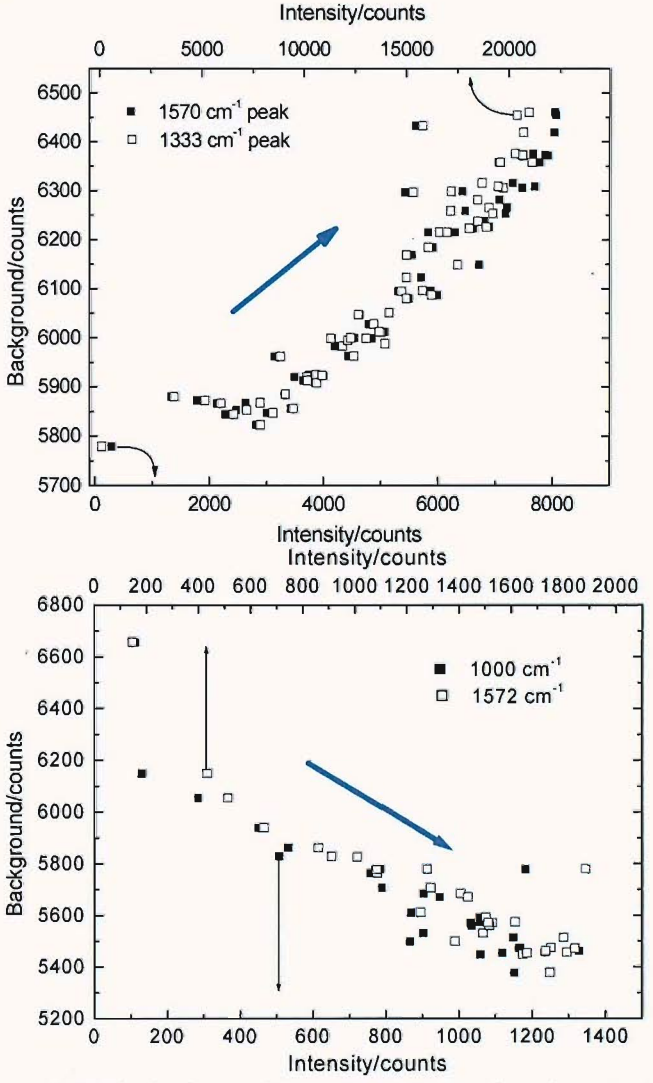

Figure 4.37 The background intensity plotted against the extracted intensity of two peaks each for (top) nitro-benzenethiol and (bottom) benzenethiol during their adsorption on gold SSV substrates. The blue arrow indicates the direction of data acquisition with time.

Benzenethiol itself resulted in a decrease in the background in solution compared to that in air. It was postulated that an increase or decrease of the background would depend on the nature of the molecule being displaced. On an untreated

substrate the behaviour of the background would be a result of displacement of water molecules at the interface by the adsorbing species but in other cases it would be with respect to the molecules already present on the surface. Therefore, an easier experiment to interpret in terms of the effect of molecules on the background, whether increase or decrease would be to study the displacement of one thiol by another employing SERS.

4.4.3.2 Exchange of thiols

As mentioned earlier, a series of para-substituted thiols were chosen for the systematic investigation of exchange of thiols on SSV substrates. A monolayer of a substituted benzenethiol was adsorbed by immersing the substrate in its 10 mM ethanolic solution for 1 h. Thereafter, it was thoroughly rinsed with ethanol and

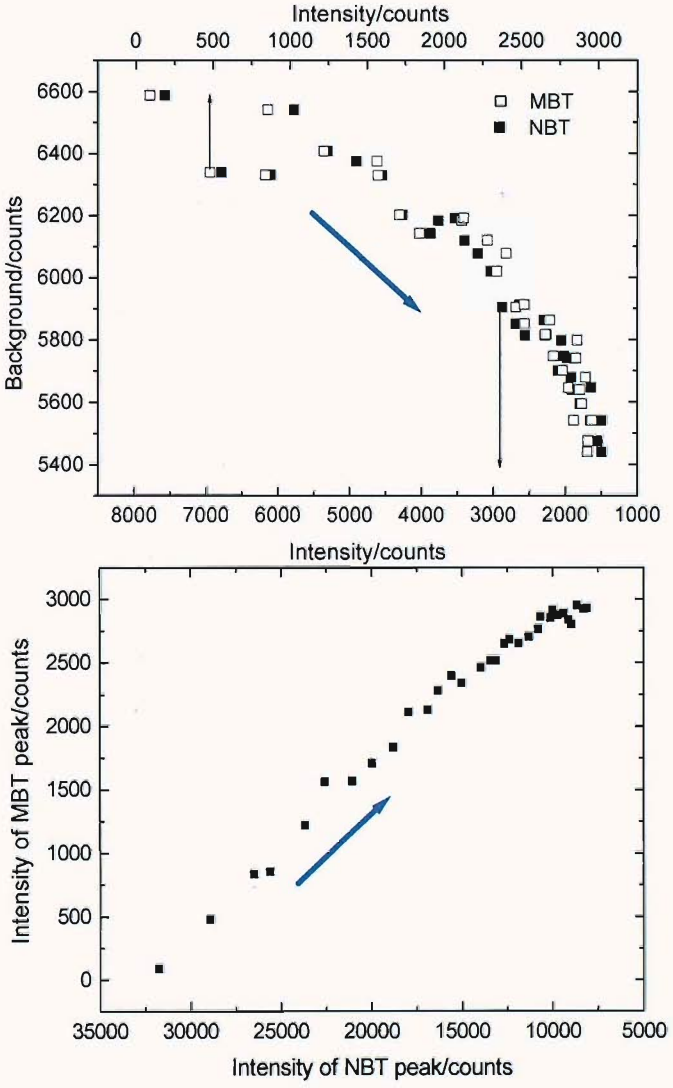

Figure 4.38 (Top) Background intensity plotted versus the decreasing nitro-benzenthiol (NBT) and increasing methoxy-benzenethiol (MBT) peak intensity. Bottom shows the intensity of the 1589 cm^{-1} MBT peak plotted against the 1333 cm^{-1} NBT peak. The blue arrow indicates the sequence of observations with increasing time.

water, sequentially and utilized in the exchange experiments. In Figure 4.38 results with a *p*-nitro-benzenethiol coated substrate is presented, wherein the adsorbed molecule is displaced by 4-methoxy-benzenethiol. It can be readily seen that the background decreases as the displacement progresses with time; the 4-methoxy-benzenethiol peaks increase in magnitude while that of nitro-benzenethiol decrease. Also, the plot for 4-methoxy-benzenethiol versus 4-nitro-benzenethiol peaks is almost linear (Figure 4.38 bottom). This indicates that there is one-on-one place exchange between the two thiols [38, 39]. The only difference between the two molecules is the nature of their para substituent, which is electron donating in the case of methoxy-benzenethiol and electron withdrawing for nitro-benzenethiol.

The idea of the dependence of increase or decrease of the background on the electron withdrawing or electron donating nature of the molecule, respectively, was tested further by using *p*-nitro-benzenethiol and *p*-carboxy-benzenethiol. The results are presented in Figure 4.39. In one case the substrate was initially coated with *p*-carboxy-benzenethiol and thereafter, the displacement reaction carried out with *p*-nitro-benzenethiol. In the second case *p*-nitro-benzenethiol was chemisorbed on the surface and then an exchange reaction carried out with *p*-carboxy-benzenethiol. Results from the experiments are completely consistent with each other; on starting with a carboxy-benzenethiol coated SSV substrate and carrying out the exchange reaction with nitro-benzenethiol the background increases and on reversing the conditions the background decreases. The exchange is again well supported by concurrent variation in the SERS peak intensities of the two species as expected.

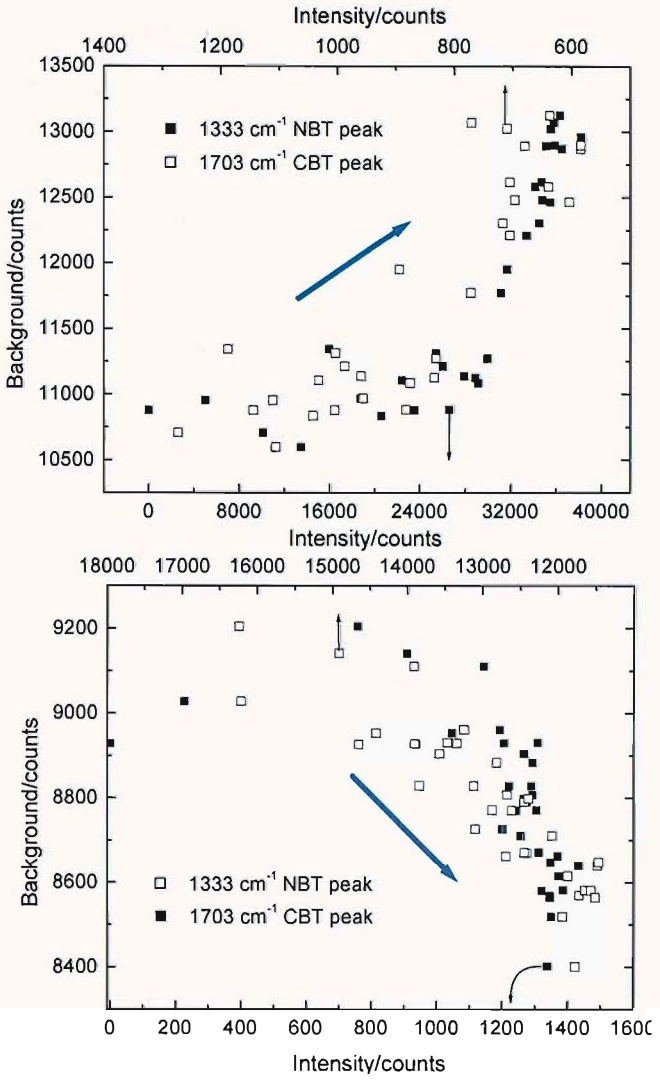

Figure 4.39 Background intensity plotted against the peak intesities in an exchange reaction (top) starting with carboxy-benzenethiol (CBT) displaced by nitro-benzenethiol (NBT) and starting with NBT and displaced by CBT. The blue arrow indicates the direction of progress of reaction with time.

From the results for the adsorption and exchange reaction of various substituted benzenethiols presented above, the hypothesis that an electron withdrawing group results in an increase in background while an electron donating group causes a decrease appears plausible. In effect these results suggest the role of charge interactions between the molecule and the metal as a cause for the affect on the background observed above. This could be easily tested further by monitoring the background intensity with increasing ion concentrations. The electric double layer would get modified and compressed with increasing ionic strength and hence, the field intensity would increase. The result should be similar to that observed for the exchange of thiols in which an electron donating molecule is adsorbed on the surface.

Therefore, an experiment was carried out with sodium chloride solutions with increasing concentrations. Chloride ions are known to specifically adsorb on gold resulting in negatively charged surfaces. With increasing ionic strength the double layer reduces in thickness thus increasing the effective electric field at the surface, which also manifests as a shift of the potential of zero charge of gold to more negative values [40]. Hence, if the postulation that electron donation towards the metal decreases the background and electron withdrawal increases the background is true then a decrease in the background intensity should be observed with increasing chloride concentrations at open circuit potentials. This is exactly what was observed as shown in Figure 4.40. The maximum intensity is plotted against log of the concentration and a decreasing trend is clearly visible. The spectra are plotted in the bottom graph of the panel. Furthermore, the position of the maximum intensity is found to decrease by 30-40 cm^{-1}. For this data

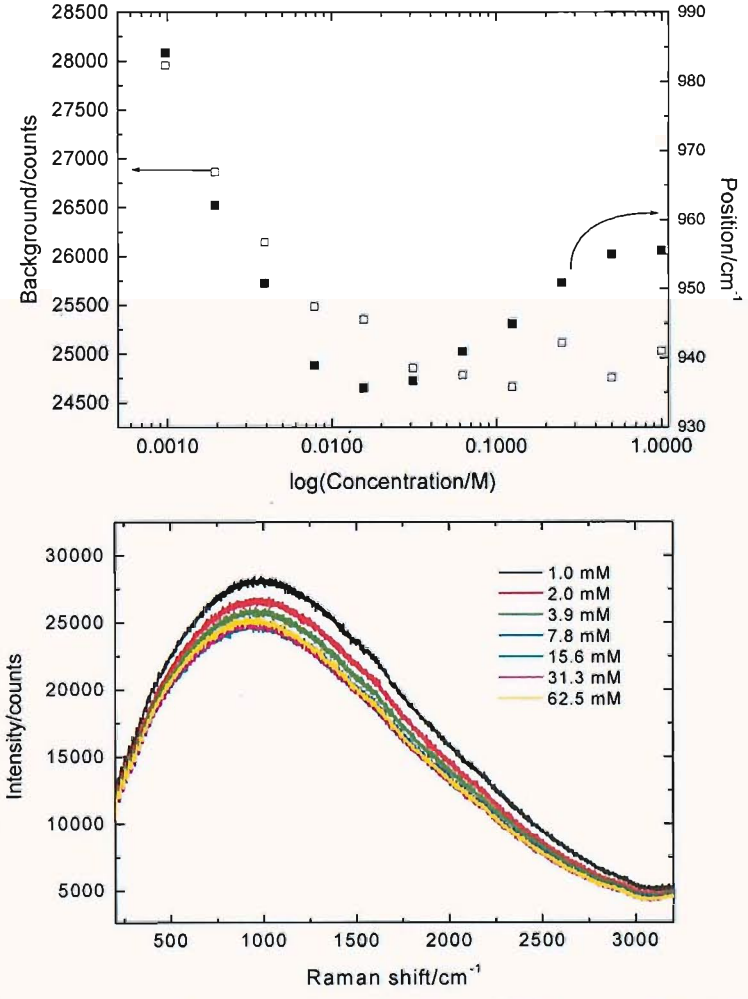

Figure 4.40 (Top) Variation of background with increasing ionic strength in sodium chloride aqueous solutions. (Bottom) The spectra at each concentration recorded with a 633 nm laser. 3 mW laser power, single accumulation of 10 s.

recorded with a 633 nm laser this corresponds to a difference of ~0.01 eV in energy; thus the shift is not significant in terms of absolute energy but suggests a quenching mechanism at work.

Another observation which reinforces the chemical dependence is the case of molecules which have an electronic resonance with the excitation laser. In this case, peaks even stronger than in SERS are observed and the effect is called surface-enhanced resonance Raman scattering (SERRS). SERRS is discussed in detail in the next chapter. Apart from the peaks the background also shows a huge enhancement. At first glance, this background could be attributed to luminescence akin to fluorescence. Hence, this aspect was investigated by choosing two molecules which are essentially the same, with almost similar excitation maxima, therefore in resonance with a 633 nm laser. One of them is fluorescent (Cy5) and the other (Cy5Q) is not by virtue of a quencher moiety attached on the chromophore. Cy5Q does not display any fluorescence in solution due to the internal quencher (see Figure 4.41). The experiment was done carefully using the same substrate split into two so that the morphology of the substrate and hence,

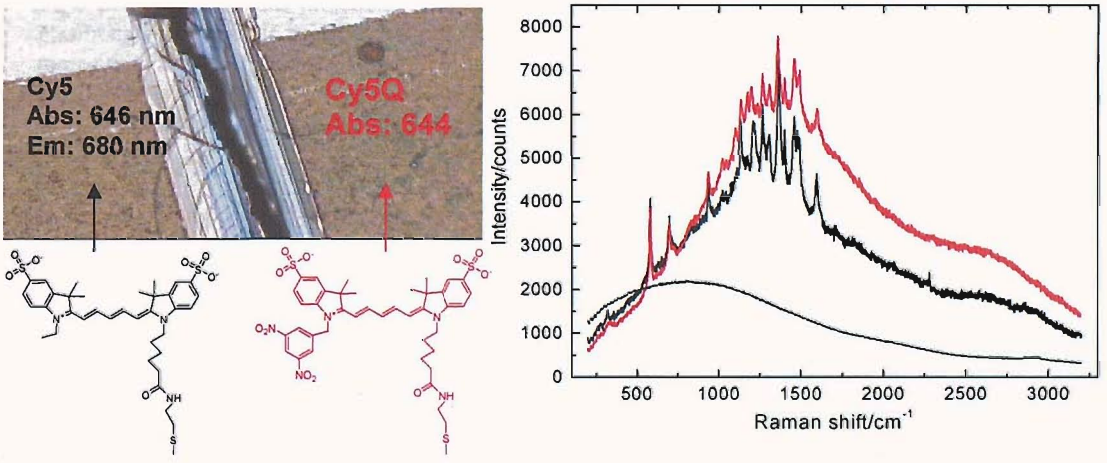

Figure 4.41 Cy5 and Cy5Q attached on the split pieces of the same gold SSV substrate (D600, t = 0.8). The structures and the substrate utilized are shown on the left and the spectra of Cy5 (solid black), Cy5Q (red) and the background before attaching the molecules (dashed black) are shown in the graph on right.

the surface enhancement is identical. However, on gold SSV substrates in air both showed similar and enhanced backgrounds which can be seen in Figure 4.41. It is well known that fluorescence is quenched on metal surfaces [23]. Therefore, this fact and the observation that both the molecules, without and with the internal fluorescence quencher show almost similar backgrounds confirms that the broad continuum is definitely not fluorescence type of luminescence directly from the molecule.

4.4.4 Model for background mechanism

Based on the above experiments and plethora of observations with SSV substrates in our group, a model is drawn proposing the mechanism for the background observed in SERS experiments. This is depicted in a band energy diagram of the metal in association with the HOMO-LUMO of a molecule at the interface in Figure 4.42. In summary, the process is described as an optical

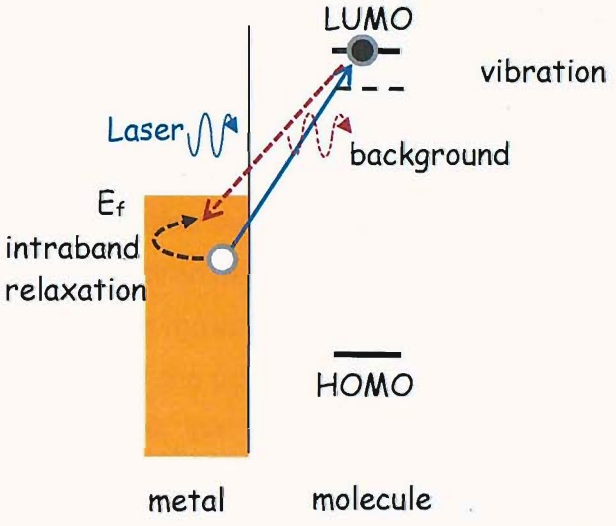

Figure 4.42 Metal and molecule band energy diagram at the interface. The laser excites (via plasmons) electron-hole pairs, which can also be described as photoluminescence from the metal to the molecule. This can lose energy to a vibration as in Raman scattering and then recombine with the hole. However, recombination can occur directly with an electron which undergoes intra-band relaxation towards the Fermi level resulting in the background.

excitation mediated by plasmons on the metal; this leads to formation of a hole and correspondingly an excitation of an electron to the molecule which can then scatter losing energy to a vibration of the molecule, to give SERS, or recombine with a hole relaxing upwards toward the Fermi level, producing the background continuum.

This model is able to explain the plasmon dependence or rather enhancement of the background by plasmon modes; since the larger the coupling (due to plasmons) to the molecule the larger would be the electron-hole pair formation. Similarly, the photon emitted on recombination radiates more efficiently if a plasmon mode exists at that frequency, hence we see side bands in the overall broad continuum of the background. The variable red shift of the background maximum is explained by the variable speed of relaxation of the hole before it recombines. The observation of a background even with near infrared radiation (apart from that it is enhanced by plasmons) can be explained by the concept that the hole can be generated from anywhere in the metal band. So a higher frequency laser is able to form excitons from deep inside metal conduction band

while a near infrared would only be able to excite electron hole pairs closer to the Fermi level than the higher frequency laser.

Further the proposed model successfully takes into account the observation that the background and SERS occur concurrently. It is also able to explain the modulation of the background by molecules and ions, by virtue of the affect on the position of the HOMO-LUMO with respect to the Fermi level. Also, these species at the interface would affect the electric field at the metal surface, favouring partial electron donation or withdrawal and thus the energy loss processes. Hence, an increase or decrease in the background will also depend on the nature of molecules being displaced and their relative electronegativity. The suggestion of a quenching like mechanism is not ruled out and fits into the model as well by the fact that a molecule with higher electron density would aid the recombination of the hole while a partially electropositive molecule would aid the formation of a hole in the metal band. Also the shifting of the position of the background maximum with increasing ionic strength reinforces this assertion as higher electron donation would reduce the lifetime of the hole and hence, shift the emission to higher energy. The case of high background in molecules possessing an electronic resonance with the excitation laser is explained by electronic excitation adding to the recombination of the holes in the metal, which otherwise would have non-radiatively dissipated, besides the plasmonic enhancement by the substrate. The huge background enhancement observed in a SERRS experiment is also consistent with the suggested model; there is increased HOMO-LUMO excitation and hence, increased throughput for the recombination process. This is supported by the observation that the quencher on a SERRS molecule still produces similar intensity for the background as the molecule without it (see Figure 4.41).

The Fermi level of the metal itself can be modulated by changing the electrochemical potential of the substrate in solution. Hence, it is expected that the background would show a shift in the position as well as intensity based on similar arguments extended above. This has been observed in several experiments in our group including those by myself. However, it is currently being explored further by carrying out well directed experiments by other group members and hence, is not discussed at present.

So far in this chapter only Stokes scattered SERS results have been presented including those on the background and the model was drawn to explain the respective observations. Therefore, it would be pertinent to test the model with the

perspective of anti-Stokes SERS. Since, the background continuum is generated by electron-hole pair excitation and the subsequent recombination, which would always be red-shifted from the excitation (since, the holes will always tend to relax towards the Fermi level) the model shown in Figure 4.42 predicts no such background in an anti-Stokes experiment. This was verified with a one-off experiment (with another instrument at University of Cambridge as our instrument

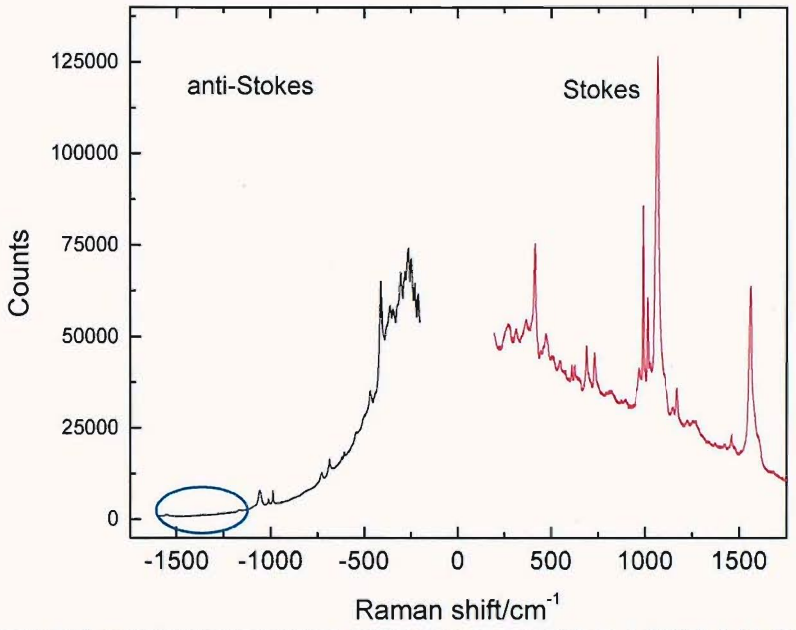

Figure 4.43 Anti-Stokes and Stokes SERS spectra recorded on a D600, 0.65 *D* gold SSV substrate. Spectra recorded with a 785 nm laser, 100 mW laser power and single accumulation with 120 s collection times for anti-Stokes and 30 s collection time for Stokes. The blue oval indicates where background similar to the corresponding region on Stokes side is not observed.

does not have the appropriate filters for recording anti-Stokes) and indeed no commensurate background was found on comparing similar wave-number regions on the respective spectra as shown in Figure 4.43. This indeed supports the robustness of the proposed model. The peculiar kind of background observed in the anti-Stokes spectrum presented in Figure 4.43, which increases after every SERS peak and seems to increase exponentially near the laser wavelength, may be generated due to e'-hole recombination processes excited by the scattered radiation itself. This is at best speculation and clearly needs further investigation.

Finally, there is a major prediction of our model which remains untested, that is, with no molecules on the surface there should be no background. A corollary to this prediction is that our model necessitates intimate contact between the metal and the molecule for the molecule-metal electron-hole pair formation. Carrying experiments under UHV on bare SSV substrates could be difficult, since it is difficult to 'completely' get rid of any adsorbed molecule on the interface or from

the atmosphere surrounding the substrates (contamination from pump oil for example). Another, possible way of testing could be by spatially offsetting the molecule from the surface by controlled oxidation of the surface using plasma techniques or insulating the surface by electrochemical control and investigating SERS in solution.

4.5 Conclusions

In this chapter it has been shown that SSV substrates, fabricated with different metals, display a variety of optical properties. It has been demonstrated by studying their reflectance properties that they exhibit rich plasmonic behaviour, which tunes with the film height and sphere diameter of the template employed to fabricate SSV substrates. This plasmonic behaviour can be studied both by a reflectance microscope or an angle resolved goniometer setup, with the former having the advantage of simplicity and the latter that of detail. It has been shown that SSV substrates produce stable and reproducible SERS as a function of sphere diameter and film height. Further, it has been established that combinatorial mapping of the substrates is a powerful tool for studying plasmons as well as SERS on these structured films.

It is clear from the results presented in this chapter that it is possible to control the generation of suitable plasmon modes and thereby SERS by varying parameters like the sphere size and film height. With respect to the latter control, electrodeposition appears much more powerful than other techniques of metal deposition like nanoparticle-assisted [41, 42] or vapour deposition [43, 44]. In addition, our high resolution FESEM images show that electrodeposited films are much smoother than the vapour deposited gold. The flat evaporated gold films yield no SERS, hence it can be concluded that it is the macro-structure of the templated films which is responsible for SERS rather than generation of nanometer scale surface roughness or 'hot spots'. This option of tuning plasmons on SSV substrates offers an unprecedented tool for designing and tailoring substrates for obtaining SERS with a particular excitation source and a target analyte molecule in a particular medium.

Lastly, SERS signals show direct correlation with the plasmonics of these structures. It confirms that plasmon resonance matching at both the ingoing and outgoing laser wavelengths is a necessary condition for obtaining maximum SERS signals in air or aqueous medium. Due to the well studied plasmonics of the

substrate, the plasmon modes which are responsible for the field enhancement leading to SERS have been identified. It has also been shown that instead of one universal mode there are a number of plasmon modes which can generate comparable SERS. However, the relative enhancement depends on the field profiles generated near the surface. The scalability of the plasmon engineering approach for maximum SERS from visible to NIR region and in different media has been established not only for gold but also for catalytically important transition metals such as palladium and platinum.

Furthermore, it has been possible to study the background accompanying SERS systematically largely because of the reproducibility of SSV substrates. It has been found that the background enhancement also is related to plasmon absorptions on the substrates. The effect of molecules has also been probed in detail where it is found that in solution electron withdrawing groups increase the background while electron donating molecules decrease it. A model has been proposed which takes into account these observations.

Finally it should be mentioned that all of the current progress on the understanding on SSV substrates has come about due to a long standing collaboration between our group and our colleagues in Physics. In some cases the theory developed for the plasmonics of SSV substrates predicted the optimum geometry and experiments verified the hypothesis; in other cases the theory itself had to be improved by the observations out of SERS experiments. It has been this two way exchange of ideas and collaboration which has been responsible for a fair understanding to enable development of analytical applications based on SERS on these substrates.

4.6 References

[1] S. Cintra, M. E. Abdelsalam, P. N. Bartlett, J. J. Baumberg, T. A. Kelf, Y. Sugawara, and A. E. Russell, Faraday Discuss. 132:191 (2006).

[2] P. Hendra, C. H. Jones, and G. M. Warnes, Fourier Transform Raman Spectroscopy - Instrumentation and Chemical Applications, Ellis Horwood Limited, 1991.

[3] P. N. Bartlett, P. R. Birkin, and M. A. Ghanem, Chem. Commun.:1671 (2000).

[4] P. N. Bartlett, T. Dunford, and M. A. Ghanem, J. Mater. Chem. 12:3130 (2002).

[5] P. N. Bartlett, P. R. Birkin, M. A. Ghanem, and C. S. Toh, J. Mater. Chem. 11:849 (2001).

[6] M. Moskovits, J. Raman Spectrosc. 36:485 (2005).

[7] J. J. Baumberg, T. A. Kelf, Y. Sugawara, S. Cintra, M. E. Abdelsalam, P. N. Bartlett, and A. E. Russell, Nano Lett. 5:2262 (2005).

[8] T. A. Kelf, Y. Sugawara, R. M. Cole, J. J. Baumberg, M. E. Abdelsalam, S. Cintra, S. Mahajan, A. E. Russell, and P. N. Bartlett, Phys. Rev. B 74 (2006).

[9] T. Kelf, in School of Physics, University of Southampton, Southampton, 2005.

[10] R. M. Cole, Y. Sugawara, J. J. Baumberg, S. Mahajan, M. Abdelsalam, and P. N. Bartlett, Phys. Rev. Letters 97 (2006).
[11] S. Coyle, M. C. Netti, J. J. Baumberg, M. A. Ghanem, P. R. Birkin, P. N. Bartlett, and D. M. Whittaker, Phys. Rev. Letters 8717 (2001).
[12] R. M. Cole, J. J. Baumberg, F. J. Garcia de Abajo, S. Mahajan, M. Abdelsalam, and P. N. Bartlett, Nano Lett. 7:2094 (2007).
[13] S. Lal, N. K. Grady, J. Kundu, C. L. Levin, J. B. Lassiterde, and N. J. Halas, Chem. Soc. Rev. 37:898 (2008).
[14] S. W. Han, H. J. Lee, and K. Kim, langmuir 17:6981 (2001).
[15] T. H. Joo, M. S. Kim, and K. Kim, J. Raman. Spectrosc. 18:57 (1987).
[16] M. Moskovits and J. S. Suh, J. Phys. Chem. 88:5526 (1984).
[17] A. Otto and M. Futamata, in Surface-Enhanced Raman Scattering - Physics and Applications, Vol. 103 (K. Kneipp, M. Moskovits, and H. Kneipp, eds.), Springer-Verlag, Berlin, 2006, p. 147.
[18] S. Cintra, M. Abdelsalem, P. N. Bartlett, J. J. Baumberg, T. Kelf, Y. Sugawara, and A. E. Russell, Faraday Discussions 132:1 (2005).
[19] L.-J. Wan, M. Terashima, H. Noda, and M. Osawa, J. Phys. Chem. B 104:3563 (2000).
[20] Z. Q. Tian, B. Ren, and D. Y. Wu, J. Phys. Chem. B 106:9463 (2002).
[21] J. C. Love, L. A. Estroff, K. J. K, R. G. Nuzzo, and G. M. Whitesides, Chem. Rev. 105:1103 (2005).
[22] J. Y. Gui, D. A. Stern, D. G. Frank, F. Lu, D. C. Zapien, and A. T. Hubbard, Langmuir 7:955 (1991).
[23] M. Moskovits, Rev. Mod. Phys. 57 (1985).
[24] A. Otto, I. Mrozek, H. Grbhorn, and W. Akemann, J. Phys.: Condens. Matter 4:1143 (1992).
[25] A. Otto, Surface Sci. 92:145 (1980).
[26] A. Otto, J. Timper, J. Billman, G. Kovacs, and I. Pockrand, Surface Sci. 92:L55 (1980).
[27] J. P. Heritage, J. G. Bergman, A. Pinczuk, and J. M. Worlock, Chem. Phys. Lett. 67:229 (1979).
[28] J. I. Gersten, R. L. Birke, and J. R. Lombardi, Phys. Rev. Letters 43:147 (1979).
[29] E. Burstein, Y. J. Chen, C. Y. Chen, S. Lundquist, and E. Tosatti, Solid State Commun. 29:567 (1979).
[30] T. E. Furtak and J. Reyes, Solid State Commun. (1980).
[31] H. Ueba, J. Chem. Phys. 73:725 (1980).
[32] E. Dulkeith, T. Niedereichholz, T. A. Klar, J. Feldmann, G. v. Plessen, D. I. Gittins, K. S. Mayya, and F. Caruso, Phys. Rev. B 70:205424 (2004).
[33] Y. Maruyama and M. Futamatab, 412:65 (2005).
[34] I. Tamitake, B. Vasudevanpillai, I. Mitsuru, K. Yasuo, H. Kazuhiro, I. Akifumi, and O. Yukihiro, J. Chem. Phys. 124:134708 (2006).
[35] C. Y. Chen and E. Burstein, Bull. Am. Phys. Soc. 24:341 (1979).
[36] A. A. Moore, M. L. Jacobson, N. Belabas, K. L. Rowlen, and D. M. Jonas, J. Amer. Chem. Soc. 127:7292 (2005).
[37] M. Fleischmann, P. J. Hendra, and A. J. McQuillan Chem. Phys. Lett. 26:163 (1974).
[38] R. Hong, J. M. Fernandez, H. Nakade, R. Arvizo, T. Emrick, and V. M. Rotello, Chem. Commun.:2347 (2006).
[39] A. Kassam, G. Bremner, B. Clark, G. Ulibarri, and R. B. Lennox, J. Amer. Chem. Soc. 128:3476 (2006).
[40] A. J. Bard and Faulkner, Electrochemical Methods: Fundamentals and Applications, John Wiley & Sons, Inc., 1996.
[41] P. M. Tessier, O. D. Velev, A. T. Kalambur, A. M. Lenhoff, J. F. Rabolt, and E. W. Kaler, Adv. Mater. 13:396 (2001).

[42] P. M. Tessier, O. D. Velev, A. T. Kalambur, J. F. Rabolt, A. M. Lenhoff, and E. W. Kaler, J. Amer. Chem. Soc. 122:9554 (2000).
[43] J. C. Hulteen, D. A. Treichel, M. T. Smith, M. L. Duval, T. R. Jensen, and R. P. Van Duyne, J. Phys. Chem. B 103:3854 (1999).
[44] T. R. Jensen, G. C. Schatz, and R. P. Van Duyne, J. Phys. Chem. B 103:2394 (1999).

Chapter 5

5 Surface enhanced resonance Raman scattering

5.1 Introduction

Surface-enhanced resonance Raman scattering (SERRS) was demonstrated by Jeanmarie and Van Duyne in their seminal paper in 1977 [1]. When the incident laser is in resonance with an electronic transition of a molecule in proximity to a surface-enhancing substrate, the cross-section of the molecule is greatly enhanced leading to even larger enhancements than observed in SERS itself. SERS enhancements of the order of 10^6 or greater are routinely reported. The SERS and resonance effects are said to be multiplicative and can give overall intensity enhancements for SERRS in the range of 10^4 to 10^8 [2-4]. The use of SERRS even offers the possibility of single-molecule detection [5, 6] wherein enhancements of the order of 10^{14} are reported.

The extreme sensitivity of SERRS giving molecule specific information is unparalleled amongst all analytical techniques. This makes it ideal for the study of trace materials such as biomolecules. Thus SERRS has been used to study heme proteins [7], to study the mechanism of electron transfer in cytochromes [8], and more recently for trace detection of DNA [9, 10] and enzyme activity [11]. The sensitivity of SERRS exceeds that of fluorescence, which is currently the most common technique employed for studying biomolecules. That SERRS rivals or even betters fluorescence in its sensitivity has been proven theoretically [12] and experimentally [13]. SERS and SERRS (SER(R)S) have another immense advantage over fluorescence in that the signals have extremely small line-widths compared to the broad spectra of fluorescence emission; and hence it is possible using SER(R)S labels to carry out multiplexed detection [14].

Despite the many advantages of SERRS, commercial exploitation has been elusive, primarily due to the irreproducibility of the substrates. The bulk of the work on SER(R)S has been carried out using electrochemically roughened silver electrodes and colloidal silver nanoparticles. Over the last decade researchers have focussed on discovering and improving methods for fabricating reproducible substrates for SER(R)S. Amongst these vapour deposited silver films [15] and silver colloids [16] have been the most heavily researched. There are relatively few [10, 17] reports of SERRS on gold substrates. Nevertheless gold is attractive as a substrate because, although the surface enhancements are ~10 times less than

for comparable silver surfaces, gold surfaces are more stable than their silver counterparts.

5.2 Overview

In this chapter SERRS and its reproducibility on gold sphere segment void substrates is described. The enhancement provided by SERRS over and above that from SERS is also demonstrated by using molecules from the family of indocarbocyanine dyes. Instead of varying the excitation energy this approach allows keeping the laser excitation at a fixed wavelength; in this study at 633 nm. Cy3, Cy5 and Cy7 were chosen as they are common fluorophores used in DNA analysis and are almost identical in structure except that the linking bridge in Cy5 is one ethylene unit longer than in Cy3 and that in Cy7 is one ethylene unit longer than in Cy5 (see Figure 5.3). Results for Cy3, Cy5 and Cy7 are presented in this chapter though the discussion is mainly centred on Cy3 and Cy5. Only Cy5 is resonant with the 633 nm laser excitation used while Cy3 is completely out of resonance and Cy7 is in pre-resonance. In the experiments described the dyes are covalently attached to the gold surface. The surface coverage of Cy3 and Cy5 molecules was measured electrochemically using cyclic voltammetry. This permitted the calculation of the corresponding enhancement factors for SERRS over and above SERS by comparing Cy5 with Cy3. This study was carried out to establish SERRS on sphere segment void substrates to serve as a prelude to developing an analytical application for detecting DNA sequences labelled with SERRS markers.

5.3 SERRS on SSV substrates

5.3.1 Absorption measurements

The absorption spectra of the dyes were recorded in water using a Perkin Elmer Lambda10 spectrometer and are given in Figure 5.1. It can be seen that the absorption peaks become broader from Cy3 to Cy7 and undergo a red shift. This is because of an increase in size of the molecules leading to an increase in the width of the electronic levels (due to additional vibrational modes). The red shift is on account of increase in conjugation (see Figure 5.3 for the structure). The two bands (hump followed by a clear peak) correspond to the most accessible $\pi - \pi^*$ and $n-\pi^*$ transitions in the molecules. The absorbance maximum of Cy5 is at 647 nm while that of Cy3 is at 549 nm and Cy7 is at 746 nm. Hence, with a laser wavelength of 633 nm, Cy5 will be electronically excited unlike Cy3 or Cy7. Therefore, with Cy5 immobilized on sphere segment void gold substrates and

probed with a 633 nm laser; surface-enhanced resonance Raman scattering (SERRS) could be observed. Since, Cy3 has absorption far away from the laser

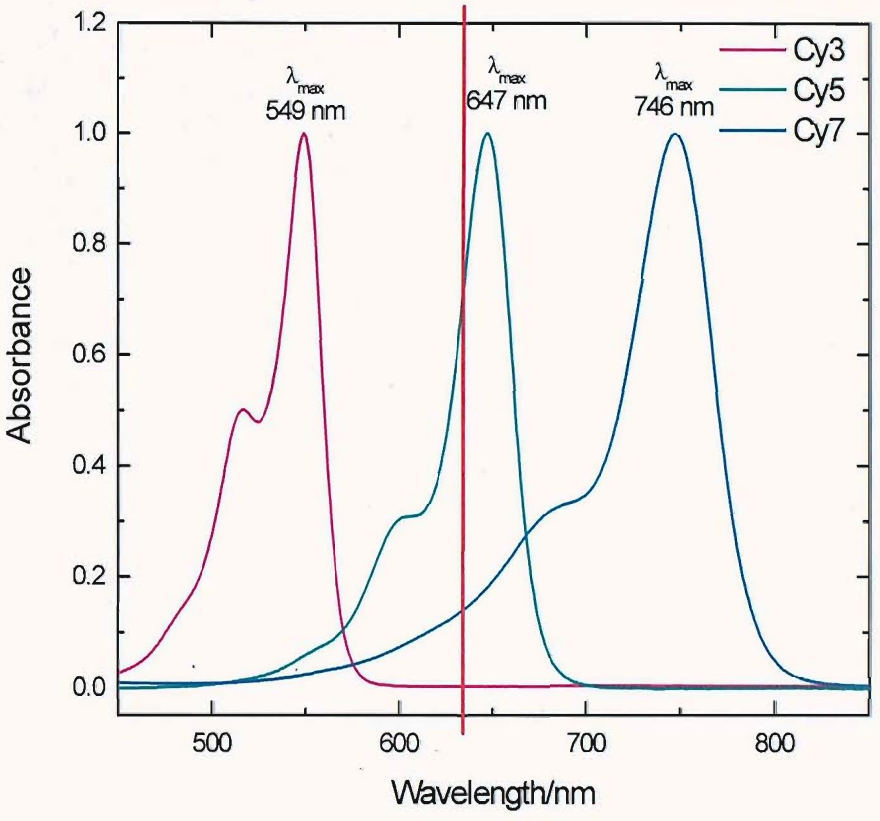

Figure 5.1 Absorption spectra of Cy3, Cy5 and Cy7 at approximately 10 μM concentrations in water. Acquisition conditions were; resolution: 1 nm; medium scan speed in 1 cm path length quartz cuvette. The red line shows the laser wavelength at 633 nm. The spectra presented here have been normalized.

line only SERS should be observed.

5.3.2 SSV Substrates used

In this study sphere segment **void** (SSV) substrates were templated with sphere diameter, *D*, of 600 nm and the film height was 480 nm, that is, 0.80 *D* (relative to sphere diameter). The 600 nm void films have been well studied and have distinct plasmon resonances at 0.80 *D* film thickness corresponding to 633 nm laser [18, 19]. Hence, this morphology was selected for this particular work on SERRS.

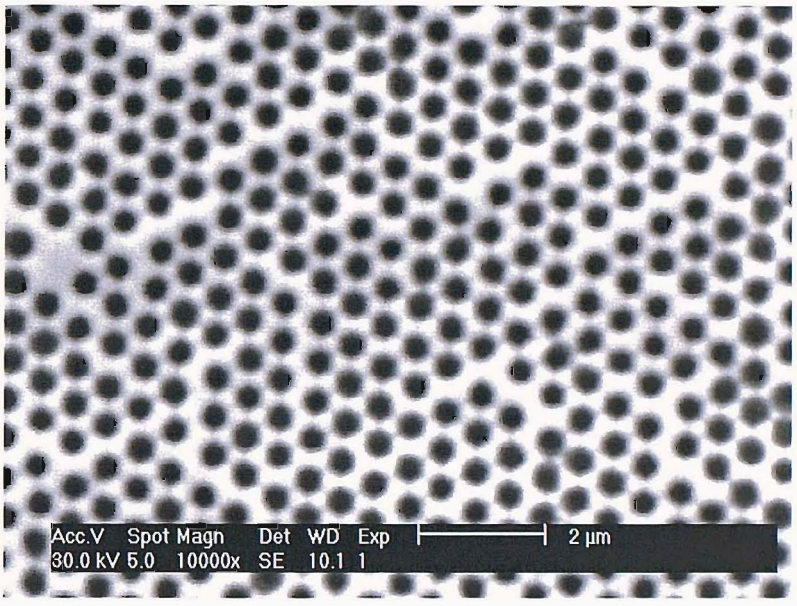

Figure 5.2 A typical SEM image of the SSV substrates (600 nm sphere templated, grown to 480 nm by electrodeposition) employed in this study.

5.3.3 Immobilization of molecules on the surface

After cleaning the substrates they were dipped in an ethanolic solution of cysteamine (10 mM) for 24 hours. The substrates were then washed and dried under argon. Displacement of N-hydroxysuccinamide esters (NHS-esters) by primary amines was employed to attach the dyes to the surface by coupling to the cysteamine. The scheme of attachment of the molecules to the surface is shown in Figure 5.3. The substrates with the cysteamine attached to the gold surface were soaked overnight under dark in ~10 µM aqueous solutions of the dyes made in pH 8.1, 0.01 M phosphate buffer. Subsequently they were thoroughly rinsed with the buffer and dried under argon. For direct valid comparisons the same substrates were split into two, so that there were minimal differences in the morphology of the substrates, for immobilizing each dye. There are only slight differences in the molecular structure of the dyes and their size. A simple energy optimization with Chem3D Ultra 9.0 revealed a difference of 1 Å in the radii along the long axis between Cy3 and Cy5. The diameter of Cy5 was found to be 23 Å. From their structures and their sizes it was expected that there would be a negligible difference in their surface chemistry and only slight differences in their surface coverage.

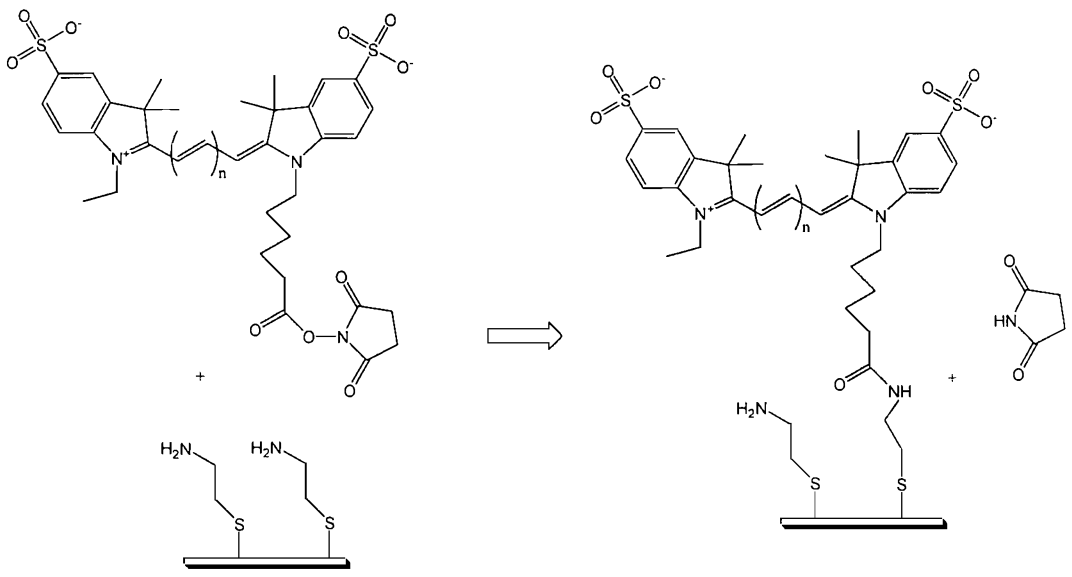

Figure 5.3 Scheme for attachment of dyes to the gold surface. N-hydroxysuccinamide (NHS) esters of the dyes readily react with primary amines resulting in amide bond formation. For Cy3, n=1; for Cy5, n=2 and for Cy7, n=3.

5.3.4 Surface coverage determination

Cyclic voltammetry was used to determine the surface coverage of the immobilized dye molecules on the gold substrates. The charge under the oxidation peak was determined from the cyclic voltammogram obtained by scanning the potential from 0 to 1.1 V versus a saturated calomel electrode (SCE). Anhydrous acetonitrile (kept under nitrogen) with 0.3 M tetra-butylammonium tetrafluoroborate (TBATFB) was used as the electrolyte. The solution was purged with high purity argon for at least 15 minutes before carrying out a measurement. During the measurement the electrochemical cell was blanketed with argon. Cyclic voltammograms for Cy3 and Cy5 immobilized on the surface are shown in Figure 5.4. The irreversible oxidation peak has been attributed to the radical cation formation in cyanine dyes [20]. Thereafter, the dyes are postulated to dimerize and/or deprotonate in an ECE (electrochemical-chemical-electrochemical) type of electrochemical reaction. This irreversibility was tested with SER(R)S on structured gold surfaces. A decrease in the SER(R)S intensities of the peaks was observed after oxidation. In the case of Cy5, no shift could be seen in any of the peaks in the spectra. This could be due to SERRS being highly selective towards resonant molecules and perhaps the oxidation destroys the conjugation of the chromophore rendering it non-resonant with the 633 nm laser or destroys the molecule itself.

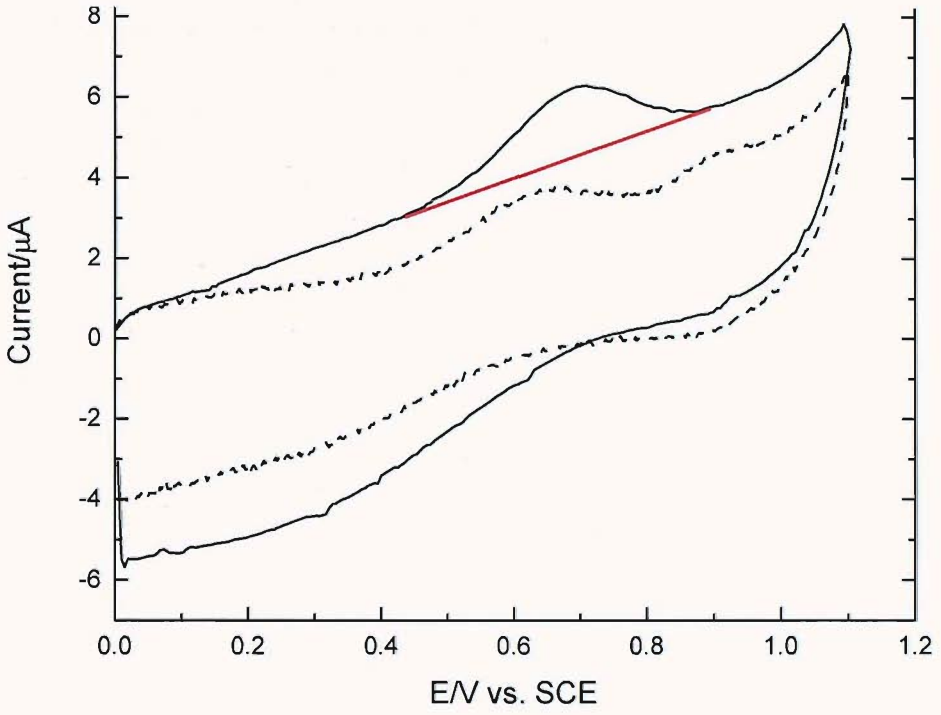

Figure 5.4 Cyclic voltammograms of Cy3 (solid line) and Cy5 (dashed line) immobilized on a 1 mm diameter gold electrode in acetonitrile (0.3 M TBATFB), degassed for 15 min. with Argon and blanketed during experiment. Scan rate: 100 mV/s.

The charge corresponding to the 1 e' oxidation of the dyes was calculated by integrating the current under the corresponding peak as shown in Figure 5.4 (peak area above the red line). The surface coverage determined for Cy3 is larger, as expected, than Cy5 as determined on the gold disc electrode. The surface coverage for Cy3 was found to be 8.64 x 10^{-11} mol/cm^2 (or 5.22 x 10^{13} molecules/cm^2) while for Cy5, coverage of 4.8 x 10^{-11} mol/cm^2 (or 2.9 x 10^{13} molecules/cm^2) was obtained. These correspond to a partial coverage of around 20% compared to a well packed monolayer on the surface. The monolayer coverage was estimated using the dimensions obtained after energy minimization with Chem3D; for example for Cy5 the length and width were found to be 23 Å and ~4.3 Å, respectively. This calculation would imply that with the current system while monitoring SERRS with a 50x objective with a laser spot of 1 micron diameter, 2.3x10^5 molecules are being monitored.

5.3.5 SERS, pre-resonance SERS and SERRS

It can be seen from the absorption spectra shown above in Figure 5.1 for the three dyes that the 633 nm laser line will not have any overlap with Cy3, only a partial resonance with Cy7 and a direct resonance with Cy5. Hence, among the three dyes, Cy5 is expected to give the strongest signal with the 633 nm laser used to record the SER(R)S spectra. Preliminary SER(R)S experiments on structured gold substrates were carried out by physically adsorbing the dyes on the surface and the spectra recorded are presented in Figure 5.5. These spectra cannot be used for quantitative comparison since the dyes were only physically adsorbed and hence, their coverage might be widely different and also the spectra were not collected strictly from morphologically identical substrates. Nevertheless,

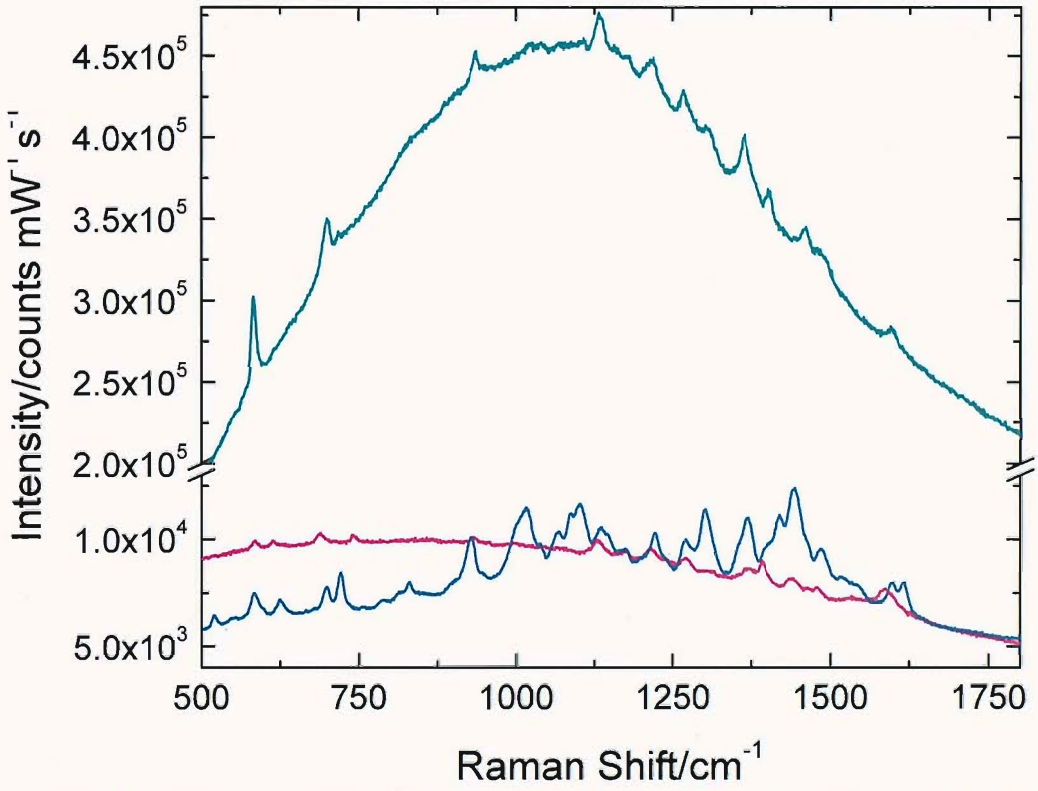

Figure 5.5 Spectra of Cy3 (magenta), Cy5 (cyan) and Cy7 (blue) recorded on D600, ~0.8 *D* sphere segment void gold substrates with 633 nm laser. Laser power was 2.8, 0.028 and 0.7 mW for Cy3, Cy5 and Cy7, respectively. (Note the break in the y-axis scale)

it is possible to qualitatively assess the relative magnitude of the enhancement factors between the three molecules from the spectra. In the spectra of three dyes the bands corresponding to the same vibration modes can be easily identified (band assignments for Cy5 is shown in Table 5.1). The relative enhancements can be determined using the intensities of corresponding peaks. As expected among the three dyes, Cy3 is the least strongly enhanced showing just SERS, the Cy7 signals are ~10-20 times stronger than Cy3 and the Cy5 signals are 20-50 times

stronger again than Cy7. Thus, the resonance enhancement of Cy5 over Cy3 is 200-1000 times. The enhancement of Cy7 peaks over Cy3 is attributed to the pre-resonance excitation of the molecule by the 633 nm laser while that of Cy5 over Cy3 is due to direct resonance with the laser, that is, SERRS enhancement over and above that of SERS.

5.3.6 SERRS *vs.* SERS

To obtain direct valid comparisons the dyes were attached to the gold surface through covalent attachment and the spectra were acquired from morphologically identical locations. A series of samples with the same height, and hence morphology were fabricated, and then split into two after cysteamine treatment. The splitting made sure that the coverage of cysteamine was identical on the two parts. This also ensured that the SER(R)S were signals recorded from morphologically identical substrates. The surface coverage of the dyes, following the attachment with cysteamine, was expected to be approximately the same, albeit slightly in favour of the non-resonant molecule Cy3; since it is slightly smaller than Cy5. On recording the Raman spectra with a 633 nm laser on our

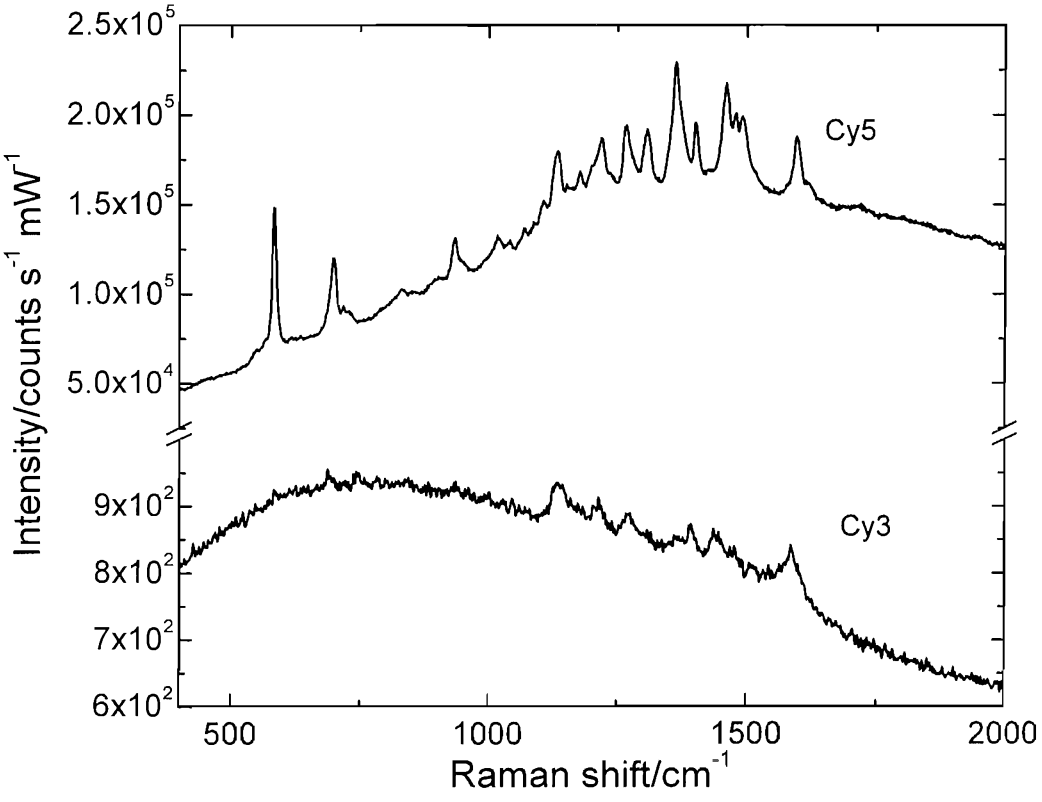

Figure 5.6 SERS spectrum of Cy3 and a SERRS spectrum of Cy5 recorded at structurally identical positions on gold sphere segment void substrates. The spectra are presented without background correction and smoothing but have been normalized with respect to laser power and collection time. Laser power for Cy5 was 0.03 mW while that for Cy3 was 3 mW. (Note the change in the y-axis scale)

substrate the signal was found to be much more intense for Cy5 as compared to Cy3 and the laser power had to be reduced to 28 μW which was 100 times less than that used for recording spectra of Cy3. Spectra recorded for both molecules on topologically similar positions on the substrates are shown in Figure 5.6.

From the figure it can be seen that there is one to one correspondence between most of the bands for the chromophore between both the indocarbocyanine dyes, with some bands showing shifts due to the difference in the structure due to the change in the number of methine bonds. To exemplify, the 1597 cm^{-1} band in Cy5 shifts to 1586 cm^{-1} in Cy3 and 1460 cm^{-1} peak in Cy5 shifts to 1438 cm^{-1} in Cy3; while the peaks at 1219, 1134 and 934 cm^{-1} show negligible shifts. The assignments for the Cy5 peaks are given in Table 5.1. The signals for Raman bands are enhanced around 1000 times in the case of SERRS *vis a vis* SERS as measured on gold SSV substrates determined by comparison of the peak intensities (enhancement factors are discussed later in the chapter). Apart from an increase in the intensity of the peaks we also see an increase in the background. This background is significantly smaller (with the maximum of the background around 300 counts s^{-1} mW^{-1}) for the clean gold surface while it is ~10^5 counts s^{-1} mW^{-1} for the Cy5 covered substrate. Comparing the intensity maxima of the backgrounds, the increase is ~200 times between the Cy5 and Cy3 spectra. The increase in background is clearly related to the resonant enhancement of the molecule in SERRS compared to that in SERS. The origin of the background in SERRS has been discussed in Chapter 4. The Raman band assignments are based on the work of Sato and coworkers on carbocyanine dyes [21]. With the attachment scheme employed here, where the chromophore is connected through a 10-atom long linker to the surface, the shift in Raman peaks for the chromophore compared to that in free solution was found to be negligible (~1 cm^{-1}).

Table 5.1 Peak assignments for Cy5 dye (Chromophore: Chr) using Sato and coworkers [21] study on similar indocarbocyanines

	SERRS peak (cm^{-1})						
	1597	**1460**	**1219**	**1134**	**934**	**697**	**583**
Assignment	Chr(C=N)	-CH Asym. def.+ Chr(Ring Stretch)	Chr (Aromatic CH in-plane bend)	Chr (CH_3-CH-CH_3 skeletal)	Chr (Aromatic CH def.)	Chr(Aromatic adj. H out of plane def.)	Chr(Methine chain def.)

5.3.7 Resonance enhancement in SERRS

On comparing the SERRS enhancements of different peaks in Cy5 over and above that of SERS from Cy3, it was found that the different bands are enhanced to varying degrees. This resonance enhancement, defined as the ratio of the corresponding band intensity for resonant Cy5 to non-resonant Cy3, was investigated further. The resonance enhancement for each peak was found by comparing their background subtracted peak intensities. Resonance Raman

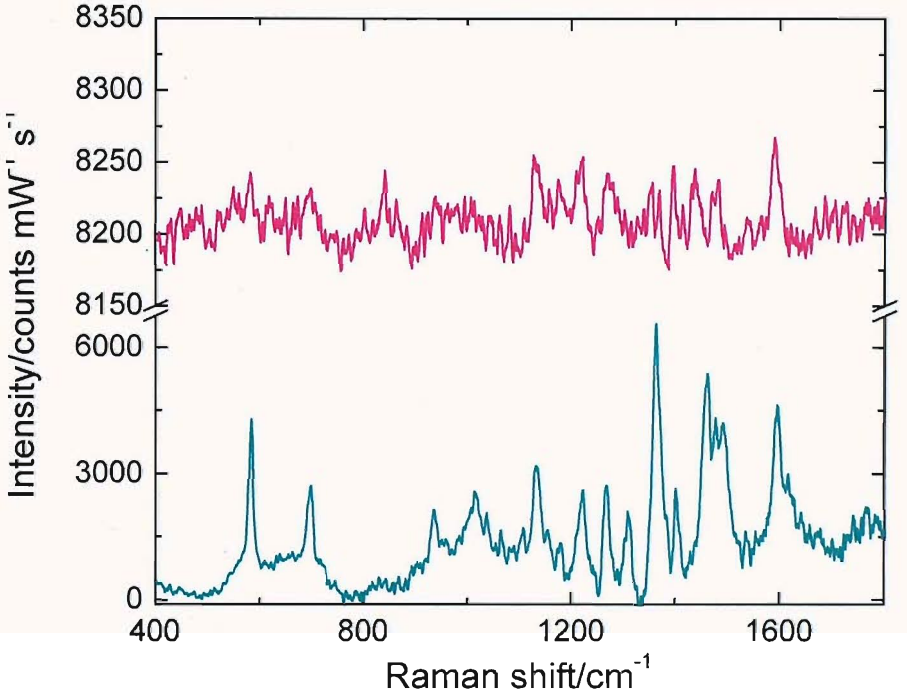

Figure 5.7 Resonance Raman spectrum of Cy5 and Raman spectrum of Cy3 from their ~10 μM aqueous solutions. The spectra have been background corrected and smoothed. Cy5 spectrum was collected at 0.03 mW and Cy3 spectrum was collected at 1.5 mW laser power with a 20x objective (NA:0.4).

spectrum of Cy5 and a Raman spectrum of Cy3 in solution were also collected to determine the ratio of resonance enhancement as shown in Figure 5.7. This was compared with the ratio of enhancements of the peaks occurring in SERRS over and above the corresponding peaks in SERS (Cy5 *vs.* Cy3). It was observed that this variation of resonance enhancement for different peaks is not significant in solution while a much larger variation is observed on the SSV gold substrate.

Further, Raman spectra of Cy5 and Cy3 in solution were collected with a 1064 nm laser. With this laser source neither of the molecules is resonant and hence, the peak intensities should be more or less the same. Their Raman spectra are plotted in Figure 5.8 and indeed it can be seen that the Cy5 peaks are only slightly stronger than those of Cy3. Hence, it was inferred that the variation in resonance enhancement of different peaks could be due to the substrate, due the existence

of plasmons on the surface which amplifies the resonance enhanced scattered radiation.

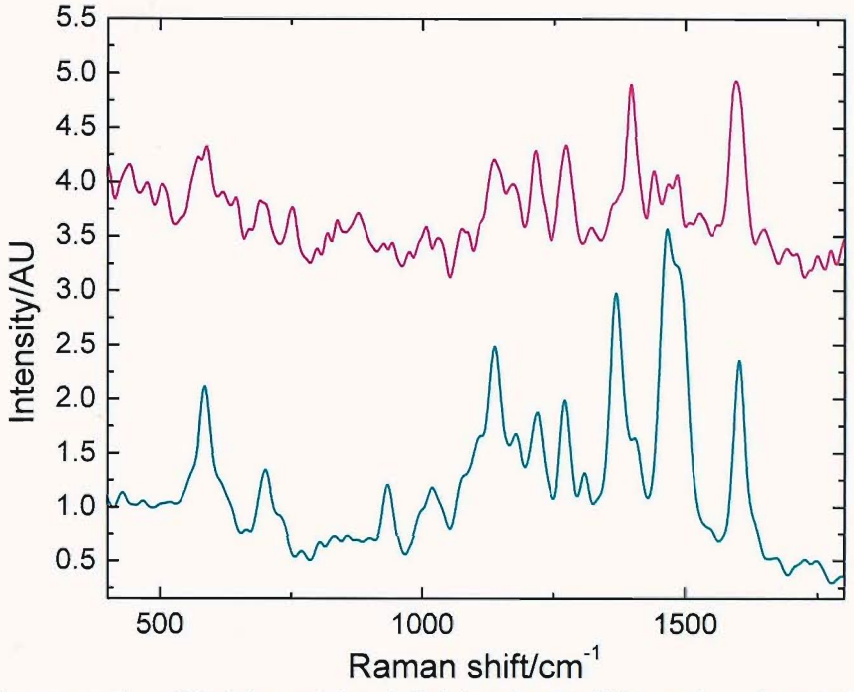

Figure 5.8 Raman spectra of Cy3 (magenta) and Cy5 (cyan) with 1064 nm laser from their ~10 μM concentrated solutions; 250 mW power, 1 scan, 4 cm^{-1} resolution.

To ascertain the plasmonic contribution to the resonance enhancement, reflectance spectra were recorded for the substrate in normal incidence mode using a microscope and a fibre couple Ocean Optics spectrometer. A spectrum showing the plasmonic resonance of the substrate is shown in Figure 5.9. On overlaying the resonance enhancements on the plasmon resonance spectrum a correlation can be seen. The enhancements follow the plasmon intensity profile. This observation means that the resonance enhancements of different peaks are amplified depending on the strength of the plasmonic field at that wavelength. This implies an electromagnetic mechanism for the resonantly enhanced scattered fields as well. It is postulated that the extent of coupling of the outcoming scattered radiation from the electronically excited molecule also contributes to the SERRS intensities observed. Therefore, the resonance enhancements of SERRS over SERS for the Stokes-shifted peaks closer to plasmonic resonance are higher compared to those which are farther away. The dependence of SERRS enhancements on the exciting wavelength has been well studied [22]. However, the resonance dependence of outgoing scattered radiation for the peaks of the same molecule has not been reported. Nevertheless, the extent of coupling of the scattered field in SERRS, that is, the outgoing resonances with plasmons on the

substrates is found to contribute a factor of 2 to 3 to the enhancement over and above the contribution due to molecular resonance. This is estimated by comparing the maximum resonant enhancement obtained at 663 nm, which ties in with the outgoing plasmon maximum, to the resonant enhancement observed far

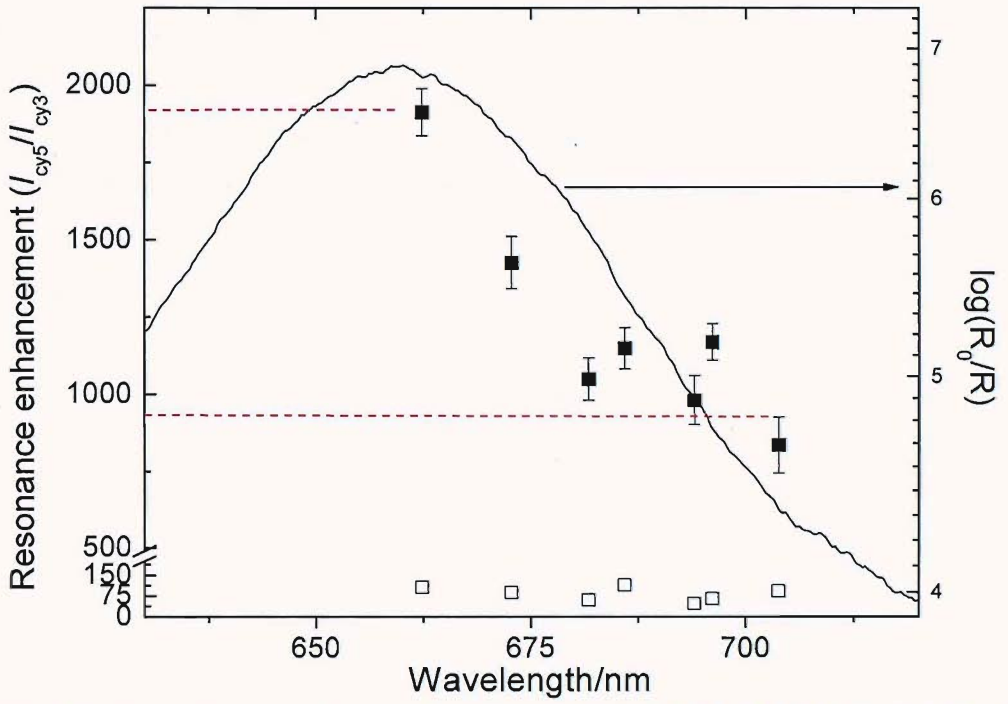

Figure 5.9 Resonance enhancements (■) comparing SERRS from Cy5 to SERS from Cy3 is overlaid on the plasmon absorption spectrum of the substrate. (□) Enhancements obtained for Cy5 over Cy3 in solution (resonance Raman vs. Raman) is also shown. The peak positions in wave-numbers have been converted to absolute wavelength. The dashed lines mark the maximum and the base resonance enhancement levels.

away from the plasmon maximum, where it reaches a baseline level (see Figure 5.8; compare the two dashed red lines). The error bars (~6%) for the enhancement ratios have been calculated from 18 measurements at different locations on a single substrate.

5.3.8 Enhancement factors

Using the surface coverages obtained for Cy5 and Cy3 (section 5.3.4) the enhancement factors were calculated. The enhancement factor (EF) was calculated using the following expression

$$EF = I_{surf}C_0V_LN_A/I_{sol}\Gamma_0A_LG_RM \qquad 5.1$$

where I_{surf} is the intensity of the peak from spectrum on the SSV substrate, C_o is the concentration of the aqueous solution of the molecule, V_L is the laser volume, N_A is Avogadro's number, I_{sol} is the intensity of the peak of the same molecule from its spectrum in solution, A_L is laser spot area, G_R is the geometrical

roughness factor[1] for the surface due to the templated structure ($1 < G_R < 4.63$) and M is the molecular weight. V_L is the volume of the cylinder illuminated by the laser ($=A_L$*path length) for the Raman measurement in solution (from which I_{sol} is obtained) .

For the most intensely enhanced peak (583 cm^{-1}) acquired with the 633 nm laser on the SSV substrate the enhancement factor was found to be 5.2 x 10^6 with respect to resonance Raman spectra in solution. However, it should be pointed out that it was extremely difficult to acquire a reasonable solution spectrum owing to the huge fluorescence of Cy5 on excitation with the 633 nm laser. Optimization of the acquisition time and laser power had to be carried out to observe the peaks while not saturating the detector. Considering the fact that resonant Raman itself could be at least 1000 times stronger than non-resonant Raman, the colloidal templated gold substrates employed in this study are expected to give enhancements of the order of ~10^9. The peak at 1597 cm^{-1} due to the –C=N vibration is not likely to undergo a significant change in polarizability between Cy5 and Cy3 and is located on the chromophore, hence it was chosen for estimating the absolute SERRS enhancement factor. Comparing the 1597 cm^{-1} SERRS band for Cy5 recorded on a SSV substrate with the corresponding Raman band for Cy3 in solution, an absolute enhancement factor of 1.6 x 10^8 for SERRS was obtained over normal Raman.

5.3.9 Reproducibility of SERRS

To demonstrate the reproducibility of the electrodeposited sphere segment void gold substrates and the SERRS signals on them, three substrates with the same morphology were fabricated. Cy5 was attached following the covalent attachment scheme depicted in Figure 5.3 and SERRS signals were recorded on each from 10 different locations by translating a distance of 10-50 microns. The spectra were collated and the average spectra along with those corresponding to upper and lower bounds of one standard deviation are presented in Figure 5.10. There appears to be slight change in the background, especially at higher wave-numbers (1500-2000 cm^{-1}) while the variation in peak intensities are less than 6 % for some peaks. The reproducibility data for each of the main peaks corresponding to the spectra is presented in Table 5.2 below. The errors obtained for the SERRS peaks vary only between 5 and 10%, which is better than any report in literature for substrates. It also compares well with the work on silver colloids by Keir *et al.*, who

[1] See Appendix I for calculation of geometrical roughness (G_R) factor of SSV substrates

report a process improvement for fabrication of silver colloids and obtain a variation of 6% in signals [16]. However, aggregation of colloidal particles is

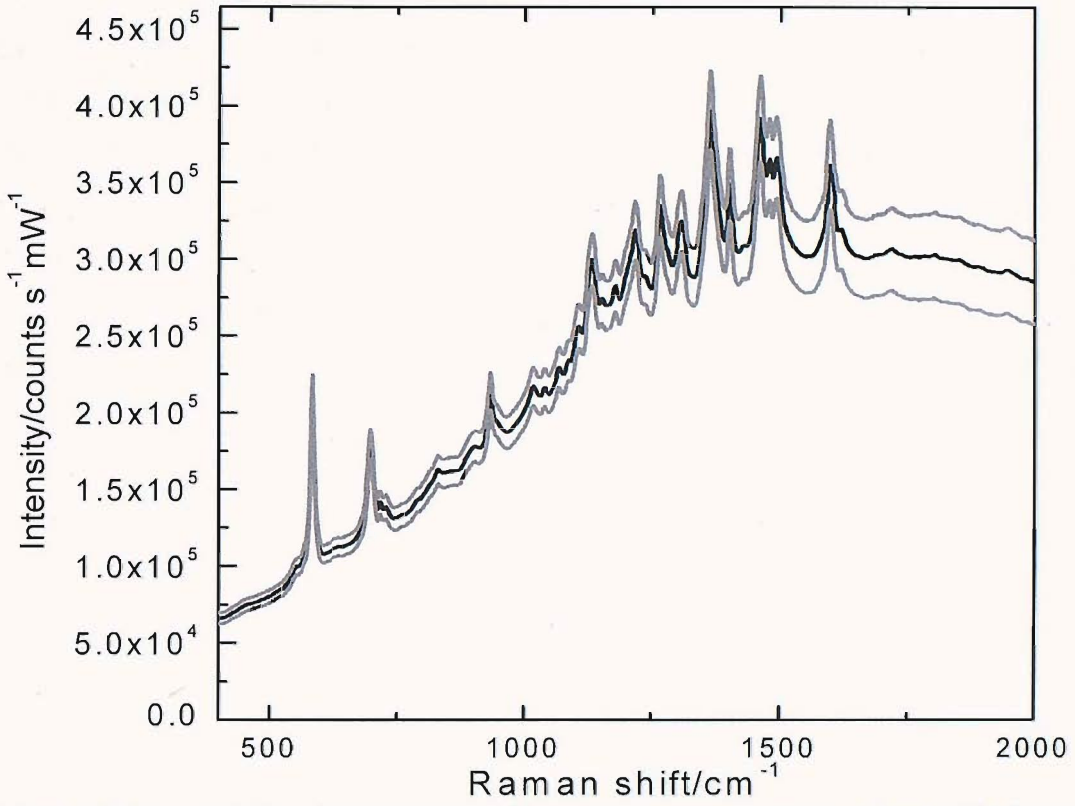

Figure 5.10 Reproducibility of SERRS spectra. The average spectrum is shown in black while the grey ones correspond to +/- 1 std. dev. The average spectrum has been calculated from 30 spectra recorded on three separately fabricated substrates having identical morphology.

carried out before obtaining SERRS from them, which is difficult to control without special equipment and introduces a lot of variability in the conditions between different laboratories. SSV substrates, besides being very reproducible, easy to fabricate, can be used as electrodes therefore are suitable for electrochemical SER(R)S, are stable, portable and easy to use for SER(R)S.

Table 5.2 Reproducibility data for different SERRS peaks

	SERRS peak (cm^{-1})						
	1597	**1460**	**1219**	**1134**	**934**	**697**	**583**
Mean intensity (counts $s^{-1}mW^{-1}$)	63054	50054	42912	42164	35267	46565	111691
Std. deviation (counts s^{-1} mW^{-1})	5686	4236	2607	2892	2191	2423	5624
% Error	9.4	8.5	6.1	6.9	6.2	5.2	5.0

Peak intensities have been calculated after background subtraction from 30 spectra recorded on three substrates with identical morphologies.

5.4 Conclusions

In this study it has been demonstrated that the sphere segment void substrates can be utilized for SERRS. This constitutes the first investigation of utilizing these substrates templated by colloidal crystals for SERRS. In the work described in this chapter SERRS and SERS have been compared by employing structurally similar molecules. Cy5 was resonant with the 633 nm laser used while Cy3 was not. Resonance enhancement, defined as the enhancement obtained in SERRS over and above that in SERS was found to be of the order of 10^3. Enhancement in SERRS over resonance Raman was found to be of the order of 10^6 on the SSV substrates, which is similar to the SERS enhancements routinely observed over normal Raman. The net enhancements in SERRS were found to be ~10^9 compared to normal Raman. Further it was demonstrated that SERRS signals on the SSV substrates were reproducible. As mentioned at the outset this study was carried out as a prelude to developing applications based on SERRS detection and it proves that developing reproducible assays utilizing SERRS analysis employing SSV substrates is feasible.

5.5 References

[1] D. L. Jeanmaire and R. P. Van Duyne, J. Electroanal. Chem. 84:1 (1977).
[2] F. W. King and G. C. Schatz, Chem. Phys. 38:245 (1979).
[3] M. Moskovits, J. Raman Spectrosc. 36:485 (2005).
[4] Z. Q. Tian, J. Raman Spectrosc. 36:466 (2005).
[5] K. Kneipp, Y. Wang, R. R. Dasari, and M. S. Feld, Appl. Spectrosc. 49:780 (1995).
[6] S. Nie and S. R. Emory, Science 275:1102 (1997).
[7] T. M. Cotton, S. G. Schultz, and R. P. Van Duyne, J. Amer. Chem. Soc. 102:7960 (1980).
[8] L. A. Dick, A. J. Haes, and R. P. Van Duyne, J. Phys. chem. B 104:11752 (2000).
[9] D. Graham, K. Faulds, and W. E. Smith, Chem. Commun.:4363 (2006).
[10] R. J. Stokes, A. Macaskill, J. A. Dougan, P. G. Hargreaves, H. M. Stanford, W. E. Smith, and D. Graham, Chem. Commun. :2811 (2007).
[11] B. D. Moore, L. Stevenson, A. Watt, S. Flitsch, N. J. Turner, C. Cassidy, and D. Graham, Nat. Biotechnol. 22:1133 (2004).
[12] M. Moskovits, Rev. Mod. Phys. 57 (1985).
[13] K. Faulds, R. P. Barbagallo, J. T. Keer, W. E. Smith, and D. Graham, Analyst 129:567 (2004).
[14] Y. C. Cao, R. Jin, and C. A. Mirkin, Science 297:1536 (2002).
[15] V. L. Schlegel and T. M. Cotton, Anal. Chem. 63:241 (1991).
[16] R. Keir, D. Sadler, and W. E. Smith, Appl. Spectrosc. 56:551 (2002).
[17] A. G. Brolo and C. J. Addison, J. Raman Spectrosc. 36:629 (2005).
[18] J. J. Baumberg, T. Kelf, Y. Sugawara, S. Cintra, M. Abdelsalam, P. N. Bartlett, and A. E. Russell, Nano Letters 5:2262 (2005).
[19] T. A. Kelf, Y. Sugawara, J. J. Baumberg, M. Abdelsalam, and P. N. Bartlett, Phys. Rev. Lett. 95 (2005).
[20] J. R. Lenbard and A. D. Cameron, J. Phys. Chem. 97:4916 (1993).

[21] H. Sato, M. Kawasaki, K. Kasatani, and M.-a. Katsumata, J. Raman Spectrosc. 19:129 (1988).
[22] P. Hildebrandt and M. Stockburger, J. Phys. Chem. 88:5935 (1984).

6 DNA detection and mutation discrimination

6.1 Introduction

Detection of deoxyribose nucleic acid (DNA) sequences, single nucleotide polymorphisms (SNPs) and mutations has gained huge importance since the unravelling of the sequence of the human genome. The repertoire of structure-function relationships between genes (and mutations in them) and inherited (genetically acquired) diseases continues to expand. As a consequence, the development of DNA-based diagnostics is becoming more significant than ever. Hence, development of simple, low cost, reliable, high-speed, high-throughput methods to detect genetic variations in DNA sequences is the need of the hour. Conventional techniques such as those based on PCR, gel electrophoresis and direct sequencing do not satisfy most of these criteria and are suitable only for the laboratory. Utilization of solid substrates is necessary for high throughput and automated analysis. In a typical solid-phase analytical system, single-strand DNA (ssDNA) is immobilized on the substrate as the 'probe' sequence. On exposure to a solution containing the 'target' molecules with a sequence complementary to that of the surface-tethered probe, hybridization occurs and is detected. Thereafter, the duplexes can be dehybridized by several methods such as raising the temperature or washing with decreasing ionic strength solutions (stringency washing). Monitoring this dehybridization (or melting) process allows mutations to be distinguished as they destabilize the duplex to varying degrees (depending on the number of mismatches) compared to the perfectly complementary target.

Fluorescence is currently the most preferred optical technique for detecting mutations using this hybridization/dehybridization strategy [1]. However, surface-enhanced Raman or resonant Raman scattering (SER(R)S) has many advantages compared to fluorescence for DNA detection [2-4] and can reach comparable or higher sensitivity levels [5]. Some of the benefits of using SERS are the ability to multiplex, use of single excitation without any inflexibility involving the donor as in FRET (Forster or Fluorescence Resonance Energy Transfer) and its insensitivity to oxygen or quenchers that affect fluorescence. Moreover, SERS provides much more information about the molecule than fluorescence. Also, compared with surface-plasmon resonance (SPR) or electrochemical detection methods, which

are some of the other commonly used methods for DNA detection, SER(R)S is molecule specific and much more sensitive. Metallic ordered sphere segment void (SSV) substrates have been developed in our group over the past several years including the duration of this thesis work. As described in the preceding chapter these substrates generate intense local electric fields under illumination and hence, are suitable for surface-enhanced Raman scattering (SERS). Their optical properties can be tuned for SERS [6, 7]. Typical enhancements of ~10^6 are observed for SERS on these substrates compared to conventional Raman [8]. The sensitivity of detection can be increased further by employing the technique of resonant SERS or surface-enhanced resonance Raman scattering (SERRS). In this case, when the molecule has an electronic transition in resonance with the laser excitation then a further enhancement of ~10^3 occurs over and above that in SERS as observed on SSV substrates [9]. Hence, SSV substrates can serve as ideal platforms for developing SER(R)S based applications. In this chapter their application in detecting DNA sequences and differentiating mutations in them is described.

6.2 Overview

In this chapter it is first shown that the SSV substrates can be used to obtain stable reproducible SERS signals for labelled ssDNA after hybridization onto surface attached DNA probe sequences. It is demonstrated that the SERS substrates remain reusable after several cycles of detection using hybridization and subsequent dehybridization in a highly sensitive detection assay.

Further, sequences in the gene responsible for coding the Cystic Fibrosis Transmembrane Regulator (CFTR) protein were used as a model system to demonstrate the discrimination of different mutations in DNA sequences using SERS or SERRS (SER(R)S). Mutations in this gene cause cystic fibrosis, which is one of the most common inherited genetic life-shortening diseases, reducing the life expectancy to 37.5 years, across different populations [10]. Two particular mutations; ΔF508 (a triple deletion) the most common CFTR mutation (70 % and 90 % of cystic fibrosis cases in UK and US, respectively) and 1653C/T a relatively rare single point mutation occurring in the same gene fragment were targeted. It is shown that it is possible to distinguish between the wild type, the single nucleotide mutation and the most common triplet deletion in the human CFTR gene by employing SER(R)S for following the melting of dsDNA from the SSV surface as either the temperature or the applied potential is scanned (called the SERS-

melting method). Thereafter, the flexibility in the choice of labels used for discriminating mutations with the SERS-melting method is demonstrated. Results with a variety of labels including electrochemically (redox) active labels are presented. The applicability of this approach in real systems is also established by discriminating between the unpurified amplicons of the wild type and triplet deletion in the human CFTR gene following asymmetric PCR of a DNA sample. Lastly some fundamental studies for understanding and probing the mechanism of electrochemically induced melting are described.

6.3 DNA detection

In all experiments described in this chapter gold SSV substrates have been utilized. Uniform height D600, 0.8 *D* substrates were fabricated using the procedure described in Chapter 2. Three representative SEM images at different magnifications and a 3-D model drawn with POV-Ray software are shown in Figure 6.1.

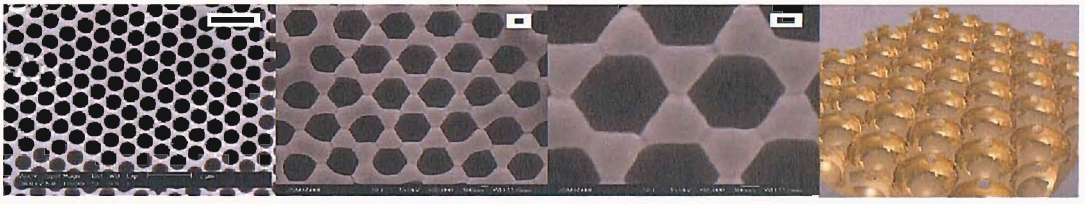

Figure 6.1 Three SEM images at different magnifications of the SSV gold substrates (templated with 600 nm spheres and electroplated to 480 nm) and a (right) 3-D model constructed with POV-Ray. The scale bar is 2 μm for the first SEM image from the left and 100 nm for the other two, respectively

Single strand DNA probe sequences were attached to the surface through three disulfide linkages and hexaethyleneglycol (HEG) spacers as shown in Figure 6.2 attached at the 5' end of the oligonucleotide sequence. The immobilization protocol has been described in Chapter 2. The 6 thiolate linkages ensure strong binding of the DNA to the surface. Following attachment of the probe sequences the substrates were washed and soaked in a 10 μM solution of mercaptohexanol

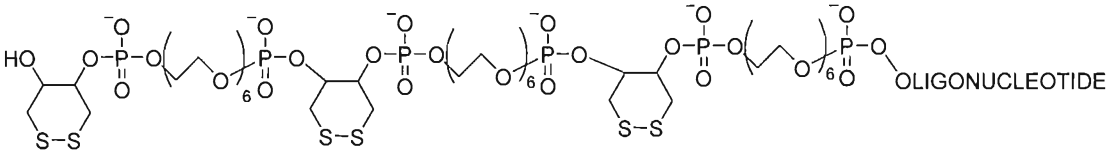

Figure 6.2 Structure of the disulfide linkages attached to the 5' end of the probe oligonucleotides. The dithiol linkages ensure strong bonding with gold on immobilization.

in a pH 8.1 phosphate buffer containing 1 M NaCl for 20 min. The mercaptohexanol adsorbs to the gold surface around the attached DNA and reduces non-specific binding of target DNA from the solution at the gold surface

[11]. The mercaptohexanol also has the effect of re-orienting the ssDNA attached to the surface into a more upright conformation [12, 13]. For efficient hybridization with target strands from the solution it is important to ensure that the probe sequences are not too closely packed on the surface [11, 14] and the immobilization and passivation conditions mentioned above were chosen for that reason. The large footprint of the disulfide monomers and HEG spacers between them ensures that the surface bound probes are well spaced on the surface with enough room between them to prevent any cross-hybridization and to ensure efficient hybridization with target species from solution.

Further, SER(R)S spectra presented in this chapter have been background corrected, unless mentioned otherwise, by using polynomial multi-point fitting function utility available in WiRe 9.0 software provided by Renishaw. The Raman intensities of the peaks mentioned in this work are their heights over and above the baseline.

6.3.1 Preliminary SERS experiments

Initial experiments were carried out by using a 3' fluorescein (FAM) labelled 25-base probe immobilized (immobilization protocol given in experimental chapter) on gold SSV substrates. A labelled probe was utilized to verify the uniformity of the

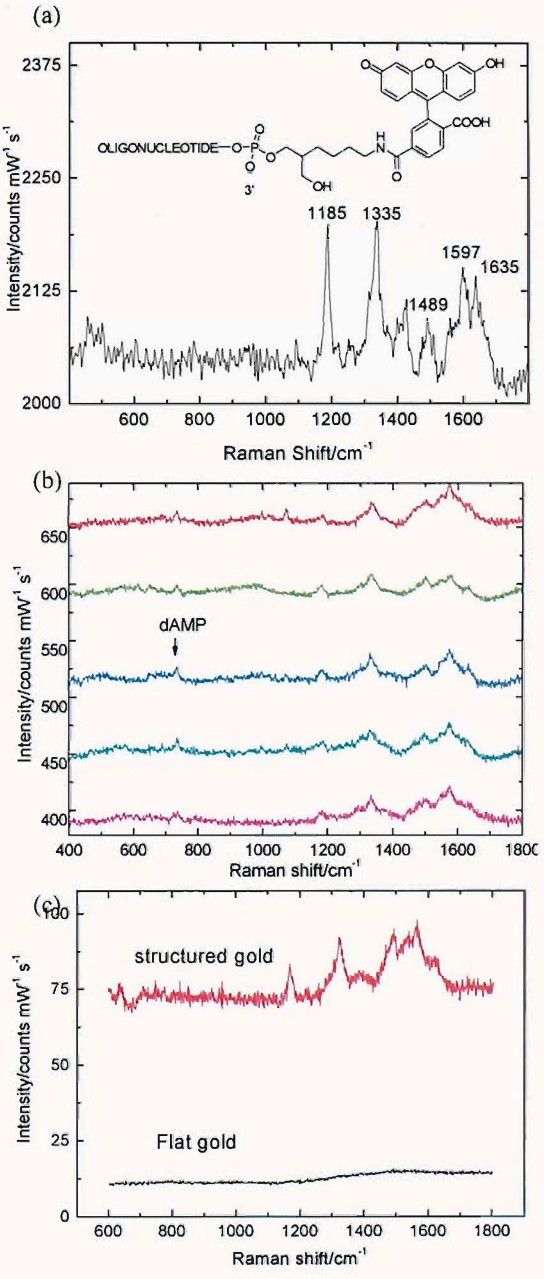

Figure 6.3 (a) Raman spectrum in 1 mM solution of FAM labelled probe. The structure and the prominent peaks are shown. (b) SERS spectra of FAM-labelled probe immobilized on the surface recorded under dry conditions at 5 different locations (50 microns apart) on a D600, 0.8 *D* gold SSV substrate and (c) shows the SERS spectrum on the same substrate under buffer and a spectrum for the immobilized oligo on evaporated (flat) gold surface. Spectra were recorded with 633 nm laser and have been offset for clarity in (b) & (c).

immobilization on the surface. The spectrum of FAM in a 1 mM solution is shown in the top panel of Figure 6.3. The prominent peaks are shown. The bands at 1179, 1322 and 1637 cm^{-1} correspond to the 3' fluorescein (FAM) label [15, 16] attached to the probe and are assigned to the C-OH bending, C-O phenoxide stretching and the ring stretching vibrations, respectively [17]. The middle panel in Figure 6.3 shows SERS spectra of the FAM labelled probe at different places 50 microns apart on a gold SSV substrate in dry conditions. It shows that the intensities for the FAM label are similar and hence, indicates that the immobilization is uniform across a large area on the substrate. Also, a peak attributable to adenosine monophosphate (dAMP) can be seen in the spectra however, the same peak is absent in the SERS spectra recorded under buffer solution while the FAM peaks can still be observed (Figure 6.3 bottom). This is probably due to the oligonucleotide lying flat in the dry condition and extending away from the surface in solution, respectively. A spectrum of the same immobilized oligonucleotide on flat (evaporated) gold on a glass slide is shown which does not show any peaks for the fluorescein label confirming the surface-enhancing properties of SSV substrates. The absence of any easily discernible peaks from the DNA bases in SERS experiments under solution necessitated having a label on the probe as well, for initial experiments, to confirm each step during the development of a repeatable assay for DNA detection.

Table 6.1 Sequences of probe and target used in preliminary SERS experiments

Probe	XHXHXHGCAGCAAATTGCACTGGAGTGCGAG-3'-(FAM)
Target	3'-GTGACCTCACGCTC-5'-Cy3

Where X is a disulfide monomer and H is a hexaethyleneglycol (HEG) spacer

For DNA assays a 25-base long non-complementary, for testing the specificity, and a 14-base long complementary target, both labelled with Cy3 on the 5'-end were used to show the stability and reusability of the substrates. The sequences employed for the probe and the target are given in Table 6.1. Figure 6.4 shows a set of SERS spectra recorded from the same substrate at different stages in one such experiment. Spectrum (a) was recorded for the ssDNA immobilised on the SSV substrate at open circuit in buffer solution. There was no observable change in the spectrum after incubation with a non-complementary Cy3 labelled 25-base long ssDNA while with a non-passivated surface strong Cy3 peaks could be seen confirming that the mercaptohexanol suppresses non-specific binding. In contrast when the 14-mer complementary DNA strand labelled with Cy3 at the 5' end is

introduced to the surface the spectrum changes, Figure 6.4(b), and new bands corresponding to the Cy3 label [15, 18] appear at 1393 cm^{-1} assigned to CH deformation and at 1590 cm^{-1} assigned to C=N stretching vibration (based on the work of Sato *et al.* [19] on indocarbocyanine dyes). At the same time the fluorescein (FAM) bands become less prominent. The changes are attributed to the hybridization of the Cy3 labelled target to the DNA probe attached to the surface and the subsequent change in conformation of the DNA which probably moves the 3' fluorescein label further from the surface thus reducing its SERS intensity [20]. The spectra for FAM labelled oligos were acquired with 3 s while those with Cy3 labelled target have been acquired with a single 30 s accumulation.

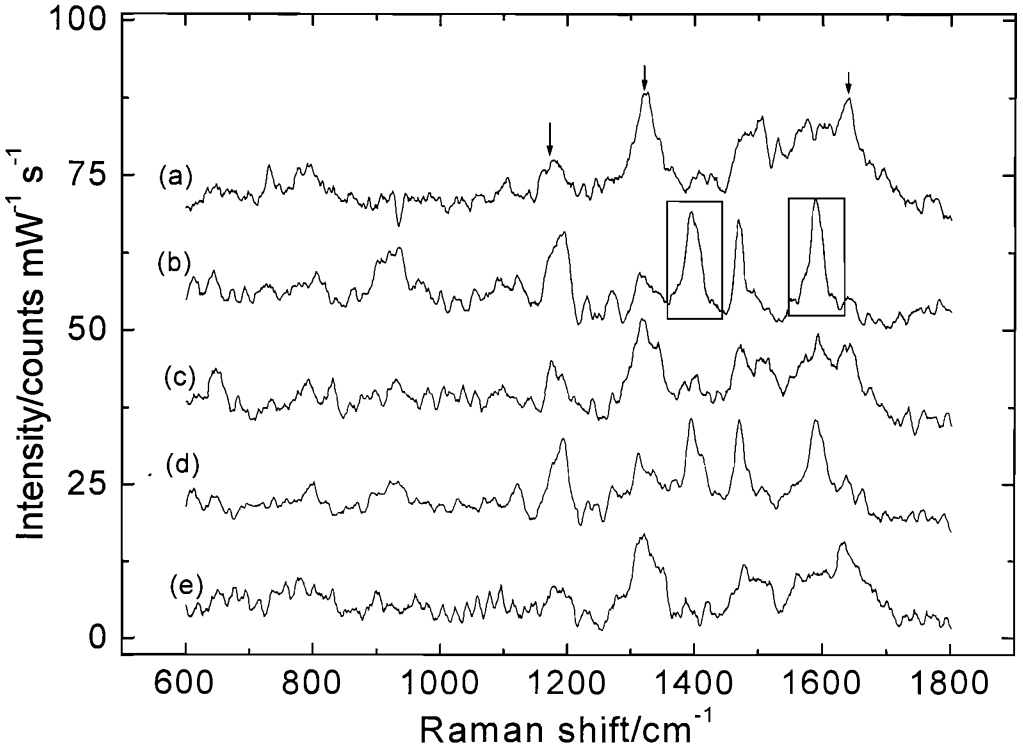

Figure 6.4 DNA assay and reusability demonstrated employing a fluorescein (FAM) 3'-labelled 25 base long probe and 14 bases long Cy3 5'-labeled target. In this study both the labels are at the distal end from the surface. (a) Even after incubation with a non-complementary Cy3 labelled strand only peaks due to FAM labelled probe (marked with arrows) are observed in the spectrum, which is identical to that of the probe DNA before incubation with the non-complementary ssDNA. (b) Hybridization with a complementary Cy3 labeled target (peaks enclosed in boxes) and (d) rehybridization occurs with almost no loss in signal from Cy3 labeled target. (c) and (e) Dehybridization is achieved by flowing hot water (~55 °C) for 5 min. over the substrate resulting in regeneration of the sensor substrate as inferred by the reappearance of the FAM peaks and loss of Cy3 peaks. Spectra are baseline corrected and smoothed. The spectra were recorded with 30 s collection time, single accumulation for Cy3 and 3 accumulations for FAM spectra at 3 mW laser power in pH 8.1 phosphate buffer containing 100 mM NaCl.

In this case the fluorescein label on the probe and the Cy3 label on the target are on the same end distal to the surface yet the intensities of the fluorescein peaks are weaker compared to Cy3. This difference could be due to the lower Raman

cross-section of fluorescein compared to Cy3 with the 633 nm laser used in this experiment. This suggests that in principle any molecule with a high Raman cross section could be employed as a label in these experiments.

To test the stability of the system the dsDNA was dehybridized by washing the surface with water at ~55 °C for 5 min, Figure 6.4 spectrum (c), then rehybridized to the complementary target, spectrum (d), and finally dehybridized with hot water again, spectrum (e). Comparing the spectra in Figure 6.4 it can be seen that on dehybridization the original spectrum for the fluorescein (FAM) labelled probe is recovered, compare spectrum (a), (c) and (e) with very similar intensities. Further, comparing spectra (b) and (d) in Figure 6.4 almost similar peak intensities of the Cy3 peaks are observed in the two cases demonstrating excellent reproducibility of the assay and reusability of the substrates.

6.3.1.1 Surface coverage determination

To determine the sensitivity of SERS detection the surface coverage of immobilized probe DNA (after mercaptohexanol treatment) was determined. The coulometric procedure of Steel *et al.* [21] using $[Ru(NH_3)_6]^{3+}$ as the redox probe was used to determine the coverage of the immobilized 25-base probes on gold surfaces. In this method the $[Ru(NH_3)_6]^{3+}$ cation binds electrostatically to the phosphate groups on the DNA. Under saturating conditions assuming that the charge on the phosphate groups is entirely compensated by $[Ru(NH_3)_6]^{3+}$ the amount of DNA bound at the surface can be deduced. This is done by measuring the charge required to completely reduce the DNA bound $[Ru(NH_3)_6]^{3+}$ using a short reductive potential pulse. Full experimental details have been given in Chapter 2.

Figure 6.5 shows typical results for the charge transients recorded and the derived binding isotherm. The adsorption isotherm in Figure 6.5b was constructed by fitting coulometric curves of the type shown in Figure 6.5a recorded for different concentrations of $[Ru(NH_3)_6]^{3+}$ to the following expression for the total charge, Q,

$$Q = \frac{2nFAD_O^{1/2}c_O t^{1/2}}{\pi^{1/2}} + Q_{dl} + nFA\Gamma_O \qquad 6.1$$

where t is the time, n is the number of electrons transferred, F is the Faraday constant, A is the area of the electrode, D_O is diffusion coefficient of the electroactive species in solution and c_O the bulk concentration of $[Ru(NH_3)_6]^{3+}$, Q_{dl} is the double layer charge, and Γ_O is the surface coverage of bound $[Ru(NH_3)_6]^{3+}$.

The first term in Equation 6.1 describes the mass transport limited reaction of $[Ru(NH_3)_6]^{3+}$ from the solution, the second term the double layer charging contribution and the final term the contribution from the electrostatically bound $[Ru(NH_3)_6]^{3+}$. The double layer charging contribution is found by performing the experiment without any added $[Ru(NH_3)_6]^{3+}$ to the solution. The coverage was found to be 1.6 x 10^{12} molecules per cm^2 so that on an average the 25-base ssDNA molecules are 8.5 nm apart leaving sufficient room to hybridize while preventing any cross-hybridization with target DNA from solution.

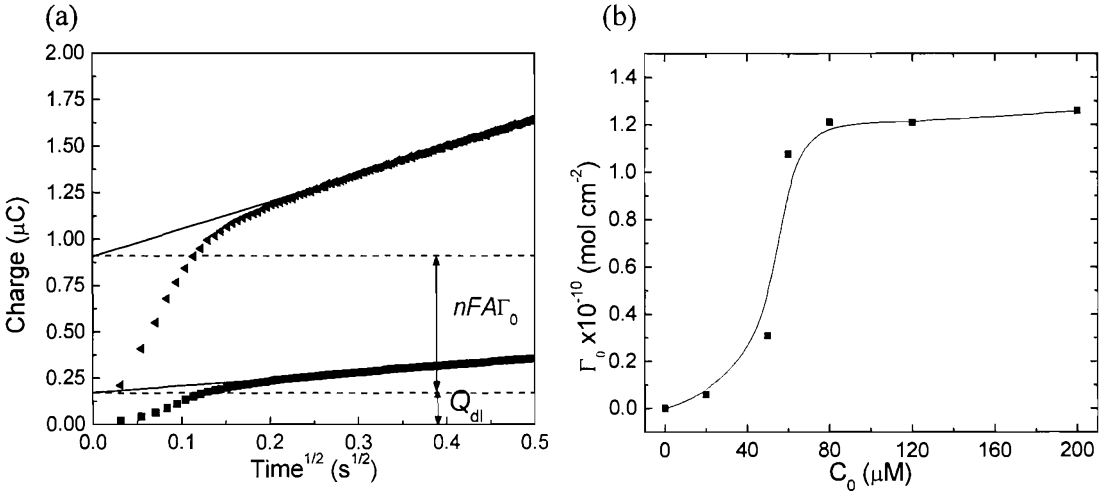

Figure 6.5 Coulometric determination of surface coverage of immobilized DNA. (A) Coulometric curves recorded by stepping the potential from 0.1 V to -0.4 V vs. SCE at a ssDNA coated electrode (6.18 mm^2) in blank electrolyte solution (pH 7, 10 mM Tris buffer) (■) and in the same electrolyte solution containing 80 μM $[Ru(NH_3)_6]^{3+}$ (◀). (B) The adsorption isotherm for $[Ru(NH_3)_6]^{3+}$ calculated from the coulometric measurements.

Based on the measured coverage of DNA on the surface and given the area illuminated by the 1 micron diameter laser spot in the spectrometer it is calculated that the spectra are recorded from approximately 12,500 molecules giving a sensitivity of detection of SERS of better than 0.02 amol. It is pointed out that this is the sensitivity of detection of SERS on SSV substrates rather than the overall limit of detection of the method implying that provided 0.02 atto-moles of molecules can be localized to the laser spot area, it should be possible to detect it easily with SERS on SSV substrates.

6.3.2 Discrimination of mutations

The allele specific 22-mer probe for detecting the synthetic wild type and mutated sequences in CFTR gene were synthesized with three disulfide linkages (Figure 6.2) at the 5'-end for attachment to the gold surface. The sequences of the probe and targets themselves are listed in Table 6.2.

Table 6.2 The probe and the target CFTR sequences for the synthetic oligonucleotides. The labels were attached to the 3' end (proximal to the surface) of the target in all cases.

Probe	5'-AGGAAACACCAAAGATGATATT-3'-HXHXHX
WT	Label-3'-TCCTTTGTGG**TTT**CTACTATAA-5'
Δf508	Label-3'-TCCTTTGTGG**---**CTACTATAA-5'
1653C/T	Label-3'-TCCTTTGT**GGTTTT**TACTATAA-5'

The oligonucleotide targets were synthesized by standard solid-phase techniques as described in Chapter 2 and labelled at the 3'-end with common fluorophores, Cy3, Texas Red and Cy5. The structures of the dyes along with their attachment are shown in Figure 6.7. In this case the 3' labelling would bring the label closer to surface which was expected to increase SER(R)S signals, as compared to the results presented in Figure 6.4 because most of the plasmons on

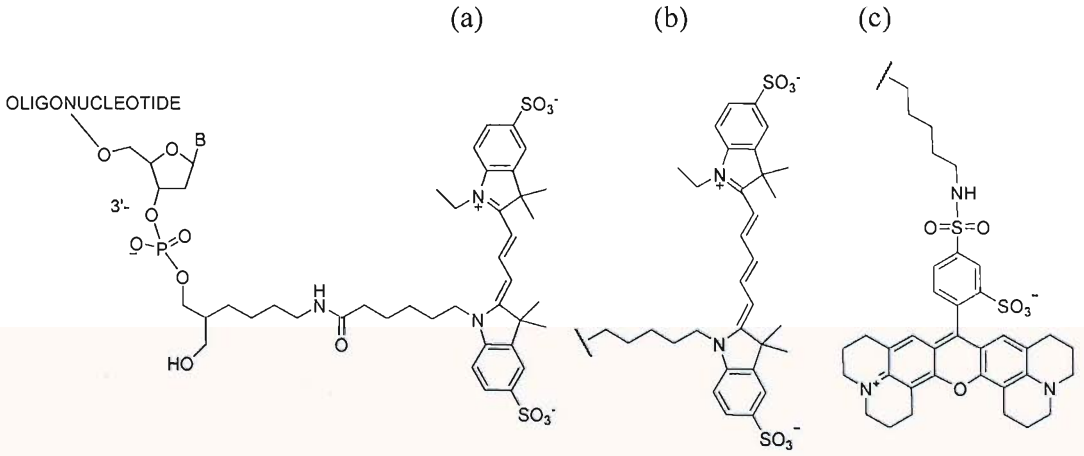

Figure 6.7 Structures of (a) Cy3 (b) Cy5 and (c) Texas Red labels coupled to the 3' end of the oligonucleotide. The linker (not shown for (b) and (c) is the same in all three cases.

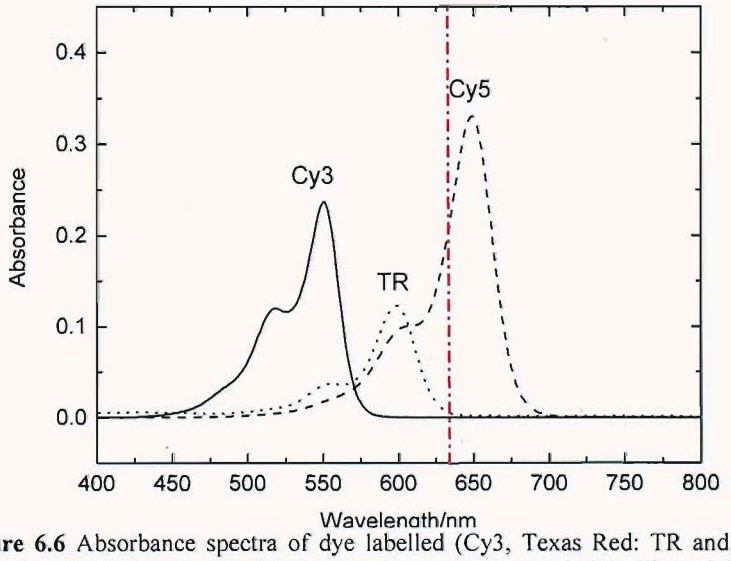

Figure 6.6 Absorbance spectra of dye labelled (Cy3, Texas Red: TR and Cy5) oligonucleotides targets at 1 μM concentration in aqueous solution. The red dashed line shows the laser wavelength at 633 nm

SSV substrates implicated in surface-enhancement have their strongest fields closest to the surface [22], though the distance dependence of SERS on SSV substrates is yet to be systematically studied. Hence, it was expected that the spectra would become much cleaner and easier to interpret. The absorbance spectra of the dye-labelled oligonucleotides are shown in Figure 6.6. Cy5 has a direct overlap of the laser at 633 nm with its electronic excitation, while the molecular absorption of Texas Red tails near the laser wavelength and that of Cy3 is distant from it. Thus, the dyes Cy3, Texas Red and Cy5 would correspond to SERS (or non-resonant SERS), pre-resonant SERS and resonant SERS (SERRS) labels, respectively, with respect to the laser wavelength of 633 nm used in this work and hence, serve to show the range of labels which can potentially be used with SSV substrates for DNA detection and mutation discrimination applications.

6.3.2.1 Scheme for distinguishing mutations

The targets were detected in a hybridization assay; the entire scheme for detection and mutation discrimination is shown in Figure 6.8. SER(R)S detection was carried out in a custom made cell with temperature and electrochemical control. Hybridization was carried out in 10 µM solutions of the labelled targets in pH 8.1 phosphate buffer containing 0.1 M NaCl for 30 min. Thereafter the substrates were rinsed by flushing the cell with the buffer at least 3 to 4 times. In experiments to discriminate mutations shown in this chapter the same substrate was used each time with the different targets, spectra were collected from the

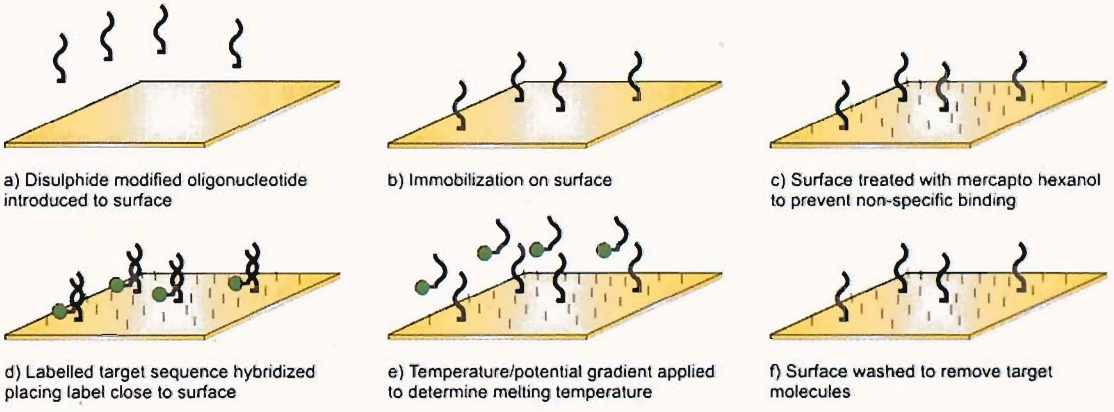

Figure 6.8 The process of detection and characterization of DNA sequences beginning with 1) and 2) preparation of the sensing surface followed by 3) passivation with mercapto-hexanol to prevent non-specific binding, 4) detection using SER(R)S labeled targets, 5) dehybridization with either temperature or potential and ending with 6) regeneration of the surface for re-use starting again at step 4). The dehybridization process is the key step and yields the information which characterizes mutations.

same area on the substrate although for each spectrum the laser spot was moved by 1-2 µm. This not only reduced any bleaching and photodegradation effects but

also serves to demonstrate that the SERS sensitivity, surface modification and melting effects are reproducible across the SSV surface. In fact the substrates are reusable and no change in melting characteristics was observed on repeated

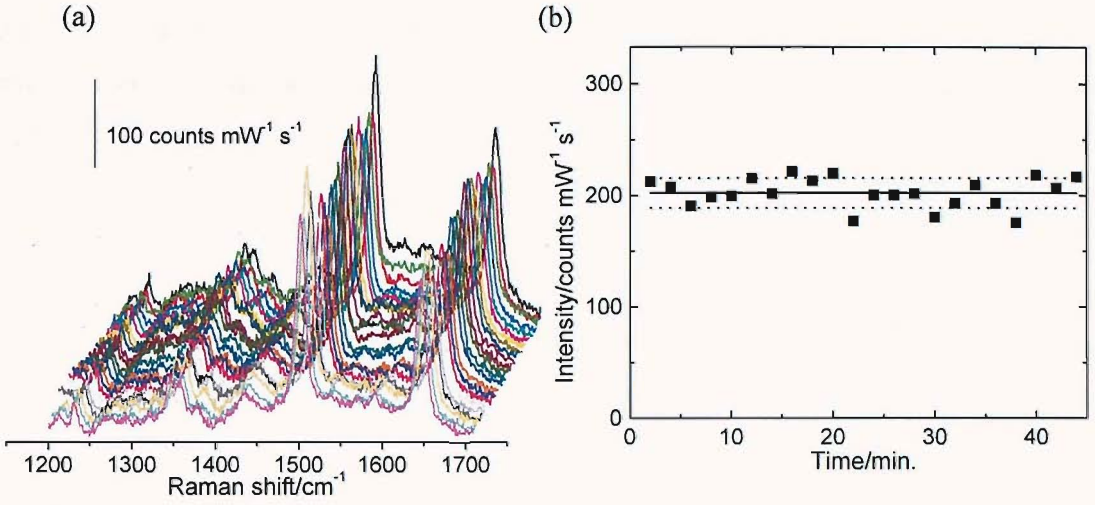

Figure 6.9 Reproducibility on the substrate with time. (a) Spectra of a Texas Red labeled target with a single mismatch (1653 C/T point mutation) after hybridization recorded on a SSV substrate recorded in blank pH 8.1, 0.01 M phosphate buffer containing 100 mM NaCl. The laser spot was moved 2 μm every ~2 min while recording the spectra in static mode with a single 10s exposure at 3 mW laser power. All spectra have been baseline corrected. (b) The peak intensity for the 1500 cm^{-1} band attributed to ring stretching mode of Texas Red plotted as a function of time for the different spectra in (a), the solid and the dotted lines show the average and std. dev (7%) range, respectively. The spectra were acquired at room temperature and open circuit potential.

measurements. Figure 6.9 shows a set of 22 spectra recorded for the Texas Red labelled 1653 C/T point mutation target hybridized to the probe on the SSV surface in the blank buffer solution at room temperature (~23 °C). The bands at 1500 cm^{-1} and 1643 cm^{-1} correspond to the Texas Red dye [18] and are assigned to the ring stretching and –NH deformation modes in the molecule. The spectra were recorded by moving the laser spot sequentially across the surface and again each spectrum is recorded in a single 10 s exposure without any spectral averaging. From the absorption spectrum of Texas Red (Figure 6.6) it can be seen that it is in pre-resonance with the 633 nm laser used here, therefore the spectra are clearer compared to Figure 6.4. A plot of the intensity of the 1500 cm^{-1} band as a function of time for the set spectra recorded at different places on the surface is shown in Figure 6.9(b). The results show excellent reproducibility and stability, < 7 % variation.

6.3.2.2 Discrimination of mutations by thermal melting

When the temperature is increased the dsDNA begins to melt, or de-hybridize, and the temperature at which this occurs will be lower if there are mismatches between the target and the probe. In the set of experiments presented for thermal

melting studies a series of SERS spectra were recorded at different temperatures on gold SSV substrates (hence, the method is called SERS-*T*melting). The temperature was ramped at 1 °C min^{-1}. Figure 6.10(a) shows a representative set of data recorded for the Cy3 labelled wild type CFTR sequence recorded in pH 8.1, 0.01 M phosphate buffer containing 100 mM NaCl (all SERS-*T*melting experiments presented in this section have been carried out using the same buffer). The bands observed at 1216, 1393, 1437, 1479 and 1589 cm^{-1} are characteristic for the Cy3 label. In this case the label is on the 3' end compared to the case of the 5' labelled target described in Figure 6.3 and Figure 6.4. The signal to noise for the 3'-Cy3 peaks is higher, probably due to proximity to the surface compared to 5'-Cy3 label in the preliminary experiments. Also, different bands are observed, probably due to a change in orientation. As the temperature increases

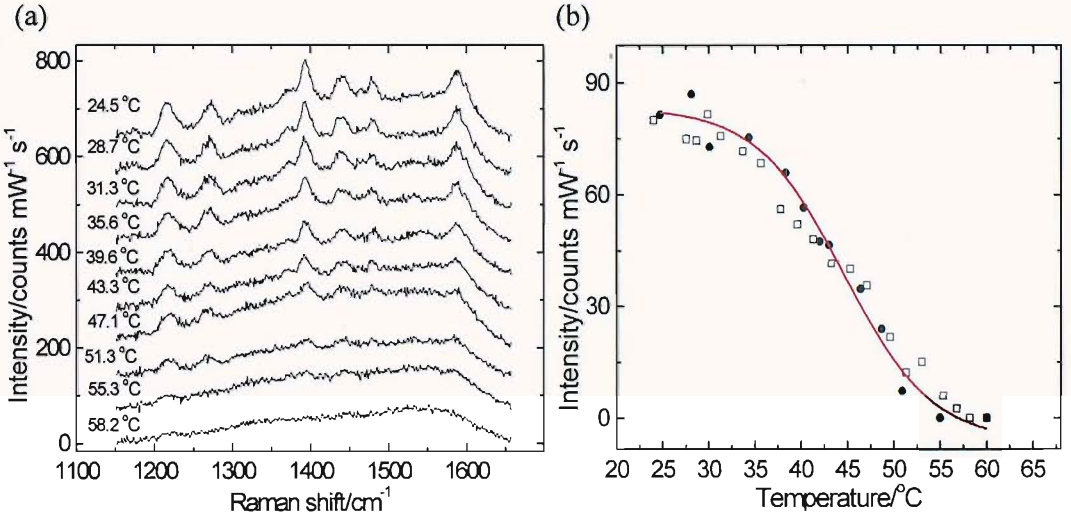

Figure 6.10 SERS-*T*melting experiment. (a) A sequential set of spectra recorded at different temperatures in a thermally induced dehybridization experiment using the Cy3 labeled wild type CFTR target sequence. The temperature of the sample was ramped at 1 degC min^{-1} in blank pH 8.1, 0.01 M phosphate buffer containing 100 mM NaCl. All spectra are baseline corrected by a straight line offset between the extremities. (b) Plot of the intensity of the 1437 cm^{-1} SERS band, corresponding to the –CH asymmetric deformation mode of the Cy3 label, as a function of temperature. Data for two consecutive replicate measurements on the same substrate are shown. Spectra were acquired under a single static scan for 20 s at 3 mW laser power.

it can be seen that the intensity of the Cy3 bands decreases sequentially, eventually disappearing at high temperature when all of the dsDNA has melted and the labelled target molecules diffuse away from the surface. It is pointed out that the SERS signal decreases because the enhancement is strongly surface specific – labelled DNA molecules which are not close to the surface (less than about 100 nm) do not contribute to the signal. The thermal melting of the dsDNA on the surface is analyzed by plotting the intensity of the SERS signal as a function of temperature. Figure 6.10b shows results for two consecutive

measurements made on the same surface, showing excellent agreement in both overall signal intensity and in the temperature variation. In both cases there is a sigmoidal drop in signal which is fitted using a Boltzmann function using Origin 7.0 software. The first derivative of the fits to the melting profiles has been taken to determine the melting points (mid-point of melting curves). In this case the analysis yields a mid point temperature of about 45 °C for both the runs. This shows that this type of SERS-*T*melting measurement is reproducible and can be used to discriminate mutations with high sensitivity.

Figure 6.11 shows SERS-*T*melting for the three different targets, wild type and two mutations. As expected the wild type, which is a perfect match for the probe melts at the highest temperature while the ΔF508 triple deletion, which is the worst match, melts at the lowest temperature. Analysis of the melting curves gives

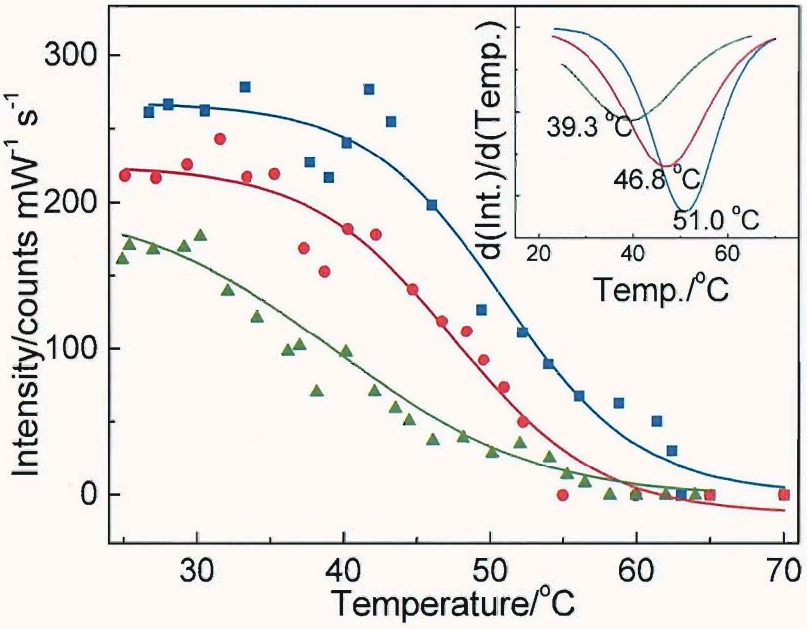

Figure 6.11 Thermally induced dehybridization monitored with SERS (SERS-*T*melting). The SERS intensity of the 1500 cm^{-1} band of the Texas Red label for the three targets, (■) wild type (no mutation), (●) 1653C/T mutation (single point mutation), and (▲) ΔF508 mutation (triple deletion) are plotted against the temperature. The first derivatives of the sigmoidal fits of the intensity curves are shown in the inset. The temperature of the sample was ramped at 1 degC min^{-1} in blank pH 8.1, 0.01 M phosphate buffer containing 100 mM NaCl. Spectra were acquired in static mode with a single 10s exposure at 3 mW laser power on the same substrate beginning with the triple deletion, followed by the single point mutation and then the perfect match.

melting temperatures (T_m), which show a difference of 4.2 °C for the single point mutation and 11.7 °C for the triple deletion as compared to the wild type. It is also noticeable that the triple deletion shows the lowest SERS intensity at all temperatures, possibly indicating lower surface coverage as a result of weaker

binding to the probe. These results demonstrate that SERS-*T*melting on SSV substrates is a very sensitive method to discriminate single nucleotide mutations.

6.3.2.3 Discrimination of mutations by electrochemical melting

The results presented above show that SERS on SSV substrates can be used to discriminate mutations by recording spectra as the temperature is increased. However, close control over the temperature and reproducible heating of the system requires special equipment and cannot be applied selectively to one region of a surface and not to a nearby region. Therefore, the effect of using the SSV substrate as an electrode and slow ramping of its potential was also investigated.

In a typical SERS-electrochemical-melting (SERS-*E*melting) experiment, after hybridization with the target the cell was flushed several times with 10 mM TRIS buffer, pH 7 and the surface equilibrated at open circuit potential for several min. Thereafter, the SSV electrode was potentiostatted and the potential decreased in steps from -0.2 V to -1.5 V *vs.* Ag/AgCl. All potentials quoted for *E*melting in this chapter are with respect to Ag/AgCl, unless stated otherwise. SER spectra were recorded at each potential step after a fixed time interval of 250 s. A typical SERS-*E*melting analysis in the present, un-optimized form therefore took less than an hour. Figure 6.12 shows results for a SERS-*E*melting experiment using the same probes and the same three Texas Red labelled targets as in the SERS-*T*melting experiment shown in Figure 6.10. As the potential is taken cathodic, Figure 6.12a, we see that the bands at 1500 and 1643 cm^{-1} characteristic of the Texas Red label first increase and then decrease in intensity, eventually disappearing at the most cathodic potential. Plotting the extracted SERS intensities of the Texas Red aromatic ring stretching band at 1500 cm^{-1} against potential yield the SERS-*E*melting profiles which are shown in Figure 6.12b. The first derivatives of the sigmoidal curve fits to the melting curves (inset) were used to define the melting potentials (E_m). As evident in Figure 6.12b, the profiles for the perfect match and the two mutations are clearly distinguishable with shifts in the melting potentials (ΔE_m) of 110 and 60 mV respectively. Again as expected the mutation with the triple deletion is the least stable and shows the most positive melting potential. In all cases the intensity of the peak for the SERS marker increases as the potential becomes more negative from -0.2 to -0.8 V before then decreasing and ultimately falling to zero at potentials more negative than -0.8 V. The initial increase is reversible and probably due to a potential dependent change in the orientation of the dsDNA and the 3' Texas Red label. This requires further study but it is worth

noting that we do not see the same effect when we use Cy5 as a label in an *E*melting experiment (presented later in Figure 6.14) or in the case of thermal melting with any of the dyes.

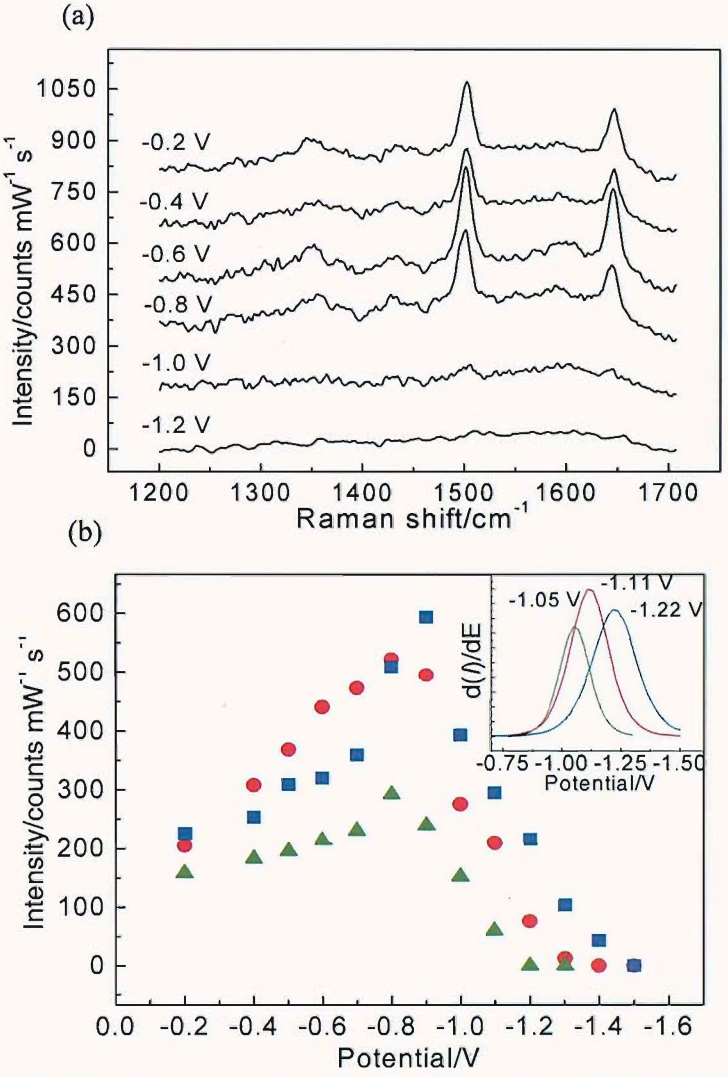

Figure 6.12 SERS-*E*melting for mutation discrimination. Electrochemical dehybridization monitored with SERS (SERS-*E*melting). (a) Representative spectra of Texas Red labelled ΔF508 synthetic target at various potentials in an actual SERS-*E*melting experiment with the intensity of peaks changing with applied potential. (b) The SERS intensities of the 1500 cm^{-1} band of the dye label (Texas Red) for the three targets, (■) wild type (no mutation), the (●) 1653C/T mutation (single point mutation) and the (▲) ΔF508 mutation (triple deletion) are plotted against the applied potential. The first derivatives of the sigmoidal fits of the intensity curves are shown in the inset with the melting potentials shown above each curve. Spectra were acquired in static mode with a single 10s exposure at 3 mW laser power on the same substrate beginning with the triple deletion, followed by the single point mutation and then the perfect match, in pH 7, 10 mM Tris buffer.

6.3.2.3.1 Reproducibility of SERS-Emelting

Figure 6.13 shows results for consecutive SERS-*E*melting experiments using the same SSV substrate and the Texas Red labelled ΔF508 target. After the first SERS-*E*melting measurement the substrate was stored in buffer solution for 3 days (to show the stability of the sensing system) and then rehybridized with the same target. There is near reproducibility in both the intensity profiles of the SERS signal and in the *E*melting characteristic with excellent agreement in the melting potential, E_m, for the two measurements. These results show that the loss of SERS signal at high cathodic potentials arises from melting of the dsDNA and loss of labelled target from the surface and not through reductive desorption of the DNA probe (reductive desorption can occur in our experiments but it does not become significant until the potential is taken more negative than -1.3 V vs. Ag/AgCl). These results demonstrate the excellent reusability of these surfaces for DNA detection and mutation discrimination and also show the stability and reproducibility of the SSV gold SERS substrates used during this work.

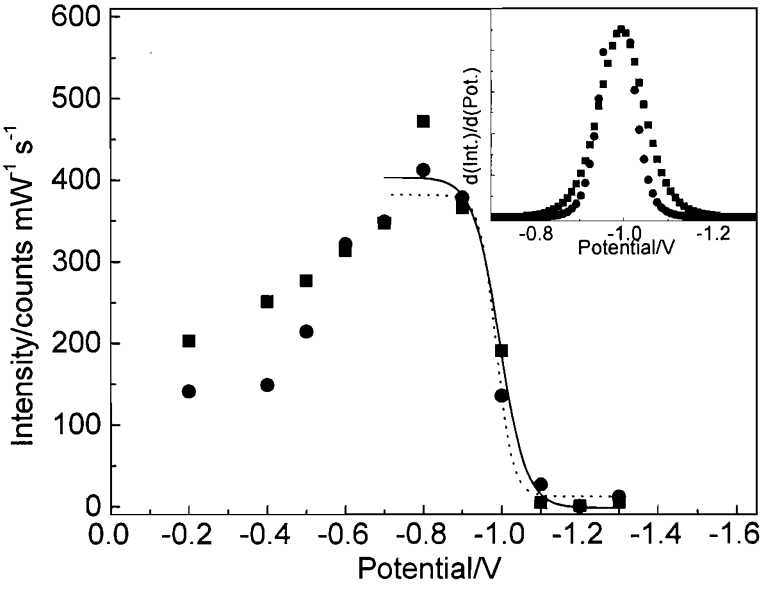

Figure 6.13 Reproducibility of SERS-*E*melting. The peak intensities for the 1500 cm^{-1} band for Texas Red labelled ΔF508 target oligonucleotides are plotted as the function of potential for two successive measurements carried out 3 days apart on the same DNA probe modified SSV substrate (■: 1st run, ●: 2nd run). The dehybridization profiles are reproducible on the substrates with almost no variation in the melting potential values; 0.99 V and 0.98 V, respectively (the first derivatives of the fitted profiles are shown in inset). Spectra were acquired in static mode with a single 10s exposure at 3 mW laser power in pH 7, 10 mM Tris buffer.

6.3.2.3.2 Flexibility and information from SERS-Emelting

SER(R)S spectra are quite rich in information about changes in orientation and can be used to study the melting process in detail. Figure 6.14a shows a set of SERRS (or resonant SERS) spectra recorded at different potentials for the 3' Cy5 labelled complementary target hybridized to the immobilized probe on the SSV surface. As mentioned earlier, Cy5 label is resonant with the 633 nm laser used in

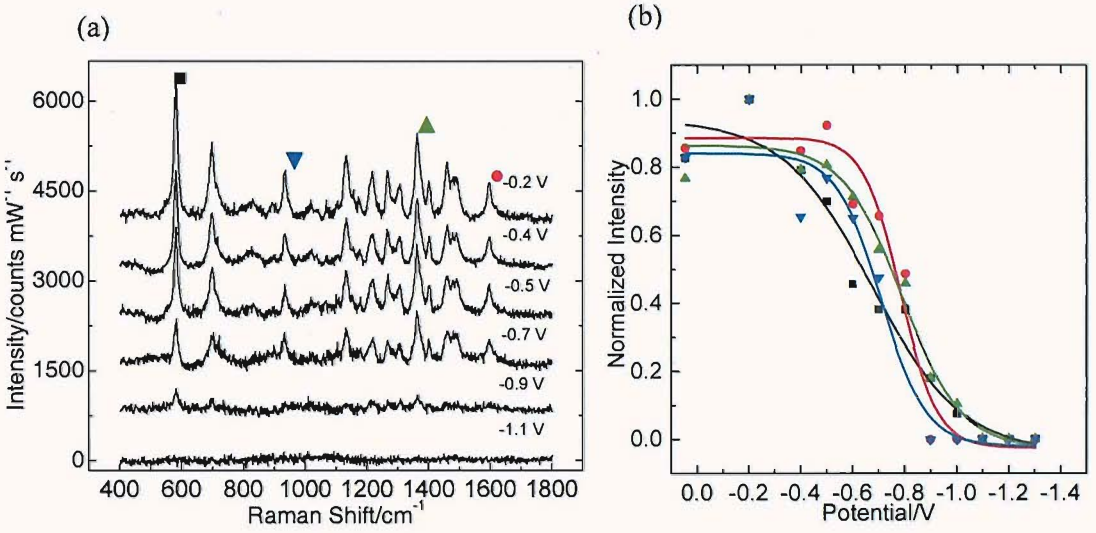

Figure 6.14 (a) SERRS (or resonant SERS) spectra of Cy5 labelled complementary strand recorded at the different potentials indicated beside each spectrum. The spectra are offset for clarity. (b) Normalized resonant SERS-*E*melting profiles extracted from the SERRS bands at (■) 583 cm^{-1} (▼) 935 cm^{-1} (▲) 1367 cm^{-1} and (●) 1597 cm^{-1} for the Cy5 labelled synthetic target strand. Spectra were acquired in the extended mode with a single scan set to 3 s collection time at 3 mW laser power in pH 7, 10 mM Tris buffer.

these experiments and so, as expected, the signals in the SERR spectra of this label are significantly more intense (in this case by a factor of 4-5) than those for the partially resonant Texas Red label. The bands at 583 and 935 are assigned to alkene chain and aromatic CH deformation modes, and those at 1367 cm^{-1} and 1597 cm^{-1} to methine chain deformation and C=N stretching modes respectively, and are characteristic of Cy5 [18]. Figure 6.14b shows normalized melting profiles calculated from four different bands in the Cy5 spectrum. In each case the intensity of the band decreases as the potential moves cathodic but it is noticeable that there are no significant shifts in peak position. The melting profiles derived from each band may give some information about the conformational changes which accompany partial melting of the dsDNA. This is an area which deserves further study.

With Cy5 as the label the electrochemical melting profile is shifted 400 to 450 mV less negative, depending on which band we take, as compared with the value for the corresponding Texas Red labelled target (Figure 6.12). Thus, the particular choice of the label has a significant effect on the stability of the surface bound dsDNA. At neutral pH Cy5 is a di-anion whereas Texas Red is a zwitterion; it is speculated that the difference in the SERS-*E*melting profiles is caused by the

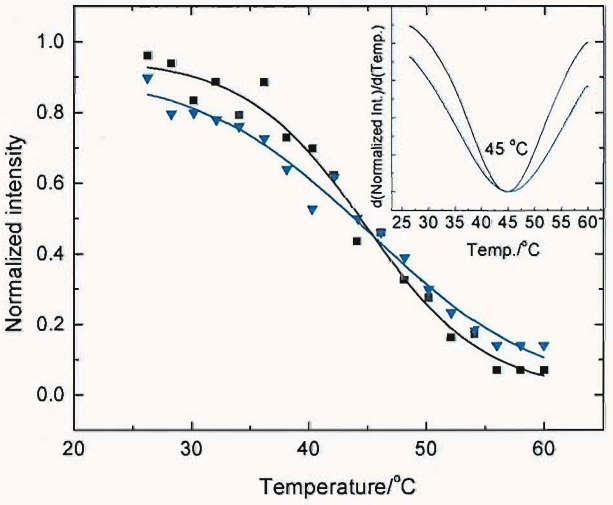

Figure 6.15 Resonant SERS-*T*melting profiles with 3'-Cy5 labelled wild type target sequence, the background corrected normalized intensities of the peaks at 583 cm^{-1} (■) and 935 cm^{-1} (▼) are plotted. The first derivatives are shown in the inset. Spectra were acquired in the static mode with a single scan set to 10 s collection time at 0.3 mW laser power.

additional negative charge on the Cy5 label at the 3' end of the target leading to dehybridization at lower potentials and temperatures. Resonant SERS-*T*melting data for Cy5-labelled target is shown in Figure 6.15 for ready reference. The melting temperature of the perfect match with 3' Cy5 label was found to be 45 °C, which is 6 degrees lower than that measured for the corresponding 3' Texas Red labelled target shown in Figure 6.11. It is also noted that for the Cy5 labelled system the initial increase in SER(R)S intensity observed with Texas Red in *E*melting experiment (Figure 6.12) is not found and also that the melting profiles for Texas Red labelled oligonucleotides are sharper as compared to Cy5 labelled sequences. These effects highlight the possibility of optimizing the choice of SER(R)S label in future work.

6.3.2.3.3 Emelting with Electroactive SERS labels on oligonucleotides

Apart from using conventional labels such as common fluorophores as SER(R)S markers, which have been discussed so far in the chapter, there exists an interesting possibility of using molecules which are electrochemically as well as SERS active. Such a strategy would combine the benefits accruing from SER(R)S

as well electrochemistry. This was investigated by using synthetic 22-mer oligonucleotides labelled with a modified anthraquinone at the 3'-end as shown in Figure 6.16. Yamana and coworkers have studied anthraquinone labelled DNA sequences utilizing electrochemical detection of mismatches relying on differential electron transfer through DNA duplex [23-25]. Their method relies on the concept

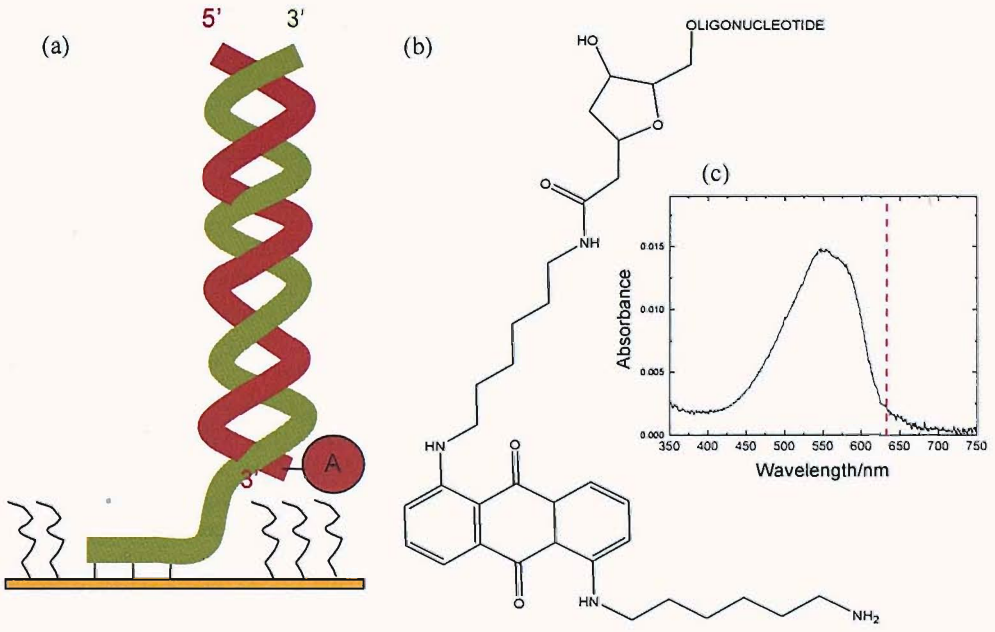

Figure 6.16 Scheme showing the (a) label position, (b) the structure of the modified anthraquinone attached at the 3'-end of the targets and (c) the absorbance spectra of a 1 μM anthraquinone labelled target in an aqueous solution.

that electron transfer through the duplex is inhibited if the anthraquinone label (which intercalates into the duplex) is located after the mismatch (farther from the surface) compared to when it is located before the mismatch (nearer the surface). The SERS-*E*melting approach is simpler than differential electron transfer methodology and does not rely on the position of the label for differentiation of mutations. Other advantages become apparent with the results presented under this sub-section for the same synthetic CFTR sequences listed in Table 6.2.

It was first confirmed that the modified anthraquinone remained electrochemically active after labelling and after hybridization with the probe on the surface. This was carried out by performing cyclic voltammetry in a pH 7, 100 mM phosphate buffer. Voltammograms acquired at various scan rates are shown in Figure 6.17a. the peak currents for the cathodic as well as anodic wave show linear dependence with scan rate as expected for surface bound redox species. The mid-peak potential is around -0.4 V. It is also observed that the peak currents show a shift with increasing scan rate. The voltammetric behaviour, such as

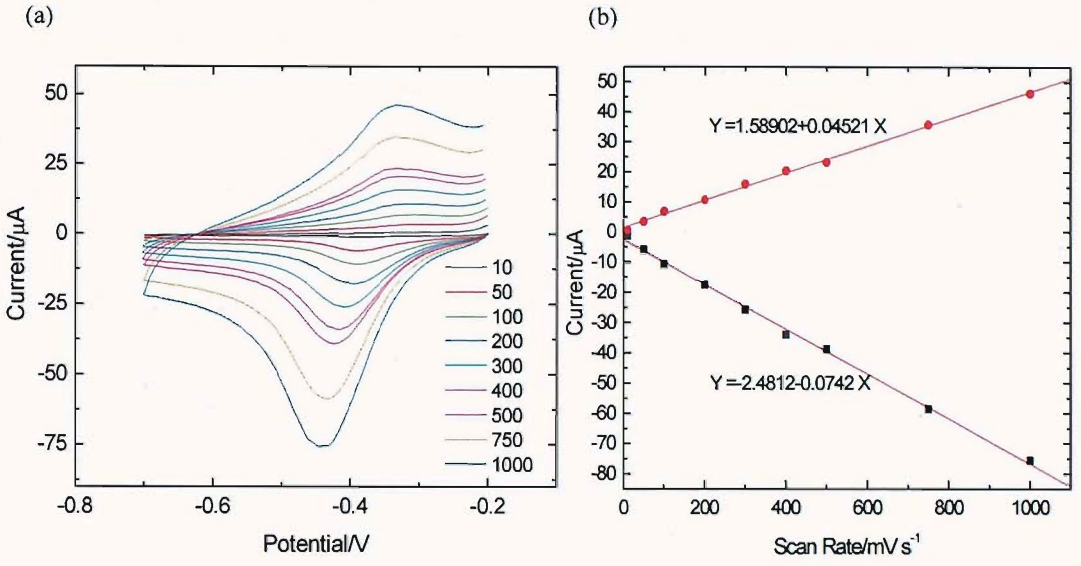

Figure 6.17 (a) Cyclic voltammograms at different scan rates (in mV s^{-1}) of anthraquinone labelled WT target hybridized to surface bound probe in pH 7, 100 mM phosphate buffer on gold surface (area : 0.5 cm^2). (b) The anodic (●) and cathodic (■) peak currents have been plotted versus scan rate. The linear regression lines are also shown. The potentials are with respect to a Ag/AgCl reference electrode.

variation of peak position with scan rate itself, is interesting and can be studied to yield information on the electron transfer kinetics and non-idealities in the reversible behaviour [26] seen for the anthraquinone label on the target. However, this is deferred to subsequent studies.

Having confirmed the redox activity and the stability of surface bound anthraquinone labelled targets, they were utilized in SERS-*E*melting experiments. Anthraquinone labelled targets were found to have an absorbance maximum around 547 nm, hence, not completely in resonance with the 633 nm laser utilized in the experiments but there is some overlap with the tail of the absorption spectrum (see Figure 6.16c). SERS spectra are presented at different potentials for the single point mutation target (1653C/T) on a gold SSV substrate in Figure 6.18. The intensity of peaks observed is larger than those observed for Cy3 and comparable to Texas Red. However, the noise in the spectra is greater than that for Texas Red label because much higher backgrounds were observed forcing either a reduction in laser power or collection times. Nevertheless, after background subtraction the SERS peaks similar to those observed for dimethyl-aminoanthraquinone on silver [27] can be clearly seen. In particular, the peaks at 1559 cm^{-1} assigned to ring stretching and at 1375 cm^{-1} assigned to C-N stretching are among the strongest at all potentials. However, on reduction at -0.4 V, among others, a new strong peak at 1301 cm^{-1} is observed which subsequently decreases in intensity at more negative potentials. Nishiyama *et al.* have studied SERS of

anthraquinone monolayers immobilized through a sulphide linkage on gold and silver surfaces [28]. In their work new bands in the region of 1300 cm^{-1} to 1450 cm^{-1} at -0.4 V (vs. Ag/AgCl) were observed on silver and are attributed to partial reduction of the anthraquinone to anthrahydroquinone (the semiquinone form) at these potentilas, though no assignment has been given for the bands around 1300 cm^{-1}. With the 3'-anthraquinone labelled oligonucleotides similar changes are seen as the reduction sets in on scanning the potential cathodic. The band at 1301 cm^{-1} observed here is assigned to *v*C=C + *v*C-N vibration based on the SERS of substituted anthraquinones by Lee *et al.* [29]. Beyond -0.4 V the semihydroquinone reduces to the hydroquinone form and the peak at 1301 cm^{-1} almost vanishes while some new peaks around 1225 cm^{-1} are observed. Nevertheless, the peak attributed to ring stretching, observed in Figure 6.18 at 1559 cm^{-1}, has been found to be independent of the redox state of the molecule [28]. Hence, for mutation discrimination using anthraquinone labelled probes the SERS-*E*melting curves are plotted by extracting the peak intensity after background subtraction for the 1558 cm^{-1} peak.

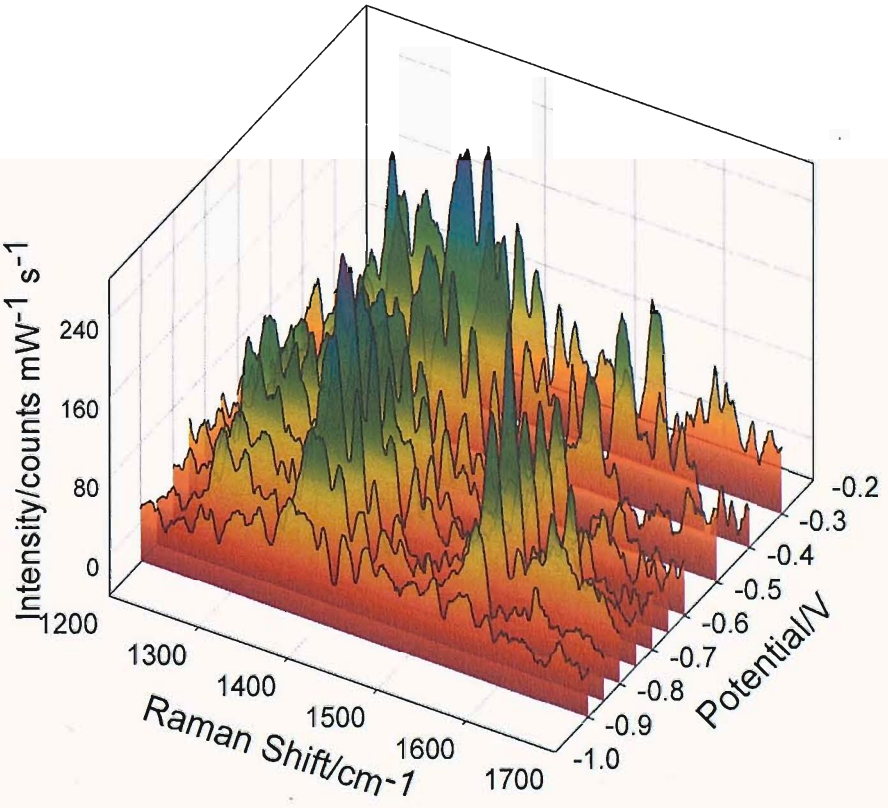

Figure 6.18 SERS spectra for anthraquinone labelled 1653C/T (single point mutation) target hybridized to the probe on a gold SSV substrate at different potentials in an *E*melting experiment. Spectra were acquired with a 633 nm laser with a single accumulation of 5 s at 1 mW laser power. The spectral intensity has been normalized by the laser power and collection time.

SERS-*E*melting profiles for the three targets corresponding to the perfect match, single mismatch and triplet deletion are shown in Figure 6.19. It can be readily seen that SERS peak intensity for the 1559 cm^{-1} shows a different profile for the three targets during electrochemical denaturation. As expected the wild type shows the most negative melting potential indicating that the hybrid is most stable in this case compared to the single and triple mismatches. The variation observed in peak intensities at potentials less negative than -0.6 V is attributed to the reduction of the label along with accompanying changes in the orientation of the duplex. It is expected from the voltammetry presented in Figure 6.17 that the anthraquinone should be fully reduced beyond -0.6 V and hence, changes in the SERS peak intensity can be wholly attributed to de-hybridization of the target and its diffusion away from the surface. The melting potentials show clear and unambiguous distinction between the three strands with E_ms determined at -0.98, -0.87 and -0.76 V for Wild type, 1653C/T and ΔF508 sequences, respectively. Thus, this experiment demonstrates that an electrochemically active label such as anthraquinone can also be used to detect and differentiate mutations in DNA sequences with SERS.

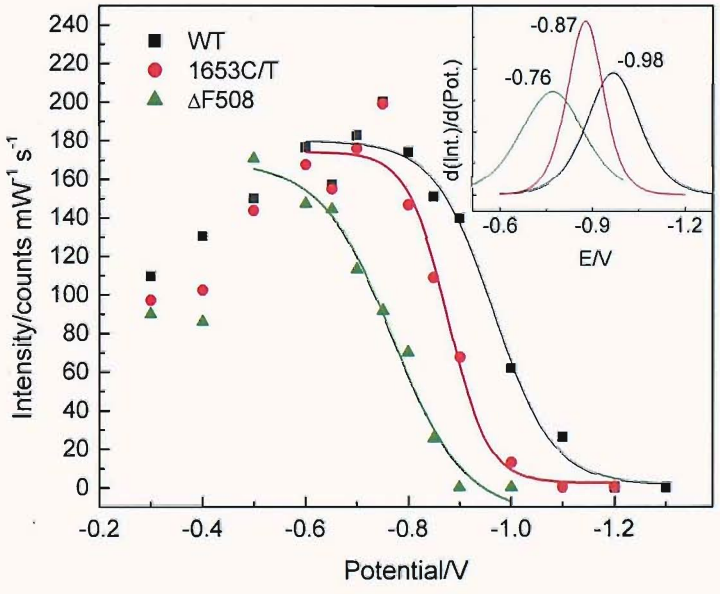

Figure 6.19 SERS-*E*melting profiles plotted using the 1559 cm^{-1} peak for (■) Wild type, perfect match, (●) 1653C/T, single mismatch and (▲) ΔF508, triple deletion, anthraquinone labelled targets on a gold SSV substrate in pH 7, 10 mM Tris buffer. The first derivatives of the sigmoidal fits are plotted in the inset along with the determined E_ms.

The real advantage of combining SERS with electrochemical activity of the label is the ability to quantify the actual number of targets hybridizing to the surface by using electrochemical techniques. Hence, with the anthraquinone labelled oligonucleotides coloumetric determination as outlined in sub-section 6.3.1.1 was carried out without the need for adding any external redox probe. The charge transients are presented in Figure 6.20. In this case a potential pulse was applied from 0.2 to -0.6 V to ensure complete reduction of the label. Compared to the ruthenium hexamine method of Steel *et al.* [21] this is much simpler and direct in that there is no need to determine the isotherm for $[Ru(NH_3)_6]^{3+}$ binding. In this case the charge consumed, on applying the reductive pulse, over and above that

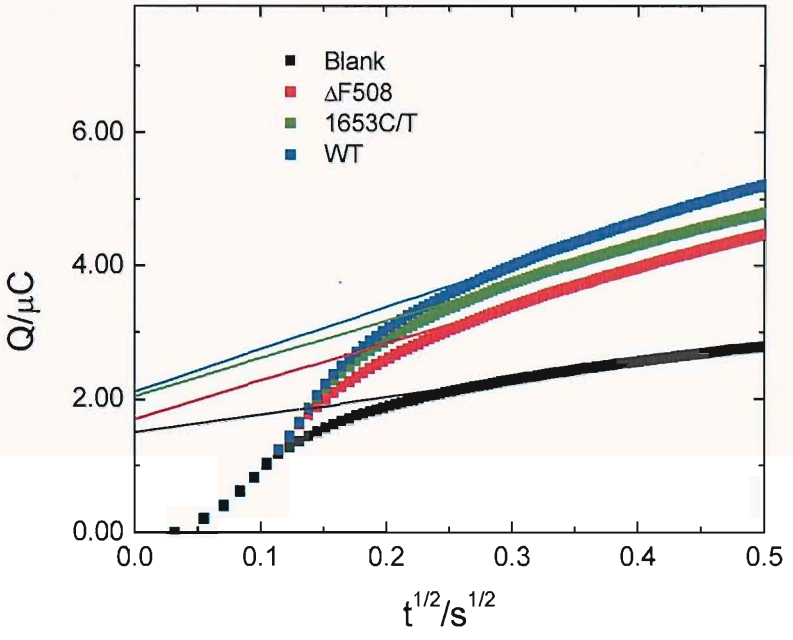

Figure 6.20 Coulometric transients recorded by stepping the potential from -0.1 V to -0.6 V **vs.** SCE with just the (black) blank probe immobilized and MCH treated gold electrode (88 mm^2) in electrolyte solution (pH 7, 10 mM Tris buffer) and in the same electrolyte solution after hybridization with anthraquinone labelled ΔF508 (red), 1653C/T (green) and WT (blue) targets. The transients were acquired with the same electrode beginning with the blank, triple mismatch, single mismatch and finally perfect match. The hybridization was carried out separately in another reaction vessel and washed before recording the charge transient. After each coulometric curve was recorded with the respective target, the surface was regenerated by leaving the electrode in 10 mM NaOH for 15 min and subsequently washing with deionized water. The regeneration was checked as the charge transient with the probe only (blank) was recovered.

for the double layer charging is directly related to the surface coverage. The only underlying assumption is that the double layer capacitance does not significantly change after hybridization, which is reasonable and stated by the authors of the $[Ru(NH_3)_6]^{3+}$ method [21] as well.

Using Equation 6.1 the charge due to the bound target possessing the electroactive label is determined by subtracting the intercept (Figure 6.20) for the

blank determination from that for each of the different targets. It is noted that for the traces obtained in Figure 6.20 the diffusion limited regions should ideally be flat in this case of only surface bound redox species; probably this indicates side reactions due to buffer components, etc. in the solution. The results are summarized in Table 6.3. The surface coverage for the fully complementary target is found to be 2.19×10^{12} molecules per cm^2, which is similar but slightly larger than that determined for the 25-base long probe in section 6.3.1 for preliminary SERS experiments. This could probably be due to the smaller probe (22-mer) used in these experiments. Further, it can be seen that the surface coverage increases as the number of mismatches decreases; thus, it is lowest at 8.15×10^{-11} molecules per cm^2 for the ΔF508 (triplet deletion) and highest for the WT (perfect match). The difference between the fully complementary and the single point mutations is significantly less compared to the triple mismatch. From the surface coverage obtained here, the number of molecules in the 1 micron diameter laser spot used in the SERS measurements can be calculated. This yields only around 6500 molecules for the ΔF508 (triplet deletion), which again reaffirms the extreme sensitivity of detection.

Table 6.3 Calculation of surface coverage of anthraquinone labelled targets using coulometry after hybridization. The hybridization was carried using 25 μM solution of the target in pH 8.1, 10 mM phosphate buffer containing 100 mM NaCl for 45 min.

Target oligo	Intercept/C (blank = 1.49E-06)	$nFA\Gamma_0$/C	Γ_0/mol cm^{-2}	Γ_0/molecules cm^{-2}	Molecules in 1 μm diameter laser spot
WT	2.11E-06	6.20E-07	3.65E-12	2.19E+12	17271
1653C/T	2.05E-06	5.60E-07	3.29E-12	1.98E+12	15600
ΔF508	1.72E-06	2.30E-07	1.35E-12	8.15E+11	6407

n=2, F is the Faraday constant (96485 C/mol), A=0.88 cm^2

6.3.2.3.4 Choice of buffer for Emelting

The work presented in this chapter on *E*melting has been carried out in pH 7, 10 mM Tris buffer while for the *T*melting work, a pH 8.1, 10 mM phosphate buffer with 100 mM added NaCl has been used. It is pointed out that both the methods work in either of the two buffers employed. This is corroborated by two examples shown in Figure 6.21 where electrochemically induced SERS-melting profile is obtained in

pH 8.1, 10 mM phosphate buffer containing 100 mM NaCl (top panel in Figure 6.21) and thermally induced melting is obtained in pH 7, 10 mM Tris buffer containing 1 M NaCl (bottom panel in Figure 6.21). Though the melting potential obtained in Figure 6.21 in phosphate buffer is slightly lower at -0.95 V compared to that in Tris buffer (Figure 6.13), the difference in the profile could possibly be due to a change in pH of the buffer. Similarly, the melting temperature obtained with SERS-*T*melting in Figure 6.21 is higher than that observed in phosphate buffer (Figure 6.11) probably due to the less alkaline pH and also due to higher concentration of salt in the buffer. Thus, the choice of buffers is of no particular significance except that Tris buffer is commonly used in electrochemical experiments and hence, was chosen initially for *E*melting experiments.

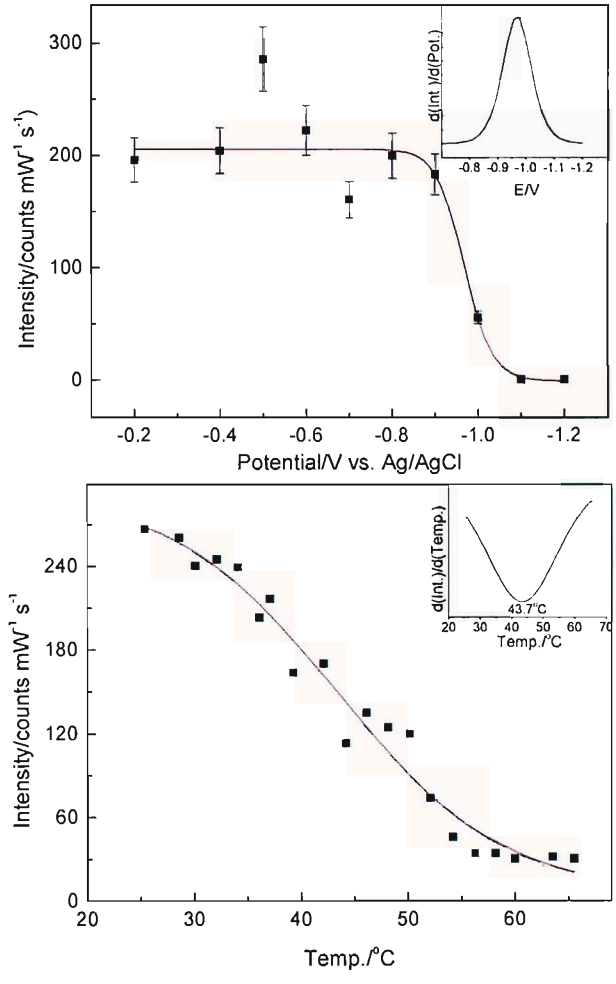

Figure 6.21 SERS-*E*melting in phosphate buffer (top) and SERS-Tmelting in Tris buffer (bottom). The peak intensities for the 1500 cm^{-1} peak for Texas Red labelled ΔF508 synthetic target oligonucleotides are plotted with potential in a SERS-*E*melting experiment in pH 8.1, 10 mM phosphate buffer containing 0.1 M NaCl and in pH 7, 10 mM Tris buffer containing 1 M NaCl

6.3.3 Application of SERS-*E*melting to analysis of PCR products

The examples described above clearly demonstrate that there are readily measurable differences in the SERS-Melting responses and that discrimination of mutations is possible for a model system. To demonstrate the potential practical utility of the method we carried out mutation discrimination experiments with PCR products of the wild type and ΔF508 mutated sequences from the CFTR gene. The primers in this case were labelled with Cy5 and the surface bound probe sequence was redesigned (for sequences see Chapter 2). For the PCR product the target strand is much longer; it is a 103-mer as compared to the synthetic 22-mer target oligonucleotides described in section 6.3.2. When hybridized to the probe sequence on the surface the PCR product has overhanging sequences at both ends with a 15 base long non-overlapping part of the primer on the 3'-end as well.

Figure 6.22 shows results for the SERS-*E*melting experiment with the PCR product. The target solution was as obtained after PCR without any purification;

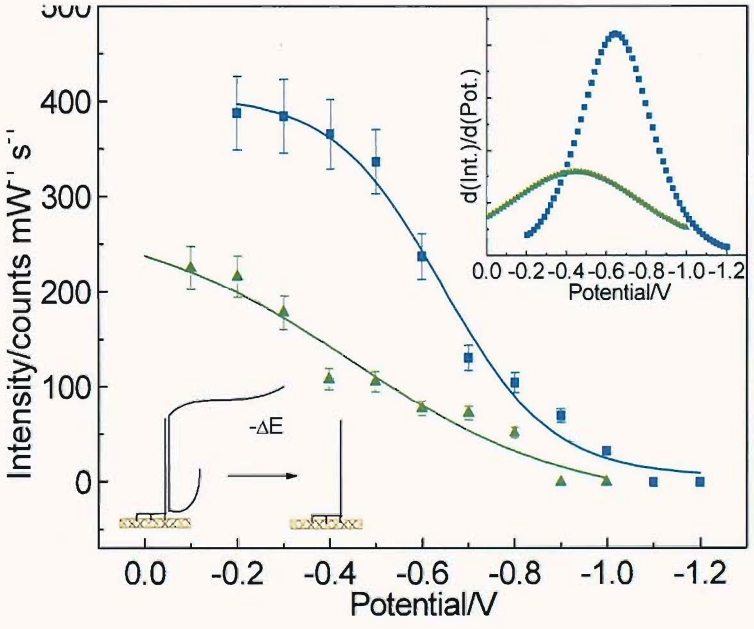

Figure 6.22 The resonant SERS-melting profiles of the PCR products for wild type (■) and ΔF508 mutation (▲) using the 1347 cm^{-1} SERRS (resonant SERS) band for Cy5. A schematic of the dehybridization process of the PCR products is shown. The first derivatives of the melting profiles are shown in the inset. The mutation has a melting potential of -0.44 V while that of the wild type is -0.64 V *vs.* SCE. Spectra were acquired with a single static scan of 2 s exposure at 1.5 mW laser power in pH 7, 10 mM Tris buffer.

hence, it contained residual dNTPs (~1 mM), primer, $MgCl_2$ and DNA polymerase, complementary amplicon (~0.05 μM) besides the target amplicon (0.2 μM). Once again there is still a significant difference of 200 mV between the melting potential (ΔE_m) of the mutation and the wild type. Compared to the results for the model system labelled with Cy5, shown in Figure 6.14, the melting profile is shifted to

less negative potentials by about 200 mV. It is probably due to the increased destabilization of the duplex at the surface due to the longer overhanging strands of the PCR product. The negative control for the PCR products was also tested with the same procedure and no signal from the Cy5 label could be observed confirming that there is no non-specific binding and no contamination of the

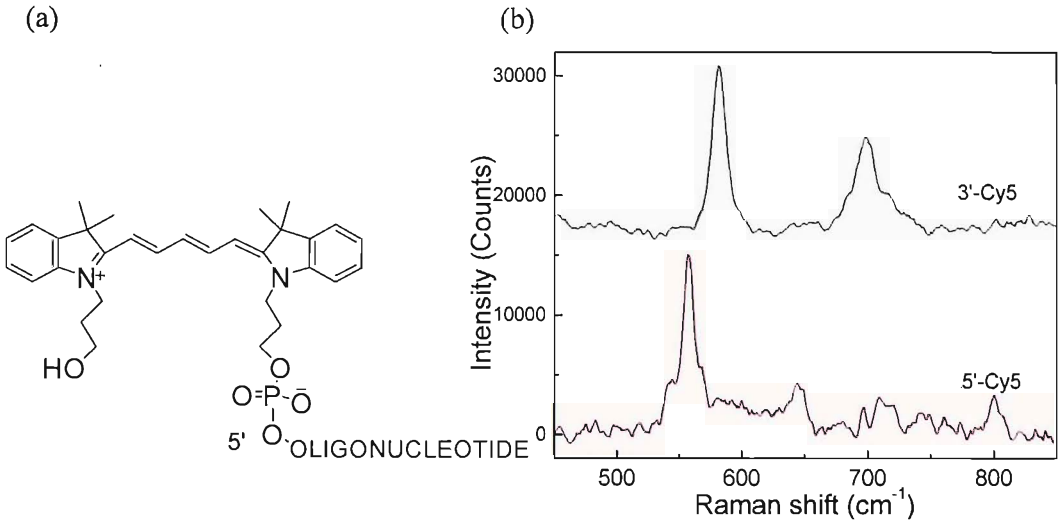

Figure 6.23 Structure and SERS spectra of Cy5 targets. (a) The Cy5 used attached using phosphoramidite chemistry. (b) Spectra for each of the target oligonucleotide labelled with the respective Cy5s. They show a distinct shift of the bands, for example the 583 cm^{-1} peak shifts to 557 cm^{-1}. The spectra have been offset for clarity.

sample during PCR, which was also separately confirmed by gel electrophoresis.

Further, in comparison with the results in Figure 6.14 the positions of several of the Cy5 bands were found to be shifted. This was traced to the fact that in case of the synthetic model oligonucleotides (22-mers) the Cy5 label was attached at the 3'-end through –NHS ester coupling while in case of the PCR products the primer was labelled at the 5'-end through a modified phosphoramidite. Also there are two sulphonate groups attached to the Cy5 coupled through –NHS ester compared to that added as a phosphoramidite (Figure 6.23a). These differences lead to a distinct spectrum for each of the labels. As shown in Figure 6.23b, it results in a 25 cm^{-1} shift in the band corresponding to the alkene chain deformation of the Cy5 molecule and was easily identified with SERRS on SSV substrates. Also, the peak at 700 cm^{-1} due to the C-S stretch is not present in the 5'-Cy5 spectrum compared to that of 3'-Cy5 as expected due to the absence of sulphonate groups. Any change due to the slight structural differences would have been extremely difficult to detect by fluorescence.

6.3.4 Discussion on SERS-*E*melting

Thermal melting of dsDNA to discriminate mutations is usually applied in solution with fluorescence monitoring rather than to surface bound DNA though such approaches have been used in microarrays. The thermal melting study described in this chapter demonstrates the first use of *in situ* SER(R)S dehybridization of dsDNA, which we show can be employed for distinguishing mutations. Peterlinz *et al.* [30] have described the application of thermal melting to dsDNA attached to a gold surface followed by SPR where they showed a clear difference in the melting temperature depending on the electrolyte concentration but did not discriminate between different DNA target strands. In our case, as described above the approach shows excellent selectivity for single point mutations and excellent sensitivity. This is in large part due to the high sensitivity of the SER(R)S technique coupled to the excellent stability of our SSV substrates which provide high SERS enhancement, even when the temperature is cycled and the substrates are reused.

Although the SERS-*T*melting method works well, the novel SERS-*E*melting approach presented in this chapter has significant advantages since potential control can be localized more easily and is therefore more suitable for miniaturization, addressability, integration with integrated circuit (IC) technology and has lower implementation costs than precise temperature control.

It is of interest to consider the mechanism of discrimination in our experiments.

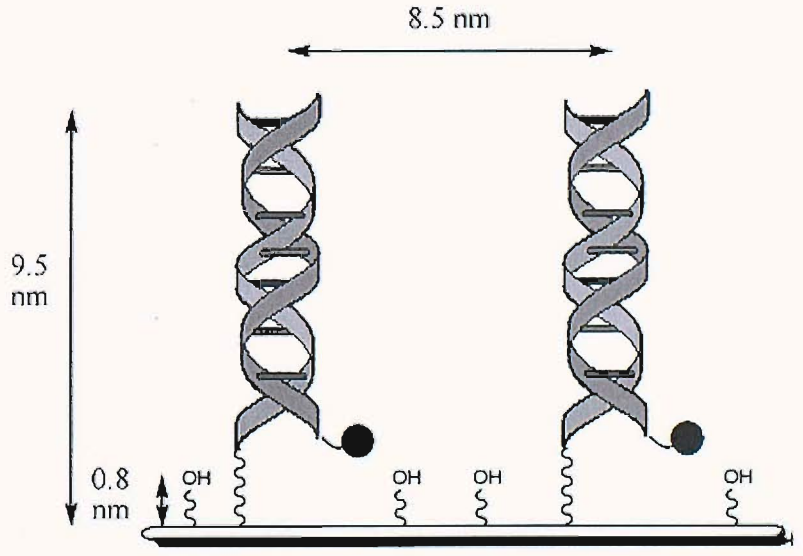

Figure 6.24 Schematic showing the configuration at negative electrochemical potentials on a gold surface with estimated dimensions (approximately to scale) of the distribution of the DNA sequences in the mercaptohexanol layer for a 25 base long probe (total length is ~9.5 nm=8.3 nm + 1.2 nm for linker to surface).

The persistence length for double stranded DNA is 80 nm [31], significantly longer than the 25-mer and 22-mer duplexes used in our experiments which are less than 10 nm long. Thus the dsDNA approximates to a rigid cylinder with a effective diameter, including the 0.5 nm thick counter-cation sheath due to Manning condensation [32], of 3 nm attached to the gold surface through the six gold thiol bonds by a flexible hexaethyleneglycol (HEG) linkage 1.2 nm long. The measurements of surface coverage give an average surface area of 0.016 nm^2 for the 25 base DNA probe so that, on average the strands are 8.5 nm apart. The gold between the DNA probes is covered by a layer of mercaptohexanol around 0.8 nm thick [33]. Several studies using a range of techniques have established that for dsDNA immobilized on gold surfaces co-immobilised with mercaptohexanol the DNA stands up and extends out into the solution [34, 35] and that as the applied potential changes the orientation of the attached dsDNA can be switched from near the surface at potentials close to the potential of zero charge (pzc) to perpendicular to the surface at potentials negative of the pzc [36, 37]. Thus we can picture the dsDNA at the electrode surface at the negative potentials where the electrochemically driven denaturation occurs as shown in Figure 6.24. The reversible change in orientation of the dsDNA with applied potential reported in the literature [34, 36, 37] is consistent with the reversible changes in SERS intensity seen in Figure 6.12 and Figure 6.13 for the Texas Red labelled molecules. The results of our experiments are in general agreement with the thermodynamic calculations of Vainrub and Pettitt [38, 39] on the electrostatic effects on DNA hybridization at electrode surfaces which predict that potentials negative of the potential of zero charge should decrease the stability of the dsDNA at the electrode surface and enhance melting. In the simple Gouy Chapman model the bulk of the potential in the double layer at the electrode surface is dropped over the Debye length [37-39], which for our buffer solution is ~3 nm, with the field decaying to zero over three multiples of the Debye length. Thus in the current work most of the dsDNA might be expected to be within the double layer. However, it is possible that the *E*melting effect is not only due to the effect of the potential but also to local changes in pH caused by electrode reactions.

6.3.4.1 Effect of pH on *E*melting

It is well known that the duplex denaturation is facilitated by an increase in pH. The affect of pH on *E*melting was verified and the results are presented in Figure 6.25. SERS-*E*melting was carried out with the synthetic ΔF508 target labelled with

Texas Red at the 3'-end (same as that used in 6.3.2) hybridized to the probe on gold SSV substrate in isotonic buffer solutions, the total ionic concentration was kept constant at 10 mM. As expected a decrease in melting potentials is observed

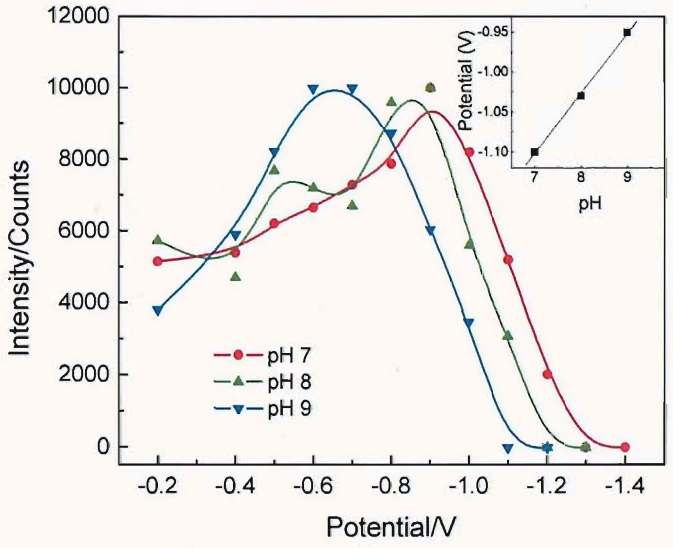

Figure 6.25 Effect of pH on electrochemical denaturation on the structured gold surface. The SERS-*E*melting profiles of the ΔF508 target in isotonic Tris buffers are shown. The ionic strength was adjusted to 10 mM by using NaCl. The intensities have been normalized to the respective maximum at each pH. The melting potentials are plotted against the pH of the solution in the inset.

on increasing the pH demonstrating that duplex binding becomes weaker with increasing pH. It is noted that the intensity maximum in the melting curve also progressively shifts towards less negative potentials with an increase in pH. Nevertheless, this experiment shows that the pH does have an effect on electrochemical denaturation in that increasing pH makes the melting easier, however, this does not show that the pH actually increases near the surface on the cathodic scanning of potential during an *E*melting experiment.

Whether or not pH change plays a role in *E*melting was tested by another experiment. *E*melting was carried out in a high concentration buffer (pH 7, 500 mM Tris buffer) in order to neutralize any small changes in local pH due its high buffering capacity. The SERS-melting profile for the synthetic ΔF508 target labelled with Texas Red at the 3'-end (same as that used in 6.3.2) hybridized to the probe on gold SSV substrate is presented in Figure 6.27. The melting profile is very similar to that obtained in pH 7, 10 mM Tris buffer with no delay in melting observed as the potential is scanned cathodic. If an increase in pH was responsible for *E*melting then in this case no melting should have been observed since, pH change should have been neutralized, at least partly, by the high concentration of the buffer. Therefore given that denaturation is not inhibited by

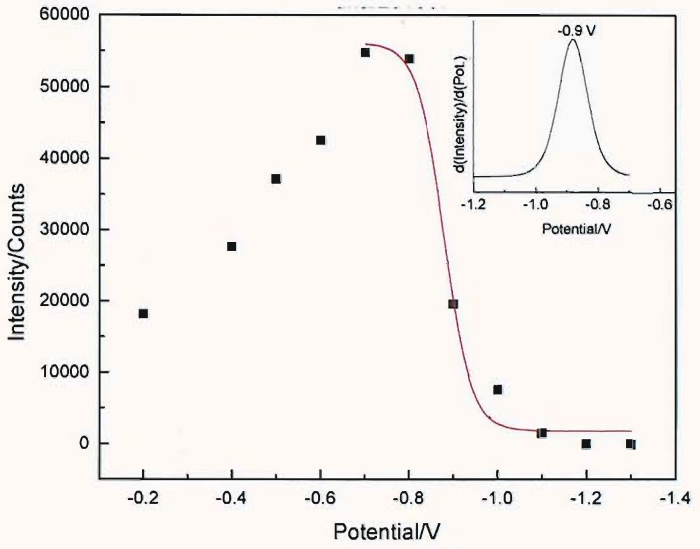

Figure 6.27 SERS-*E*melting profile of the ΔF508 target in pH7, 500 mM Tris buffer solution. The first derivative of the fitted part of the melting profile is plotted in the inset.

the high buffer concentration indicates that pH increase is not the primary factor causing denaturation in an *E*melting experiment.

On the basis of the evidence presented above and also the large range of *E*melting potentials observed (from -0.44 V for the Cy5 labelled ΔF508 PCR product to -1.22 V for Texas Red labelled wild type), it is unlikely that an increase in pH is responsible for the observed electrochemically induced melting. Further, comparing the corresponding *E*melting and *T*melting experimental data (from section 6.3.2), a reasonable correlation is found between the two, as shown in Figure 6.26. This suggests that the *E*melting effect is directly probing the

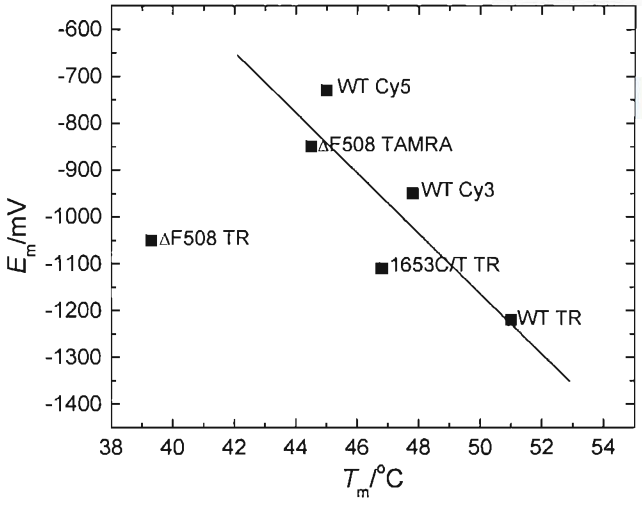

Figure 6.26 The melting potentials (E_m) plotted versus melting temperatures (T_m) for different targets bearing various labels determined from the SERS-melting experiments with the 22-mer oligonucleotide targets.

thermodynamic stability of the duplex. Clearly further work is required to understand the full details of the *E*melting process. Nevertheless the results presented in the chapter prove that SERS-*E*melting is a simple reproducible, sensitive, flexible and accurate method to discriminate mutations.

6.4 Conclusions

The preliminary experiments show that SERS detection on the SSV substrates gives excellent sensitivity and that we can clearly distinguish the signals of the two different dye labels, fluorescein (FAM) and Cy3. It also proved that the attachment of the probe to the gold surface through the 6 thiols (3 disulfides) is robust, that the mercaptohexanol prevents non-specific binding of labelled DNA to the surface and that the SSV surfaces are reusable.

Thereafter 'proof of concept' has been provided of a new method for distinguishing mutations employing SERS detection (termed SERS-melting) on ordered gold sphere segment void substrates. Both thermally and electrochemically induced melting can be followed *in situ* by SERS on SSV substrates. It has been shown that a range of labels with different spectral properties rendering them non-resonant, partially resonant or resonant in SERS experiments can potentially be employed for detection. It is clear that SERRS labels such as Cy5 provide the strongest signals. It has also been established that electrochemically active molecules with SERS signatures can also be utilized with the proposed method and additional benefits such as quantification of hybrids on the surface accrue in this case. The potential utility of the SERS-melting method is also established in a PCR-based application using unpurified amplicons.

Apart from opening up a new field with many open and unanswered questions many practical applications are envisaged leveraging the advantages of SER(R)S over fluorescence and other detection methods especially in being able to combine immense molecule-specific information with high sensitivity. The other advantage of our SERS substrate approach is its fundamental suitability for high throughput analysis, miniaturization and the possibility of multidimensional control of the denaturation process by electrochemical potential, temperature and/or solution composition. Thus, SERS-melting could prove to be an important enabling technology in the fields of diagnostics, genomics and forensic science.

6.5 References

[1] R. T. Ranasinghe and T. Brown, Chem. Commun.:5487 (2005).

[2] Y. C. Cao, R. Jin, and C. A. Mirkin, Science 297:1536 (2002).
[3] M. Culha, D. Stokes, L. R. Allain, and T. Vo-Dinh, Anal. Chem. 75:6196 (2003).
[4] G. Braun, S. J. Lee, M. Dante, T. Q. Nguyen, M. Moskovits, and N. Reich, J. Amer. Chem. Soc. 129:6378 (2007).
[5] K. Faulds, R. P. Barbagallo, J. T. Keer, W. E. Smith, and D. Graham, Analyst 129:567 (2004).
[6] S. Mahajan , M. Abdelsalam, Y. Suguwara, S. Cintra, A. Russell, J. Baumberg, and P. Bartlett, Phys. Chem. Chem. Phys. 9:104 (2007).
[7] J. J. Baumberg, T. Kelf, Y. Sugawara, S. Cintra, M. Abdelsalam, P. N. Bartlett, and A. E. Russell, Nano Lett. 5:2262 (2005).
[8] S. Cintra, M. Abdelsalem, P. N. Bartlett, J. J. Baumberg, T. Kelf, Y. Sugawara, and A. E. Russell, Faraday Discuss. 132:191 (2005).
[9] S. Mahajan, J. Baumberg, A. Russell, and P. Bartlett, Phys. Chem. Chem. Phys. 9:6016 (2007).
[10] B-S. Kerem, J. M. Rommens, J. A. Buchanan, D. Markiewicz, T. K. Cox, A. Chakravarti, M. Buchwald, and L-C. Tsui, Science 245:1073 (1989).
[11] T. M. Herne and M. J. Tarlov, J. Amer. Chem. Soc. 119:8916 (1997).
[12] C.-Y. Lee, P. Gong, G. M. Harbers, D. W. Grainger, D. G. Castner, and L. J. Gamble, Anal. Chem. 78:3316 (2006).
[13] D. Erts, B. Polyakov, H. Olin, and E. Tuite, J. Phys. Chem. B 107:3591 (2003).
[14] A. W. Peterson, R. J. Heaton, and R. M. Georgiadis, Nucl. Acids Res. 21:5163 (2001).
[15] K. Faulds, L. Fruk, D. C. Robson, D. G. Thompson, A. Enright, W. E. Smith, and D. Graham, Faraday Discuss. 132:261 (2006).
[16] K. Faulds, F. McKenzie, W. E. Smith, and D. Graham, Angew. Chem. Int. Ed. 46:1829 (2007).
[17] L. Wang, A. Roitberg, C. Meuse, and A. K. Gaigalas, Spectrochim. Acta A 57:1781 (2001).
[18] Y. C. Cao, R. Jin, and C. A. Mirkin, Science:1536 (2002).
[19] H. Sato, M. Kawasaki, K. Kasatani, and M.-A. Katsumata, J. Raman. Spectrosc. 19:129 (1988).
[20] Q. Ye, J. Fang, and L. Sun, J. Phys. Chem. B 101:8221 (1997).
[21] A. B. Steel, T. M. Herne, and M. J. Tarlov, Anal. Chem. 70:4670 (1998).
[22] R. M. Cole, J. J. Baumberg, F. J. Garcia de Abajo, S. Mahajan, M. Abdelsalam, and P. N. Bartlett, Nano Lett. 7:2094 (2007).
[23] S. Kumamoto, M. Watanabe, N. Kawakami, M. Nakamura, and K. Yamana, Bioconjugate Chem. 19:65 (2008).
[24] K. Yamana, N. Kawakami, T. Ohtsuka, Y. Sugie, H. Nakano, and I. Saito, Nucleic Acids Res. Supplement No. 3:89 (2003).
[25] K. Yamana, S. Kumamoto, T. Hasegawa, H. Nakano, and Y. Sugie, Chem. Lett.:506 (2002).
[26] M. J. Honeychurch and G. A. Rechnitz, Electroanalysis 10:285 (1998).
[27] M. Umadevi and V. Ramakrishnan, Spectrochim. Acta A 58:2941 (2002).
[28] K. Nishiyama, S.-I. Tahara, Y. Uchida, S. Tanoue, and I. Taniguchi, J. Electroanal. Chem. 478:83 (1999).
[29] C. J. Lee, J. S. Kang, Y.-T. Park, K. M. Rezaul, and M. S. Lee, Bull. Korean Chem. Soc. 25:1779 (2004).
[30] K. A. Peterlinz, R. M. Georgiadis, T. M. Herne, and M. J. Tarlov, J. Amer. Chem. Soc. 119:3401 (1997).
[31] J. Bednar, P. Furrer, V. Katritch, A. Z. Stasiak, J. Dubochet, and A. Stasiak, J. Mol. Biol. 254:579 (1995).
[32] G. Manning, Acc. Chem. Res. 12:443 (1979).

[33] C. Nogues, S. R. Cohen, S. S. Daube, and R. Naaman. Phys. Chem. Chem. Phys. 6:4459 (2004).
[34] S. O. Kelley, J. K. Barton, N. M. Jackson, L. D. McPherson, A. B. Potter, E. M. Spain, M. J. Allen, and M. G. Hill, Langmuir 14:6781 (1998).
[35] R. Levicky, T. M. Herne, M. J. Tarlov, and S. K. Satija, J. Amer. Chem. Soc. 120:9787 (1998).
[36] U. Rant, K. Arinaga, S. Fujita, N. Yokoyama, G. Abstreiter, and M. Tornow, Nano Lett. 4:2441 (2004).
[37] U. Rant, K. Arinaga, S. Fujita, N. Yokoyama, G. Abstreitera, and M. Tornowa, Org. Biomol. Chem. 4:3448 (2006).
[38] A. Vainrub and B. M. Pettitt, Chem. Phys. Lett. 323 (2000).
[39] A. Vainrub and B. M. Pettitt, Biopolymers 68:265 (2003).

7 Conclusions and further work

7.1 Conclusions

Work on monolayer assembly of colloidal polystyrene spheres was extended and optimization of the temperature and slant angle conditions was carried out. As a result templates can now be obtained from 200 nm to 1600 nm sphere diameters. The optimized assembly method reproducibly gave large area (1 cm x 1 cm) templates for 400 to 1100 nm. Below 400 nm sphere diameter on account of the low temperatures used the evaporation rate becomes extremely slow, and with 1600 nm the settling rate increases; this reduced the reproducibility, though large areas could still be obtained. Nevertheless, it has to be pointed out that the assembly being a many variable process has to be carried out in the utmost cautious manner failing which it can easily appear to be a random process. In retrospect, it can be stated that cleanliness of the surfaces (base as well as cover glass) at all stages is of primary importance.

From the study of the effect of different thiols on the assembly process, it can be concluded that treatment of evaporated gold surfaces with 10 mM ethanolic solutions of cysteamine yielded the best results. The quality of templates became better if the soaking time of flat gold substrates was extended to a month compared to those obtained after just 48 h of treatment. This improvement in quality was not only due to the hydrophilicity induced by cysteamine adsorption on the surface but also due to a decrease in surface roughness on prolonged treatment.

Though hexagonally packed colloidal crystals were the main emphasis of the work presented in this thesis; the twin templating and wire patterning strategies clearly show the possibilities and the avenues available for further work. The wire patterning with colloidal crystals itself is a unique and promising concept suitable for many applications, which hopefully will be explored in the future.

Further, employing the colloidal crystal templating strategy sphere segment void substrates (SSV) could be obtained with gold, rhodium, palladium, platinum and nickel. This demonstrates the versatility of the templating method although the bulk of the work described in this thesis work pertained to that on gold SSV substrates. Nevertheless, it has been clearly shown that SSV substrates display

interesting optical properties, owing to their plasmonic nature. Due to their plasmonic properties they are suitable for SERS. In this thesis the correlation between plasmons and SERS enhancements is unambiguously established for visible as well as near IR SERS. This has also been found true for air as well as water as the medium and for gold, palladium and platinum metal SSV substrates. The maximum SERS enhancements are coincident with the maximum plasmonic absorption on the substrates. Two modes; the $^1P+$ and the $^1P-$ have been identified as the most prominent plasmon modes leading to SERS on SSV substrates with a 633 nm laser.

The issue of the spectral continuum observed in SERS has been explored in some detail on SSV substrates. The studies enable some very explicit conclusions to be drawn such as that SERS intensities and the background are strongly correlated; the background increases on adsorption of molecules as observed in air. Further, the background is enhanced in a similar manner as SERS since the intensity maxima of the background have been found to be directly correlated to the strength of plasmonic absorptions on the substrates. Also the background increases when an electron withdrawing molecule displaces an electron donating molecule on the surface and *vice versa* as observed in thiol exchange experiments in solution. The enhanced background observed in SERRS is not simple fluorescence as it is not inhibited by the presence of a quencher on the molecule. In the anti-Stokes region the background is negligible compared to the corresponding region in the Stokes SER spectrum. These observations have permitted the drawing up of a preliminary model for the background observed on SSV substrates.

The SERRS study on SSV substrates establishes its reproducibility on gold SSV substrates. It also enables the conclusion that SERS and the resonance effect are multiplicative leading to an enhancement of the order of $\sim 10^9$ on SSV substrates. This clearly demonstrated that highly sensitive detection is feasible utilizing SERRS on SSV substrates.

Studies with DNA sequences establish the unique stability, repeatability and high sensitivity of detection with SSV substrates. The method of SERS-melting has been proved to be successful in detecting mutations using either thermal or electrochemical denaturation on SSV substrates. Again this application clearly shows the thermal, electrochemical and solution stability of SSV substrates and the reproducibility of the processes observed on them. The method itself is novel

in employing SER(R)S for distinguishing mutations and hence, the consequent advantages in flexibility of labels and immense molecule specific information obtained can be realized. A full spectral range of dyes right from being non-resonant, partially resonant or fully resonant with the laser can be potentially employed in SERS-melting experiments. The fact that SSV substrates are electronically conducting in nature adds a further advantage of simultaneous electrochemical interrogation by choosing appropriate markers as shown with anthraquinone labelled sequences. The mechanism of electrochemically induced melting has also been investigated and it can be concluded that pH changes near the surface do not seem to be the primary factor causing the melting of DNA duplexes on the surface.

7.2 Further work

Further work is necessary to increase the reproducibility of self-assembly of spheres sizes below 400 nm and above 1600 nm. For the twin templating patterns observed during this thesis work opportunity exists for studying these using the concept of tiles (tesselations) and Voronoi diagrams for which software are available on the web.

The SSV patterning of wires has been carried out with Rhodium and gold but only with 600 nm diameter sphere templates. Larger spheres, around 1000 nm diameter, templated structures are required to shift the blackbody emission modulation into the near IR. This emission work is highly promising and needs to be pursued further.

The finding that the $^{1}P+$ and $^{1}P-$ modes are the most important for SERS with a 633 nm laser excitation also points to further study. Similar systematic experiments with other lasers especially, 785 nm need to carried out to find whether other modes lead or do not lead to SERS enhancements and the reasons therein. Furthermore, the involvement of these two modes in SERS predicts that the enhancements originate from different places in the voids. These positions can be switched by changing the medium as well as the sphere size or the laser wavelength. This prediction needs to be tested by design of suitable experiments such as putting different molecules on the rim and in the void itself. Another avenue which requires further investigation is the low energy mode currently postulated to originate in the windows existing between neighbouring voids which has been found to scale into the infrared region. Although non-close packed samples fabricated by the double templating method showed the absence of the

low energy mode the samples were not very uniform. Therefore, this line of investigation could not be pursued vigorously and more samples with different periodicities need to be fabricated to reach a full conclusion.

The model for the background obviously needs rigorous testing and probably, improvement to stand the test of time. Studies with a greater number of molecules and with different lasers including anti-Stokes studies are necessary. The dependence on surface roughness can be tested by simple experiments such as seeing the effect of electrochemical cycling in acid on the background. The proposed model relies on generation of electron-hole pairs, which have a spatial dispersion of less than 0.5 nm unlike SPPs which can have a dispersion of ~100 nm. Hence, even a thin layer of oxide/damping material should completely alter the background in SERS. This prediction needs to be tested.

The SERS-melting method with DNA sequences opens a new area with many open questions to be answered. These include the dependence of melting on the length of the sequence, position of the mutation relative to the surface and the dependence on the label. Optimization of the label is also required. The mechanism of thermal and electrochemical melting on surfaces needs to be studied in detail and modelled. In the thermal melting of DNA duplexes in solutions the denaturation temperature becomes higher and the melting profile becomes sharper with increasing salt concentrations. This has been tested on SSV substrates but only a few experiments have been done so far and more are required. One experiment which showed an increase in melting temperature on increasing the salt concentration is shown in Figure 7.1. The melting of ΔF508

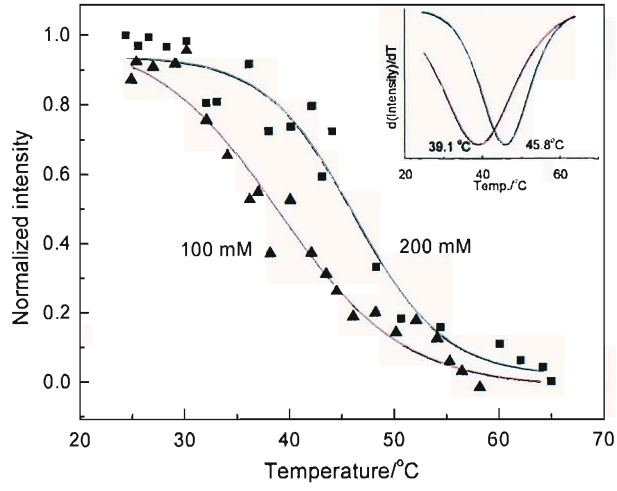

Figure 7.1 SERS-*T*melting with ΔF508 target at 100 and 200 mM salt concentrations in a 0.01 M pH 8.1 phosphate buffer. The intensities have been normalized to their maximum value obtained during each of the runs. The first derivatives of the sigmoidal fits to the melting profiles are shown in the inset. The runs were carried out on different substrates.

target was carried out in 0.01 M phosphate buffer containing 100 and 200 mM NaCl, respectively. The melting temperatures show an increase of 5-6 degC. These experiments need to be done over a wider range of ionic strength and on the same substrate (if possible).

With electrochemically induced melting the increase in ionic strength is expected to have two effects, one is to increase the stability of the duplex as observed in solution melting studies and the second is to reduce the double layer thickness. It was expected that at salt concentrations beyond 1 M NaCl when the extent of the electric field (double layer thickness) reduces below 0.1 nm electrochemical melting should be inhibited. However, the opposite has been observed in present

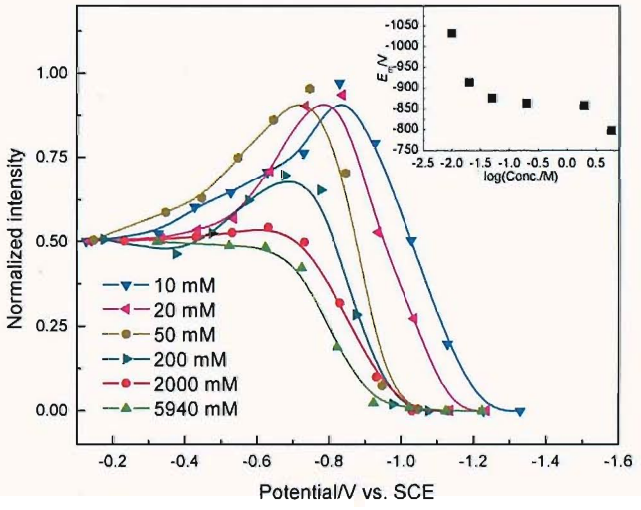

Figure 7.2 SERS-*E*melting profiles of ΔF508 target in pH 7, 10 mM Tris buffer containing different salt concentrations. The melting potentials are shown in the inset.

experiments as shown in Figure 7.2. The melting potentials show a decreasing trend though a plateau is observed at intermediate concentrations even after correcting for the change in the reference potential of the Ag/AgCl electrode with increasing chloride concentration. It is noted that the maximum in the intensity attributed to the change in orientation of the label decreases with increasing salt concentration. So the label does not see the electric field due to increased screening yet the melting takes place. Another feature observed is the slight change in the shape of the SERS-Emelting profile at higher concentrations of salt becoming more gradual (less sharp) compared to *E*melting at lower salt concentrations. This behaviour of Emelting with increasing ionic concentrations is intriguing and needs to be studied in detail including the possibility of the dependence of reductive desorption of thiols on ionic strength.

Another area with great promise is label-free detection with SER(R)S, wherein the need to label targets is done away with. Among the many approaches possible, one using an intercalating probe was investigated and is discussed here.

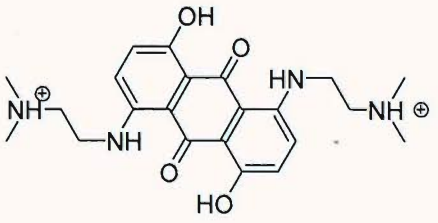

Figure 7.4 Structure of DRAQ5

The intercalation methodology is widely used in fluorescence melting measurements and the same strategy was used with SER(R)S detection on SSV substrates. First attempts were carried out with a simple chloro-anthraquinone with which no signals could be observed from the intercalator probably due to its high hyrdophobicity preventing its localization near the surface. Another trial was carried out with 7-aminoactinamycin which is another well known groove binding intercalator without any success. Then DRAQ5 (Biostatus Ltd.), which is also a modified anthraquinone intercalator possessing hydroxyl and amino groups was used (structure shown in Figure 7.4). DRAQ5 (λ_{max}: 646 nm) is also resonant with 633 nm laser used and binds exclusively to dsDNA; hence, in principle melting profiles can be easily obtained. Results[1] from one of the few times the experiment worked are shown in Figure 7.3. Two problems were encountered; that of non-specific binding owing to the hydrophilic and electropositive nature of the

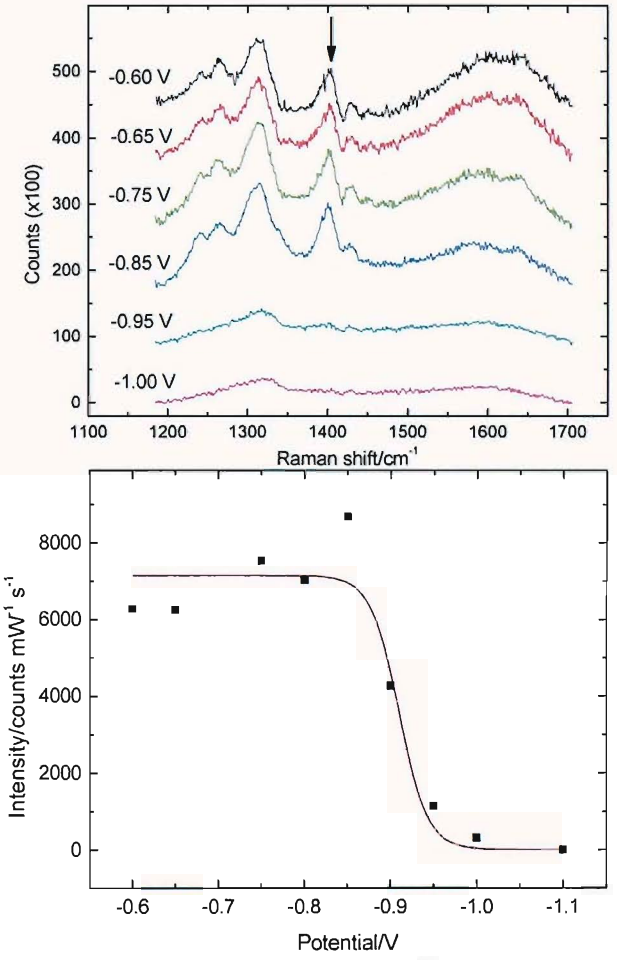

Figure 7.3 Representative spectra at different potentials for DRAQ5 intercalated into a ΔF508 target-hybrid (top) in pH 7, 10 mM Tris acquired with a 633 nm laser (3 accumulations of 2 s each). Label free resonant SERS-melting profile (bottom) using the background corrected intensities of the 1402 cm^{-1} band in the DRAQ5 spectrum.

[1] Hybridization was carried out for 1 h with label free target followed by soaking in 25 μM DRAQ5 solution in pH 7 10 mM Tris with 100 mM NaCl for 10 min. The surface was then washed with pH 7 10 mM Tris buffer before commencing *E*melting experiment.

molecule and that due to the weak peaks at open circuit potential. The non-specific binding was confirmed by carrying out experiments with the intercalator treatment in the absence of target and without immobilized probe. Due to this, differentiation between mutations and wild type has not been possible so far and it is felt that further optimization of the passivation conditions by mercaptohexanol (or longer thiol) and/or concentration of intercalator used in solution is necessary to obtain clear results. An electro-inactive, SERRS active, intercalator binding selectively to dsDNA (and not to ssDNA) would be ideal for label free detection and should be tried, if further headway with DRAQ5 cannot be made.

At the end it would be apt to conclude that an overwhelming number of ideas remain to be implemented and work remains to be carried out using the concepts of colloidal templating, SERS on SSV substrates, biosensing applications etc. propounded in this thesis and prevailing in the group. It would not be an exaggeration to admit that the research work during the duration of this thesis was highly fulfilling to me. This satisfaction not only stems from the output results discussed in the thesis but also for being able to explore so many different things, many of which could not be presented in the thesis because they were rather out of fun and incoherent with the work presented. Therefore, it would be reiterated that innumerable opportunities continue to exist and are limited only by one's imagination.

Appendix 1

Surface area of sphere segment voids

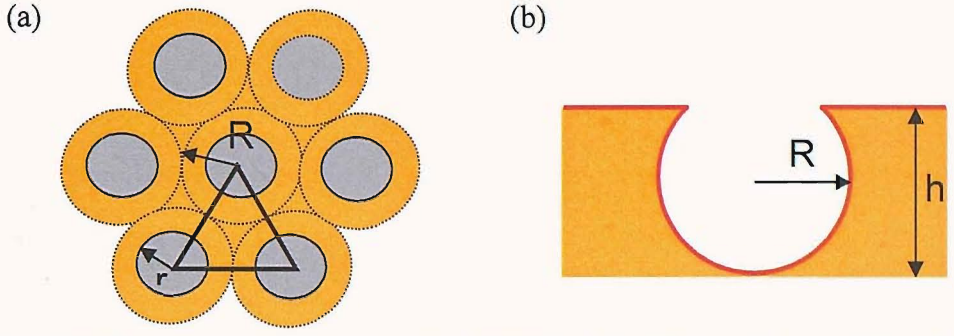

Figure 1. (a) Schematic of the arrangement of voids in the ideal packing condition. The dotted lines show the original positions of the spheres in the template in a hexagonal close packed arrangement. The equilateral triangle is the unit cell for the arrangement of voids. (b) Side view of a void embedded in the electrodeposited metal. For calculation of the surface area of sphere segment voids the inside as well as the top surface is taken into account (outline shown in dark orange).

The expression for the total area (S) of sphere segment voids with reference to the unit cell shown in Figure 1 is given by Equation 1.

$$S = \frac{1}{2}\pi Rh + \sqrt{3}R^2 + \frac{\pi}{4}h^2 \qquad 1$$

Where R is the radius of the sphere used for templating the voids and h is the film height (the electrodeposited thickness).

Using Equation 1, the geometrical surface "roughness" factor (G_R) can be theoretically estimated. The equation for G_R is given by Equation 2, where the unit cell area is $\sqrt{3}R^2$ (the plan area):

$$G_R = \frac{\frac{1}{2}\pi Rh + \sqrt{3}R^2 + \frac{\pi}{4}h^2}{\sqrt{3}R^2} \qquad 2$$

Hence, with this expression for h= 2R G_R will be 4.63; while for h=0, G_R will be equal to 1.